AD-A148 081   THE SHOCK AND VIBRATION BULLETIN PART 3 VIBRATION   1/3
               TESTING INSTRUMENTATION..(U) NAVAL RESEARCH LAB
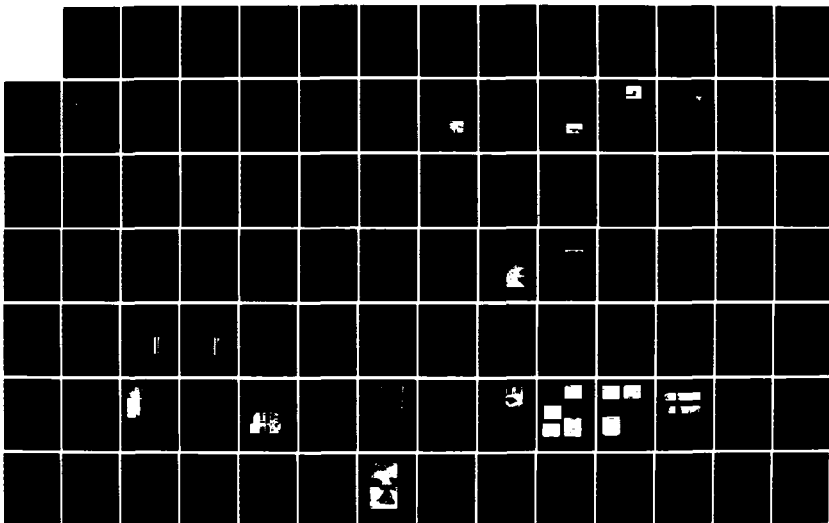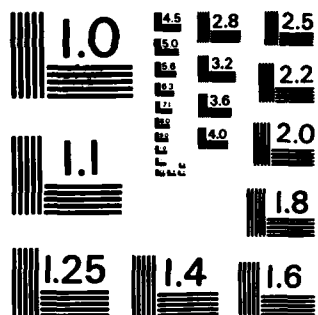   WASHINGTON DC SHOCK AND VIBRATION INFORMAT..   SEP 77
UNCLASSIFIED   BULL-47-PT-3   F/G 20/11   NL

MICROCOPY RESOLUTION TEST CHART
NATIONAL BUREAU OF STANDARDS-1963-A

AD-A148 081

THE SHOCK AND VIBRATION BULLETIN

Part 3
Vibration Testing, Instumentation and Data Analysis,
Loads and Environments

SEPTEMBER 1977

A Publication of
THE SHOCK AND VIBRATION
INFORMATION CENTER
Naval Research Laboratory, Washington, D.C.

Office of
The Director of Defense
Research and Engineering

84 11 26 197

SYMPOSIUM MANAGEMENT

THE SHOCK AND VIBRATION INFORMATION CENTER

Henry C. Pusey, Director
Rudolph H. Volin
J. Gordan Showalter
Barbara Szymanski
Carol Healey

Bulletin Production

THE
SHOCK AND VIBRATION
BULLETIN

SEPTEMBER 1977

A Publication of
THE SHOCK AND VIBRATION
INFORMATION CENTER
Naval Research Laboratory, Washington, D.C.

The 47th Symposium on Shock and Vibration was held
at the Albuquerque Inn and Convention Center, Albu-
querque, New Mexico on October 19-21, 1976. The
Defense Nuclear Agency, Washington, D.C., the Field
Command Defense Nuclear Agency, and the Air Force
Weapons Laboratory, Kirtland Air Force Base, New
Mexico were the hosts.

Office of
The Director of Defense
Research and Engineering

CONTENTS

iii

PAPERS APPEARING IN PART 1

Keynote Address

IMPACTS OF SHOCK AND VIBRATION CONSIDERATIONS ON WEAPON
    DEVELOPMENT
    Dr. Hua Lin, Assistant Director (Offensive Systems) Office Director of
    Defense Research and Engineering, Washington, DC

Invited Paper

NUCLEAR HARDENING IN A MISSILE DEFENSE SYSTEM
    Noah J. Hurst, Ballistic Missile Defense Systems Command, Huntsville, AL

Panel Session

DYNAMICS EFFECTS ON RELIABILITY

Shock Analysis

SCALING OF STRONG SHOCK HUGONIOTS
    W.E. Baker, Southwest Research Institute, San Antonio, TX

SHOCK SPECTRA AND RESPONSES BY POCKET CALCULATOR
    C.T. Morrow, Consultant, Dallas, TX

IMPACT RESPONSE MODELING OF BULK CUSHIONING SYSTEMS ON A
PROGRAMMABLE DESK-TOP CALCULATOR
    D.M. McDaniel, U.S. Army Missile Command, Redstone Arsenal, AL and
    R.M. Wyskida, J.D. Johannes, The University of Alabama in Huntsville,
    Huntsville, AL

PAPERS APPEARING IN PART 2

Vibration Analysis

PAPERS APPEARING IN PART 4

Structural Dynamics

VIBRATION TESTING

COST-EFFECTIVELY EXCITING VIBRATION FAILURE MODES
FOR LONG-TIME RELIABILITY DEMONSTRATIONS

Wayne Tustin
Tustin Institute of Technology, Inc.
Santa Barbara, California

The principal purpose of this paper is to review various methods
for inducing vibration failure modes. Cost-effective methods are
emphasized.

In-flight vibration and noise aboard high-performance military aircraft are known to reduce the reliability of

avionics units within the aircraft, &

externally-carried weapons and stores.

Relatively ancient reliability-demonstration tests which incorporated sinusoidal vibration testing have resulted in mean times between failure (MTBF's) far superior to in-service experience. Optimism factors range as high as 20:1.[1]

Many authorities feel that random vibration is far superior to sinusoidal vibration for simulating the effects of in-flight vibration.[2] Certain modes of vibration-induced failure, found in flight and in random vibration testing, never appear with sinusoidal vibration.

Certain authorities[3] feel that vibration and other harmful environments should not be applied sequentially, but rather simultaneously. A mild form of combined-environment testing was required by *MIL-STD-781, -781A* and *-781B*. Much more vigorous vibration, in many cases random, is required by *MIL-STD-781C*[4] etc. The amount of combined-environment reliability testing being done today is still rather small, but results are highly encouraging. Laboratory failure modes closely resemble in-flight failure modes, Laboratory MTBF's closely approximate in-service MTBF's.[5]

Other authorities feel that laboratory attempts to simulate in-flight vibration by means of shakers (of any type, utilizing either sine or random forcing) are doomed to failure. They feel that reliability-demonstration and other dynamics testing should incorporate intense-noise acoustic forcing.[6]

In view of these and related controversies, it seems appropriate to review the different methods of inducing vibration failure modes. Individuals who argue test methods and applications can at least agree on descriptions of test machines. A brief history of the development of today's shaker systems may interest newcomers to the field and help them to understand today's test equipment and methods. The advantages and disadvantages of each method will be examined. Costs are given some consideration.

MECHANICAL SHAKERS Nearly all shakers (except for calibration) used during the 'forties and the early 'fifties for the nominally-sinusoidal tests of the era were mechanical. Designers attempted to create pure sinusoidal motion but unavoidable loosenees, gear drives and bearings introduced considerable distortion. The upper frequency limit was 100 Hz.

1

At that time the principal advantages of mechanical shakers were that they:

(1) were cheap to build,

(2) used design technology available at that time,

(3) were highly reliable,

(4) had large tables for mounting test items, and

(5) easily supported test items without any external springs.

Advantage (3) is most important for long-time reliability demonstrations. Neither of the other types of shakers (electro-hydraulic or electromagnetic), discussed later, while widely used today in aerospace testing laboratories, has achieved the reliability needed for long-time reliability-demonstration testing.

Advantage (1) is still important, particularly when one considers the great increase in the amount of random vibration testing which will be required.
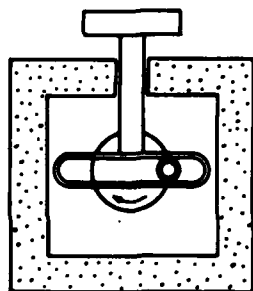
Figure 1. Concept of simplest type shaker

The earliest practical vibration generators were simple "brute force" or "direct drive" machines, as suggested by Figure 1. Variable-ratio pulleys give variable shaft speed. Shaft rotation is converted by a cam or yoke to variable-forcing-frequency f_f reciprocating motion of a shaft attached to a table. Items to be tested are attached to the table. f_f can be adjusted during a test, but resetting the peak-to-peak displacement or stroke D requires interrupting the test. Generated force F may be calculated by F = MA, where M is the total mass of vibrating parts (load + any attachment fixture + table) and A is the maximum acceleration. If the total mass M is too great, F may exceed the shaker's strength limitations, causing damage to the shaker.

With other types of shakers discussed later, vibratory force F is limited. The available acceleration A varies inversely with the total mass M, as

$$A = \frac{F}{M} .$$

Several advantages were gained by the added sophistication of the "reaction type" shakers suggested by Figure 2. Contra-rotating masses, locked together in phase, spin at the adjustable forcing frequency f_f. Most such shakers must be stopped in order to readjust the unbalance masses for a different vibration intensity.
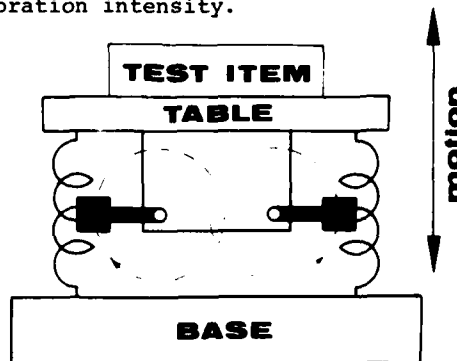
Figure 2. Concept of improved "reaction" shaker

Reaction shakers cost more than do direct drive shakers, but generally go to higher frequencies with a cleaner waveform having less "hash" and less harmonic distortion. Further, installation is eased because only small reaction vibratory forces pass through the base. By contrast, most direct-drive shakers are attached to heavy reaction masses in turn supported by rubber or springs.

A number of shakers of various types have been designed to fit environmental chambers in order to permit combined environmental tests.[7] These have mainly been mechanical shakers, not only the least expensive but also the only type capable of operating for hundreds of hours without failure. These superiorities are encouraging the development of inexpensive, reliable, large-table mechanical shakers capable of a form of vibration that at least approaches the broad, continuous spectrum (and Gaussian amplitude probability density) random vibration required by many test specifications, current and near future.

2

The "Rotocon" shaker[8,9] features a series of hammers attached to a 3 000 rev/min rotating element. These hammers strike an anvil, to which is attached the test item. The resulting force and motion have a line spectrum, a line every 50 Hz (as opposed to a continuous spectrum) to 10 000 Hz.

Marshall[10] has described a machine with a number of unbalanced rotating masses, the f_f of each being tuned to produce a line spectrum at approximately 1/3-octave intervals. His goal is the simultaneous excitation of all test item resonances. He is not attempting to produce Gaussian distribution, but rather a collection of simultaneous sinusoids.

Hubbard[11] describes a mechanical random vibrator attached to the underside of a table which can form the vibrating floor of an environmental chamber, much as *MIL-STD-781* combined-environmental tests are now being run. The vibrator employs a "wobble plate" and hammer assembly that apply vertical impacts against an anvil plate. Motor speed and point of impact vary continually, producing $2g$ RMS into a 500 pound load, and as much as $10g$ into lighter loads. The spectrum is by no means flat, but it does appear to be continuous from perhaps 50 to 5 000 Hz, with most energy between 300 and 3 500 Hz. The amplitude distribution appears rather Gaussian. Motion of the large table surface generates considerable noise pollution, as much as 90 dBA for $3g$ RMS and over 110 dBA for $10g$ RMS, at 3 feet distance. This is not troublesome when the shaker is used with a chamber. Cost of the entire shaker and controls is said to be under $10,000.

Klass[1] reported a rumor that Hughes Aircraft (Culver City) had devised a low-cost modification to sinusoidal mechanical shakers, attaching one or more drums partially filled with ball bearings between shaker and load. However, the writer understands the Hughes efforts more closely resemble those of General Dynamics (Pomona)[21], discussed later, which employ pneumatic vibrators.

One significant disadvantage of mechanical shakers is that they lack "feedback loops" (as with electrohydraulic and electromagnetic shakers). Thus loads on mechanical shakers can and do affect their own vibration environment. This is a difficulty only when one attempts to meet the usual present-day constant-motion MIL-type test specifications and standards. In a sense, this lack is an advantage, when one reflects that loads mounted in aircraft, on ships etc. clearly affect their own vibration environments.

ELECTROHYDRAULIC SHAKER The tremendous dynamic force that is available from hydraulic actuators, makes these very attractive for generating vibratory force and motion. This dynamic force became available for vibration testing in the mid-fifties when actuators were first combined with fast-acting electronic servo valves. Figure 3 suggests the major elements of a complete system. The "input" signal here is taken from a signal oscillator for nominally-sinusoidal vibration testing. However, it can also be taken from a tape playback[12] in order to reproduce (in the laboratory) some previously-recorded vibration. It can also be taken from a noise generator in order to synthesize random vibration.[13] Either line or continuous vibration spectra can be generated.
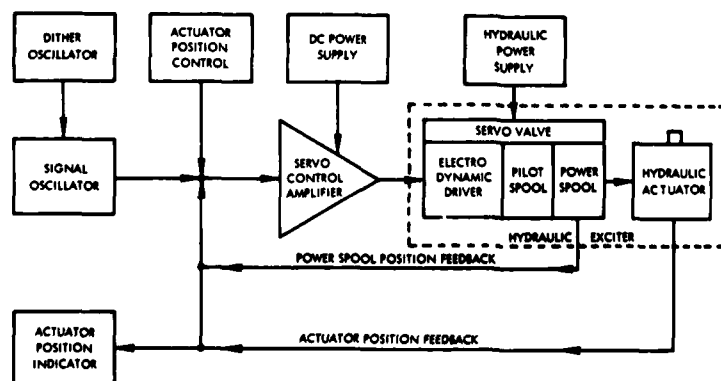
Figure 3. Major elements of electrohydraulic shaker system

3

Figure 4 shows a load or test item attached via a table (not always provided) to the shaker's piston. High pressure oil, typically $2\,000\ \text{lb/in}^2$ net, is valved alternately to the two sides of the piston. This valving is accomplished by an electromagnetic (electrodynamic) driver unit which in principle resembles a loudspeaker, and a power valve or "hydraulic amplifier." Typical piston strokes D are 4 to 6 inches, although some (mainly intended for higher-frequency testing to perhaps 200 Hz) are 1 inch or less. One manufacturer claims $2\,000\ \text{Hz}$ capability. The maximum D known to the author is 20 feet.[14] The low-frequency limit of electrohydraulic shakers is usually zero.
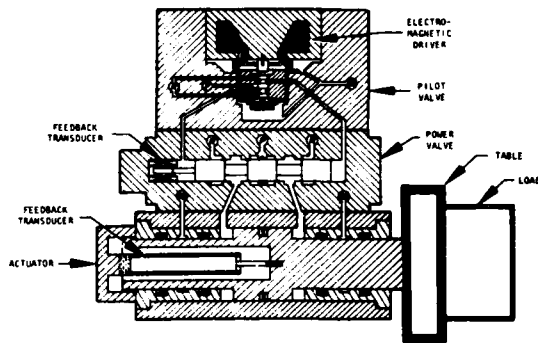
Figure 4. Electrohydraulic shaker construction

Force and acceleration are limited by pressure and piston area. Still another limitation, peak or vector velocity, must be considered; it may be caused by insufficient hydraulic supply flow or by insufficient opening of the power valve.

Waveforms are generally considered to be better than with mechanical shakers but are not as "clean" as with the electromagnetic shakers to be discussed below.

As generated force is usually many times greater than shaker mass, the shaker must be "backed up" by a heavy reaction mass, if much vibratory force is to be introduced into a large test structure. When the test article can be brought to the shaker, as in an environmental testing laboratory, this creates little difficulty. But for portable operations, where shakers are taken to large, fixed structures, it is an extra complication. Others: high pressure oil hoses tend to be stiff and awkward, also cooling the oil may be difficult.

Four or more laboratory electrohydraulic shakers are often connected to large loads such as trucks. Sometimes the shakers vibrate an intermediate platform on which the load rests, as in simulating transportation or earthquakes. Generally the shakers vibrate horizontally or vertically, but they are sometimes set at an intermediate angle so that the resulting motion has both vertical and horizontal components. Sometimes vertical and horizontal-acting shakers simultaneously drive a common load via hydrostatic spherical couplings.[15]

Multiple shakers may be driven by a common electronic signal source, if coherence is desired, or by separate signal sources.

One of today's most interesting shaker applications is earthquake simulation, requiring forces and motions over continuous spectra from perhaps 0.5 to 50 Hz, with greatest energy 6 to 10 Hz.[16 17 18]

Most mechanical and electromagnetic shakers provide a "table" for attaching the test load, either directly or via some form of adapting fixture.[19] However, electrohydraulic shakers usually provide only a threaded shaft connection. The user often combines a table with a fixture to hold the test item, then threads the combination onto the shaft.

The shaft can pass through the floor or wall of an environmental chamber so that test items can receive several environmental stresses simultaneously, with the shaker outside.

ELECTROMAGNETIC SHAKERS These are also called electrodynamic shakers, probably because of their similarity to electrodynamic loudspeakers. Figure 5 identifies some of the essential parts. Magnetic flux passes through a cast steel body and across a gap in which is located the driver coil. Alternating current at the vibration test forcing frequency f_f flows in that coil, and the developed force F is proportional to
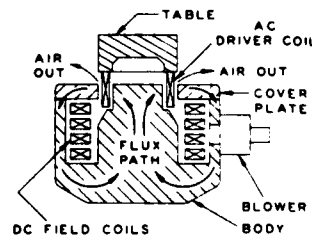
Figure 5. Electromagnetic shaker construction

4

current magnitude I. The magnetic flux is generated by permanent magnets (in the case of shakers with force F rating to 100 pounds or 440 newtons) or by direct current flowing in field coils, as shown, in the case of larger shakers. Current flow generates I^2R losses, and heated air is blown out as shown, or is sucked out, either by a fan mounted on the shaker or at the end of a duct. Many shakers utilize flow of oil or of distilled water for heat removal.

Combined environment testing *circa* 1960 utilized liquid-cooled electromagnetic shakers inside environmental test chambers, so that test items could be close-coupled to shaker tables (necessary for testing to say 2 000 Hz). However, most laboratories today keep the shaker outside the chamber, and connect to the test load through the chamber wall or floor.[7 20]

Not shown in Figure 5 are the electrical connections to the usual multi-turn driver coil. These leads fail often. This weakness has been eliminated in one recent high-reliability design that employs an aluminum sheet single turn coil into which high AC currents are induced by transformer action.

Also not shown in Figure 5 are provisions for shielding test items against stray magnetic fields, which may harm the test item. The flexures that constrain motion to a straight line were also omitted.

As with electrohydraulic shakers, the source of signal may be a sinusoidal oscillator, tape playback or a random noise generator or any combination of these, depending upon the type of force o. motion desired. However, considerably more power amplification is required, up to 150 kilowatts for the larger shakers having force ratings F over 30 000 pounds (133 000 newtons). Today's solid-state power amplifiers offer many advantages (over earlier power-tube types), including greatly increased reliability.

Electromagnetic shakers respond to any frequency down to zero, but not all power amplifiers will deliver power at extremely low frequencies. The high-frequency limit is usually somewhat below one of the table/coil assembly's natural frequencies, which should be avoided:

(1) table oil-canning or dia-phragming, in which the center of the table has perhaps 50 times greater motion than the edges, also

(2) axial resonance, in which the table/coil assembly alternately lengthens and shortens.

PNEUMATIC SHAKERS Air-driven vibrators[8] offer an inexpensive and reliable approach to generating motions and forces, if one is willing to forego demands for pure sinusoidal motion, demands for "flat" random spectra, demands for reproducing magnetic tapes, etc. The driving units are usually adapted from the pneumatic vibrators employed by industry to move bulk materials, to release entrapped gasses from castings, etc. Pistons alternately strike cyl-inder ends, creating repetitive shock impulses, and resulting in vibration line spectra. Such motion and force spectra simultaneously excite all the response modes of electronic assemblies being tested and thereby cause failures among poorly-soldered connections, cause bits of wire, loose screws, etc. to dance about and be identified.

With current interest in more realistic reliability demonstration tests on avionics units and missiles, several USA laboratories are utilizing pneumatic shakers. Van de Griff *et al*[21] describe one longitudinal and 8 radial (at different missile locations) General Dynamics/Pomona pneumatic shakers delivering 6 to 14 *g* RMS vibration at frequencies up to 5 000 Hz. Varying the air pressure at about 7 Hz "smears" the spectral lines so that internal vibration responses have fairly continuous spectra, with shapes approximating the responses noted during flight tests. The amplitude distribution is somewhat Gaussian. The repetition rate is 30 to 120 impacts/second.

ACOUSTIC SOURCES   All the shakers described herein generate force mechani-cally and couple it mechanically into items being investigated or tested. This is a reasonable approach at low frequencies, where service vibration is generated and transmitted mechanically.

However, particularly aboard high-performance aircraft and missiles, the vibration path is not exclusively mechanical. Rather, air forms an im-portant part of the transmission path. It seems logical, then, for high-frequency tests, to utilize intense

sound (airborne vibration), rather than shakers, in order to generate vibratory responses of avionic and missile internal parts.

Eldred[22] wrote about large scale USA vibroacoustic facilities and why acoustic tests are preferred. Murray[23] described the design, construction, instrumentation and usage of the large Wyle chamber at Huntsville. Wren et al[24] similarly described the NASA facility at Houston. In a related paper, Peverley[25] discussed the acoustic energy needed to conduct vibration tests at NASA Houston. Demas[26] told about the "launch phase simulator" at NASA-Goddard, in which temperature and altitude extremes, along with vibration and noise, act on a specimen being spun on a centrifuge.

Most vibroacoustic test facilities employ high-velocity flow of vast quantities of nitrogen gas or of air. Flow is modulated by fast-acting valves, either electromagnetically (similar to Figure 5) or electrohydraulically (similar to Figure 4) driven. Valves are generally activated by random noise generators and suitable power amplifiers, in order to create a flow containing all desired test frequencies in a continuous spectrum. Equalizers permit shaping the spectrum as desired. Slusser[27] described the JPL/Pasadena facility, with particular emphasis on its digital controls.

After passing through the valve, the gas expands through a horn which opens into the test chamber, in which the test article is supported. Chamber dimensions must be quite large in order to develop high intensity at low audio test frequencies. Large chambers unfortunately require much acoustic power in order to develop high acoustic pressures as specified for many tests.

A simpler, less expensive approach utilizes a complex of sirens (up to 35 of them) to modulate air flow and to produce up to 35 pure or narrow band tones, fixed or sweeping. By sweeping these at different rates, continuous-spectrum sound is developed. Kolb and Magrath[28] discussed the 156 000 cubic foot chamber at Wright-Patterson Air Force Base (WPAFB), which features 1 000 000 watts acoustic power and intensities to 170 db. 40 000 hp is used for the air compressor. Maurer[29] and Van der Heyde[30] described tests in the WPAFB noise chamber.

One of the goals of acoustic tests is to excite high-frequency vibratory responses of exceedingly small components in large assemblies. Such tests are also very useful for "burn in" tests of vast numbers of unmounted components. Some reliability specialists feel these tests should be extended to lower frequencies. The necessary large test chambers are unfortunately very expensive to build, but a few organizations could cooperatively fill them with vast numbers of components simultaneously needing acoustic "burn in."

Most chambers are reverberant, with maximum reflections from internal surfaces, but with a design that maximizes dispersion so as to minimize standing waves. Some chambers are progressive wave, rather than reverberant. Chamber design (massive construction) and external acoustic treatment minimize sound leaks to personnel spaces outside the chamber. Chambers are costly and hard to relocate. Hancock et al[31] in 1975 surveyed USA acoustic testing facilities.

Everett[6] describes current noise + temperature extremes for tests on Navy missile electronics sections. Laboratory failure modes and MTBF's closely resemble those found on similar missiles when captive-carried by Navy aircraft.

CONCLUSIONS The principal purpose of this paper is to review various methods for inducing vibration failure modes. Cost-effective methods are emphasized. By this is meant:

(1) Laboratory vibration should induce failure modes similar to those induced by actual in-flight service.

(2) Laboratory MTBF's should approximate those observed in actual in-flight service.

(3) Equipment costs, operation costs and maintenance costs are reduced, if possible. Modifying traditional test methods and permitting novel shaker types may permit such reductions and yet may accomplish the desired stimulation of vibration failure modes.

The author recognizes that for some applications laboratory vibration should truly be random, with a continuous spectrum equalized to a particular shape (as, for example, in Method 514.2-IV of MIL-STD-781C), with

tolerances on that shape held to ±3 dB (or even closer), and, finally, with Gaussian amplitude probability density. But he feels that for long-term reliability demonstration tests, such sophistication is not required.

The military services should ease their demands, and should encourage the development of excitation methods that do the necessary job (similar failure modes and similar MTBF's). This goal may well be reached via some form of mechanical or pneumatic shaker, at quite low cost. Such a goal is certainly worthwhile, when one considers the tremendous cost of hundreds of electrohydraulic and electromagnetic shakers, acoustic sources and chambers, driving amplifiers, random equalizers, etc.

REFERENCES

1. P. J. Klass, "Reliability Test Procedure Changes Set," *Aviation Week & Space Technology*, pp. 59-60, April 19, 1976.

2. F. Kube and G. Hirschberger, "An Investigation to Determine Effective Equipment Environmental Acceptance Test Methods," Report No. ADR 14-04-73.2, Grumman Aerospace Corp., April 1973.

3. Lt. Col. Ben H. Swett, "Avionics Reliability," Part I in Sept/Oct issue and Part II in Nov/Dec 1975 issue, *The Journal of Environmental Sciences*. Also appeared in *The Shock and Vibration Bulletin 45*, Part 2.

4. *Draft Military Standard MIL-STD-781C*, drafts dated 5 Mar 1976 & 30 Aug 1976.

5. David K. Prather and David L. Earls, "Combined Environment Reliability Test (CERT) for Avionics Subsystems," *The Journal of Environmental Sciences*, Mar/Apr 1976, pp. 11-22.

6. Douglas W. Everett, "Thermo-Acoustic Simulation of Captive Flight Environment," *Shock and Vibration Bulletin 46*, Part III, pg. 103-112, August 1976.

7. Wayne Tustin, "Combined Environmental Testing," *Shock, Vibration & Associated Environments, Part III, Bulletin 27*, June 1959.

8. Wayne Tustin, "Inexpensive Approaches to Random Vibration Testing," *Test Engineering and Management*, Apr/May 1976.

9. Daniel Lieberman, "Vibration Testing as a QA/QC Tool," *Test Engineering and Management*, June 1968.

10. Philip Marshall, private discussion at IES Meeting, Seattle WA, August 1976, Mr. Marshall's business address is M/RAD, 112 Cummings Park, Woburn, MA 01801.

11. J. T. Hubbard, private correspondence April 1976. Mr. Hubbard's business address is L.A.B. Div., 968 Onandaga St., Skaneateles, NY 13152.

12. Wayne Tustin, "Basic Considerations for Simulation of Vibration Environments," *Experimental Mechanics*, Sept. 1973.

13. Allen J. Curtis, Nickolas G. Tinling and Henry T. Abstein, Jr., *Selection and Performance of Vibration Tests*, SVM-8, published by the Shock & Vibration Information Center, Washington, D.C. 20375.

14. J. F. O'Hanlon and M. E. McCauley, "Motion Sickness Incidence as a Function of the Frequency and Acceleration of Vertical Sinusoidal Motion," *Aerospace Medicine*, Vol. 45, pp. 366-369, 1974.

15. Douglas A. Lund, "Vibration Testing Can be Improved with Hydrostatic Spherical Couplings," *Test Engineering and Management*, Apr/May 1974.

16. Wayne Tustin, "Dynamic Aspects of Nuclear Power" (Part II in a Series), *Test Engineering and Management*, Oct/Nov 1975.

17. D. O. Smallwood and N. F. Hunter, "A Transportable 56-kN, 200-mm Displacement Hydraulic Shaker for Seismic Simulation," *Proceedings of IES Annual Meeting*, pg. 125, Apr 1975.

18. G. C. Kao, "Testing Techniques for Simulating Earthquake Motion," *Journal of Environmental Sciences*, Mar/Apr 1975.

19. B. J. Klee, D. V. Kimball and Wayne Tustin, "Vibration and Shock Test Fixture Design, Fabrication and Evaluation," available from Tustin Institute of Technology, Inc., 22 E. Los Olivos St., Santa Barbara, CA 93105.

20. Wayne Tustin, "An Inexpensive Piggy-Back Chamber for Use with Shakers," *Test Engineering and Management*, April 1967.

21. D. G. Van de Griff, Weston D. Ayers and John G. Maloney, "Simulating Tactical Missile Flight Vibration with Pneumatic Vibrators," *The Shock and Vibration Bulletin 46*, Oct 1975.

22. Kenneth McK. Eldred, "Vibroacoustic Environmental Simulation for Aerospace Vehicles," *The Shock and Vibration Bulletin 37*, Part 5, pg. 1, Jan 1968.

23. Fancher M. Murray, "Operational Characteristics of a 100,000-Cubic-Foot Acoustic Reverberation Chamber," *The Shock and Vibration Bulletin 37*, Part 5, pg. 13, Jan 1968.

24. Robert J. Wren, Wade D. Dorland, James D. Johnston and Kenneth McK. Eldred, "Concept, Design and Performance of the Spacecraft Acoustic Laboratory," *The Shock and Vibration Bulletin 37*, Part 5, pg. 25, Jan 1968.

25. Richard W. Peverley, "Vibroacoustic Test Methods for Vibration Qualification of Apollo Flight Hardware," *The Shock and Vibration Bulletin 37*, pg. 153, Jan 1968.

26. Louis J. Demas, "Real Time Combined Acoustic-Vacuum Testing of Spacecraft," *The Shock and Vibration Bulletin 37*, Part 5, pg. 175, Jan 1968.

27. Ronald A. Slusser, "Digital Control of High-Intensity Acoustic Testing," *Proceedings of the 1975 National Meeting of the IES, Vol. II*, Apr 14-16, 1975, pg. 160.

28. A. W. Kolb and H. A. Magrath, "RTD Sonic Fatigue Facility, Design and Performance Characteristics," *The Shock and Vibration Bulletin 37* (Supplement), pg. 17, Jan 1968.

29. Otto F. Maurer, "Facility Sonic Fatigue Proof Testing," *The Shock and Vibration Bulletin 37* (Supplement), pg. 43, Jan 1968.

30. Roelof C. W. Van der Heyde, "Simulation of Acoustic Fatigue Failure in the Wideband Noise Test Facility of the Air Force Flight Dynamics Laboratory," *The Shock and Vibration Bulletin 37* (Supplement), pg. 63, Jan 1968.

31. Robert N. Hancock, "IES Acoustics Test Facility Survey," *Institute of Environmental Sciences 1976 Proceedings*, 22nd Annual Technical Meeting, Philadelphia, PA, pg. 106, Apr 26-28, 1976.

SELF-TUNING RESONANT FIXTURES

R.T. Fandrich
Harris Corporation
Electronic Systems Division
Melbourne, Florida

Three methods of amplifying vibration over a broad frequency
band are described and evaluated. Amplification by mechani-
cal resonance is used and the major problem discussed is the
means for tuning the resonant frequency to coincide with the
input or desired frequency. A success criterion is establi-
shed and three methods compared.

Introduction

A test requirement to expose minia-
ture electronic components to high vib-
ration levels prompted this investiga-
tion of self-tuning resonant fixtures.
Various testing requirements (ranging
above 100 G's in the frequency range of
200 Hertz) are imposed on components and
many of these requirements can not be
met due to the lack of high-level vibra-
tion capability in the average test lab-
oratory.

Although many component shakers are
rated at 100 G's, this rating refers to
vibration of the shaker armature only,
so that when the weight of the test
item, holding fixture, bolts, and accel-
erometers is added, the maximum capabil-
ity is closer to 80 G's.

If these high level requirements
are to be met, it is clear that a means
of amplifying the vibration input is re-
quired. This laboratory has designed
and used resonant fixtures in the past,
but they have been used to develop very
high levels over a narrow frequency
range and have usually simulated some
actual mounting configuration which re-
sulted in this high level vibration in
the first place. For reliability test-
ing, a high level is required over a
wide frequency range. If an amplifica-
tion of 125% is required (representing
100 G's required divided by 80 G's
available), and a low damped resonant
fixture is used, this amplification or
greater can be obtained between 200 Hz
and 600 Hz, with a resonance occurring

at 447 Hz. These relationships are de-
rived from the equations for single de-
gree of freedom, undamped resonant sys-
tems as depicted in Figure I. The addi-
tion of small amounts of damping does
not significantly affect the conclusions
drawn from these equations. Three such
fixtures could cover the range from 200
to 2000 Hz; however, it would be more
convenient to use one fixture which is
capable of changing resonant frequency
to preclude moving the test item to
three different fixtures.

Resonant Fixtures

Three basic concepts were evaluated
with the major selection criterion being
ease of changing the resonant frequency.

The first concept considered was a
double-action pneumatic cylinder. The
piston, rod, and fixture are the reson-
ant mass, with the air on both sides of
the piston acting as springs. Changing
the air pressure changes the spring
force and thereby the resonant frequency.

A second method is modeled after a
stringed musical instrument, with
strings supporting a fixture. The ten-
sion on the strings is adjusted to
change the resonant frequency.

A third method uses a steel dia-
phragm with air pressure on one side. A
change in air pressure changes the nat-
ural frequency by increasing the tension

Natural frequency = f_n

Normalized amplification = Q

K = Spring constant M = Mass

$$f_n = \frac{1}{2\pi}\sqrt{\frac{K}{M}}$$

$$Q = \frac{1}{1-\left(\frac{f}{f_n}\right)^2}$$
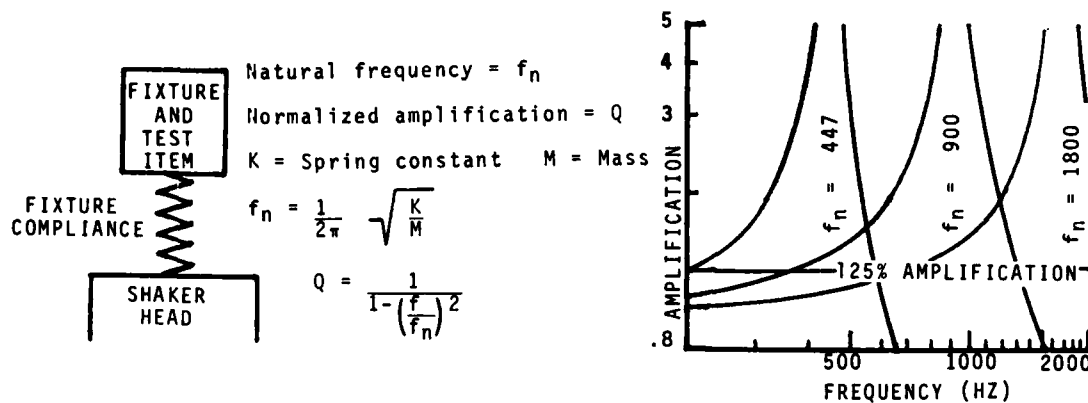
FIGURE I
RESONANT FIXTURE CHARACTERISTICS

in the diaphragm, similar to the change resulting from tuning a Timpani by stretching the drum head.

A method for correlating the shaker input frequency with the fixture frequency must be used to insure input amplification. A mini-computer was programmed to establish a phase angle feedback loop. The phase angle on an undamped, single degree of freedom resonant system passes through 90° at resonance, therefore the computer was programmed to change the air pressure or string tension to maintain a 90° phase lag between the input and the test item, thereby retaining the fixture in resonance as the shaker input frequency changes. (See reference).

A second method used increased the fixture resonant frequency whenever the shaker head acceleration exceeded a present limit. This method assumes that first the fixture is capable of amplifying the present limit adequately to obtain the desired level, and second, the input frequency is always above the fixture resonant frequency, so an increase in resonant frequency results in an increase in amplification, and therefore a decrease in shaker head acceleration.
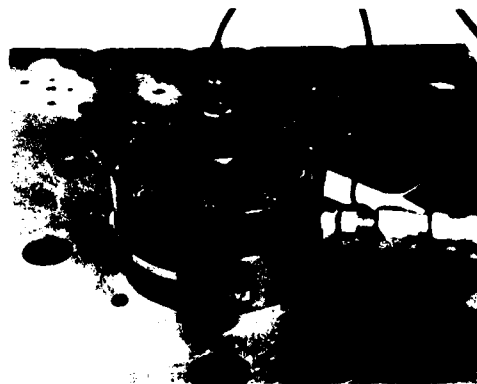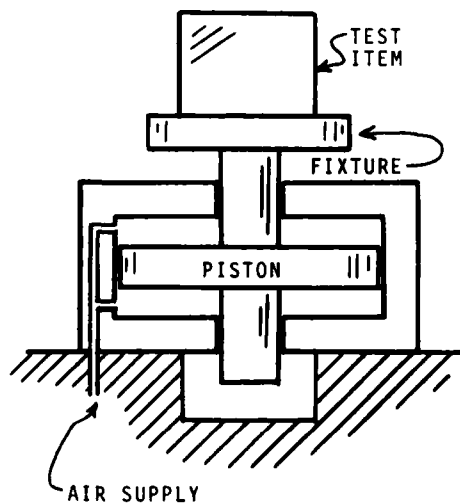
FIGURE II

PISTON FIXTURE

10

Piston Fixture

The first resonant fixture to be discussed utilizes an air cylinder containing a piston. The cylinder is normally used to activate mechanisms. In such cases, air is pumped to one side of the piston to produce a movement toward the other side. For this application, the piston is the resonant mass and equal air pressure is supplied to each side of the piston. This air acts as a spring, with the spring force dependent on air pressure. A piston with piston rods on both sides was used to insure equal area and therefore equal force on each side of the piston. A small mechanical spring was used to maintain the piston at the center of its stroke under zero load. A 5 cm diameter piston with a 3 mm stroke was used. Figure II shows a schematic and photograph of this concept. In the photograph, an accelerometer will be seen attached to the piston rod.

For the piston fixture, a process occurs inside the piston which produces increased air pressure on the side as the piston moves off the center position. This increased pressure tends to restore the piston to its original position, thereby acting as a spring. Since the opposite process results in reduced pressure on the other side of the piston, and since no energy is being extracted from the system (other than an insignificant amount of damping energy), this process may be approximated as isothermal. The Ideal Gas Law therefore simplifies to: Pressure x Volume=Constant. The upward force on the piston (discounting any constant loads) is Pressure x Area (P x A) on the bottom, minus (P x A) on the top. The pressure and the piston position, with the long-term average pressure being the supply pressure (P_n). Let delta (δ) represent the displacement of the piston from its neutral position. The pressure on one side of the piston is:

$$P = P_n \left(\frac{V_n}{V}\right)$$

(Subscript n refers to neutral position, throw (D) is total possible motion of piston from center position).

$$= P_n \left(\frac{Area \times D}{Area \times D \ (\pm \delta)}\right)$$

$$= P_n \frac{1}{1 \pm \frac{\delta}{D}}$$

The displacement ratio (R) is δ/D, and the $\pm$ is determined by the direction of motion of the piston. Assuming a downward δ summing the upward and downward forces we get:
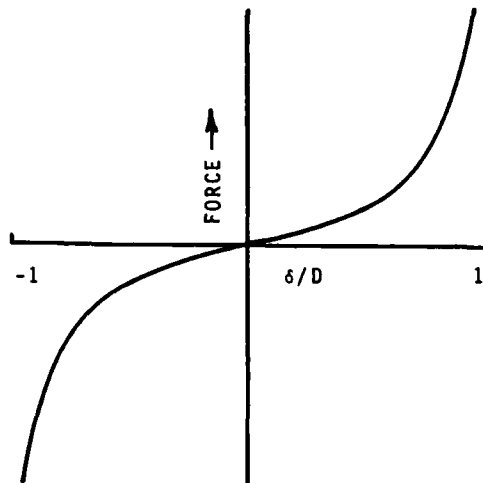
FIGURE III

FORCE VERSUS DISPLACEMENT
PISTON FIXTURE

Force $(F) = \Sigma$Pressure x Area

$$= P_n A \left[\frac{1}{1-R} - \frac{1}{1+R} \right]$$

$$= P_n A \frac{2R}{1-R^2}$$

Plotting this relationship, we get Figure III. The response due to this spring is not sinusoidal since the spring rate is not linear. Additionally, this nonlinearity will result in an effective spring constant which is dependent on deflection and; therefore, the system resonant frequency is a function of displacement and thereby vibration amplitude. This dependence further complicates the task of tuning the fixture to the input frequency. The function approaches linearity at $\frac{\delta}{D} = 0$; however, very high supply pressures would be required to reach high natural frequencies at small deflections.

The pressure seal between the piston and cylinder wall is a rubber o-ring. When the piston moves up in response to vibration, the o-ring first deflects, then, when stiction is overcome, slides along the cylinder wall. This introduces a nonlinear force for each direction reversal, or twice per cycle. This nonlinearity is a constant force not related to the frequency but rather to the distance the cylinder must move to over-

11
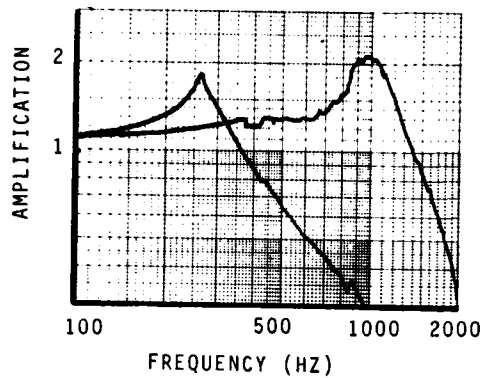
FIGURE IV
RESPONSE OF PISTON FIXTURE

come the stiction. The nonlinear force is added to the other forces acting on the cylinder. The nonlinear contribution is more significant for small deflections than for large deflections, since small oscillations result in operation in the nonlinear zone. Since higher frequencies result in smaller deflections for a fixed peak acceleration, this method is expected to produce cleaner data signals at lower frequencies. This expectation is verified by Figure IV, which shows the system response when tuned to 260 Hz at ambient pressure and 1000 Hz at maximum pressure. The operational range of this device is 200 to 1300 Hz, that range which results in greater than 125% amplification, for a variation over the entire pressure range.

Guitar Fixture

The second fixture to be discussed uses the concept of a stringed musical instrument to vary the resonant frequency. The test fixture is suspended
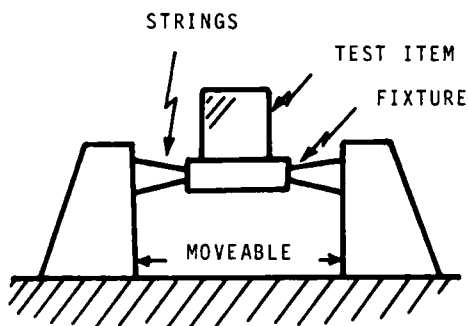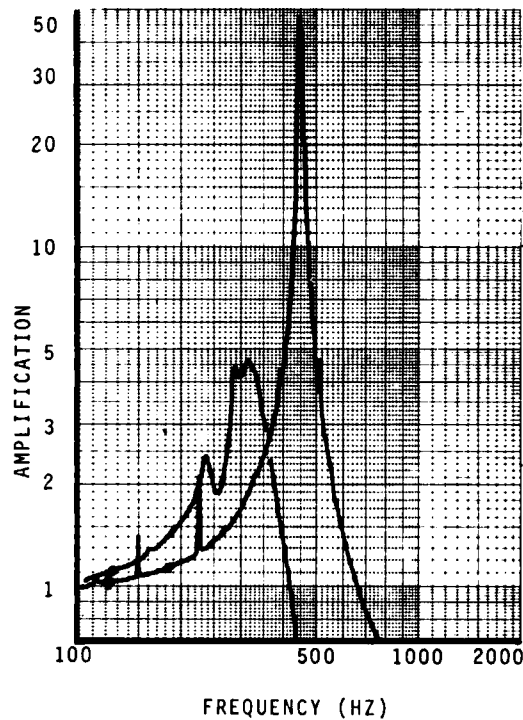
FIGURE VI
RESPONSE OF GUITAR FIXTURE

by strings and the tension in the strings varied to change the system resonant frequency. The strings used are guitar strings and are installed at a slight angle, as indicated in Figure V, to keep the fixture centered and to eliminate string slap in the oversized holes. The distance between the two bars at the ends of the strings can be varied to change tension. Figure VI shows the response of the fixture when tuned to the minimum frequency of 200 Hz and the maximum frequency of 450 Hz.

FIGURE V

GUITAR FIXTURE

12
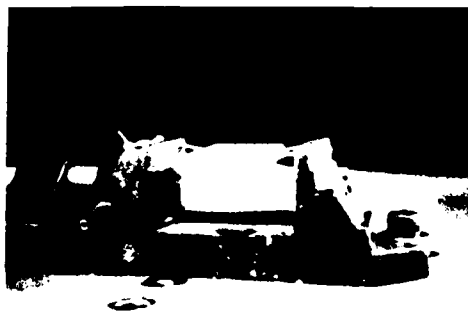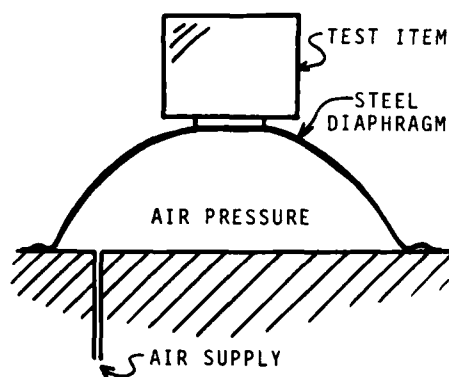
FIGURE VII

DIAPHRAGM FIXTURE

The limited range of this fixture is its major disadvantage. If the active length of the string could be changed, a much greater range of frequency would result.

Diaphragm Fixture

The third fixture discussed consists of a steel diaphragm with air pressure on one side, as indicated in Figure VII. As the air pressure is increased, the diaphragm stretches and its resonant frequency increases. The test item is mounted on a platform at the center of the diaphragm. This type of mechanism is used on pressure tranducers and switches; the experiment was performed with a pressure switch diaphragm rated at zero to 5.5 atmospheres (gauge). The diaphragm was 5 cm in diameter and was a section of a sphere. The photograph in Figure VII does not show the diaphragm but only the outer switch case. The usable range of this fixture was 250 to 2000 Hz. The zero pressure resonance occurred at 560 Hz with a simulated test item of 500 grams. An internal pressure of 5.1 atmospheres resulted in a 2000-Hz resonance. The amplification at resonance varied from 8 to 140 with a 1 G sinusoidal input. These high amplifications result in low required inputs. They also result in very low signal distortion at resonance; therefore, this fixture produced the cleanest sinusoids.

Figure VIII shows the response of the fixture when tuned to 560 Hz, 1000 Hz, and 1900 Hz.

Summary

Of the three fixtures evaluated, the diaphragm fixture emerged as the best candidate for vibration amplification, due to its high amplifications and its wide frequency range. The intrinsic nonlinearities of the piston fixture make it an undesirable choice to consider further. The limited frequency
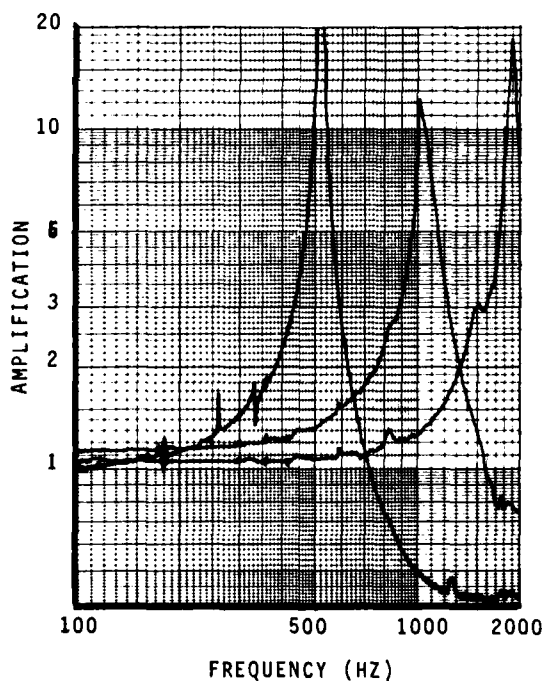
FIGURE VIII
RESPONSE OF DIAPHRAGM FIXTURE

13

range of the guitar fixture is its major disadvantage. However, a modification of this concept which would allow adjustment of the effective string length would overcome this drawback.

Figure IX shows the amplifications of the three fixtures compared and demonstrates the superiority of the diaphragm concept and the inability of the other fixtures to perform over the de-

FIGURE X
SHAKER VERSUS FIXTURE
PERFORMANCE

sired range.

Based on these conclusions, the diaphragm fixture was loaded with a 500-gram test item and the test item acceleration controlled at a constant level (limited by displacement at low frequencies) to establish the fixture performance. Figure X shows the vibration level of the test item, along with the vibration level of the shaker head required to produce this level on the test item. The goal of maintaining levels below 80 G's on the shaker is met above 270 Hz. Since this fixture could not be tuned below 560 Hz, adequate amplification was not available between 170 Hz and 270 Hz. Selection of a low frequency diaphragm would alleviate this problem.

Reference: D. Cerasuolo, J. Chin

Description of a Shock and Vibration Displacement Amplifier
Shock and Vibration Bulletin, 41, 1970

FIGURE IX
COMPARISON OF AMPLIFICATION
OF THREE FIXTURES STUDIED

DISCUSSION

Mr. Curtis (Hughes Aircraft Co.): Have you
contemplated trying to broaden the resonance
by introducing damping into your diaphragm,
for example, cut down the Q a little bit and
not have to control so narrow a bandwidth?

Mr. Fandrich: I didn't consider that. I think
adding damping increases the amplification
but after the amplification is below a 1/1
rate; although adding damping would probably
increase the controlability of the system, I
don't think it would make a fixed frequency
resonant fixture cover a wider bandwidth.

Mr. Dillon (Jet Propulsion Laboratory):
Regarding the first system, have you tried to
conclude something about what you've done so
far? Does the system look like it is a sound
approach?

Mr. Fandrich: The first system did not look
like a sound approach in the way it was
configured. I want to take the seals off
and see if I can get rid of the noise that
the rubbing of the seals generate. We may
lose a lot of air through it but I don't think
it will matter. I think by taking the seals
off this system, and perhaps trying to get an
air bearing effect where the pistons penetrate
the cylinder, I may be able to get rid of the
noise and non-linearities produced by the seals
and then have a workable system. At this time
with the seals on the pistons and on the piston
rods, it is not a workable system.

15

ANALYSIS OF SINUSOIDAL AND RANDOM VIBRATION ENERGIES

J. N. Tait
Naval Air Development Center
Warminster, Pennsylvania 18974

A method of analysis of the total available kinetic energy of si-
nusoidal and random vibration programs has been developed, using
the common basis of unit mass. This method has been applied to
fifteen sinusoidal patterns, including logarithmic sweep, linear
sweep and dwell, with constant displacement, constant velocity,
and constant or sloped acceleration. The method has also been
applied to twenty-six random patterns including broadband, swept
narrowband with logarithmic and linear sweep and with constant
bandwidth or constant percent bandwidth, and harmonic spike series,
all with constant or sloped acceleration spectral density. Using
energy transfer functions for both viscous and coulomb damping,
four sets of expressions have been derived for energy density
spectra and energy summations in the response domain, for one
degree of freedom. This paper outlines the basic theory, illus-
trates the method with expressions for four excitation patterns,
presents applications in which two of these expressions are used,
and lists a bibliography of reports by the author in which the
method has been rigorously treated.

BASIC THEORY

The instantaneous kinetic energy
of a unit mass undergoing any form of
mechanical vibration is one-half the
square of its instantaneous velocity.
If the mass is a vibration source hav-
ing known or controlled motion param-
eters, the excitation energy summation
during a given time period T is the
integral of instantaneous excitation
energy from zero to T. If a second
mass is coupled to the excitation mass
by an elastic interface, the instan-
taneous response energy of a unit mass
is the product of instantaneous excita-
tion energy and an appropriate trans-
fer function. The response energy
summation during time period T is the
integral of instantaneous response
energy from zero to T. Inasmuch as
time and frequency are interrelated,
the excitation and response integrands
have been converted to equivalent
functions of frequency. The energy
summations during time period T are
the integrals over the frequency band
or range.

TRANSFER FUNCTIONS

The study program has been limited
to a single degree of freedom, using

the following two types of elastic
interface:

    a. *Rigidly-connected viscous
       damper.*

    b. Rigidly-connected coulomb
       damper.

For each type of damper, the transfer
function is the square of the appro-
priate classical expression for abso-
lute transmissibility.

For the rigidly-connected viscous
damper, the transfer function is

$$V(w) = \frac{1 + (2dw)^2}{(1 + w^2)^2 + (2dw)^2}, \qquad (1)$$

where d = ratio of actual to critical
        damping coefficients, C/C_c

      w = ratio of actual to natural
        frequencies, f/f_n

Inasmuch as every response energy in-
tegrand contains the transfer function,
$V(w)$ must be re-expressed in terms
which will facilitate integration.
Accordingly, with

    $b = 4d^2 - 2,$

17

$$V(w) = \frac{(b + 2)w^2 + 1}{w^4 + bw^2 + 1} \qquad (2)$$

The denominator can be factored directly, i.e.,

$$w^4 + bw^2 + 1 = W_1 W_2$$
$$= (w^2 + \sqrt{2-b}\,w + 1)(w^2 - \sqrt{2-b}\,w + 1)$$

The denominator can also be factored by completing the square, i.e.,

$$w^4 + bw^2 + 1 = (w^4 + bw^2 + \frac{b^2}{4})$$
$$- (\frac{b^2}{4} - 1)$$
$$= X_1 X_2$$
$$= (w^2 + a_1{}^2)(w^2 + a_2{}^2)$$

where $a_1 = \sqrt{\dfrac{b + \sqrt{b^2 - 4}}{2}}$, and

$$a_2 = \sqrt{\frac{b - \sqrt{b^2 - 4}}{2}}$$

Then, $X_1 = w^2 + \dfrac{b + \sqrt{b^2 - 4}}{2}$, and

$$X_2 = w^2 + \frac{b - \sqrt{b^2 - 4}}{2}$$

For $b < 2$, i.e., for $d < 1$,
$$V(w) = \frac{(b + 2)w^2 + 1}{W_1 W_2} \qquad (3)$$

For $b = 2$, i.e., for $d = 1$,

$$V(w) = \frac{4w^2 + 1}{(w^2 + 1)^2} \qquad (4)$$

For $b > 2$, i.e., for $d > 1$,

$$V(w) = \frac{(b + 2)w^2 + 1}{X_1 X_2} \qquad (5)$$

For the rigidly-connected coulomb damper, the transfer function for $1 \le d \le 2$ is

$$C(w) = \frac{1 + d^2(1 - \frac{2}{w^2})}{(w^2 - 1)^2}$$
$$= \frac{(d^2 + 1)w^2 - 2d^2}{w^2(w^2 - 1)^2} \qquad (6)$$

where $d = 4n/\pi$
n = ratio of damper's dry friction force to spring's retaining force

Recalling the coulomb damper's behavior as a function of n and w, and letting w_1 represent the "break-loose" frequency ratio,
$$w_1 = \sqrt{d}.$$

For $n < \pi/4$, i.e., $d < 1.0$, $C(w)$ tends to become infinitely large.

For $n = \pi/4$, $d = w_1 = 1$, the finite response is maximum, and

$$C(w) = \frac{2}{w^2(w^2 - 1)} \qquad (7)$$

For $(\pi/4 < n < \pi/2)$, $(1 < d < 2)$, $(1 < w_1 < \sqrt{2})$, and

$$1 < C(w) < \frac{2w^2 - 2}{w^2(w^2 - 1)^2} \qquad (8)$$

For $n = \pi/2$, $d = 2$, $w_1 = \sqrt{2}$, and

$$C(w) = 1 \qquad (9)$$

For $n > \pi/2$, $d > 2$, $w_1 > \sqrt{2}$, and

$$C(w) = 1 \qquad (\text{for } w < w_1)$$
$$C(w) < 1 \qquad (\text{for } w > w_1)$$

EXCITATION PATTERN CODE ASSIGNMENT

For the forty-one excitation patterns, codes were assigned. Codes S1 through S15 represent sinusoidal patterns. Codes B1 through B4 represent broadband random patterns. Codes N1 through N16 represent swept narrowband patterns. Codes H1 through H6 represent harmonic spike series patterns. This paper will not present the derivations for the many expressions for both excitation and response domains; the majority have been presented in references 1 through 7. Instead, the applicable expressions for four representative excitation patterns are presented in the next section. Applications of two of these patterns will be presented in subsequent sections. The chosen patterns are as follows:

Code S1 - Sinusoidal logarithmic sweep with constant displacement

Code S4 - Sinusoidal logarithmic sweep with sloped acceleration

Code S15- Sinusoidal dwell with constant acceleration

Code B1 - Broadband random with constant acceleration spectral density.

ENERGY SUMMATION EXAMPLES

Energy summations are next presented for the four excitation patterns having Codes S1, S4, S15 and B1. For each pattern, the symbols $G(f)$ or $G(w)$, $Q(w)$, and $E(f)$ or $E(w)$ represent energy

18

level, integrand, and energy summation, respectively. With no prime superscripts, they represent the excitation domain. With single prime superscripts, they represent the response domain with viscous damper. With double prime superscripts, they represent the response domain with coulomb damper. For the response domain, each improper integrand was reduced to a single proper fraction, then expanded into a series of integrable partial fractions.

The following additional symbols are defined:

$A \quad - \tan^{-1}\left[\dfrac{2w + \sqrt{2-b}}{\sqrt{2+b}}\right]$

$B \quad - \tan^{-1}\left[\dfrac{2w - \sqrt{2-b}}{\sqrt{2+b}}\right]$

$C \quad - \tan^{-1}\left[\dfrac{w}{a_1}\right]$

$D \quad - \tan^{-1}\left[\dfrac{w}{a_2}\right]$

$f_o \quad$ - the reference frequency for sloped energy gradient, i.e., the frequency at the knee between flat and sloped gradients. Hz.

$G_o \quad$ - the vector value of sinusoidal excitation acceleration at f_o, Hz.

$H \quad$ - the acceleration spectral density level of random excitation, g^2/Hz.

$K \quad$ - lumped constant which includes excitation level, sweep rate if applicable, f_n raised to a power, f_o raised to a power if applicable, and a numerical constant.

$K_{log} \quad$ - logarithmic sweep rate, $\ln(f_2/f_1)/T$ where f_1 and f_2 are the lower and upper frequencies of the range swept during T.

$n \quad$ - slope constant, (db/octave)/3

$T \quad$ - time, sec.

$Y \quad$ - peak-to-peak sinusoidal excitation displacement, in.

For each of the four chosen excitation patterns, the corresponding expressions are presented in the following order:

a. Excitation domain

$G(f) = K \cdot$ (function of f)

$E(f) = \int G(f)df$

b. Response domain (viscous damper)

$G'(w) = K \cdot$ (function of w) $\cdot V(w)/fn = KQ'(w)/fn$

(1) $\underline{b < 2}$ $Q'(w) =$ (function of w)

$E'(w)/K = \dfrac{1}{K}\int G'(w)dw$

(2) $\underline{b = 2}$ Similar to (1)

(3) $\underline{b > 2}$ Similar to (1)

c. Response domain (coulomb damper)

$G''(w) = K \cdot$ (function of w) $\cdot C(w)/fn = KQ''(w)/fn$

(1) $\underline{1 < d \le 2}$ $Q''(w) =$ (function of w) $\cdot C(w)$

$E''(w)/K = \dfrac{1}{K}\int G''(w)dw$

(2) $\underline{d > 2 \text{ and } w < w_1}$

$E''(w) = E(w)$

1. Sinusoidal logarithmic sweep with constant displacement (Code S1)

a. Excitation domain

$G(f) = Kf^2 = \left[\dfrac{2.468Y^2}{K_{log}}\right]f^2 \quad (10)$

$E(f) = \dfrac{Kf^3}{3} \; ; \quad \dfrac{E(w)}{K} = \dfrac{fn^3w^3}{3} \quad (11)$

b. Response domain (viscous damper.

$G'(w) = Kw^2 \, V(w)/fn$
$\quad\quad = KQ'(w)/fn \quad (12)$

(1) $\underline{b < 2}$

$Q'(w) = w^2 \, V(w)$

$\quad = \dfrac{(b + 2)w^4 + w^2}{W_1 \quad W_2}$

$\quad = \dfrac{1}{2}\left[\dfrac{w^2}{W_2} + \dfrac{w^2}{W_1}\right]$

$\quad + \dfrac{b + 1}{2\sqrt{2-b}}\left[\dfrac{w^3}{W_2} - \dfrac{w^3}{W_1}\right] \quad (13)$

19

$$\frac{E'(w)}{K} = (b + 2)w + \frac{b^2 + b - 3}{4\sqrt{2-b}} \ln\left[\frac{W_1}{W_2}\right]$$

$$- \frac{b^2 + 3b + 1}{2\sqrt{2+b}} (A + B) \quad (14)$$

(2) <u>b = 2</u>

$$Q'(w) = \frac{4w^4 + w^2}{(w^2 + 1)^2} \quad (15)$$

$$\frac{E'(w)}{K} = 4w + \frac{1.5w}{w^2 + 1} - 5.5 \tan^{-1}(w) \quad (16)$$

(3) <u>b > 2</u>

$$Q'(w) = \frac{b + 2}{2}\left[\frac{w^2}{X_2} + \frac{w^2}{X_1}\right]$$
$$- \frac{b^2 + 2b - 2}{2\sqrt{b^2-4}}\left[\frac{w^2}{X_2} - \frac{w^2}{X_1}\right] \quad (17)$$

$$\frac{E'(w)}{K} = (b + 2)w - \frac{b + 2}{2}\cdot\left[a_1 C + a_2 D\right]$$
$$- \frac{b^2 + 2b - 2}{2\sqrt{b^2-4}}\left[a_1 C - a_2 D\right] \quad (18)$$

c. <u>Response domain (coulomb damper.</u>

$$G''(w) = Kw^2 C(w)/fn = KQ''(w)/fn \quad (19)$$

(1) <u>1 ≤ d ≤ 2</u>

$$Q''(w) = \frac{(d^2 + 1)\ w^2 - 2d^2}{(w^2 - 1)^2}$$
$$= \frac{3d^2 + 1}{2(w^2 - 1)} - \frac{d^2 - 1}{4}$$
$$\cdot\left[\frac{1}{(w - 1)^2} + \frac{1}{(w + 1)^2}\right] \quad (20)$$

$$\frac{E''(w)}{K} = \frac{3d^2 + 1}{4} \ln\left[\frac{w - 1}{w + 1}\right]$$
$$+ \frac{(d^2 - 1)w}{2(w^2 - 1)} \quad (21)$$

(2) <u>d > 2 and w < w_1</u>

$$E''(w) = E(w) \quad (22)$$

Figures 1 and 2 show plots of E'(15.62/fn) - E'(7.81/fn) vs. f$_n$ for Code S1, using two ranges of d for b < 2. Figures 3 and 4 show similar plots of

E"(w) vs. f$_n$ for Code S1, using two ranges of d for $1 \le d \le 16$. For all plots, Y = 0.1 in. peak-to-peak.

2. <u>Sinusoidal logarithmic sweep with sloped acceleration (Code S4).</u>

a. <u>Excitation domain.</u>

$$G(f) = Kf^{n-2} = \left[\frac{943.5\ G_o^2}{K \log f_o^n}\right] f^{n-2} \quad (23)$$

$$E(f) = \frac{Kf^{n-1}}{n-1}; \quad \frac{E(w)}{K} = \frac{w^{n-1}f_n^{n-1}}{n-1} \quad (24)$$

b. <u>Response domain (viscous damper).</u>

The response domain expressions involve unique integration problems for each value of n. Inasmuch as the Code S4 application, presented in a subsequent section of this paper, requires the excitation domain only, no further response domain treatment will be presented. The expressions and their derivations for (n = +2) and (n = -2) can be found in references 4, 5 and 7.

c. <u>Response domain (coulomb damper).</u>

The above remarks for the viscous damper apply.

3. <u>Sinusoidal dwell with constant acceleration (Code S15).</u>

a. <u>Excitation domain.</u>

$$G(f) = K = \frac{943.5\ G_o^2 T}{f}$$

(f = constant) (25)

$$E(f) = G(f) = K; \quad \frac{E(w)}{K} = 1.0 \quad (26)$$

b. <u>Response domain (viscous damper).</u>

$$G'(w) = KV(w)/f_n = KQ'(w)/f_n \quad (27)$$

(1) <u>b < 2</u>

$$Q'(w) = V(w) = \frac{(b + 2)\ w^2 + 1}{W_1\ W_2}$$
$$= \frac{1}{2}\left[\frac{1}{W_2} + \frac{1}{W_1}\right]$$
$$+ \frac{b + 1}{2\sqrt{2-b}}\left[\frac{w}{W_2} - \frac{w}{W_1}\right] \quad (28)$$

20
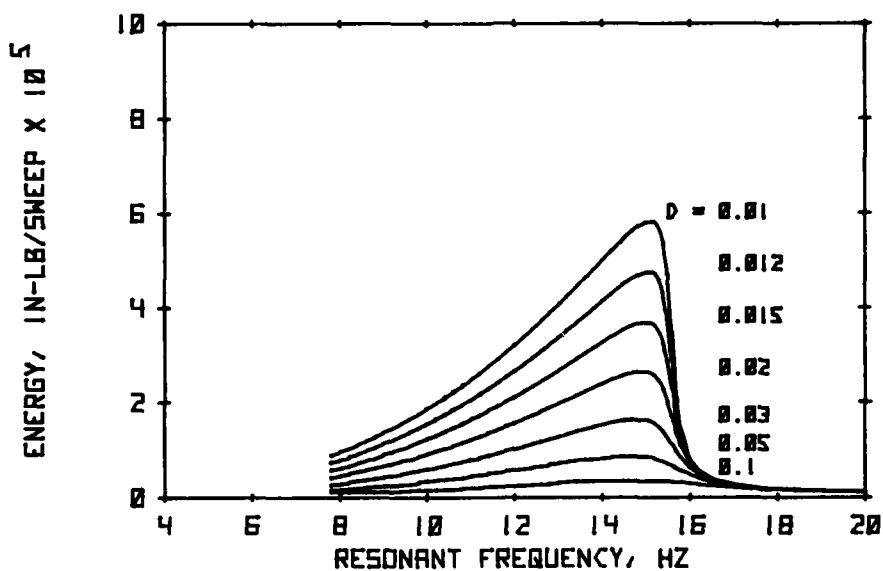
Figure 1.   Response Energy Summation for Logarithmic
Sinusoidal Sweep with Low Viscous Damping
(E' vs. f_n)
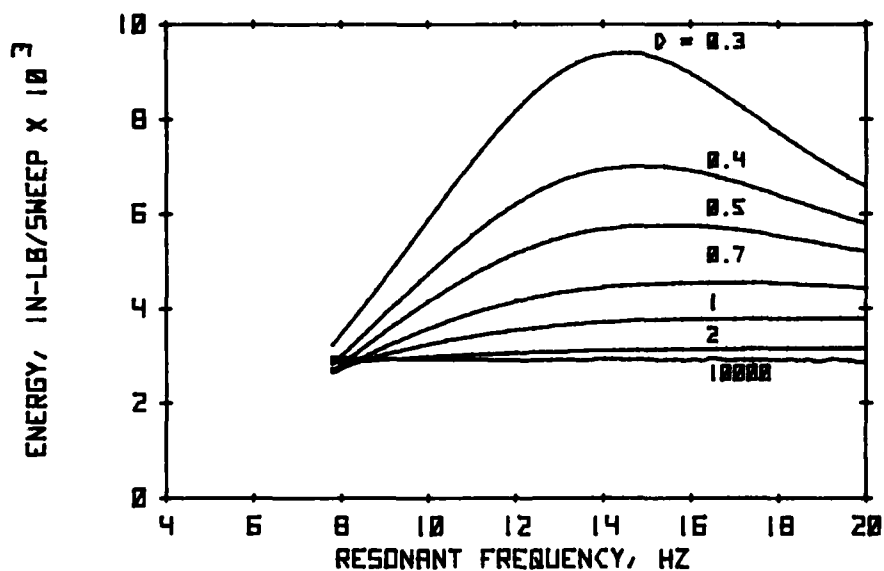
Figure 2.   Response Energy Summation for Logarithmic
Sinusoidal Sweep with High Viscous Damping
(E' vs. f_n).

21
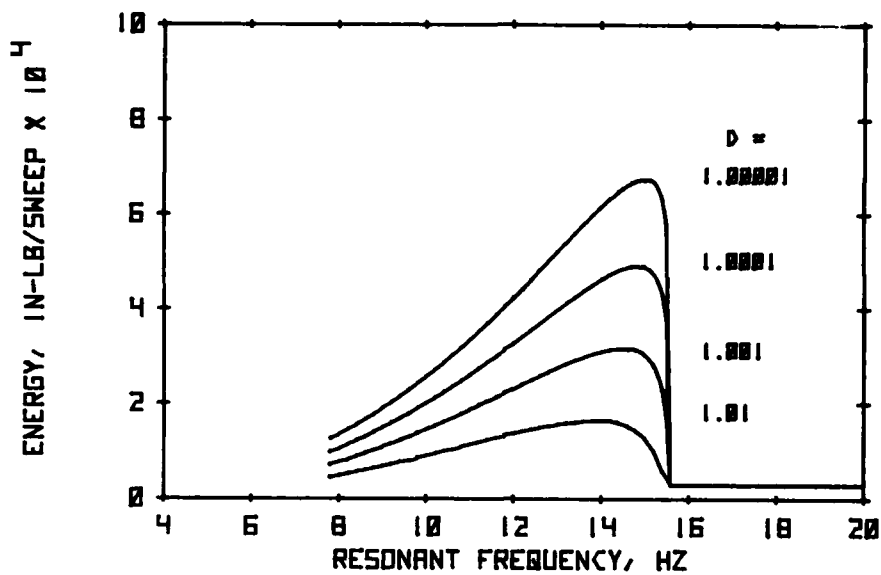
Figure 3. Response Energy Summation for Logarithmic
Sinusoidal Sweep with Low Coulomb Damping
(E" vs. f_n).
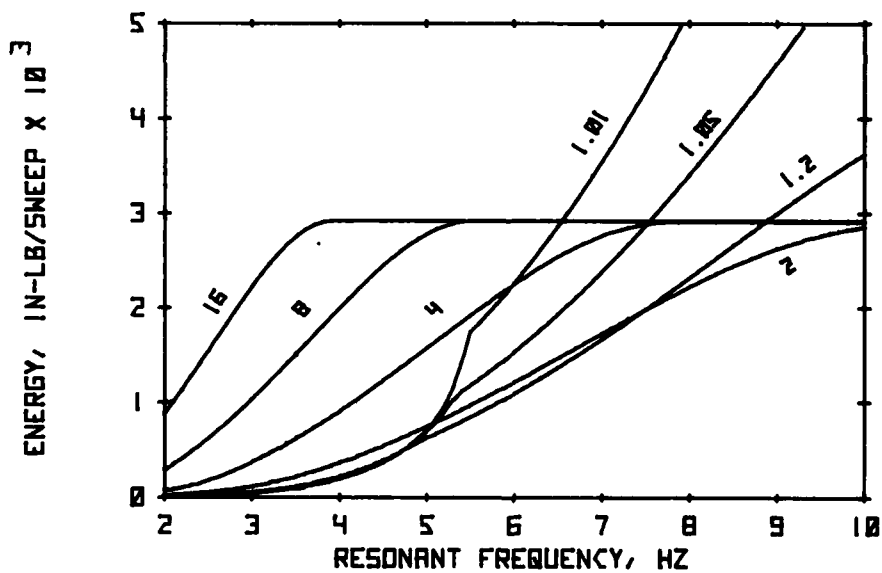
Figure 4. Response Energy Summation for Logarithmic
Sinusoidal Sweep with High Coulomb Damping
(E" vs. f_n).

$$\frac{E'(w)}{K} = -\frac{b+1}{4\sqrt{2-b}}\ \ln\left[\frac{W_1}{W_2}\right] + \frac{b+3}{2\sqrt{2+b}}\ (A+B) \tag{29}$$

(2) __b = 2__

$$Q'(w) = V(w) = \frac{(b+2)w^2 + 1}{(w^2+1)^2}$$

$$= \frac{4w^2+1}{(w^2+1)^2} \tag{30}$$

$$\frac{E'(w)}{K} = \frac{-1.5}{w^2+1}w + 2.5\ \tan^{-1}(w) \tag{31}$$

(3) __b > 2__

$$Q'(w) = V(w) = \frac{(b+2)w^2+1}{X_1\ X_2}$$

$$= \frac{b+2}{2}\left[\frac{1}{X_1} + \frac{1}{X_2}\right]$$

$$+ \frac{b^2+2b-2}{2\sqrt{b^2-4}}\left[\frac{1}{X_1} - \frac{1}{X_2}\right] \tag{32}$$

$$\frac{E'(w)}{K} = \frac{b+2}{2}\left[\frac{C}{a_1} + \frac{D}{a_2}\right]$$

$$+ \frac{b^2+2b-2}{2\sqrt{b^2-4}}\left[\frac{C}{a_1} - \frac{D}{a_2}\right] \tag{33}$$

c. __Response domain (coulomb damper).__

$$G''(w) = KC(w)/f_n = KQ''(w)/f_n \tag{34}$$

(1) __$1 \leq d \leq 2$__

$$Q''(w) = C(w) = \frac{(d^2+1)\ w^2 - 2d^2}{w^2(w^2-1)^2}$$

$$= -\frac{2d^2}{w^2} + \frac{5d^2-1}{2(w^2-1)} - \frac{d^2-1}{4}$$

$$\cdot\left[\frac{1}{(w-1)^2} + \frac{1}{(w+1)^2}\right] \tag{35}$$

$$\frac{E''(w)}{K} = \frac{5d^2-1}{4}\ \ln\left[\frac{w-1}{w+1}\right]$$

$$+ \frac{2(d^2-1)w}{4(w^2-1)} + \frac{2d^2}{w} \tag{36}$$

(2) __$d > 2$ and $w < w_1$__

$$E''(w) = E(w) \tag{37}$$

4. __Broadband random with constant ac-__
__celeration spectral density (Code B1).__

a. __Excitation domain__

$$G(f) = \frac{K}{f} = \left[1887HT\right]\frac{1}{f} \tag{38}$$

$$E(f) = K\ln(f);\ \ \frac{E(w)}{K} = \ln(w) \tag{39}$$

b. __Response domain (viscous__
__damper.__

$$G'(w) = \frac{KV(w)}{f_n w} = KQ'(w)/f_n \tag{40}$$

(1) __b < 2__

$$Q'(w) = \frac{V(w)}{w} = \frac{(b+2)w^2+1}{w\ W_1\ W_2}$$

$$= \frac{1}{w} + \frac{3}{2\sqrt{2-b}}\left[\frac{1}{W_2} - \frac{1}{W_1}\right]$$

$$- \frac{1}{2}\left[\frac{w}{W_2} + \frac{w}{W_1}\right] \tag{41}$$

$$\frac{E'(w)}{K} = \ln(w) - \frac{1}{4}\ \ln(W_1\ W_2)$$

$$- \frac{b+4}{2\sqrt{4-b^2}}\ (A-B) \tag{42}$$

(2) __b = 2__

$$Q'(w) = \frac{V(w)}{w} = \frac{4w^2+1}{w(w^2+1)^2} \tag{43}$$

$$\frac{E'(w)}{K} = \frac{-1.5}{w^2+1}$$

$$+ 0.5\ \ln\left[\frac{w^2}{w^2+1}\right] \tag{44}$$

(3) __b > 2__

$$Q'(w) = \frac{V(w)}{w} = \frac{(b+2)w^2+1}{wX_1\ X_2}$$

$$= \frac{1}{w} - \frac{1}{2}\left[\frac{w}{X_1} + \frac{w}{X_2}\right]$$

$$- \frac{b+4}{2\sqrt{b^2-4}}\left[\frac{w}{X_1} - \frac{w}{X_2}\right] \tag{45}$$

$$\frac{E'(w)}{K} = \ln(w) - \frac{1}{4}\ \ln(X_1\ X_2)$$

$$- \frac{b+4}{4\sqrt{b^2-4}}\ \ln\left[\frac{X_1}{X_2}\right] \tag{46}$$

c. __Response domain (coulomb__
__damper.__

$$G''(w) = \frac{KC(w)}{f_n w} = KQ''(w)/f_n \tag{47}$$

(1) __$1 \leq d \leq 2$__

$$Q''(w) = \frac{C(w)}{w} = \frac{(d^2 + 1)w^2 - 2d^2}{w^3 (w^2 - 1)^2}$$

$$= \frac{1 - 3d^2}{w} - \frac{2d^2}{w^3}$$

$$+ \frac{(3d^2 - 1)w}{w^2 - 1} + \frac{(d^2 - 1)w}{(w^2 - 1)^2}$$

$$\tag{48}$$

$$\frac{E''(w)}{K} = \frac{d^2}{w^2} - (3d^2 - 1)\ln(w)$$

$$+ \frac{d^2 - 1}{2(w^2 - 1)} + \frac{3d^2 - 1}{2}$$

$$\cdot \ln(w^2 - 1) \tag{49}$$

DAMPING VARIATIONS

All of the response energy summation expressions presented herein treat the damping parameter, i.e., $b = 4d^2 - 2$ or $d = 4n/\pi$, as applicable, as a constant. In reality, any elastic structure undergoes progressive change in its damping characteristic as it absorbs vibratory fatigue energy. One of the major concerns during the energy study program has been the need to define the damping parameter relationships as functions of initial value, instantaneous frequency and level parameters, material and accumulated fatigue. Although this problem has not been completely solved, it has been bounded in that the initial and terminal damping parameter values are known.

For any given excitation pattern, a highly damped response summation will approach the excitation summation. As an example, pattern code S1 summations are as follows, using $f_n = 100$ Hz, and $(99 \le f \le 101)$, i.e., $(0.99 \le w \le 1.01)$:

For $(b = 2)$, $E'/K = 0.025$ $(d = 1)$
For $(b = 14)$, $E'/K = 0.02125$ $(d = 2)$
For $(b = 398)$, $E'/K = 0.02005$ $(d = 10)$
$E/K = 0.02$

Using computer programs, it is readily feasible to examine the effects of many trial damping functions. During the energy summing process, the damping parameter, i.e., b or d, is calculated for each iterative step as a function of the instantaneous frequency, time, excitation level and/or other trial factor. The various trial functions are currently being applied to the specimen failure data from a laboratory test program. In the laboratory, groups of identical specimens were subjected to controlled sinusoidal logarithmic sweep (Code S1) and

resonance dwell (Code S13) tests to failure, and to broadband and non-swept narrowband random (Code B1) tests to failure. In all cases, the various response energy summations were calculated. The early trial damping functions used in these calculations have yielded good sine-random correlation in that the various energy absorption values were nearly equal.

APPLICATION TO MECHANICAL SHOCK

The energy analysis method has been extended and applied to the mechanical shock pulses specified by various military standards. The process began with the definition of the frequency spectrum of each pulse, and the numerical integration of a selected number of pairs of real and imaginary components of its Fourier integral. This process has been amply treated in the literature, and will therefore not be detailed herein.

Once the spectral (velocity)^2 values were determined, the equivalent energy level values were calculated, based upon the premise that the time duration of each spectral component was that of the pulse itself. Accordingly, the excitation domain for Code S14 was applied, since the shock pulses being analyzed were excitation pulses. Thus, for M components, the energy of the mth component was determined:

$$E(f_m) = \frac{1}{4} (V_{vector})_m^2 \, f_m T \tag{50}$$

where $(V_{vector})_m$ = velocity, in/sec.

T = pulse time duration, sec.

A computer program was developed for generating and plotting the energy spectra of a half-sinusoidal pulse and a terminal peak sawtooth pulse. These waveforms are specified by Military Standard MIL-STD-810, Method 516. The program provides for user entry of pulse duration and maximum acceleration level, calculates 200 spectral energy values over a frequency ratio range extending to 6, where the ratio is f_m/f_n, and plots the two energy spectra superimposed upon a labeled grid. Figure 5 shows the plots for 30g peak acceleration and 0.011 sec. duration.

APPLICATION TO ELASTOMER SPECIMENS

The energy analysis method has been applied to the response acceleration plots of a mock-up, successively isolated by six types of polyurethane foam elastomers. Significant frequency/

24
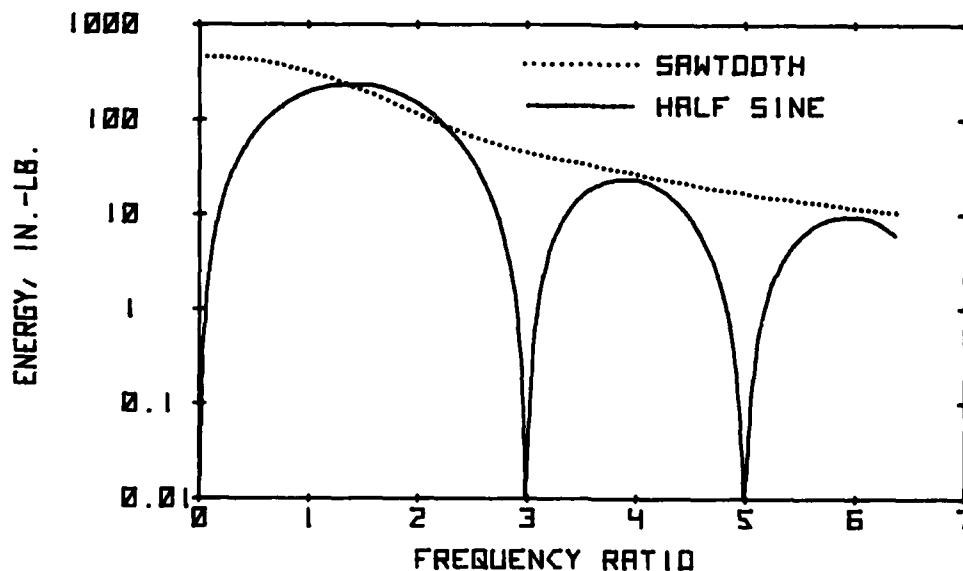
Figure 5. Energy Level Spectra of Half-Sine and Terminal
Peak Sawtooth Shock Pulses.

level pairs were entered into a com-
puter program, especially written for
the purpose. The program calculated
the slopes, octave-band junction fre-
quencies and levels, octave-band and
overall energy summations, and provided
complete tabular readout. In addition,
the performance of all specimens was
graded for each octave, and on an
overall basis. The grading readout
tabulated the specimen/test identity
codes in ascending order of merit.
The process is outlined in the follow-
ing paragraphs.

The six candidate specimens were
numbered 1 through 6. The ten sinus-
oidal vibration tests were numbered 1
through 10. For each test, each speci-
men was assigned a specimen/test iden-
tity code consisting of the test num-
ber followed by the specimen number.
Thus, Code 35 represents Specimen No. 5
in Test No. 3, Code 101 represents
Specimen No. 1 in Test No. 10, etc.

For each test, logarithmic sweep
was applied between 5 Hz and 500 Hz,
successively along each of the three
major axes of the mockup serving as a

load for the foam specimen being
tested. Response accelerations were
measured and recorded along the three
major axes for the following two ex-
citation level envelopes:

5 Hz $\leq$ (0.1 in. peak-to-peak)
$\leq$ 14 Hz $\leq$ ($\pm$ 1g) $\leq$ 500 Hz

5 Hz $\leq$ (0.1 in. peak-to-peak)
$\leq$ 44 Hz $\leq$ ($\pm$ 10g) $\leq$ 500 Hz

For each test, the response plot was
visually inspected for significant
peaks, notches and plateaus. A maxi-
mum of 22 individual sub-bands were
thus established. The corresponding
frequency/level pairs were tabulated
and entered into a computer file. The
major peak frequencies ranged from
10 Hz (Code 84) to 50 Hz (Code 12).
A constant 5-octave spectrum was orig-
inally planned for the analysis. How-
ever, this would have resulted in a
subjective grading because the speci-
men performance would have been as-
sessed in terms of the arbitrarily
chosen spectrum. Accordingly, a four-
octave relative spectrum was chosen
for each of the 51 tests such that the

25

major peak frequency, F, would be centered in the 2nd octave.

The octave-band junction frequencies are F1 through F5. For each test, the program assigns each sub-band intercept pair to the octave containing it, and selects the two pairs closest to each octave-band intercept. These two pairs will normally straddle F2, F3 or F4. They may both be above F1, or below F5. The program calculates the slope between the two pairs, and the octave-band junction level, The resulting levels are G1 through G5.

Table I is the computer printout of the octave-band junction frequency/level pairs for Test No. 1. Specimens 1 through 6 were assigned identity codes of 11 through 16.

where L = lower sub-band frequency, Hz
M = lower sub-band level, g
U = upper sub=band frequency, Hz
V = upper sub-band level, g

The sweep constant was based upon a one-second traverse from 5 Hz to 14 Hz. Then,

$$K_{Log} = \ln\left[\frac{14}{5}\right] = 1.03$$

The time to traverse from L to U is

$$T = \frac{\ln\left[\frac{U}{L}\right]}{1.03}$$

Choosing the upper pair, U and V, to be the reference pair, f_o and G_o,

TABLE I

OCTAVE JUNCTION FREQUENCIES AND LEVELS

TEST	F	F1 G1	F2 G2	F3 G3	F4 G4	F5 G5
11	22.0	7.78 0.3519	15.56 1.7192	31.11 1.9052	62.23 0.4776	124.45 0.1192
12	50.0	17.68 1.1087	35.36 1.5218	70.71 2.2329	141.42 0.9811	282:84 1.0920
13	19.0	6.72 0.2448	13.44 1.3806	26.87 0.7538	53.74 0.2072	107.48 0.0669
14	16.0	5.66 0.1581	11.31 0.9450	22.63 1.1000	45.25 0.2659	90.51 0.1295
15	29.5	10.43 0.5986	20.86 1.6689	41.72 1.9500	83.44 0.5170	166.88 0.0417
16	22.5	7.95 0.3235	15.91 1.3902	31.82 1.7453	63.64 0.5286	127.28 0.0941

For each octave band, the program then calculates all sub-band slope values, and the individual sub-band energy summations. Inasmuch as each sub-band slope is considered to be constant, the excitation energy summation pattern code S4, i.e., Eq. (24), was applied:

$$E(f) = \frac{Kf^{n-1}}{n-1} = \frac{943.5}{(n-1)} \frac{G_o^2 f^{n-1}}{K_{Log} f_o^n}$$

For each sub-band,

$$n = \frac{2\ln\left[\frac{V}{M}\right]}{\ln\left[\frac{U}{L}\right]} = 2\ln\left[\frac{VL}{MU}\right], \qquad (51)$$

$$E(f) = \left[\frac{943.5 \; V^2}{1.03(n-1) \; U^n}\right] f^{n-1}$$

$$= \left[\frac{916 \; V^2}{(n-1) \; U^n}\right] f^{n-1} \qquad (52)$$

Summing from L to U,

$$\sum_L^U E(f) = 916 \; V^2 \left[\frac{U^{n-1} - L^{n-1}}{(n-1)U^n}\right] \qquad (53)$$

For each test, the program calculates the sub-band summations for the 1st octave, adds them, then repeats the procedure for each of the higher octaves in turn, finally adding the overall energy summations. Table II is the computer printout of the octave band energy summations for Test No. 1. The identity codes are those of

26

Table I.

The final criterion for the dynamic performance assessment was a simple relative scoring or grading. For each of the ten groups of responses, the specimen yielding the lowest response energy summation in any one octave was assigned a grade of 1. The specimen yielding the next higher summation in that octave was assigned a grade of 2. Similar grading was applied to each of the octaves in turn, and to the overall band. Table III is the computer grading printout for Test No. 1. The identity codes are those of Tables I and II.

Report NADC-AE-7030, 19 Feb. 1971.

4. J.N. Tait, "Vibration Energy Summations in Response Domain for Coulomb Damped Elastic Systems with Sinusoidal Excitation," NAVAIRDEVCEN Report NADC-72185-AD, 2 Feb. 1973.

5. J.N. Tait, Supplement to the above NAVAIRDEVCEN report, Report NADC-73153-81, 20 Dec. 1973.

6. J.N. Tait, "Vibration Energy Density Spectra in Response Domain for Viscous Damped Elastic Systems with Sinusoidal and Broadband

TABLE II

OCTAVE BAND ENERGY SUMMATIONS

TEST	OCTAVE				OVERALL
	1	2	3	4	
11	64.3	630.8	62.8	1.5	759.3
12	120.7	322.7	45.0	10.7	499.1
13	165.8	773.7	35.6	0.8	976.0
14	30.0	1100.6	143.7	1.4	1275.7
15	273.4	609.2	140.0	4.4	1027.0
16	221.6	1149.9	70.0	1.7	1443.2

TABLE III

INDIVIDUAL GROUP GRADING

GRADE	OCTAVE				OVERALL
	1	2	3	4	
1	14	12	13	13	12
2	11	15	12	14	11
3	12	11	11	11	13
4	13	13	16	16	15
5	16	14	15	15	14
6	15	16	14	12	16

BIBLIOGRAPHY

1. J.N. Tait, "Analysis of Sinusoidal and Random Vibration Energies," NAVAIRDEVCEN Report No. NADC-AE-7023, 19 Nov. 1970.

2. J.N. Tait, "Analysis of Vibration Energy Density Spectra in the Excitation Domain," NAVAIRDEVCEN Report NADC-AE-7024, 19 Feb. 1971.

3. J.N. Tait, "Application of Vibration Energy Parameters to MIL-STD-810B Shock Pulses," NAVAIRDEVCEN

Random Excitation," NAVAIRDEVCEN Report NADC-73227-81, 2 Aug. 1974.

7. J.N. Tait, "Vibration Energy Summation in Response Doman for Viscous Damped Elastic Systems with Sinusoidal Excitation," NAVAIRDEVCEN Report NADC-73111-81, 31 Oct. 1974.
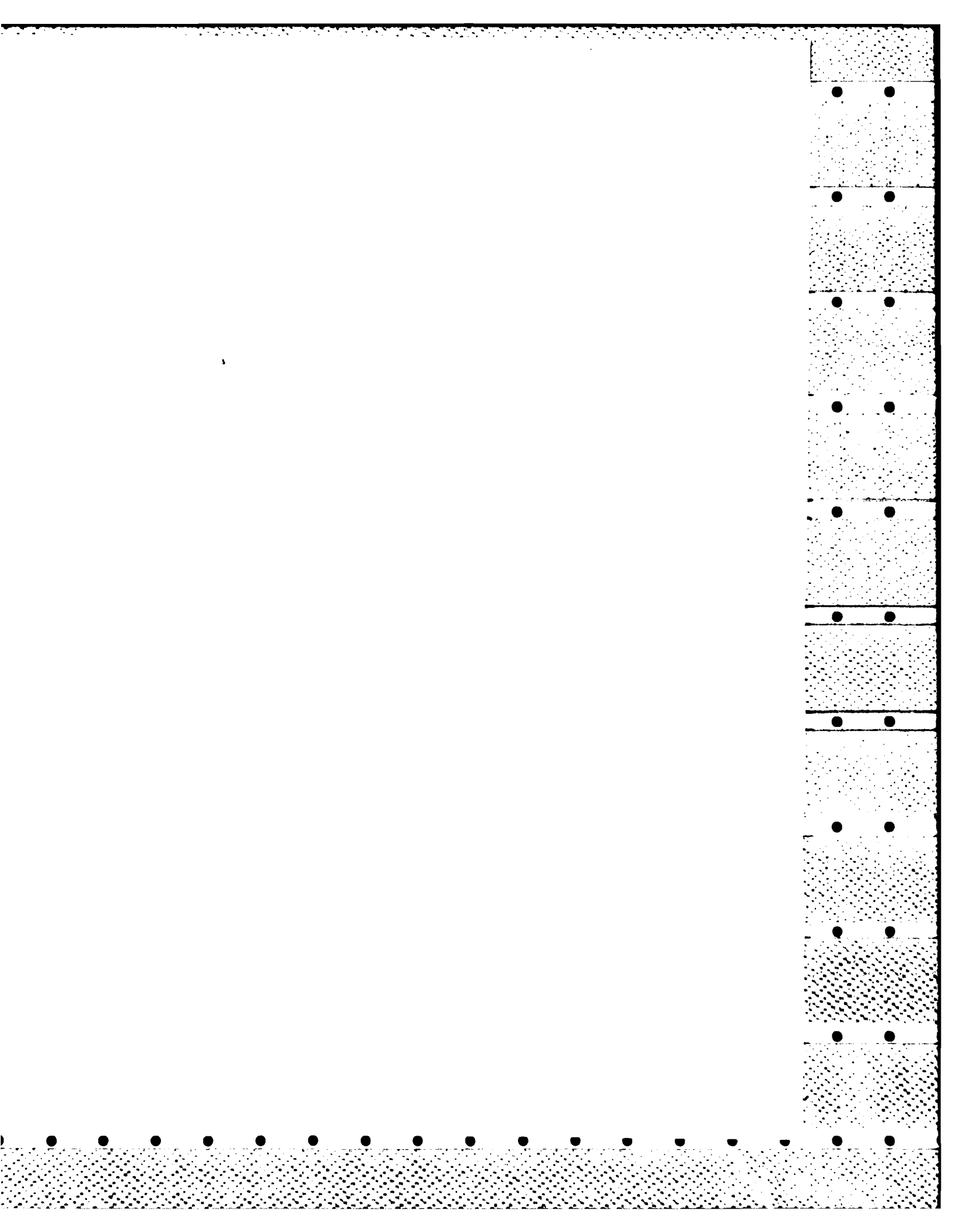
EVALUATION OF AN ADAPTIVE FILTER

AS A DIGITAL TRACKING FILTER[*]

D. O. Smallwood and D. L. Gregory
Sandia Laboratories
Albuquerque, New Mexico

An adaptive filter that is nonrecursive with two weights was developed for use as a digital tracking filter. The weights were adapted in response to an error signal, driving the error signal to a minimum mean square value. It is shown that the tracking filter is easy to implement (four multiply-adds/stage/sample point) and effective. Filter theory and characteristics are discussed, and several examples are presented.

NOMENCLATURE

d_j = jth sample of the primary input;

y_j = jth sample of the filter output;

x_{1j} = jth sample of a reference sine wave (the center frequency of the tracking filter);

x_{2j} = jth sample of a reference sine wave delayed by $\pi/2$ radians;

$\left.\begin{array}{c} W_{1j} \\ W_{2j} \end{array}\right\}$ = adaptive filter weights;

u = a constant that determines the bandwidth and convergence time of the filter;

e_j = the difference between the jth sample of the primary signal (the distorted filter input) (d_j) and the jth sample of the filter output (y_j);

ω = frequency rad/s;

f = frequency Hz;

ω_o = center frequency of tracking filter, rad/s;

f_o = center frequency of tracking filter, Hz;

T = sampling interval seconds;

z = complex operator used in the z transform;

$\omega_d = \omega - \omega_o$;

C = magnitude of the reference input;

$\theta = \omega T$;

$\theta_o = \omega_o T$;

H = filter transfer function;

H_p = band-pass filter transfer function;

H_r = band-reject filter transfer function;

τ = time constant (s);

BW = bandwidth (Hz);

$E[\ ]$ = expected value;

SR = sample rate $1/T$; and

h = distance from a pole to a point on the unit circle in the z plane.

PREVIOUS PAGE IS BLANK

INTRODUCTION

A recurring problem in digital sine-wave vibration control and digital sine vibration data reduction has been the extraction of the fundamental component from a signal distorted by noise and harmonics. Several methods are now in use that reduce to computing one (or a few) components of the discrete Fourier spectrum. These techniques, while successful, suffer some disadvantages. The data must be handled on a block basis, which means that a block of data has to be collected before the computation can start. Also, the limitations of the discrete Fourier transform are evident in results using these techniques. For example, the effective filter shape is a sin x/x function unless a window is used, in which case additional computations are required. Fourier techniques usually skip data; i.e., the data is not sampled continuously. Therefore, the results can miss a significant event; and, further, if a noise spike or other anomaly occurs during data sampling, a large error can result.

Wiener [1], Widrow [2] and others have proposed a class of digital filters known as adaptive filters. One form of an adaptive filter appears to be well suited for use as a digital tracking filter and is described in this paper. The filter can be implemented in hardware and/ or software.

BASIC THEORY OF AN ADAPTIVE DIGITAL TRACKING FILTER

Filter Algorithm

A single stage of the proposed tracking filter, shown in block diagram form in Fig. 1, is described as follows. The filter output is given by

$$y_j = W_{1j}x_{1j} + W_{2j}x_{2j} . \tag{1}$$

The filter is nonrecursive with two weights that are adapted using the simple algorithm

$$W_{1(j+1)} = W_{1j} + 2ue_j x_{1j} , \tag{2}$$

$$W_{2(j+1)} = W_{2j} + 2ue_j x_{2j} , \tag{3}$$

where

$$e_j = d_j - y_j .$$

The nonrecursive filter weights (W_{1j} and W_{2j}) are not constant but change in response to the error signal, e_j; hence the name "adaptive filter." The constant u controls the convergence time of the weights. Since e_j (and hence W_{1j} and W_{2j}) is modified for each sample, the filter acts as a tracking filter in the case of a distorted sine wave, which has a continually changing fundamental frequency.
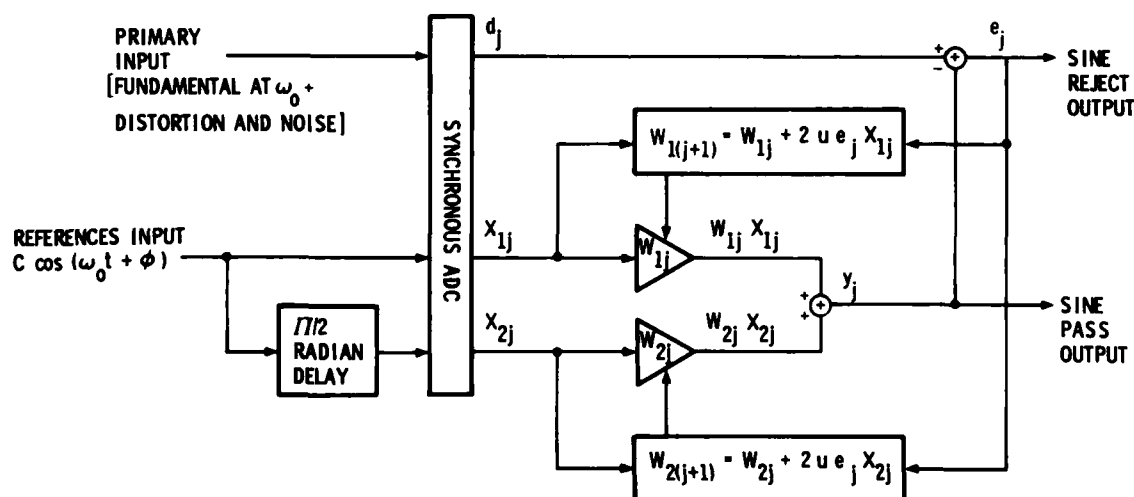
Fig. 1 - Block diagram of a single-stage adaptive tracking filter

30

The filter uses the error signal e_j to modify the weights so that the output y_j has the same amplitude and phase as the ω_0 component of the primary input signal. Therefore, the output y_j is an estimate of the primary input signal at ω_0. The signal e_j represents the primary input minus the ω_0 component and is therefore a sine reject output of the filter. If an estimate of the amplitude and phase of the component at ω_0 in the primary input with respect to the reference is required, it is not necessary to process the output y_j since the weights contain that information.

FILTER TRANSFER FUNCTIONS

The derivation of the transfer function for this deceptively simple filter is somewhat lengthy (although not too difficult) and is not repeated here. The interested reader is referred to Widrow [2], pp. 1698-1699, and Glover [3] p. 76.

The band-pass filter is of primary interest here and is discussed first. The transfer function is given in the z domain by

$$H_p(z) = \frac{2uC^2 \left[z \cos (\omega_o T) - 1 \right]}{z^2 - 2z (1 - uC^2) \cos (\omega_o T) + (1 - 2uC^2)} . \quad (4)$$

H_p has a single zero on the real axis at

$$z = 1/\cos (\omega_o T) . \quad (5)$$

This zero is always outside the unit circle for nonzero frequencies since

$$\left| 1/\cos (\omega_o T) \right| > 1 .$$

The poles of H_p are located at

$$z = (1 - uC^2) \cos (\omega_o T) \pm i \left[(1 - 2uC^2) - (1 - uC^2) \right.$$

$$\left. \cos^2 (\omega_o T) \right]^{1/2} . \quad (6)$$

The poles are inside the unit circle and for small values of uC^2, at a distance approximately equal to $1 - uC^2$ from the origin, at the same angle as the center frequency. The locations of the poles and zero of H_p are plotted on Fig. 2.
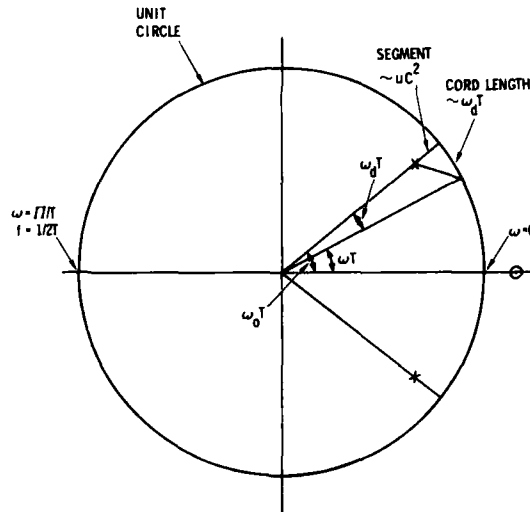
Fig. 2 - Locations of poles and zero of H_p (z)

The behavior of the function $\left| H_p(z) \right|$ near the center frequency ω_0 is determined by examining Fig. 2 and noting that the magnitude is dominated by the distance h of the pole from the frequency where the function is being evaluated. Referring to Fig. 2, the function $\left| H_p(z) \right|$ can be evaluated on the unit circle at the frequency ω by letting $\omega_d = \omega - \omega_o$. This gives

$$h^2 \sim (uC^2)^2 + (\omega_d T)^2 \quad \text{and}$$

$$\left| H_p \right| \sim uC^2/h \qquad \text{or}$$

$$\left| H_p \right|^2 \sim 1/\left[1 + (\omega_d T/uC^2)^2 \right] . \quad (7)$$

If

$$\omega_d T/uC^2 \ll 1, \quad \text{then}$$

$$\left| H_p \right|^2 \sim 1 - (\omega_d T/uC^2)^2 . \quad (8)$$

31

Equation (8) shows that $|H_p|^2$ assumes a parabolic shape near the center frequency. Equation (7) shows that the 3-dB points ($|H_p|^2 = 1/2$) are at

$$\omega_d T = uC^2 \quad . \tag{9}$$

If H_p is evaluated on the unit circle, $z = e^{i\theta}$, Eq. (4) can be reduced to

$$|H_p(\theta)|^2 = \cfrac{1}{\cfrac{(\cos\theta - \cos\theta_o)^2 (1 - 2 uC^2)}{(uC^2)^2 (\cos^2\theta_o - 2\cos\theta\cos\theta_o + 1)} + 1} \tag{10}$$

The magnitude and phase of H_p for a particular ω_o, T and u evaluated on the unit circle, are plotted as Fig. 3.
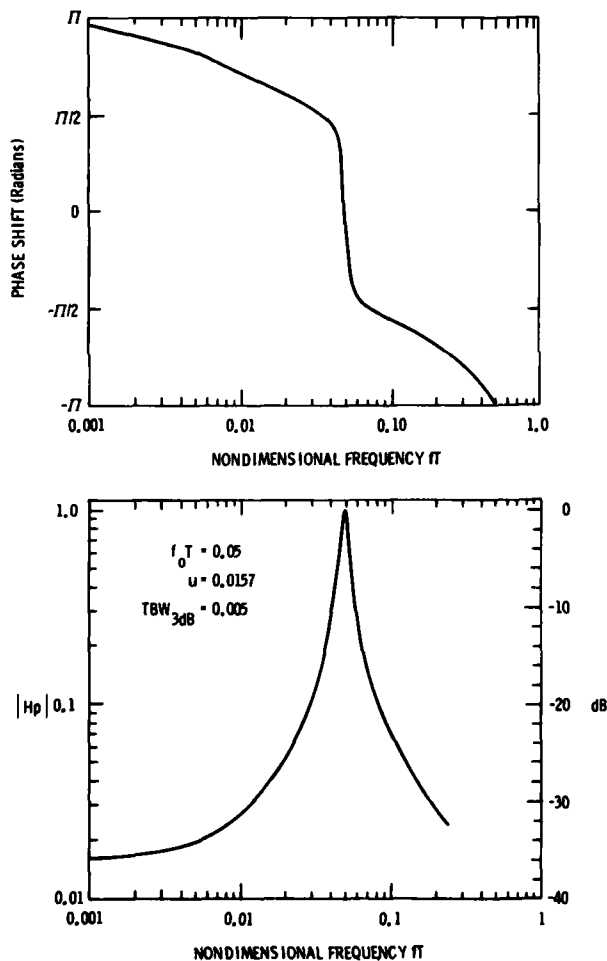
Fig. 3 - Amplitude and phase of a single-stage bandpass adaptive filter

The sine-reject filter is discussed extensively by Widrow [2] and Glover [3]. The filter transfer function is given by

$$H_r(z) = \frac{z^2 - 2z\cos(\omega_o T) + 1}{z^2 - 2z(1 - uC^2)\cos(\omega_o T) + (1 - 2uC^2)} \tag{11}$$

The poles are located at the same locations as for H_p. The sine-reject filter is ideal in the sense that the rejection is infinite for the steady-state case. This can be seen by noting that the zeros of $H_r(z)$ are located at

$$z = \exp[\pm i\omega_o T] \tag{12}$$

and are precisely on the unit circle at $\pm$ the center frequency of the filter. Therefore, the transfer function evaluated at the center frequency ($z = \exp[\pm i\omega_o T]$) is precisely zero.

FILTER BANDWIDTH AND TIME CONSTANTS

As mentioned earlier in Eq. (9), the 3-dB bandwidth is given by

$$\omega_{3\,dB} = 2uC^2/T \quad ,$$

$$BW_{3\,dB} = uC^2/\pi T \quad . \tag{13}$$

The filter responds to a step change in input with an exponential change to the correct value. The time constant of this exponential curve is fundamental to the filter. Widrow gives the time constant for a notch filter in terms of the number of iterations required to reduce the mean square error. The time constant for the band-pass filter is expressed as

$$\tau = T/uC^2 \quad , \tag{14}$$

where τ is the time constant of the filter output, y, to a step change in the filter input, d. Combining Eqs. (13) and (14) gives

$$\omega_{3\,dB} = 2/\tau \quad ,$$

$$BW_{3\,dB} = 1/(\pi\tau) \quad . \tag{15}$$

If the input is limited to frequencies of less than half the sample rate, the noise bandwidth is determined from

$$BW_{noise} = \int_0^{1/2T} |H|^2 \, df \; . \qquad (16)$$

Because this expression proved to be very difficult to evaluate explicitly, a numerical integration was used to determine an approximate expression,

$$BW_{noise} = BW_{3\,dB}(1.83\,u + 1.57), \qquad (17)$$

for

$$0.001 < u < 0.14,$$

or

$$BW_{noise} \sim 1.57 \, BW_{3\,dB} \; . \qquad (18)$$

BEHAVIOR OF FILTER WEIGHTS

An explanation of how the filter works in terms of the behavior of the filter weights follows.

The result of the adaptive algorithm, Eqs. (2) and (3), is to drive the error signal e_j to a minimum in the mean square; i.e.,

$$E\left[e_j^2\right] = \text{a minimum} \; .$$

It has been shown [2] that the algorithm will converge, and that the result is unbiased. This particular algorithm is successful with only two weights because of the $\pi/2$ rad (90°) phase lag between x_{1j} and x_{2j}. If the delay is not $\pi/2$, many more weights are required to achieve as narrow a band-pass filter as the one described. Errors encountered when the lag is near but not equal to $\pi/2$ will be discussed later. The advantage of the $\pi/2$ delay is easily understood in the special case where the primary input and the reference input frequency are the same (with only an amplitude and phase difference). In this case, the weights (W_{1j} and W_{2j}) converge to stable values such that the vector sum of $W_{1j}\,x_{1j}$ and $W_{2j}\,x_{2j}$ is exactly equal to the primary input d_j. The error signal e_j is then zero; and from Eqs. (2) and (3) it can be seen that no further changes in the weights occur.

If the primary input consists of a sine wave (the same frequency as the reference input) plus uncorrelated noise, the weights converge to the correct answer that gives the magnitude and phase of the primary input with respect to the reference input, plus a time-varying part with a zero mean. This time-varying part is caused by the fact that the error signal e_j cannot be driven to zero. The time-varying weights modulate the reference input such that the output y_j has an uncorrelated component riding on the steady-state solution, precisely the component expected when the filter is considered as a black box with the transfer function given in Eq. (5). The uncorrelated component can be made smaller by making u smaller as in Eqs. (2) and (3); or by noting that the bandwidth has been decreased as in Eq. (13), thereby reducing leakage through the filter. When u is reduced, however, the convergence time constant of the filter is increased as in Eq. (14).

Consider now the case where the primary input d_j and the reference input are at different frequencies. In this case, the weights vary sinusoidally at the difference frequency, converting the reference frequency into the primary frequency. The amplitude and phase of the converted frequency y_j are as predicted by Eq. (4).

When the filter weights are used to estimate the primary component at ω_0 with respect to the reference, the time-varying part of the weights cause an error in the estimate. The error has a zero mean, which suggests that smoothing the estimate can alleviate this problem. Note that the actual weights are not smoothed, only the estimate (or average weight).

EFFECT OF A NONORTHOGONAL PHASE DELAY

Glover [3] investigated the effect of phase delay between x_{1j} and x_{2j}, different from $\pi/2$ rad. This work indicated that the principal effect is to introduce harmonic distortion into the output waveform. Frequencies at which the distortion can appear are given by

$$f_{distortion} = 2f_r \pm f_d \; ,$$

where

$$f_r = \text{the reference frequency,}$$

$$f_d = \text{the primary frequency} \; .$$

33

For the special case where $f_r = f_d$, a stable solution can be found where $e_j = $ nd where the harmonic distortion is not present. In a tracking filter application this implies that the fundamental component of the primary input will not cause distortion.

Glover also showed that if the phase delay is close to $\pi/2$, the distortion becomes quite small. Thus some error is permissible for the filter to produce satisfactory results.

MULTIPLE-STATE ADAPTIVE FILTER

If a single-stage filter as described does not produce a filter with enough attenuation, the filters can be cascaded to produce steeper skirts. A two-stage filter is shown in Fig. 4. The method can be extended easily to N stages.

The transfer function for an N stage filter is simply

$$H_{N\ stages}(z) = (H_p(z))^N \ ,$$

and can be determined directly from Eq. (4) and Fig. 3. The time constant (or convergence time) is

$$\tau_{N\ stages} = N\tau \ ,$$

where τ is given in Eq. (14). Several important parameters for multiple stage filters are summarized in Table 1. The shape factor for a single-stage filter does not exist because the attenuation is never 60 dB.
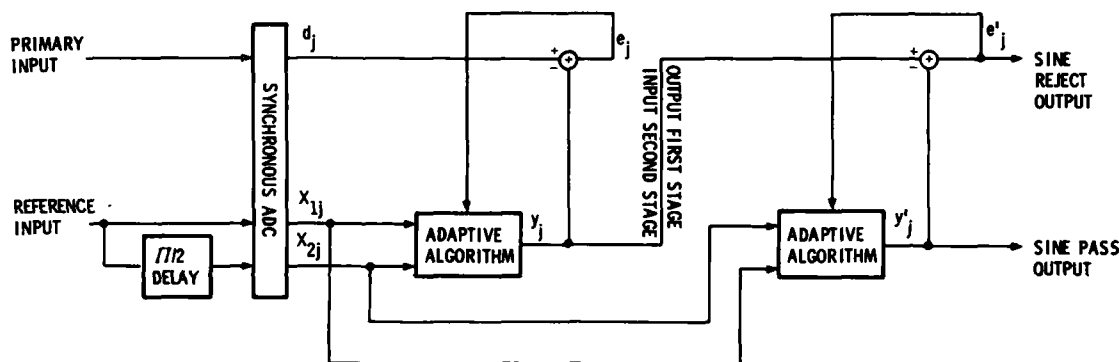
Fig. 4 - Block diagram of a two-stage adaptive tracking filter

TABLE 1
Summary of Tracking Filter Characteristics

Number of Stages	1	2	3	4
3-dB Bandwidth	$\dfrac{1}{\pi \tau *}$	$\dfrac{0.642}{\pi \tau}$	$\dfrac{0.509}{\pi \tau}$	$\dfrac{0.434}{\pi \tau}$
Shape Factor (ratio of 60-dB BW to 3-dB BW)	--	60	20	6
$\dfrac{\text{Noise BW}}{\text{3-dB BW}}$	1.83u+1.57	1.53u+1.22		
Time Constant	τ	2τ	3τ	4τ

$*\tau = T/uC^2$

34

To compare these values with an analog filter, a typical analog tracking filter has a time constant equal to 1/BW and a shape factor of from 4 to 10. Thus a two-stage adaptive filter is about 2.5 times as fast but has a poorer shape factor than a comparable analog filter.

EXAMPLES

The first example illustrates the response of the filter to a unity step change in input. The filter was single-stage; the center frequency was set at 100 Hz; the sample rate was 2000 samples/s, and the 3-dB bandwidth was 1.6 Hz. A time constant of 0.2 s results. Input to the filter was a 100-Hz sine wave with unity amplitude beginning at t = 0. Peak response of the filter is plotted as Fig. 5. As can be seen, the response follows an exponential curve with the predicted time constant.
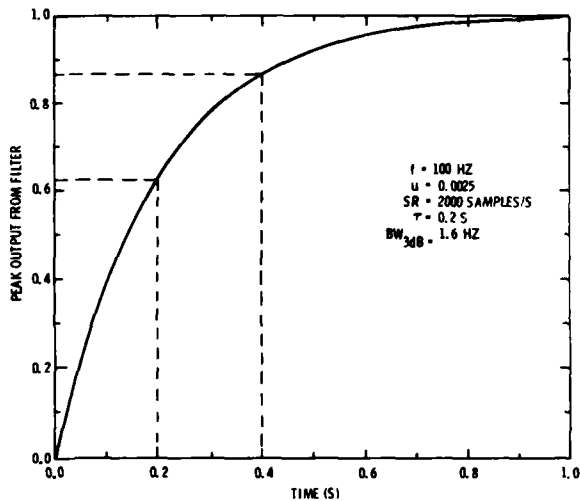
Fig. 5 - Response of a filter to a unit step change in input

For the second example, the reference input was a unity amplitude sine wave that was swept from 50 to 150 Hz at 1 octave/min. The primary input was set equal to the reference input plus a third harmonic term equal to the input. The unfiltered waveform and the filtered waveform were sampled when the frequency was 80 Hz and are plotted as Fig. 6. The filter was a two-stage filter with a 3-dB bandwidth of 10 Hz and a sample rate of 2000 samples/s.

For the third example, the reference input was the same as for the second example. The primary input was formed by first filtering

the reference input with a single-degree-of-freedom filter with a natural frequency of 100 Hz and 2-percent damping. A broadband white random noise with a bandwidth of 200-2000 Hz was then added to the single-degree-of-freedom filtered reference signal. The rms level of the random signal was 0.89. The adaptive filter was a two-stage filter with a 3-dB bandwidth of 10 Hz. The sample rate was again set at 2000 samples/s. The time histories of the filter input and output were sampled at 80 Hz and are plotted as Fig. 7. Note that the filter did an excellent job of removing random noise.
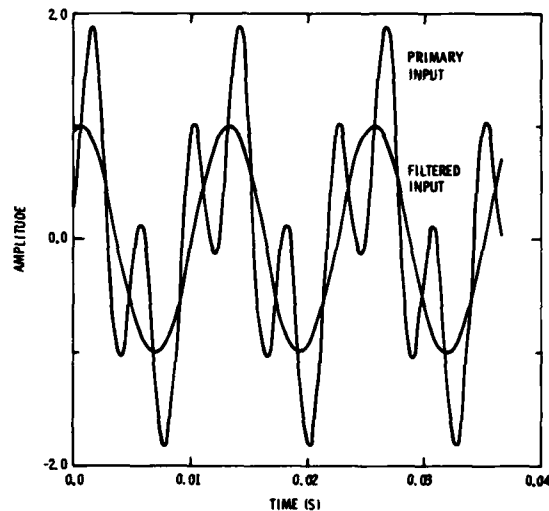
Fig. 6 - Response of a filter to a sine with 3rd-harmonic distortion
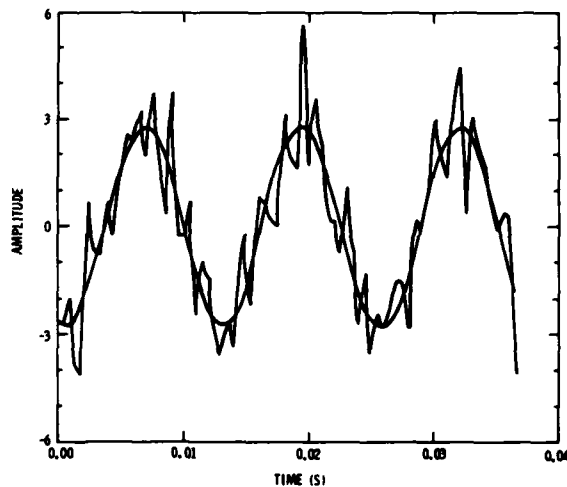
Fig. 7 - Response of a filter to a sine with white noise added

The filter output has an amplitude of almost three because the adaptive filter input is already on the resonance curve of the single-degree-of-freedom system. Also note that there is no apparent phase shift between the filter input and output. The last-stage filter weights were smoothed by an exponential weighting function with a time constant of 100 samples. Results are plotted as Fig. 8. The filter correctly measured the response of the single-degree-of-freedom system.

CONCLUSIONS

It has been shown that an adaptive filter can provide an easily implemented effective digital tracking filter with several useful outputs (Fig. 9). If it is assumed that the filter bandwidth can be quantized to the extent that multiplication by 2 u can be accomplished with a shift, the filter can be implemented with four multiply-adds for each sample point and each stage of the filter. Two multiply-adds are required to compute the filter output, Eq. (1); and two multiply-adds are required to update the filter weights, Eqs. (2) and (3). The filter can be used as either a band-pass or a band-reject filter. The gain of the filter at the center frequency is unity with a zero phase shift. If the magnitude and phase of the fundamental component of the primary input with respect to the reference input are required, this information is contained in the filter weights, and no further processing of the output is necessary.

A two-stage filter appears to be a reasonable compromise between the increased computational effort required and the filter time delay associated with filters with more stages and the noise rejection properties of a single-stage filter.
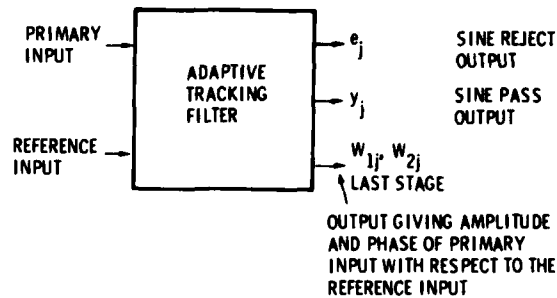
Fig. 9 - Block diagram of an adaptive tracking filter

Fig. 8 - Response of a single-degree-of-freedom system measured with an adaptive filter

REFERENCES

1. N. Wiener, Extrapolation, Interpolation and Smoothing of Stationary Time Series, with Engineering Application. Wiley, New York, 1949

2. B. Widrow, et al., "Adaptive Noise Cancelling: Principles and Applications," Proceedings of the IEEE, Vol. 63, No. 12, pp. 1692-1716, Dec. 1975

3. J. Glover, "Adaptive Noise Cancelling of Sinusoidal Frequencies" Ph. D. dissertation, Stanford University 1975

DISCUSSION

Mr. Stroud (Lockheed Missiles and Space Co.): How do you expect to use this filter? Are you using it in a post processor or a real time application?

Mr. Smallwood: The idea is to use it in the real time application. I have not implemented it in any of our systems yet.

Mr. Stroud: The "Modalab" system that Strether Smith described here a couple of years ago is based on a discrete sine sweep or a series of dwells. We have had some success with this technique and we find that there is time to do all of the "number crunching" that is required by this technique while the structure settles.

Mr. Chapman (Jet Propulsion Laboratory): I wrote a software program to do exactly what you did, and we are using that for analysis. I don't know if you are implementing yours in software, hardware, or both, but there is a limitation in the software version, you run out of time as you get up in frequency. But we went one step further, we computed the RMS of the signal and then we plotted that against the unfiltered RMS output so that we show the RMS of the fundamental and then the unfiltered signal on a single plot; using our sine analysis program this gives one insight into some of the dynamics of the structure, particularly if you are recording the response acceleration all over a structure. We were doing everything in software. I was computing the cosine from the constant sine and I built some hardware to obtain the frequency and also the cosine, the 90° difference in the signal, in the hope that we can speed up this process and do it in real time.

Mr. Smallwood: Everything he said was true. I was not anticipating computing those two sample points, X1 and X2. But if I were to do it I would use software with some type of look up table, or something that is relatively fast, to avoid this problem of the time that it takes to compute the cosine from the sine.
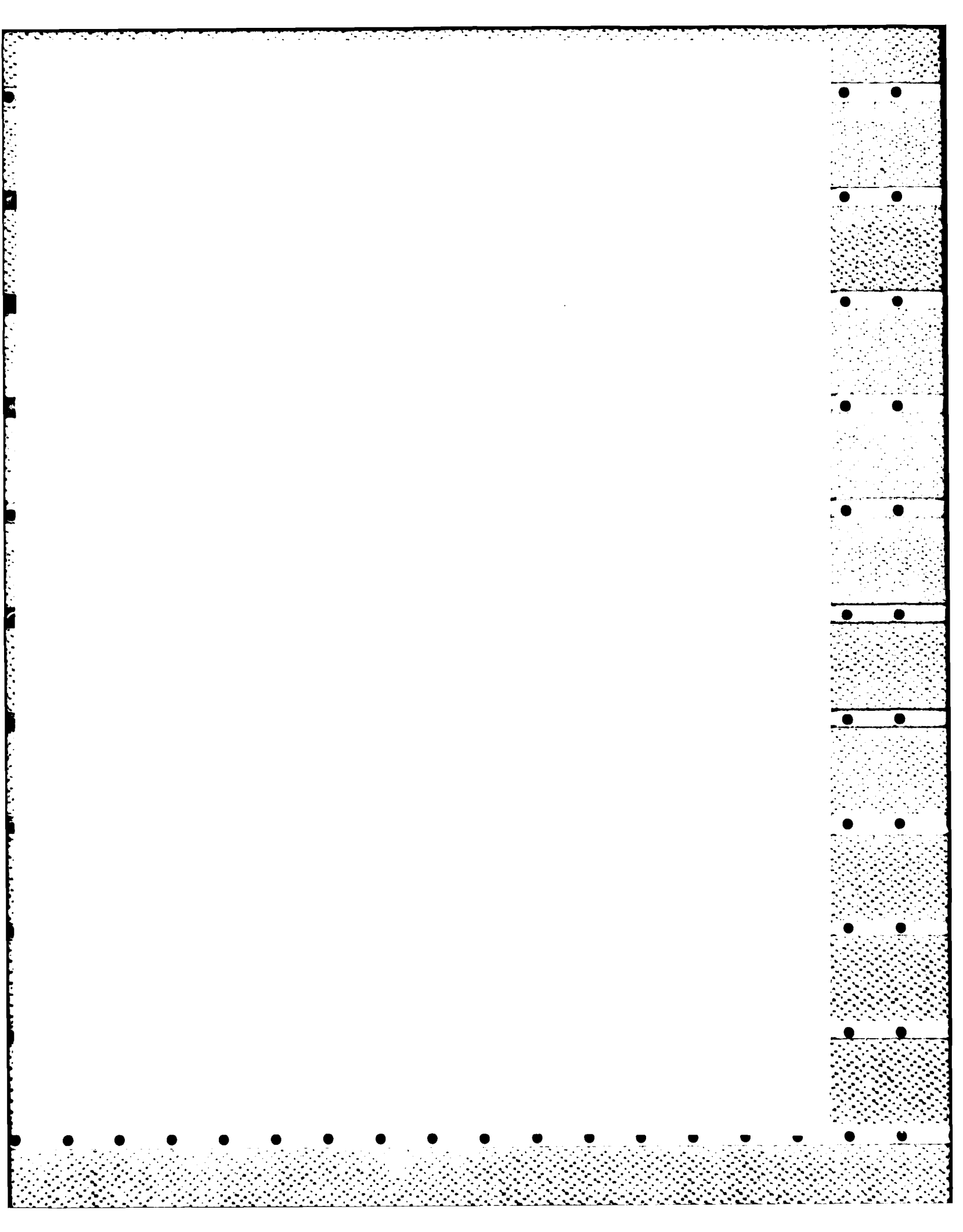
TOTAL MISSION ENVIRONMENTAL SIMULATION

THROUGH DIGITALLY CONTROLLED ELECTROMAGNETIC VIBRATION

D. Hinckley and F. Foley
Boeing Aerospace Company
Seattle, Washington

and

P. Moseley and W. Ross
Hewlett-Packard Company
Santa Clara, California

Software for use with a standard digital vibration control system has been developed which implements the capability to combine shock, random, and sinusoidal tests in close sequence to provide a real time dynamic simulation for missions of a broad range of missiles, spacecraft, and torpedoes.

INTRODUCTION

The determination of missile guidance accuracy and hardware reliability has in the past been based on flight data. Economic considerations have recently limited flight test programs to a point where a source of supplemental flight quality data is required. Experimental test programs have been performed to evaluate methods for obtaining these data. One program, which proved successful, subjected test hardware to a simulated recorded flight environment. Boost phase shock and vibration data which included that produced by vehicle ordnance ignition, engine burning, and air pressure and acoustical noise were reproduced on an electromagnetic vibration system to simulate the mission environment on a missile guidance system. Data obtained from this program indicated this was a viable approach to obtaining flight type information to support reliability determinations.

A closed loop system was required to insure proper test environments and provide adequate protection for flight hardware. A digital computer based system was developed which met these requirements.

SYSTEM REQUIREMENTS

It was determined the following requirements would have to be met if a system were to be procured:

1. The system must provide simulation representative of all elements of the mission boost phase.

2. The system must provide closed-loop control with controlled shutdown in case of an aborted test.

3. The system must have full data analysis capability to allow its use at a remote facility.

4. The system must be cost effective.

The primary requirement of the control system was that it be able to provide the dynamic environments representative of those the missile guidance system experiences in the boost phase of flight, in the same sequence and with the same timing. Figure 1 shows an acceleration/time plot of the dynamic response of a typical module obtained from telemetered data. It is seen the mission consists of six separate shocks, five random episodes, one sinusoidal sweep and one period with no input. In reviewing data from a number of flights, it was found that there was a very broad response envelope which would simplify the control problem. On the other hand, the time between events was quite short, ranging from only 1.0 to 2.0 seconds. This timing is critical to proper mission simulation. The hardware under

39

test is preprogrammed and functions independently of the vibration test sequence. The proper environments must be correlated to the appropriate test article functions by rigid control of timing.
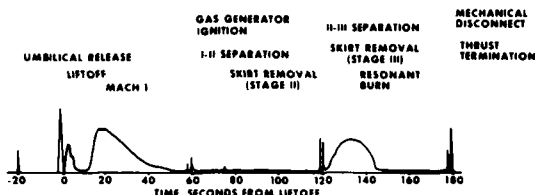
Fig. 1 - Typical Flight Profile

Since the articles being tested were to be operational guidance systems in the logistics pipeline, it was mandatory that a number of safeguards be incorporated into the system. Considering the possibility of changes in the dynamic characteristics of the vibration system and differences between individual test articles it was imperative that, insomuch as it was possible, the full test sequence must be under closed-loop control. In addition, a controlled shutdowm must occur following an abort signal generated:

1. Internally by the system upon exceeding the upper dynamic test tolerance;

2. by the test director actuating an abort button;

3. by the guidance system control unit upon recognition of a potentially dangerous out-of-tolerance operating condition.

It was anticipated that the closed-loop control, in addition to being a safety feature, would provide a high level of repeatability between tests which could be supportive of the statistical analysis which would be performed in making system reliability determinations.

The Hill Air Force Base, Little Mountain Test Annex, where this program will be carried out, is a newly opened remote site. Due to this fact, it was highly desirable that the test laboratory be self-sufficient with regard to test operations, data recording and data analysis. To achieve this self-sufficiency in the most economical way, the requirement was levied against this control system that it be capable of handling all necessary dynamic data analysis. This would include time histories, X-Y plots and power spectral densities as a minimum, with the desirability of also having Fourier Transforms, transfer

functions and coherence functions. These plots would have to be fully annotated and of document quality.

In addition to these technical requirements, the system had to meet the ever present budget restraints. To make this possible it was necessary that the hardware and software be off-the-shelf, standard commercial product wherever possible. Meeting these objectives would provide the necessary data for determining guidance accuracy and hardware reliability at a cost several orders of magnitude below equivalent range testing.

SYSTEM DESCRIPTION

The system is a general purpose digital vibration control and data analysis system. A 32 K minicomputer, Fast Fourier Analyzer and a control system are the basis of the system. This hardware is supported by a disk, operator terminal, magnetic tape, plotter and paper tape subsystems. All the hardware was standard "off-the-shelf". The standard software provided with the system included sinusoidal, transient and random control packages and a data analysis package. Special purpose software developed for this system included the long duration transient and the mission simulation control functions. Figure 2 is a photograph of the system.

Fig. 2 - Control System

40

Figure 3 is a block diagram showing the major system elements and how they are interconnected.
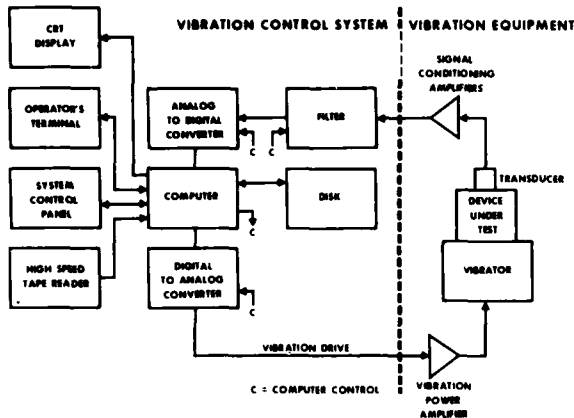
Fig. 3 – Vibration System Block Diagram

SYSTEM OPERATION

The use of special purpose Mission Simulation Control software is the major feature of the system. A mission profile simulation consists of a sequence of contiguous environmental tests which can be random, sinusoidal and/or transient and intervals with no excitation. The interval between environmental tests does not exceed 2.0 seconds and the dynamic control range of the environments is 65 db.

The system has the capability to synthesize a mission profile containing up to:

1. Six random excitations, each defined by different amplitudes, shock spectra and duration. One amplitude change may be programmed during each environment.

2. Ten transient excitations of different amplitudes, time domain wave shapes and durations.

3. Six sinusoidal environments of different amplitudes and sweep rates.

4. Six periods of no-environment inputs.

These environments are automatically sequenced to provide a single mission profile.

The short time interval between environments, 1.5 to 2.0 seconds, was required to simulate the flight environments. During this interval the test in process is programmed to a no-excitation level, the parameters for the next envi-

ronment are loaded into the computer and the excitation is increased to the full level of the new environment.

Each test environment is set up individually by an interactive dialogue through the system terminal and the system control panel (see Figure 4). Once an environment is set up, it is stored in a one of three catalogs (one each for sine, random and transient environments) each with room for 50 environments. An example of this dialogue for Random Vibration Control Setup is shown in Figure 5. Figure 5 Line 12 is an example of the setup for varying randome levels during a test segment.
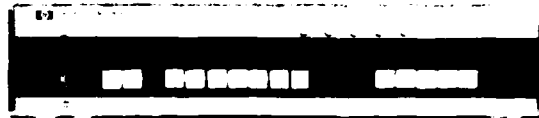
Fig. 4 – Mission Simulation
Control Panel

VIBRATION CONTROL SETUP

0 = DATA RECALL, 1 = RANDOM, 2 = SINE,
3 = TRANSIENT, 4 = MISSION SIMULATION,
5 = POST TEST PLOT
1

RANDOM VIBRATION CONTROL SETUP

FUNCTION? TY, PR, DS, DL, PU, ??
TY

1. IDENT:
RVC OPERATIONAL CHECKOUT

2. TRUE RANDOM MODE? YES;NO
NO

3. AVERAGING WEIGHTING FACTOR?
16

4. 3 SIGMA CLIPPING?   YES;NO
NO

5. MEASUREMENT MODE?   YES;NO
NO

6. # CONTROL CHANNELS?
1

7. CALIBRATION?   MV/G
    CHANNEL A

500

8. SYSTEM GAIN? G/VOLT @ INPUT
2

9. INITIAL LEVEL?   -DB
0

41

10. TIME/STEP? 2Ø SEC MAX
1

11. ABORT TIME? 1Ø SEC MAX
.2

12. FULL LEVEL TEST TIME? SEC
2Ø

   SECOND FULL LEVEL? % OF FIRST
   LEVEL
5Ø

   SECOND FULL LEVEL TEST TIME? SEC
1Ø

13. LINE ALARM LIMIT? %
5Ø

14. RMS ABORT LIMIT? DB
3

15. # LINES?
256

16. LOWEST FREQ?
2Ø

17. HIGHEST FREQ?
2ØØØ
   MAX FREQ. = 25ØØ.ØØ HZ
   RESOLUTION = 9.7 HZ
   LOG HORIZ. = 3 DECADES
   SET OUTPUT FILTER = 2ØØØ HZ
   SET INPUT FILTERS = 3ØØØ HZ

18. INPUT MODE?

   1 = MAG., FREQ, LIMIT(DB);
   2 = SLOPE, FREQ, LIMIT(DB);
   3 = TAPE
2

19. INITIAL SLOPE? DB/OCT
6

2Ø. 1ST BRKPT? GSQR/HZ, FREQ, LIMIT
.ØØ2, 65Ø, 3

21. SLCPE, FREQ, LIMIT?
6, 12ØØ, 3

22. SLOPE, FREQ, LIMIT?
Ø, 15ØØ, 3

23. SLOPE, FREQ, LIMIT?
-6, 2ØØØ, 3

   RMS VALUE = 2.7Ø8 G'S

   FUNCTION? /C, /R, /L, /P, /S,DL,PU,/E,
   ??, /S
   RANDOM RECORD #? (ØØ-48)
   Ø

   FUNCTION? /C, /R, /L, /P,/S,DL,PU,/E,
   ??,/E

Fig. 5 - Random Setup

   After each new test environment need-
ed for the mission has been stored, the
mission profile setup is accomplished.
This also is done through a dialogue
between the system and the operator.
An example of this dialogue is shown in
Figure 6. Referring to item 2 in the
Figure, the operator specifies a mis-
sion by entering a list of all the test
environments to be sequenced in the

mission profile.

   The operator can also request that
event marker outputs be generated by the
mission simulation control system.
These are TTL compatible logic signals
that are issued prior to the beginning
of an environment. The signal can be
used for test control, test article
control or data system event markers.
The first entry in Figure 6, item 2
specifies an event marker to occur at
200 msec before the beginning of Random
Environment Ø.

VIBRATION CONTROL SETUP

Ø = DATA RECALL, 1 = RANDOM, 2 = SINE,
3 = TRANSIENT, 4 = MISSION SIMULATION,
5 = POST TEST PLOT
4

MISSION SIMULATION

MISSION SIMULATION SETUP

FUNCTION? TY, PR, LS, DS, DL, PU, ??
TY

1. IDENT: MSC OPERATIONAL CHECKOUT

2. MISSION KEYWORD LIST:

RANDØØ, 2ØØ
RANDØØ, Ø
SINEØØ, 4ØØ
NI, 1ØØ, 3ØØ
TRANØØ, 5ØØ
/E

3. ADC OVERLOAD VOLTAGE: 8

4. SELF-CHECK LEVEL (MV): 1ØØØ

5. CALIBRATION (MV/G): 5ØØ

FUNCTION? DL, PU, RT, /L, /R, /S, /P,
/E,?? /S

ENTER SEARCH KEY:
MSC OPCHECK

FUNCTION? DL, PU, RT, /L, /R, /S, /P,
/E??
/E

END OF SETUP

Fig. 6 - Mission Simulation Setup

   In addition to Random, Sine and Tran-
sient environments, the system can pro-
vide periods of zero excitation, or
"No-Input", to the shaker. The fourth
item on the list is such an event and
is designated by NI for "No-Input". It
is specified to have a duration of 10
seconds with a precursor event marker
300 msecs preceding it.

   As with the setups of the various

42

test environments, the mission profile setup can be listed and edited, then saved on the disk in a setup catalog of up to 50 entries.

After all the test environments and the mission profile have been set up, the system has all the information needed to run a test. This information is all permanently stored on the disk, and can be used immediately or at any time in the future. If desired, the disk can be used immediately or at any time in the future. If desired, the disk can at this point be removed from the system and the system can be used for other purposes.

Once the mission profile has been setup and stored, the remaining functions required to complete a Mission Simulation are a self-check and an operate sequence.

When the individual tests were set up and stored in the catalog, certain parameters for these tests were stored on the disk. However, additional information must be generated before any of the test environments are actually ready to be run. This consists of reference spectra, with the amplitude and spectral characteristics required for the test, and drive waveforms which have compensated for the transfer function of the device to be tested. All of these additional data are generated and stored on the disk during the Self-Check Phase.

During the Self-Check Phase, the system actually performs three relatively independent functions: Self Setup, Master Self-Check and Individual Self-Checks.

During Self-Setup, the setup information for each of the tests to be run in the mission profile is loaded from the setup catalogs on the disk; the data required to generate the test signals is computed; and all of these data are stored back on the disk in the mission profile data area.

During Master Self-Check the system transfer function is computed. The system generates a random waveform with a flat frequency/voltage spectrum extending over the frequency range of the profile. This environment is applied at a selectable low calibration level to the test article. The response of the system to this environment is measured and the system transfer function is computed. This calibration is performed for each frequency band width which exists in the Mission profile. The transfer function information is used to pre-equalize each drive spectrum to be used during the test.

This pre-equlization allows the test to proceed to full level under closed loop control conditions in a shorter time duration.

During the Individual Self-Checks, the appropriate operate coreload for each test environment in the profile is read from the disk and initialized. This initialization consists of storing in it a pre-equalized drive spectrum and setting various flags so that during the mission profile the test environment can proceed immediately to full level test with the properly equalized waveform.

After the Self-Check Phase, execution of the mission can be initiated by the operator or by a remotely generated logic signal. When this occurs and since the coreload was initialized in advance, the test proceeds immediately to full level and runs for the time the operator had previously specified. Random and sinusoidal tests are continuously equalized during operation to compensate dynamically for any changes in the transfer function of the device under test. Pseudo random excitation is used during the random environment. Using pseudo random, a shorter time interval to full level was achieved and a more accurate control of the environment was obtained. When the specified time interval for a test has passed, the excitation is removed in a pre-programmed method and the next coreload in the profile sequence is read from the disk. It was the requirement for the fast transition times between environments that dictated use of the pre-equalization and coreload swapping incorporated in this software system. Figure 7 shows a timing diagram for a typical transition from one test environment to another.

The operation described above is repeated until all test environments specified for the mission have been executed. During the mission, the operator is continuously cued regarding the status of the mission profile. At all times during the test, the signals from the device are being monitored and if any signal deviates from normal by more than an operator-specifiable amount, the system will automatically abort. An abort can also be initiated by externally generated signals from independent instrumentation or by the test director.

Figure 8 shows a typical signal that could be generated during a mission profile.

When the entire profile is completed, the operator can either rerun the mission or proceed to analyze, display and plot

43

the measurements that were automatically saved on the disk throughout the entire mission.

RANDOM/RANDOM   1 SEC

RANDOM/SHOCK/RANDOM   1 SEC

RANDOM/SHOCK/SINE   1 SEC
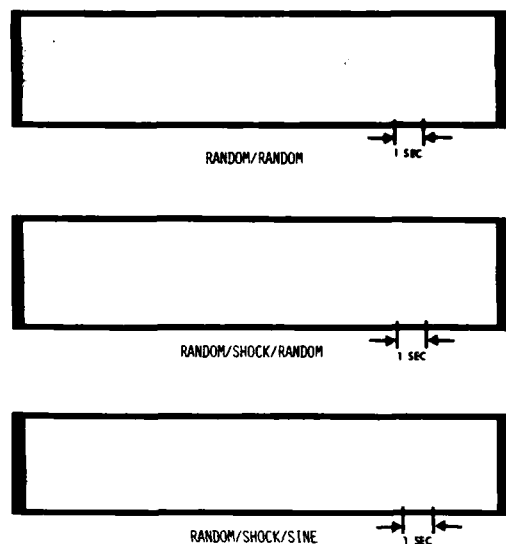
Fig. 7 - Typical Transition Times Between Environments

UMBILICAL RELEASE   I-II SEPARATION   II-III SEPARATION   THRUST
LIFTOFF   SKIRT REMOVAL   TERMINATION
     MACH 1   RESONANT BURN

-20   0   20   40   60   80   100   120   140   160   180
TIME, SECONDS FROM LIFTOFF
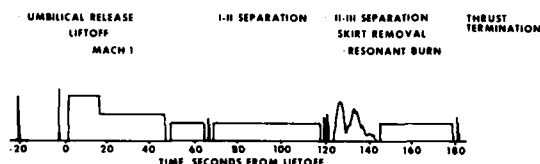
Fig. 8 - Mission Simulation, Typical Module Response Acceleration (Peak) vs Time

During the course of a Mission Simulation Test, the data from each segment of the test was saved on the disk and identified. The Data Recall phase is designed to retrieve these data from the disk and document it for record-keeping purposes.

The system will list the tests that were used to make up the particular Mission Simulation just performed and allows selection of the test to be documented. This is shown in Figure 9. If, for example, "Ø3" were given as the answer to the "Enter Test No" question, then the data from the Sine ØØ segment of this test would be available for viewing. Exercising the Display Select buttons on the System control cause the software to retrieve the data of any indicated type for the selected test. For example, if the control spectrum is to be viewed, pushing the button labeled

CONTROL will cause this data to be recalled from the disk and displayed on the CRT. In addition, the type of data and the time during the test at which it was saved are printed on the system terminal.

```
VIBRATION CONTROL SETUP
0 = DATA RECALL, 1 = RANDOM, 2 = SINE,
3 = TRANSIENT, 4 = MISSION SIMULATION,
5 = POST TEST PLOT
5

01 TRAN42

02 TRAN36

03 RAND27

04 RAND28

05 RAND29

06 TRAN43

07 RAND30

08 TRAN42

09 TRAN42

10 SINE02

11 RAND31

12 TRAN42

ENTER TEST NO.
3

RANDOM VIBRATION TEST DATA
1ST STAGE HI LEVEL RANDOM R1

OUTPUT DEVICE?
1 = PRINT, 2 = PUNCH, 3=7210, 4=TEK
```

Fig. 9 - Typical Post Test Environment List

To plot the data just retrieved is accomplished by actuating the PLOT button on a Digital Plotter or Graphics Terminal. A typical example of such a plot is shown in Figure 10.

Thus, the machine has the capability to look at any of the data individually from each segment of the Mission Simulation sequence or to generate post-test plots of any segment of the Mission Simulation sequence.
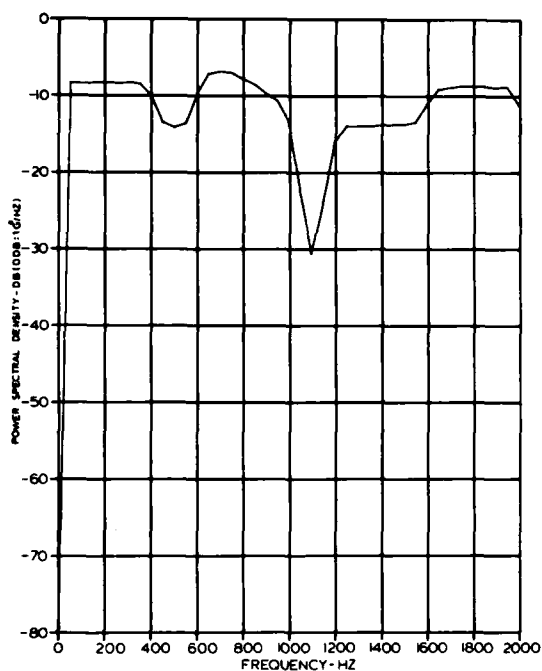
44

POWER SPECTRAL DENSITY - DB(10DB=10²/HZ)

FREQUENCY - HZ

CIC	8-04		FIXTURE CONTROL Z AXIS 1ST STAGE HI LEVEL RANDOM RR3H PSD ANALYSIS DELTA F=50HZ	AHP-0622
CHECK				
APP				0.715 GRMS
APP			BOEING	

2-2052-101-308

Fig. 10 - Fixture Control Z Axis
1st Stage Hi Level Random RR3H
PSD Analysis Delta F = 50 HZ

CONCLUSION

The system has been supporting test activities at Hill Air Force Base since February, 1976. All noted discrepancies have been resolved and the system is performing within specification. This test activity proves that a general purpose closed loop digital vibration control system has been developed which is capable of providing full dynamic simulation of a broad range of missions on an electromagnetic vibration system. It is especially suited for hardware with single-shot missions such as torpedoes, tactical and strategic missiles and spacecraft.

ACKNOWLEDGMENTS

Design of the Mission Simulation Control System was done at Hewlett-Packard Company, Santa Clara Division, by James Hardin, Dean Johnson, and Mark Skrzynski.

A COMPARISON BETWEEN SINUSOIDAL SWEEP AND BROADBAND DIGITAL TECHNIQUES FOR
RESONANCE SEARCH AND TRANSMISSIBILITY MEASUREMENTS

Peter Moseley
Hewlett-Packard Company
Santa Clara, California

Stimulus response measurements using broadband excitation are discussed.
Pseudo random and periodic random excitation signals are described and
their advantage in obtaining all of the frequency response data at once
is presented. The effects of limited resolution are discussed and
results of narrow band sine sweep and broadband measurements are com-
pared. Applications for broadband testing are presented.

INTRODUCTION

Digital vibration control and measurement
systems are gaining wide acceptance in vibra-
tion test laboratories, and the range of appli-
cations is being steadily expanded. The ease
of set-up and use of such machines has made
them very attractive for control applications,
and they have produced real economies in the
laboratory.

The use of broadband digital techniques
for measurements, such as resonance search or
transmissibility offers similar advantages in
ease of set-up, use and test time. This paper
describes how digital techniques can be applied
to these measurements.

BACKGROUND

"Stimulus-response" measurements are very
useful tools for understanding the behavior of
devices. If this type of testing is performed
as a function of frequency, then frequency res-
ponse plots (transfer functions) can be obtain-
ed which reveal information about the modal pro-
perties of the device under test.

A system can be modeled as shown in Figure
1. Using the notation that small letters re-
fer to time domain functions and capital let-
ters to frequency domain functions, and recog-
nizing that these are Fourier transform pairs,
we may write an expression for the input and
output relations as follows:

$$Y(f) = X(f) \cdot H(f) + N(F)$$

Figure 1

If we define the noise (N) to be uncorrelated
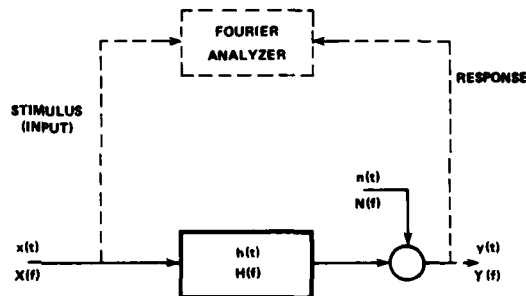and post-multiply by the conjugate of the input
and perform averaging, then we get the expected
values to be

$$E[Y \cdot X^*] = H \cdot E[X \cdot X^*] + E[N \cdot X^*]$$

where $E[N \cdot X^*]$ goes to zero.

Solving for H we get

$$H = \frac{E[YX^*]}{E[XX^*]}$$

47

If we consider the relation between the input and response power we get:

$$E[YY^*] = |H|^2 E[XX^*] + E[NN^*]$$

We define a function γ^2 (the coherence function) such that

$$E[YY^*] = \gamma^2 E[YY^*] + (1-\gamma^2) E[YY^*]$$

Thus

$$\gamma^2 E[YY^*] = |H|^2 E[XX^*]$$

and

$$[1-\gamma^2] E[YY^*] = E[NN^*]$$

γ^2, the coherence function, tells us what fraction of the output power has been caused by the input. The transfer function H and the coherence function γ^2 are readily calculated in digital systems, and together are powerful tools for understanding systems.

The power of the fast Fourier transform (FFT) lies in the fact that measurements can be made simultaneously at many frequencies over a wide bandwidth, which means that broadband excitation can be used as a stimulus. The stimulus can be random noise or periodic random or any other broadband input such as impulses.

Figure 2 shows, in block diagram form, a typical test set-up. Measurements are made between the "input", typically at the mounting point of the device, and the "response" typically at various points around the device under test. Figures 3, 4 & 5 show example frequency response plots portrayed in 3 different ways, that is, log magnitude and phase, magnitude and phase and real and imaginary. Figure 6 is the coherence function.

SIGNAL GENERATION

Pseudo Random Excitation

When making a measurement, we generally want to excite the device under test over a specified frequency range, for example 5 to 2000 Hz. By constructing a sampled representation of the desired excitation spectrum in the frequency domain with say n/2 points we may limit the bandwidth, and control the magnitude of the spectral components. If a signal constructed in the frequency domain has a random distribution of phase angles among the various frequency components, then the central limit theorem tells us that the Fourier transform of this will result in a signal in the time domain having an essentially gaussian amplitude distribution. Since the original frequency domain representation of this signal has n/2 different frequency components, the time waveform will consist of n samples of the desired waveform. These samples can be sequentially output via a Digital to Analog Converter, low pass filtered and then applied to the exciter system. Since the record is n samples long, (say n = 2048 points) it is necessary to repeat it to get a continuous signal. This results in a pseudo random signal which is periodic with a period $T = n\Delta t$ (where Δt is the clock period of the DAC). The lowest frequency component that can be in this signal is 1/T. This signal can be thought of as that which would result from summing the output of n/2 oscillators set at frequencies 1/T apart beginning at frequency 1/T, assuming the phasing between the signals is constant but initially chosen at random.

If such a signal is applied to the device under test then the steady state response will be the superposition of the frequency response
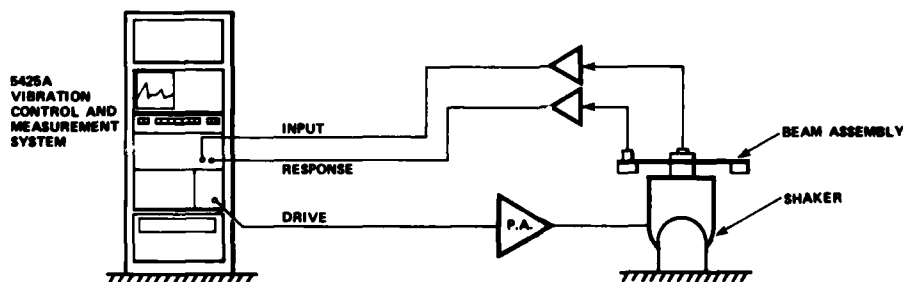
Figure 2

Test Set-up

DUAL CHANNEL MEASUREMENT

48
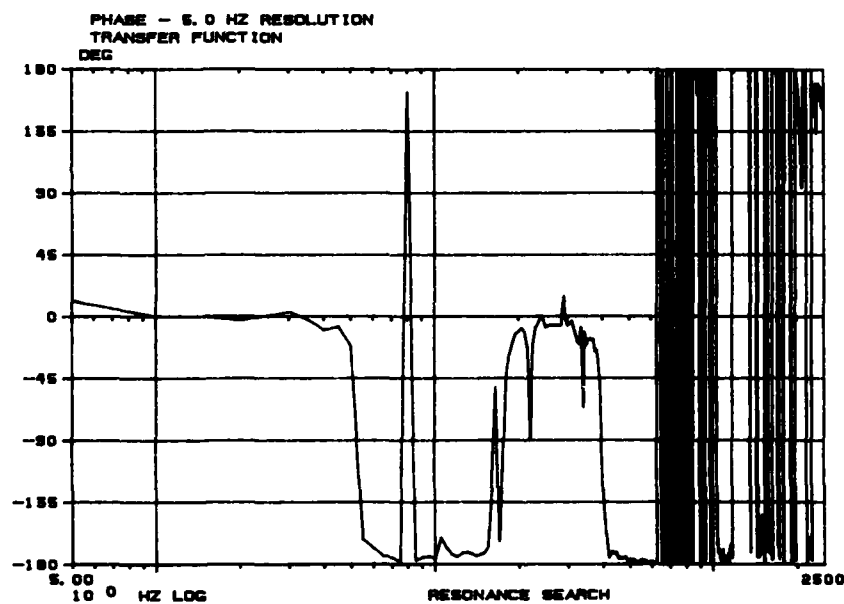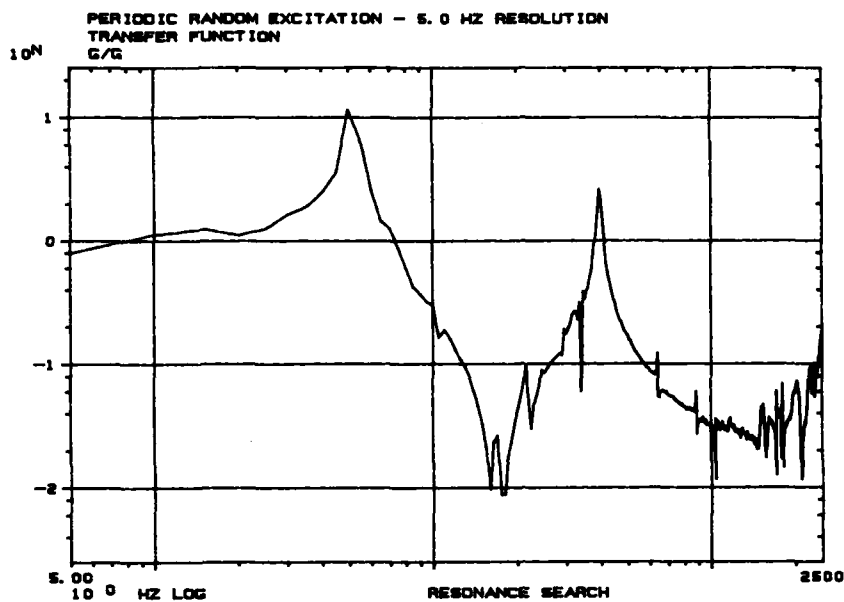
Log Magnitude and Phase vs Log Frequency

Figure 3

49
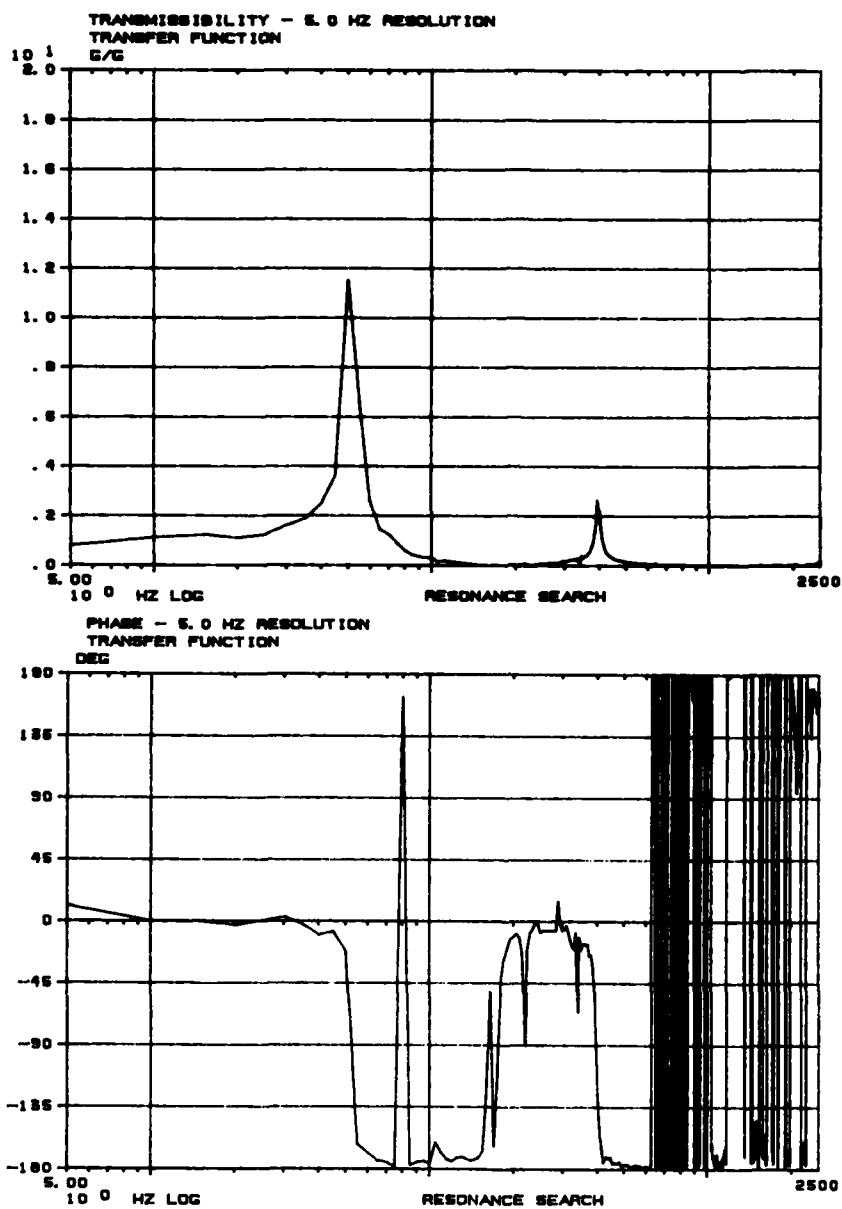
Magnitude and Phase vs Frequency

Figure 4

50

PERIODIC RANDOM EXCITATION — 0.5 HZ RESOLUTION
TRANSFER FUNCTION
G/G

RESONANCE SEARCH

PERIODIC RANDOM EXCITATION — 0.5 HZ RESOLUTION
TRANSFER FUNCTION
G/G

RESONANCE SEARCH
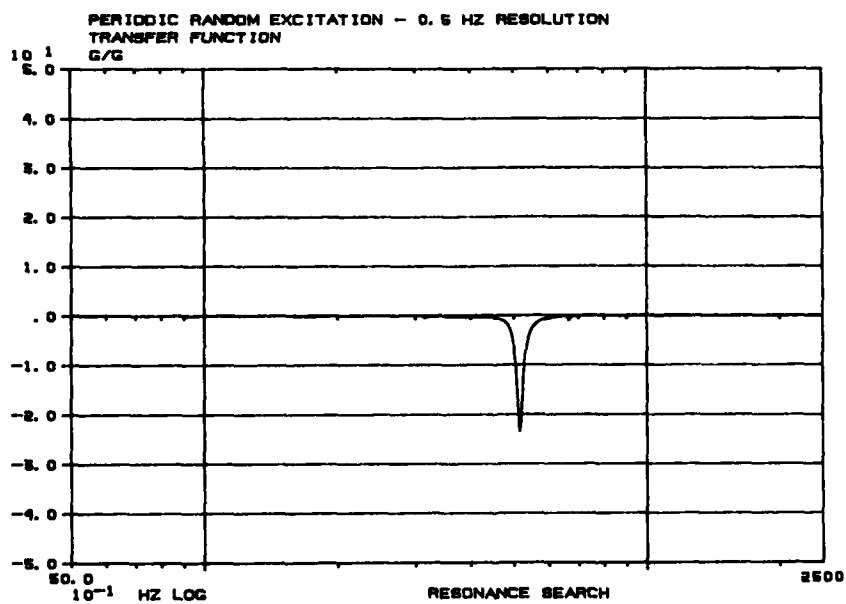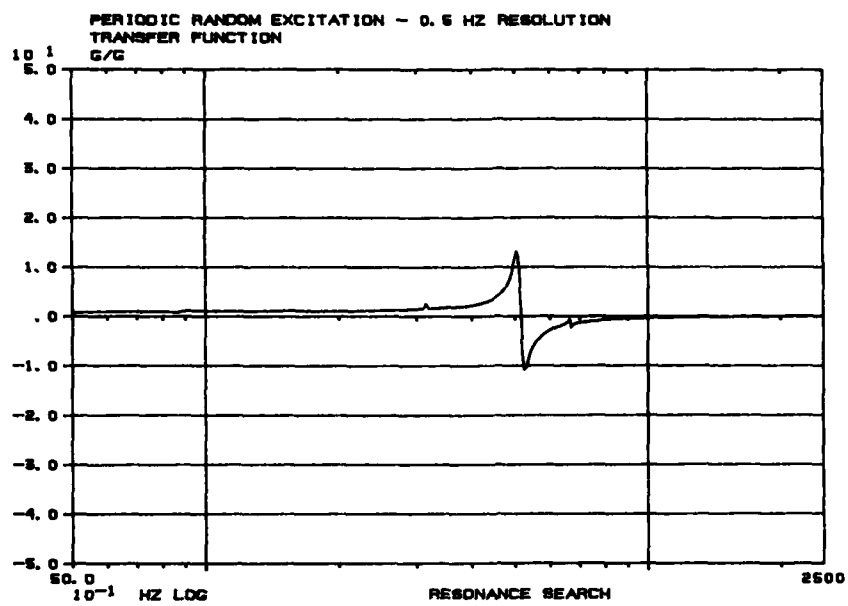
Real and Imaginary vs Log Frequency

Figure 5

51

PERIODIC RANDOM EXCITATION - 0.5 HZ RESOLUTION
TRANSFER FUNCTION
COHERENCE

Coherence vs Log Frequency
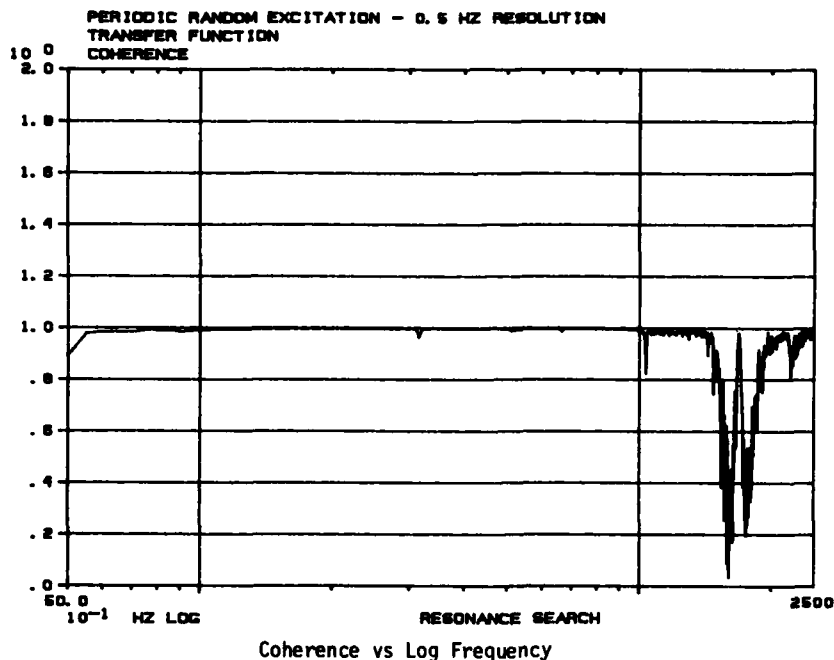
Figure 6

at each of the applied frequencies. Since the FFT allows the signal to be measured at all frequencies simultaneously, we get an estimate of the frequency response in far less time than is required to sweep over the same bandwidth. In addition, we avoid the effects of sweeping the input which tends to cause frequency shifts in the results, unless the sweep speeds are very low, and consequently take a long time.

"Periodic Random" Excitation

If a pseudo random signal is applied repetitively to the system, the steady state response will become stationary, and any non-linearities in the system will be excited in a repeatable way and hence will not be distinguishable from the linear behavior. If, however, the applied waveform is made to vary in some manner, then the output will vary in a different manner, depending upon the type and magnitude of any non-linearities. To account for non-linearities, a "periodic random" signal can be applied to the device under test. Such a signal is derived by taking a signal and applying it to the system, waiting for the transient response to die out, making a measurement, changing the signal and repeating the process. The measured signals are averaged, in the frequency domain, and the resulting measurement becomes a least squares estimate of

the linear portion of the system frequency response. To obtain similar results with a sine sweep measurement, would require averaging the ratio of input to output over repeated measurements at different levels.

Equalized vs Unequalized Input

One assertion often made is that the input must be equalized. The primary reason for this seems to be that, if a flat input, as a function of frequency, can be assumed, then all of the response measurements appear as amplification or transmissibilities and no further arithmetic is required. If, however, the measurements as originally made, are ratios between the input and the response, then no assumptions about the input has to be made and amplification or transmissibilities are explicitely measured. Figure 4 shows the transmissibility measured in this way. Any point above 1 indicates that amplification of input signals takes place.

Another argument against an unleveled or unequalized input is that the measurements will be in error because of non-linearities. Typically, broadband tests are run at lower levels than sine tests so the argument can be made that the excitation is not at the "correct" level. The importance of this depends very

52

much upon the test objective. If for example the test is being performed to locate resonances in preparation for a resonant dwell test at a high level, then finding the resonances with lower level excitation is perfectly proper, and indeed allowed by specifications such as MIL-810C. If the objective of the test is to measure the damping of a mode while excited at a particular level, then it may be appropriate to excite the system at just the desired level. This case appears to be the exception rather than the rule however. In any case, the use of periodic random excitation will give a least squares estimate of the system response at the RMS level used for the particular test. Varying the test level allows insight into the type of non-linearity.

If ADC's having at least 10 bits are used and a 16 bit word size is used for computation, then frequency response functions can be measured over an 80dB dynamic range, even though the input has not been equalized.

Resolution

Most resonance search test specifications call for logarithmic sweeps. This results in approximately equal numbers of cycles of excitation at all frequencies, and allows resonances of equal bandwidth at different frequencies to build to nearly the same percentage of their steady state amplification. This is an important consideration, since the excitation is non-stationary. If steady state responses are to be approximated, then slow sweeps must be used, at least when high Q modes are suspected.

The process of applying a swept sine to a dynamic device can be viewed as a convolution of the impulse response of the device and the time varying swept sine. The calculation of the peak values that occur from this convolution is complicated.

Qualitatively we can see that the apparent amplitude of high Q modes will be lower if we sweep fast, and further that the apparent frequency of the mode will be shifted in the direction of the sweep. The higher the Q and the faster the sweep, the more the shift. The amount of the frequency shift and the peak value measured depends heavily on the spacing and relative phasing of the modes so that a simple analytical expression for the ratio of the true amplitude to the measured amplitude, and for the frequency shift, does not exist. Reference 1 treated the case of linear sweeps through a single degree of freedom system but even here graphical (and nowadays numerical) methods are required for evaluation of the expressions.

Thus there is some uncertainty in interpreting swept sine data due to the non-stationary nature of the excitation. With slow enough sweeps on low enough Q responses

these problems become unimportant, but the determination of how slow is slow enough is not trivial. If we pick very conservative sweep speeds then we take too long to run the tests and we put too much excitation into the system.

A different resolution problem exists in using digital techniques. Since only discrete frequencies are used, the spacing between these frequencies limits the width of resonance that can be measured without using curve fitting techniques. The FFT produces a frequency response function of uniform bandwidth over the entire frequency range. If the bandwidth of the resonance is exactly Δf then a 3 dB error in measuring the peak could occur if the resonant frequency is exactly centered between Δf. If curve fitting is done on the data then the actual peak and resonant frequency can be reconstructed. However, except in the case of modal analysis this is not generally employed. (Refs. 2, 3 & 4).

Figure 7 shows the ratio of measured to actual peak value vs center frequency for various Q's for a single degree of freedom system, assuming the resonance falls between the sampled frequencies*.

To illustrate the effects of this, observe in Figure 8 the results of a 1 OCT/MIN swept sine test on a structure and in Figure 9, a 5 Hz resolution digital frequency response. These have been plotted to the same scale on a log-log basis. Note that two low frequency resonances are not picked up in the digital measurement and that the amplitude of the major resonance is lower than the sine results by about 3 dB. Quite clearly, 5 Hz resolution is not enough in this case. To obtain 1 Hz resolution over a 2 kHz bandwidth would require input records of at least 4000 points and because of aliasing considerations 8000 would be preferable. Since two channels of data are measured simultaneously, this requires up to 16K of data which becomes unwieldly.

The solution to this is to make several measurements, one from 5 Hz to 250 Hz at .5 Hz resolution, and another from 250 Hz to 2000 Hz at 5 Hz resolution. Figures 10 and 11 show the results of this. Note the good agreement between the sine and digital techniques from 10 to 250 Hz and the superior measurement by the digital method above 250 Hz. To resolve the lowest resonance another measurement is required, and this is shown in Figure 12. Here we see that the resonance at 8.5 Hz is still not well resolved although the resonance at 40 Hz is more clearly resolved than with the sine excitation.

*Figure 7 was obtained by evaluating the magnitude of a resonance at $f = f_c - \Delta f/2$ as a function of the resonant frequency f_c for constant Q with the indicated resolution Δf.

53
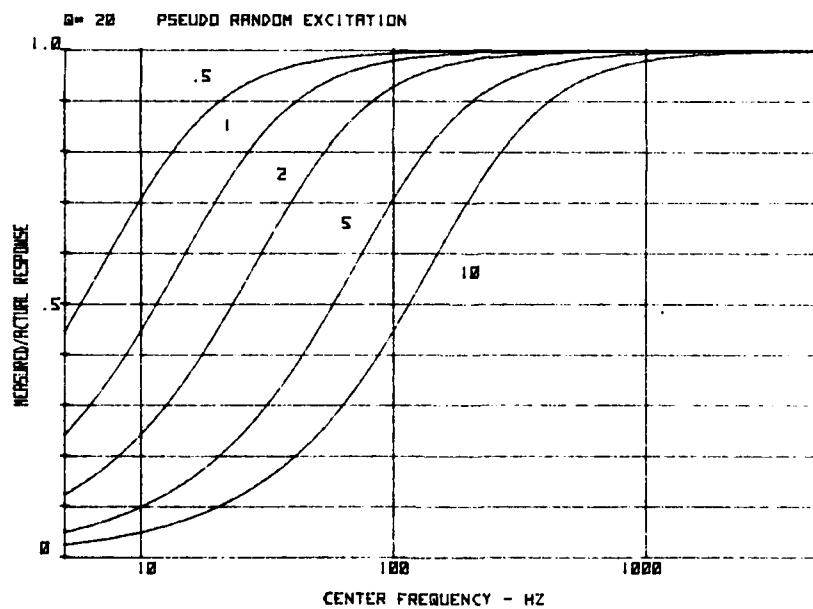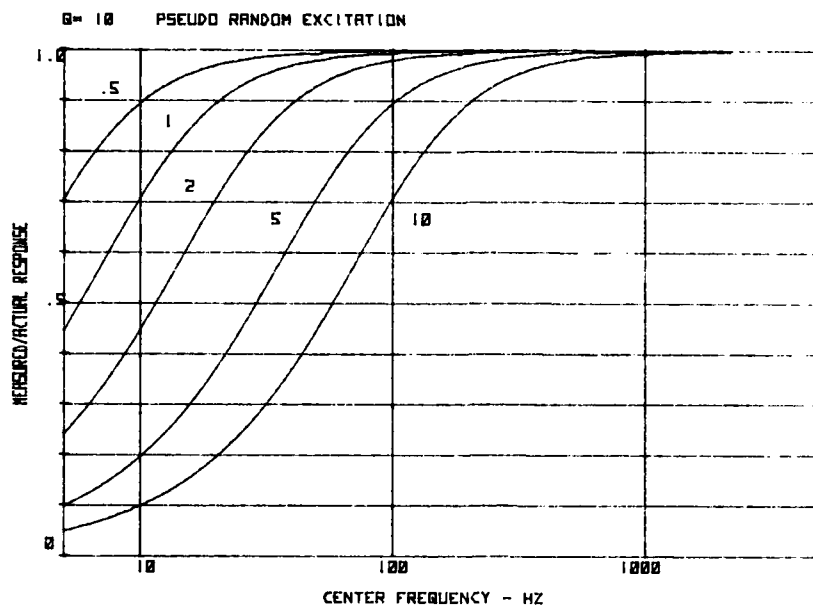
Measured vs True Peak vs Center
Frequency for Various Q's and Resolutions

Figure 7A

54

Figure 7B

55

Sine Sweep Frequency Response 5 to 2000 Hz

Figure 8

Periodic Random Frequency Response 5 to 2000 Hz

Figure 9

PERIODIC RANDOM EXCITATION - 0.5 HZ RESOLUTION
TRANSFER FUNCTION
DB RE G/G

.5 Hz Resolution Frequency Response 2 to 250 Hz

Figure 10

5 HZ RESOLUTION PERIODIC RANDOM EXCITATION
TRANSFER FUNCTION
DB RE G/G

5 Hz Resolution Frequency Response 250 to 2000 Hz

Figure 11

57

.1 HZ RESOLUTION PERIODIC RANDOM EXCITATION
TRANSFER FUNCTION
DB RE C/C
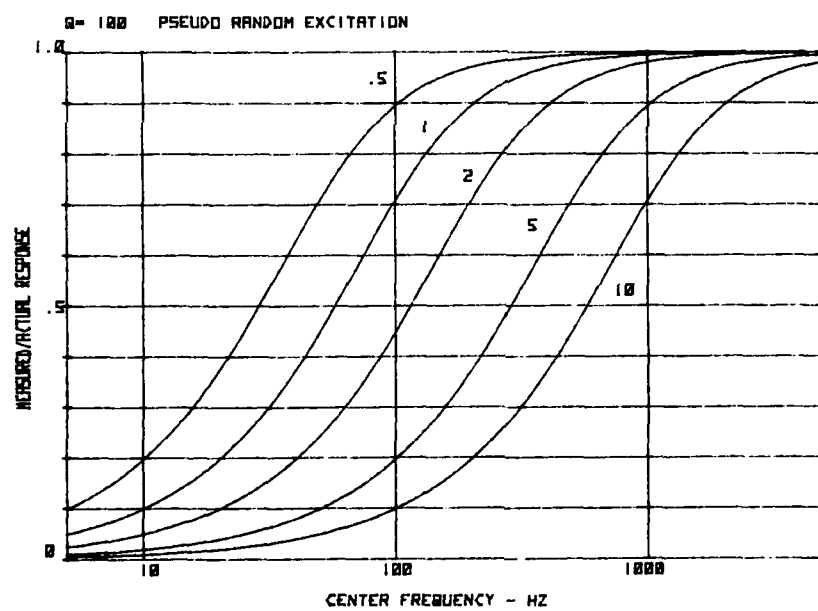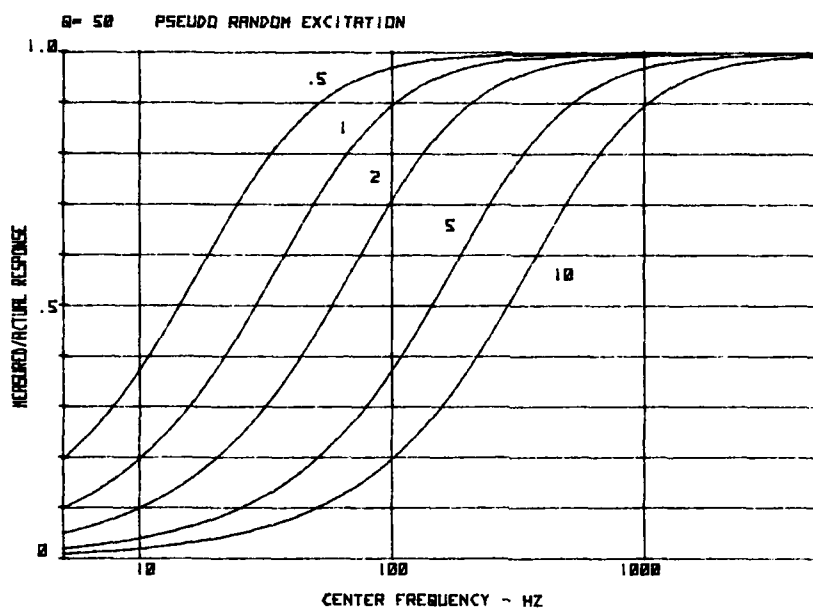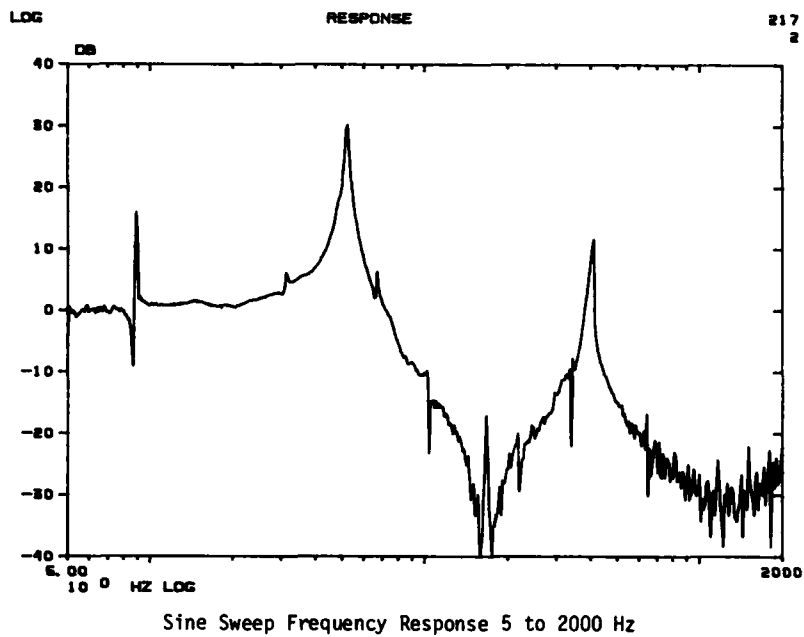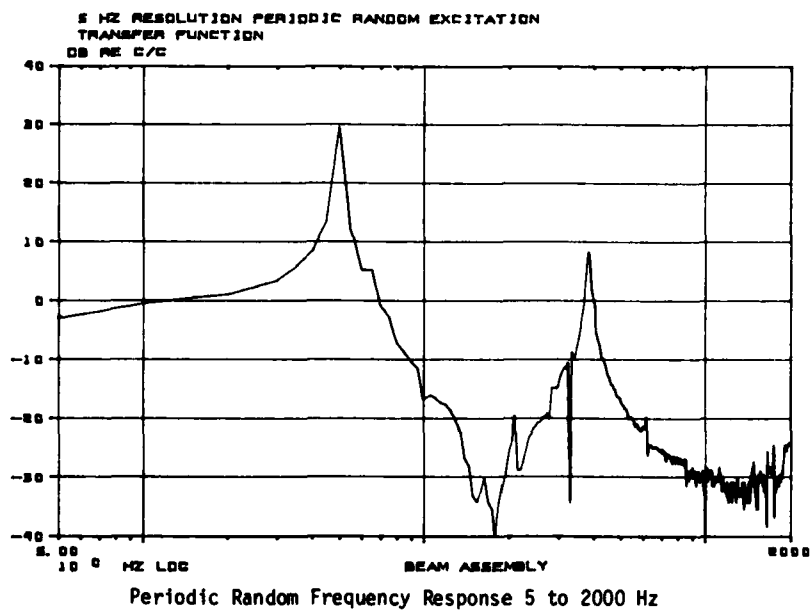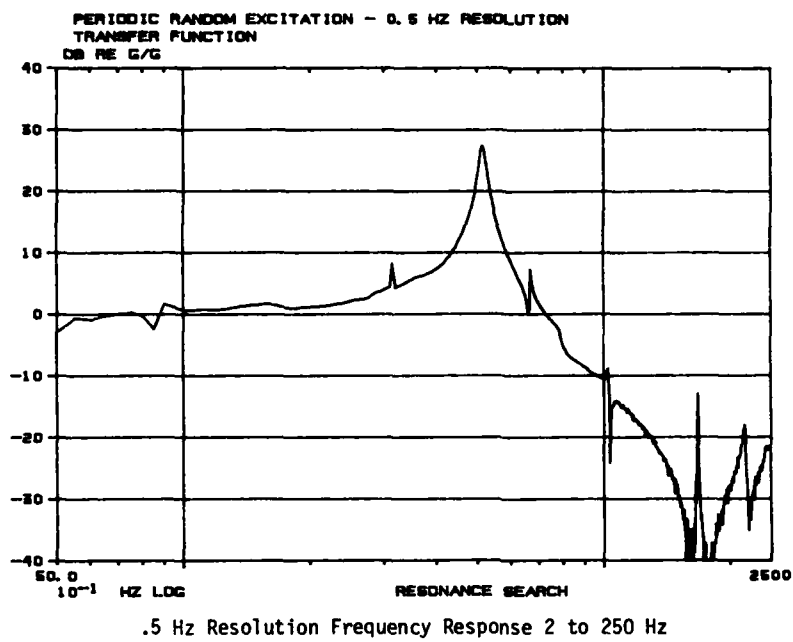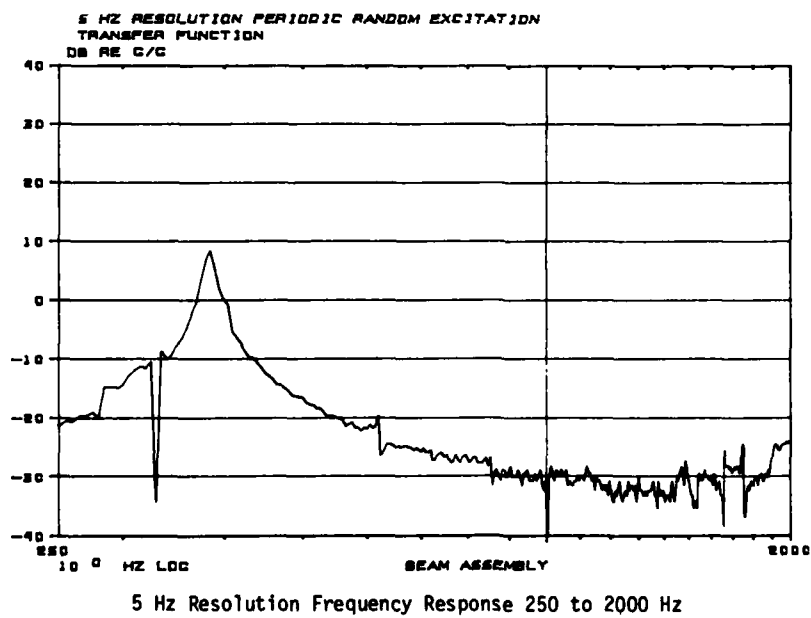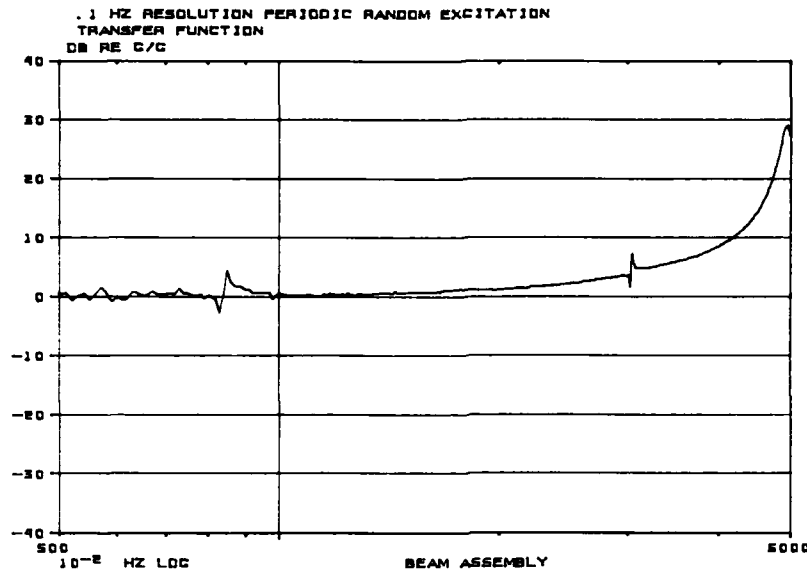
.1 Hz Resolution Frequency Response 5 to 50 Hz

Figure 12

Thus we see that the use of periodic random excitation can yield high quality results, but just as in sine sweeps, some care must be taken to optimize these results. Note that the stationary nature of the excitation does not result in any frequency shift so that the only problem is one of resolution.

Band Selectable Fourier Analysis

Yet another approach to high resolution measurements is band selectable Fourier analysis (Refs. 5&6). This technique allows very high resolution, wide dynamic range measurements over limited bandwidths. For example resolution of up to 1 millihertz at a center frequency of 1 kilohertz, can be achieved. Band selectable Fourier analysis is an all digital technique that involves down converting, filtering and resampling the data stream to produce, say 512 lines of resolution over a very narrow bandwidth centered around the down converter frequency. The use of digital filters allows filters of much higher quality than are realized using analog techniques, with a consequent improvement in dynamic range.

Speed

The time to obtain a record of data is the reciprocal of the desired resolution. Thus

for 1 Hz resolution, each record must be one second long. Added to this is the computation time, and finally the time to get plots in the desired form.

If the measurement is noise free, then the measurement of the transfer function using pseudo-random excitation could be performed with a single measurement. In fact, there is usually some noise so averaging generally improves the results. As few as five averages will often yield satisfactory results.

If periodic random excitation is being used, then more averaging is generally employed to allow several averages of several different excitation waveforms to be used. Typically 10 to 20 averages will yield satisfactory results.

Table 1 lists the time required for several typical transfer function measurements using a Hewlett-Packard 5425A Vibration Control and Measurement System.

The time to obtain only the magnitude of the response, over the same bandwidth with a sine sweep is shown in Table 2 for various sweep speeds.

58

TABLE 1

Broadband Measurements

BANDWIDTH HZ	RESOLUTION HZ	# OF AVGS	EXCITATION TIME MIN:SEC	TOTAL MEAS. TIME MIN:SEC	TOTAL TIME WITH PLOT	
					HP-7210	TEK
5-2500	5	10	0:23	0:40	4:15	1:05
5-500	1	10	0:40	0:48	4:23	1:13
5-250	.5	10	1:15	1:30	5:05	1:55
5-100	.1	10	6:37	6:50	10:25	7:15

TABLE 2

OCT/MIN	TIME/ MIN
1	8.64
2	4.32
4	2.16

If the sine data is reduced as an off line process then the time to obtain final results is more than twice that indicated, that is the time for the actual sweep and then the time to set-up and analyze the data. Thus, even for dual resolution digital measurements there is a considerable saving in excitation time as well as measurement time.

Applications

Among the many applications for these kinds of measurements are:

1. Fixture Analysis

2. Resonance Search

3. Transmissibility

4. System Integrity Checking

Periodic random excitation and transfer function measurements can be used to rapidly survey fixtures to see how uniform the excitation is at various mounting points. The effect of adding damping material can be rapidly evaluated with just a few seconds of excitation. The change in the fixture response when it is loaded can also be easily observed, even with low input levels.

The application to resonance search has already been illustrated in Figures 9 through 12. Similarily transmissibility measurements have been shown in Figure 4.

The last application involves making a measurement on the device before it is stressed in some manner and then repeating the measurement after the stress is applied to see that no changes have occurred that would indicate structural failure. This procedure has been successfully used during spacecraft development to look for changes that occurred during high level sine qualification testing.

CONCLUSIONS

Although classical sine sweeps offer high resolution measurements if the sweep is slow enough, the time required is relatively long. Digital transfer function measurements using broadband random excitation can offer a wide variety of data formats, including magnitude and log magnitude vs phase, real vs imaginary, input and output power and coherence, with less excitation time and good resolution.

The capability to plot the data in a variety of formats, over selectable frequency ranges with complete anotation offers many advantages over the magnitude data alone that usually results from sine sweep tests.

59

REFERENCES

(1) Lewis, Frank M., "Vibration During Acceleration Through a Critical Speed", Transactions of the ASME, (Dec. 15, 1932), Vol. 54, No. 23, pp 253-261.

(2) Richardson, M. and Potter, R., "Identification of the Modal Properties of an Elastic Structure from Measured Transfer Function Data", 20th Intl. Instrum. Symp., Albuquerque, N. Mex. (May 21-23, 1974).

(3) Potter, R. and Richardson, M., "Mass, Stiffness, and Damping Matrixes from Measured Modal Parameters", ISA Intl. Instrum.-Automat. Conf., New York, N.Y., (Oct. 28-31, 1974).

(4) Potter, R., "A General Theory of Modal Analysis for Linear Systems", The Shock and Vibration Digest, (Nov. 1974), Vol. 7, No. 11.

(5) McKinney, H. Webber, "Band Selectable Fourier Analysis", Hewlett-Packard Journal, (April 1974), Vol. 26, No. 8.

(6) Moseley, Peter, "Digital Analysis & Control in the Vibration Laboratory", Seminar on Understanding Digital Control and Analysis in Vibration Test Systems, a Publication of the Shock & Vibration Information Center, Naval Research Laboratory, Washington, D.C., (May 1975), pp 79-90.

DISCUSSION

Mr. Curtis (Hughes Aircraft Company):
Almost all of the items that we deal with have nonlinearities. All I can hope to do is to get a transfer function that somehow takes some kind of an average accounting of those nonlinearities. It seems to me the best way to do that is to measure them under conditions as close as possible to those under which they will be or have some impact on whatever I am doing. It seems to me that it is important to measure them under the kind of signals, be they random or sine, that my structure has to withstand and to also do it at more or less the same level that my structure has to withstand; then I will have a proper accounting of the right amount of damping which is the greatest virtue for measuring transfer functions under some sort of complex or random shaped spectrum.

Dr. Morrow (Consultant): When I hear a talk about the measurement of transfer functions there is a very strong implication that we are trying to make measurements so that in a sophisticated way we can predict responses, after the fact, after the thing is designed. It would be more fruitful if we could place more emphasis in the course of the design on the particular resonances in the hardware that one wants to change and not so much on the magnitude of the transfer function. For this sort of approach you would work more with frequency and damping than with transfer functions as such, although the two ideas are very closely related. Furthermore, if you want to look at frequency and damping, you don't necessarily have to have the utmost accuracy or precision in your measurements. You want to know whether you have a potentially unfavorable relationship in your hardware and you don't necessarily need to know that to a tenth of a percent. You need to know that you are potentially in a situation that you would like to avoid. I would like to see a little bit more emphasis in this direction in the future.

Mr. Henderson (Air Force Materials Lab.):
Sometimes, our experiences have shown, that it is advantageous not to simulate the environment but rather to test a low level. If you have a resonant fatigue problem, probably because of the lack of prior knowledge, and you want to change the modal characteristics of the system, such as by added damping, we have found it much more advantageous to work within the linear range. Thus you can separate nonlinearities from an increase in damping, and in fact optimize a system within the linear range and finally check it out under the levels of excitation that you would expect to see in service. If you try to optimize a damping fix in a nonlinear range, then you can get yourself very confused between increases in damping and nonlinear effects. There are cases where you should look at a system well within the linear range and understand the linear behavior of the structure before you try to simulate the actual service conditions which are typically nonlinear.

MODAL INVESTIGATION OF LIGHTWEIGHT AIRCRAFT
STRUCTURES USING DIGITAL TECHNIQUES

R. W. GORDON
and
H. F. WOLFE

Air Force Flight Dynamics Laboratory
Wright-Patterson Air Force Base, Ohio

Digital impact response test techniques were used to measure the dynamic properties of lightweight aircraft structures to include natural frequencies, mode shapes and modal damping. Two different types of structures were tested; honeycomb and skin-stiffened panels. The digital impact response method used consisted of applying a transient force pulse to the structure, measuring the structure's response at various points, digitizing, calculating the transfer functions using fast Fourier transforms, and determining the dynamic properties from these data. A second method was used on these same structures for direct comparison purposes. This method was an analog technique using sine sweep tests and accelerometer mapping. The comparison indicated close agreement in the results. The use of the digital technique has resulted in a considerable savings in the manhours required to obtain the dynamic properties of the structures.

INTRODUCTION

The sonic fatigue life of lightweight aircraft structures (skin and stiffeners) affects the reliability and life cycle cost of these structures. The Air Force Flight Dynamics Laboratory conducts sonic fatigue tests on laboratory structural specimens and actual aircraft structures to determine their life and to establish prediction techniques. The dynamic properties of the structure such as the natural frequencies, mode shapes and modal damping are needed. Mode shapes are useful in determining high stress locations for strain gage placement to determine the stresses producing the greatest damage in the structure.

The methods previously used to determine the dynamic properties of test structures were analog sine sweeps, sand patterns and accelerometer mapping. These methods are relatively slow and cumbersome to use, especially for complex structures where many resonant frequencies are present. The digital impact testing techniques introduced in recent years offered greatly reduced test time and effort and a broader flexibility available with handling digital data [1,2]. Digital impact testing reported in the literature has been limited mainly to relatively stiff, massive structures such as machine tools and automobile frames [3,4]. Few studies of the digital techniques used on lightweight aircraft skin type structure have been reported [5].

This paper describes the use of a digital impact test technique on two types of lightweight aircraft structures used later in sonic fatigue tests. The first structure was an F-4 boron-epoxy honeycomb rudder and the second was a series of skin stiffened panels typical of aircraft fuselage structure. The specific problems encountered using this technique on lightweight structures are discussed. A second test was conducted on the rudder and one skin stiffened test panel using the analog technique. The results obtained from both tests are compared directly.

DESCRIPTION OF DIGITAL TECHNIQUE

The basic digital modal analysis technique can be applied using a number of types of structural excitation. These include hammer impact, point excitation by a shaker, and acoustic excitation. Various spectra such as wide band and narrow band random can be used or fast sine-sweep techniques [2]. The digital technique of this program used a hammer impact for excitation, but the technique is basically the same for all the above excitation methods.

The digital impact test technique consists of the application of a force pulse at a point on the test structure and the measurement of the response at another point. The input force and response acceleration are digitally processed to form the frequency response function or transfer function relating the points.

61

The transfer function is a complex valued function which gives the response of the structure at the measurement point due to a unit force input at the impact point for all frequencies. A group of transfer functions measured by impacting the structure at selected points and measuring the response at a single point contains all necessary information about the dynamic response of the structure including natural frequencies, mode shapes and modal damping. The reciprocity property of the transfer function permits interchanging the impact and response points. An identical group of transfer functions are measured if the structure is impacted at a common point and the response is measured at the selected points.

When a force impact is applied to the structure, the force time signal, $x(t)$, and the response acceleration time signal, $y(t)$, are inputs to a Fourier Analyzer System. The signals are simutaneously digitized and stored. The transfer function is then computed using the digital Fourier transform algorithm. The transfer function, $H(f)$, may be expressed

$$H(f) = \frac{Y(f)}{X(f)} \qquad (1)$$

where $X(f)$ and $Y(f)$ are the Fourier transforms of $x(t)$ and $y(t)$ respectively. This expression of the transfer function is adequate for systems where no extraneous noise is present, but when one or more noise signals are superimposed on $x(t)$ or $y(t)$ they add error to the transfer function even if averaging is used [6]. Another expression of the transfer function is commonly used involving power spectral density functions which eliminates added noise when used with averaging. The auto power spectrum of the input, $x(t)$ is defined as:

$$G_{xx} = X(f) \; X*(f) \qquad (2)$$

where * denotes the complex conjugate. The cross power spectrum between the response output and the impact input is defined as:

$$G_{yx} = Y(f) \; X*(f) \qquad (3)$$

Multiplying the numerator and denominator of (1) by $X*(f)$:

$$H(f) = \frac{Y(f)}{X(f)} \frac{X*(f)}{X*(f)} = \frac{G_{yx}(f)}{G_{xx}(f)} \qquad (4)$$

When average values of $G_{xx}(f)$ and $G_{xy}(f)$ are used in (4) the error is greatly reduced [1,6]. The Fourier Analyzer uses (2), (3), and (4) to compute the transfer function and also computes the coherence function, $\gamma^2(f)$, which is defined as:

$$\gamma^2(f) = \frac{\overline{[G_{yx}]}^2}{\overline{G_{xx}} \; \overline{G_{yy}}}, \; 0 \le \gamma^2 \le 1, \qquad (5)$$

where $\overline{}$ denotes averaging. The coherence function is a measure of the causal relationship between the force input and the response output. A value of γ^2 near 1 means that the measured response is due solely to the measured force input. Values of γ^2 much less than 1 indicate system nonlinearities or response due to extraneous force inputs [1,6,7]. The coherence function gives a good indication of the quality of a measured transfer function as it is taken. "Bad" data can be recognized and discarded.

The required dynamic information can be obtained after the structure's transfer functions have been computed. A natural frequency is noted as a peak in the imaginary part of the transfer function with a corresponding zero value for the real part. The modal displacement for any point on a structure at a specific natural frequency is the value of the imaginary part of the transfer function for the point. The mode shape is formed by mapping the modal displacements of transfer functions measured at grid locations on a structure. The damping of a particular mode can be determined from a Nyquist plot of the transfer function in the frequency range close to the natural frequency. The plot approximates a circle. The damping factor C/C_c is calculated from a least square circle fit to data by:

$$C/C_c = 2R/[f_n(\Delta f/\Delta S_{max})] \qquad (6)$$

where R is the circle radius, f_n is the natural frequency, Δf is the discrete frequency interval of the transfer function and ΔS_{max} is the maximum arc length between frequency points on the circle [8].

A transfer function can be digitally smoothed or "windowed". Windowing is the multiplication of the acceleration response signal by an exponential decay function. This forces the response to die out more quickly which offers two advantages. Damping is added to transfer function peaks which smooths and broadens them (with little effect on amplitudes) and the response time signal goes to zero more quickly in the sample time which reduces leakage error [6]. Windowing must be used with care since the added damping effect may smear together closely spaced modes. Modal damping data should not be determined from windowed transfer functions due to the added damping effect of windowing.

TESTS PERFORMED
    F-4 Rudder
    The dynamic properties of an F-4 boron-epoxy rudder were determined using the digital and analog techniques, and the results from these two methods were compared. The boron-epoxy rudder was previously installed on an operational F-4 aircraft for an in-service evaluation of composite technology. The rudder consisted of laminated boron-epoxy skins over a full depth aluminum
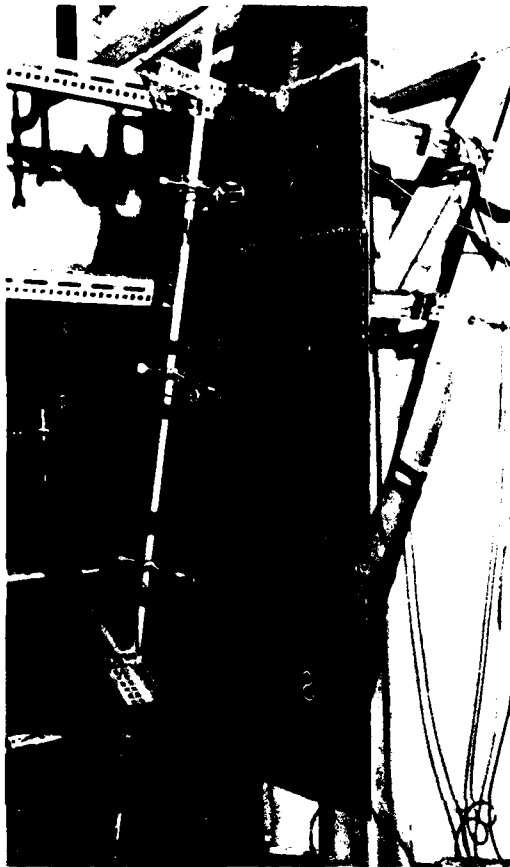
Fig. 1 - F-4 rudder in sonic fatigue
test chamber

honeycomb core, a fiberglass spar and a
titanium drive rib. The construction consisted
of a 4 ply ±45° laminate, one 0° ply added
along the spar and two 25° plies added
along the drive rib. The rudder was mounted
from its hinge points and torque tube on
a frame assembly shown in Figure 1 to simulate
the boundary conditions of the aircraft
mounting. Details of the sonic fatigue
tests of the rudder can be found in [9].

The analog method used in the F-4
rudder test consisted of determining the
most responsive resonant frequencies, determin-
ing the mode shape of those considered
most likely to produce a fatigue failure
later during the sonic fatigue test, and
finding the modal damping of the structure.
Excitation was produced by a large loudspeaker
set-up next to the rudder and the rudder
response was measured by an accelerometer.
The frequency of a discrete input to the
loudspeaker was varied until peaks in the
accelerometer response were obtained.
From these, the following frequencies were
selected for further study: 64, 122, 229,
269, 340, 460, and 560 Hz. While dwelling
at the frequency of interest, the acceleration
was measured at 36 locations on one surface
of the rudder and the relative phase angle
was measured using a second accelerometer
which remained at a reference location.
From these measurements, the relative displace-
ments were calculated, normalized, and
plotted by hand, mapping the displacements.
Typical examples of the mode shapes obtained
for 122, 229, 340 and 460 Hz are shown
in Figures 2, 3, 4, and 5. The most responsive
modes were considered to be the 229 Hz
followed by 122, 340, and 460 Hz. The
damping factor (C/C_c) was determined using

Fig. 2 - F-4 rudder mode shape from accelerometer mapping; 122Hz

63

Fig. 3 - F-4 rudder mode shape from
accelerometer mapping, 229Hz

Fig. 4 - F-4 rudder mode shape from
accelerometer mapping, 340Hz

Fig. 5 - F-4 rudder mode shape from
accelerometer mapping, 460Hz

64

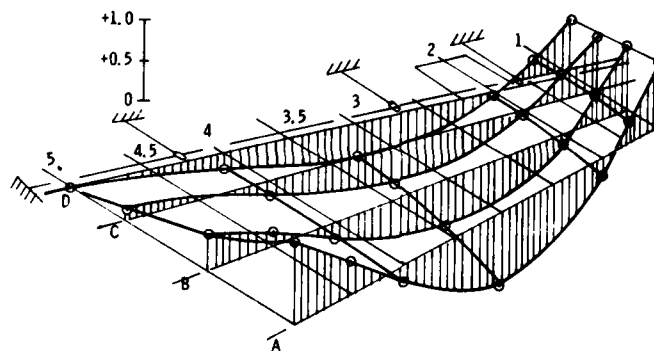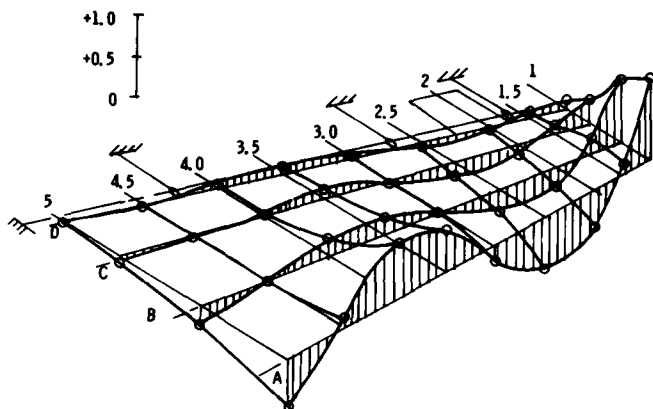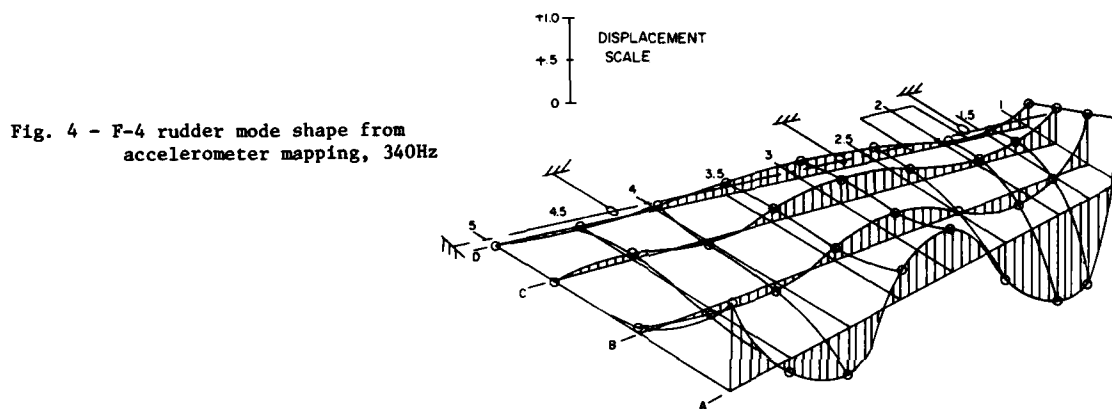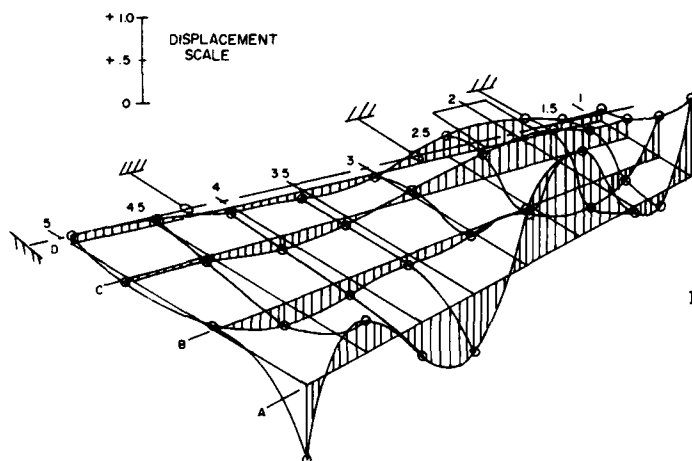the bandwidth method. The response was measured with a strain gage which was installed for use later during the fatigue test. The excitation was a discrete frequency sweep from 50-600 Hz at a constant relatively low sound pressure level provided by a Wyle WAS3000 air modulator. Resonant peaks too close in frequency which did not meet the necessary criteria were not considered suitable for evaluation and omitted from damping calculation. The damping factors determined were in the range of 0.0045 to 0.0140.

The digital modal analysis method used the same grid on the rudder's surface. The rudder was impacted once at each grid point using a small hammer containing a force gage. The response was measured at a common point on the rudder with an accelerometer. The frequency content of the impact using a low mass hammer depends mainly on the hammer tip stiffness and the local structural stiffness at the impact point. The hammer used for this test was light with a hard tip, so the rudder's local stiffness was the limiting factor for the upper frequency cutoff of the input energy spectrum. The stiff, honeycomb rudder surface allowed impacts with adequate spectral content up to 500 Hz.

Transfer functions were computed and stored for each grid point using the Hewlett Packard Fourier Analyzer System shown in Figures 6 and 7. The transfer functions were displayed and resonant frequencies selected. The resonant modes of the rudder were well spaced and lightly damped. Transfer functions were computed for a few grid points with response measured at a different location. This helped identify any resonant modes which may have had a node line near the original response point and therefore may have appeared low in amplitude. Mode shapes were generated by the Fourier Analyzer System and an animated display of each mode shape was produced. The relative displacement data were printed out and used to generate contour maps of the mode shape using a commercially available computer program (General Purpose Contouring Program, California Computer Products, Inc.) and a large computer (CDC 6600). Typical examples of the mode shapes obtained are shown for 121, 224, 320, and 448 Hz in Figures 8, 9, 10 and 11. The damping factors were determined from the structure's transfer functions using a Nyquist curve fitting routine. The range of values was 0.0022-0.0130 with an average value of 0.0072 as shown in Table I. The average values of the two techniques compared closely.
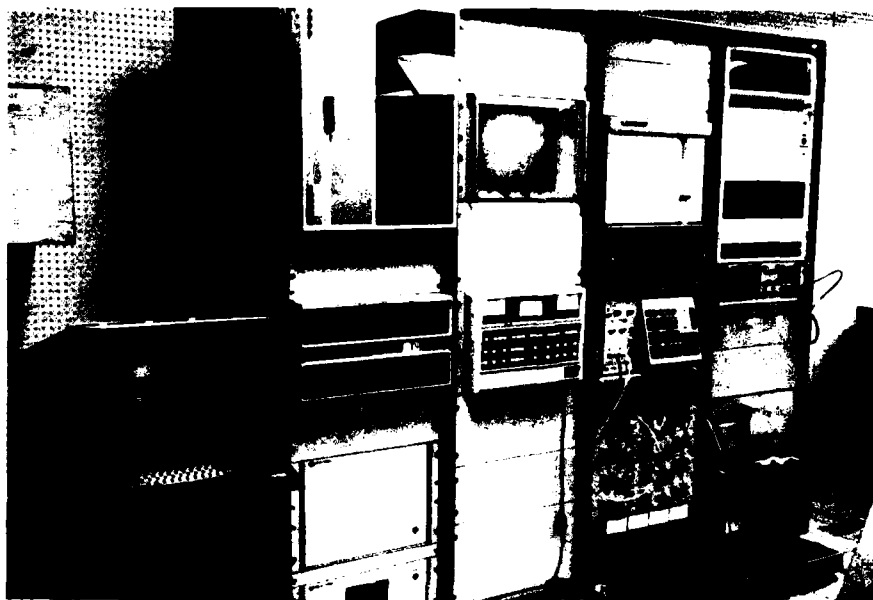
Fig. 6 — Hewlett-Packard Fourier Analyzer System
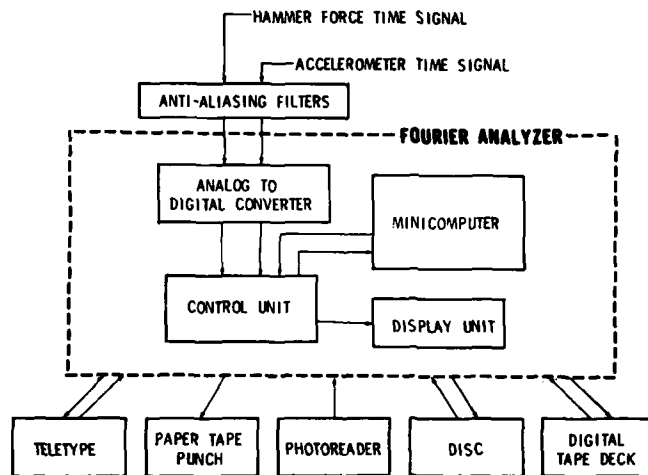
Fig. 7 – Block diagram of Fourier Analyzer System
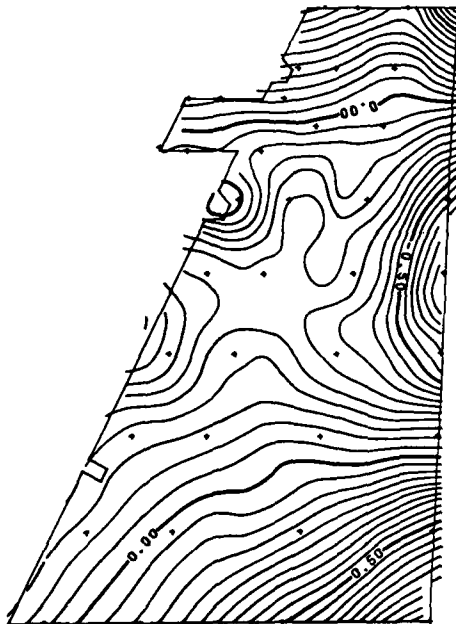
Fig. 8 – F-4 rudder mode shape from digital method, 121Hz
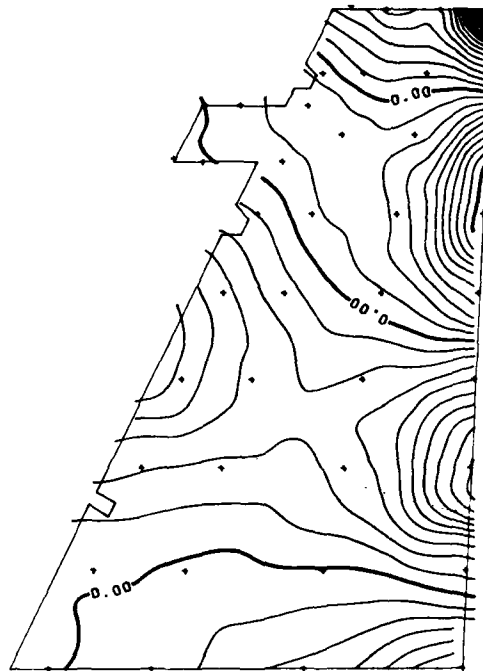
Fig. 9 – F-4 rudder mode shape from digital method, 244Hz

Fig. 10 - F-4 rudder mode shape from
digital method, 320Hz
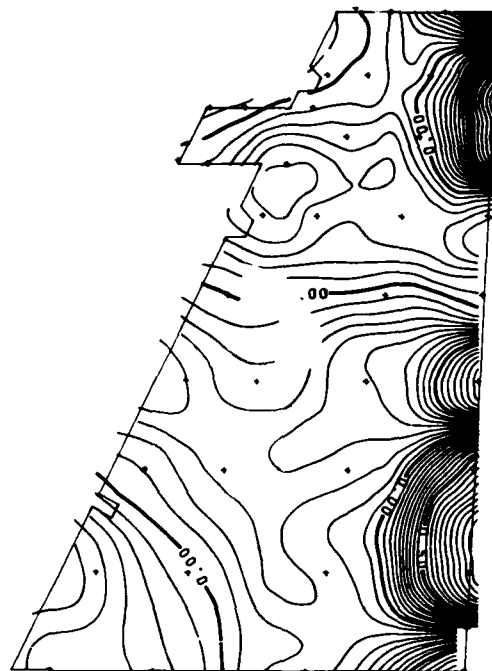
Fig. 11 - F-4 rudder mode shape from
digital method, 448Hz

TABLE I

F-4 RUDDER DAMPING COMPARISON

ANALOG TECHNIQUE (BANDWIDTH METHOD)		DIGITAL TECHNIQUE (NYQUIST CURVE FIT)	
Modal Frequency (Hz)	Damping Factor (C/Cc)	Modal Frequency (Hz)	Damping Factor (C/Cc)
220.5	.0079	58.5	.0112
223.5*	.0100	121.5	.0061
224.5*	.0134	162.5	.0124
225 *	.0140	223.5	.0070
226.5*	.0077	303.5	.0054
440	.0045	319.5	.0059
441	.0052	395.5	.0022
521	.0053	448.5	.0022
	.0085 AVG		.0072 AVG
	.0045-.0140 RANGE		.0022-.0130 RANGE

*The same mode measured by different strain gages

67

A direct comparison of the mode shapes obtained using both digital and analogue techniques was made by plotting the data simultaneously in an isometric view as shown in Figures 12 and 13. Close agreement between the techniques was obtained. Some variations in frequency and amplitudes are expected. Small variations have been noted in previous cases when the same techniques were repeated on the structures a second time.
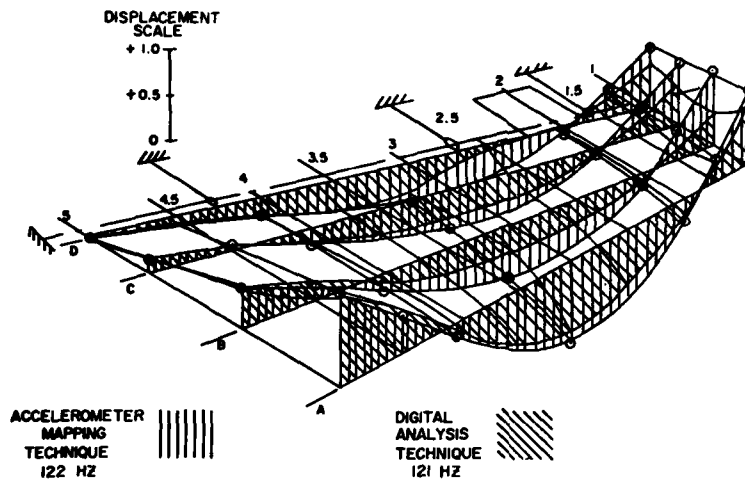
Fig. 12 - Comparison of digital and analog techniques
121 and 122Hz
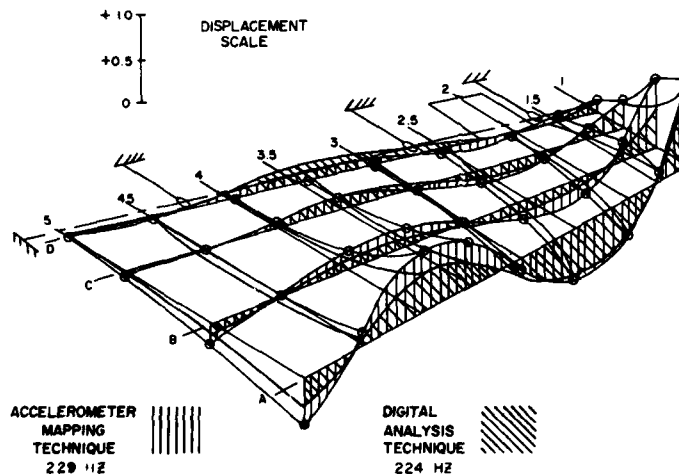
Fig. 13 - Comparison of digital and analog techniques
224 and 229 Hz

Weldbond Panel Test

The digital impact method was used
to perform the modal analysis of a group
of weldbonded and riveted skin-stringer
test panels. The test panels were modeled
from sections of the C-140 aircraft fuselage
except thinner gage skins were used. Eight
of the panels were flat and eight were
curved with a 42.5" radius as indicated
in Table II. The panels were bolted in
test frames used later in sonic fatigue
tests.

The first two panels were tested using
accelerometer mapping (analog sine-sweep)
and sand pattern techniques similar to
those described for the F-4 rudder. Grids
of 48 and 50 measurement points were selected
for 12 of the remaining 3 bay and 4 bay
panels respectively since the modal analysis
program used could handle a maximum of 50
transfer functions. An updated program with
a 66 point grid was used on the last two
panels. A typical curved panel is shown being
tested in Figure 14.

The panel tests were performed with
the same Fourier Analyzer System and hammer
and the test procedure was similar to that
described for the F-4 rudder, except the
hammer impacts were applied at a common
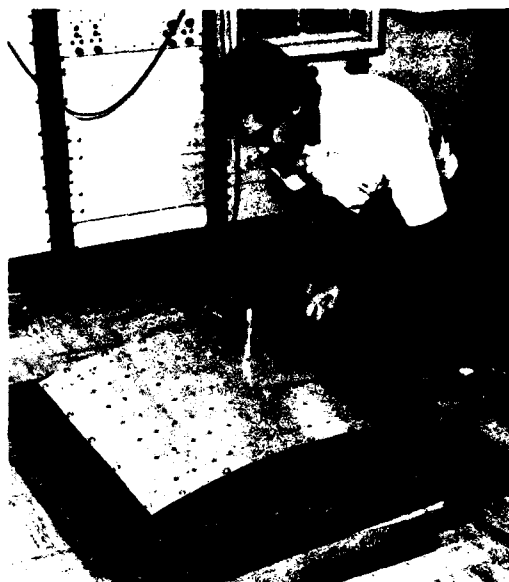
Fig. 14 - Weldbond panel test setup

TABLE II

WELDBOND TEST PROGRAM

PANEL NO.	TYPE JOINT*	SKIN THICKNESS	NUMBER OF BAYS	MID BAY	RADIUS OF CURVATURE
		inches		inches	inches
1	R	0.032	3	7 X 21	∞
2	WB	"	3	"	"
3	R	0.040	3	"	"
4	WB	"	3	"	"
5	R	0.032	4	5.25 X 20.75	"
6	WB	"	4	"	"
7	R	0.040	4	"	"
8	WB	"	4	"	"
9	R	0.032	3	7 X 21	42.5
10	WB	"	3	"	"
11	R	0.040	3	"	"
12	WB	"	3	"	"
13	R	0.032	4	5.25 X 20.75	"
14	WB	"	4	"	"
15	R	0.040	4	"	"
16	WB	"	4	"	"

* R = Riveted
WB = Weldbonded

point and the response was measured at each grid point. This method was selected since the local stiffness at grid points on the unsupported panel skin was relatively low which limited spectral energy of hammer impacts to a maximum of 100 Hz or less for many points. Impacts on skin directly adjacent to stringers provided good force spectra to at least 500 Hz for most panels. Therefore, the impacts were applied on the skin above a stringer. Prior estimates of the frequencies for the modes of interest indicated that 0-500 Hz range was sufficient. Typical force spectra for various impact locations are shown in Figures 15, 16, and 17. The specific impact location was determined by a trial and error method for each panel. Care was taken to place the impact point away from any node lines of expected modes.

The transfer functions were computed from the average of five hammer impacts. The coherence function for each point was checked to ensure good data. The coherence

Fig. 17 - Force spectrum of hammer impact on center of panel bay

functions for most of the measured transfer functions were near unity. Any questionable data caused by bad hammer impacts or other problems was retaken. A typical transfer function and its coherence function are shown in Figures 18 and 19. An exponential window of the form e^{-at} was used to smooth the transfer function [10]. The damping of the window added approximately .007 to the damping factor, C/C_c, for all modes. A few unwindowed transfer functions were then used to select natural frequencies and calculate modal damping. The windowed transfer functions were used to generate mode shapes.

Fig. 15 - Force spectrum of hammer impact at panel edge
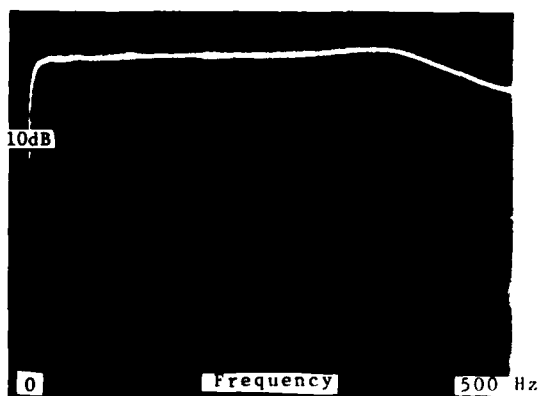
Fig. 16 - Force spectrum of hammer impact on panel near stiffener
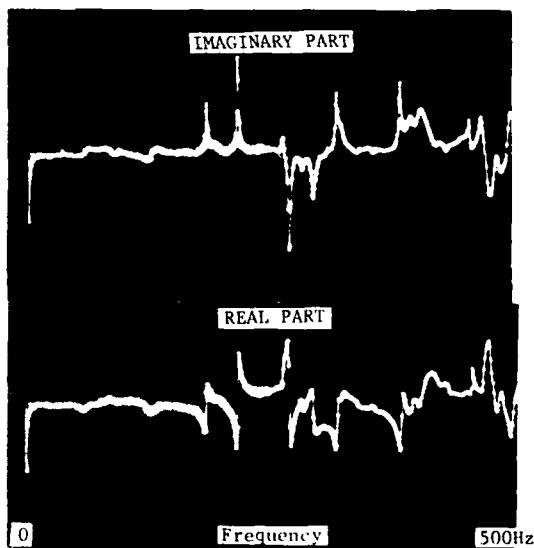
Fig. 18 - Weldbond panel transfer function

70

Fig. 19 – Weldbond panel coherence function

Fig. 21 – Nyquist plot of resonant peak in a transfer function

Damping of each mode was calculated by a Nyquist-plot, least squares curve fitting routine [8]. Figure 20 shows a single transfer function resonant peak and Figure 21 shows a Nyquist plot of the peak. Values of the damping factor, C/C_c, for the 16 panels ranged from .024 for low frequency whole panel modes to .003 for high frequency modes with 5 and 6 node lines per bay.
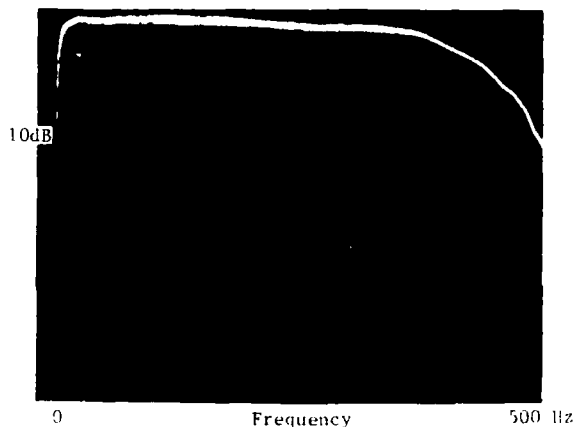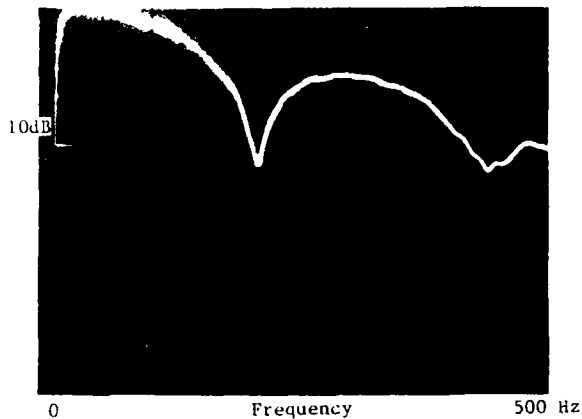
Natural frequencies were selected from the unwindowed transfer functions and mode shapes were generated for each chosen natural frequency. An animated display of each mode was observed and contour plots of each were made. Two sequences of typical animated mode shapes are shown in Figures 22 and 23. Resonant frequencies were observed from 80 Hz to the 500 Hz upper limit. Mode shapes consisting of whole panel response, multiple bay modes, and individual bay response were observed. Contour plots of a few typical mode shapes are shown in Figures 24, 25, 26, and 27.

Bonded Panels

The dynamic properties of a bonded panel were determined using both digital and analog techniques and the results from these methods were compared.

The test structure was essentially the same as the first two test panels of the weldbond program, 3 bay flat 0.032 skins, except the skin-to-substructural joints were adhesively bonded without rivets or spot welds. The panel was mounted in the test fixture used later during the sonic fatigue tests.

The analog method used for the bonded cargo fuselage panel was similar to that described above for the boron-epoxy rudder with a few exceptions. The resonant frequencies were determined from Chladni patterns or sand patterns. These were obtained by sprinkling colored sand particles on the surface of the test panel excited underneath by a loudspeaker. The frequency of a discrete input of the loudspeaker was varied until the sand particles became aligned with the node lines and a well defined pattern was observed. From these, two frequencies were selected for further study: 126 and 307 Hz. The acceleration mapping technique was used to obtain the mode shapes shown in Figures 28 and 29. The same contour plotting program described in the digital method was used to generate the plots.

Fig. 20 – Resonant peak in a transfer function

The damping factor was not determined using analog methods.

The digital impact method used on the bonded panel used the same grid points. The same procedures described above were used to obtain the data. Contour plots of the mode shapes obtained are shown in Figures 30 and 31. A direct comparison of the mode shapes obtained using both digital and analogue techniques was made. Close agreement was obtained as shown in Figures 32 and 33.
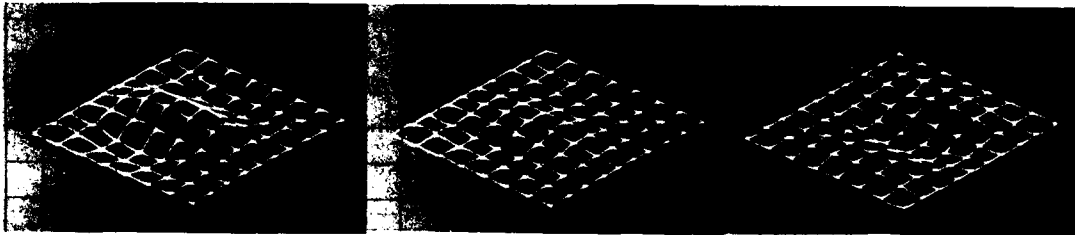
Fig. 22 - Animated mode shape sequence, 123Hz
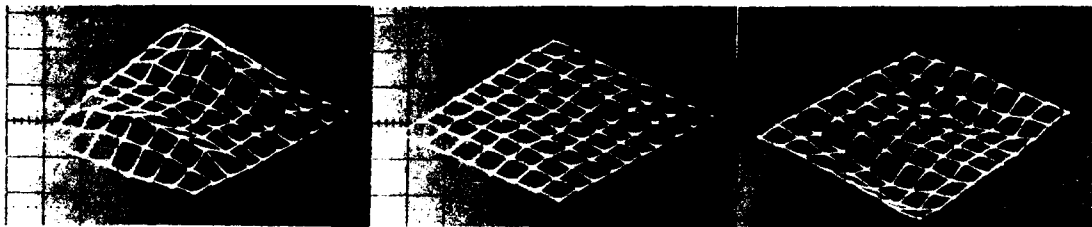
Fig. 23 - Animated mode shape sequence, 97Hz
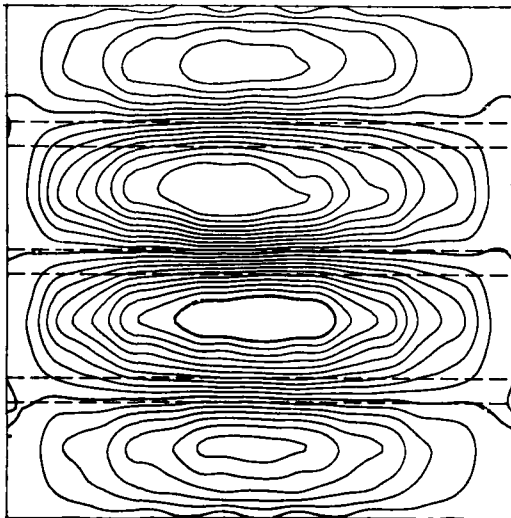
Fig. 24 - Weldbond mode shape, digital, 202Hz
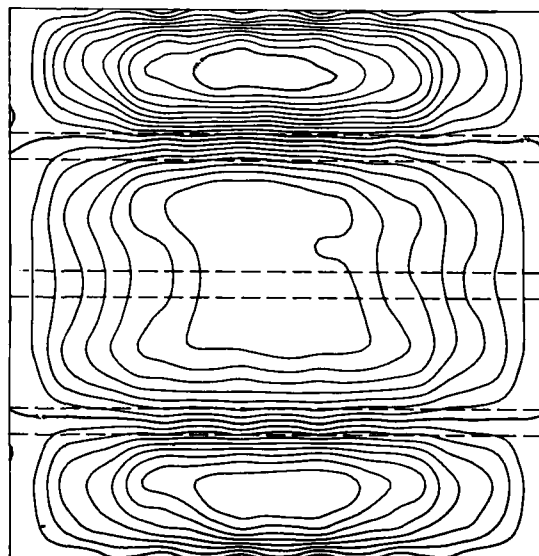
Fig. 25 - Weldbond mode shape, digital, 223Hz

72
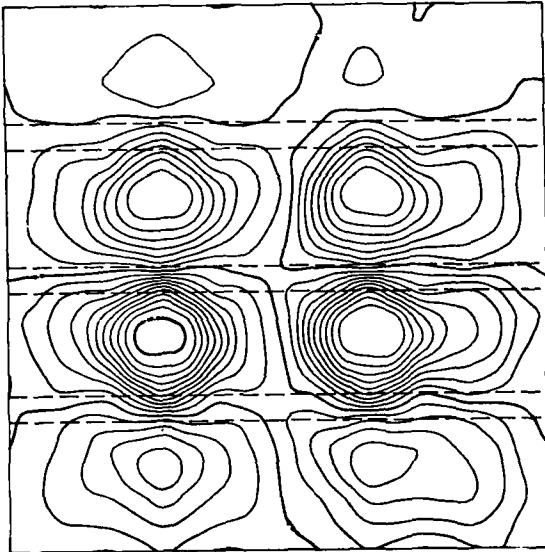
Fig. 26 - Weldbond mode shape, digital, 198Hz
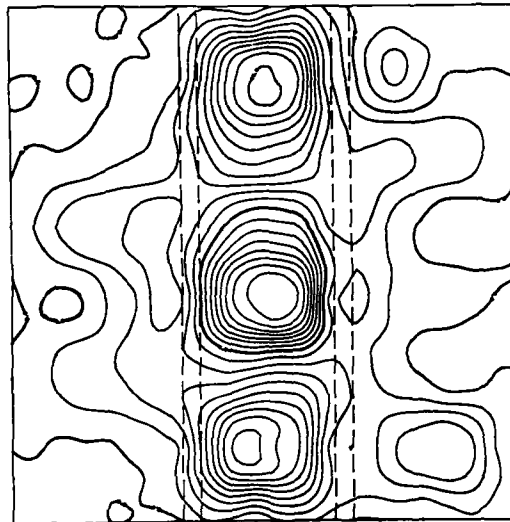
Fig. 27 - Weldbond mode shape, digital, 231Hz
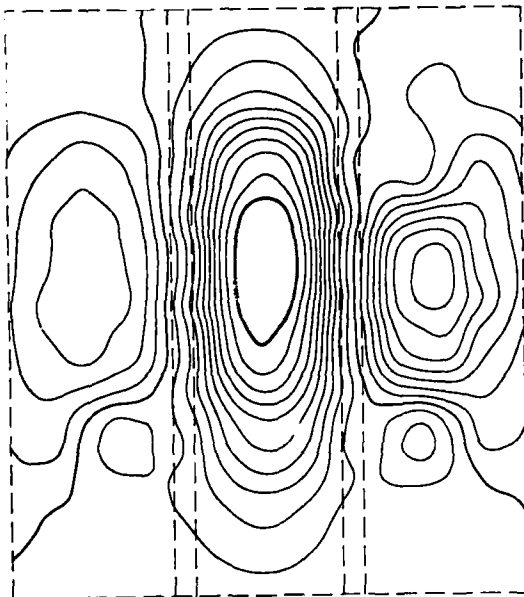
Fig. 28 - Bonded panel mode shape,
accelerometer mapping, 126Hz
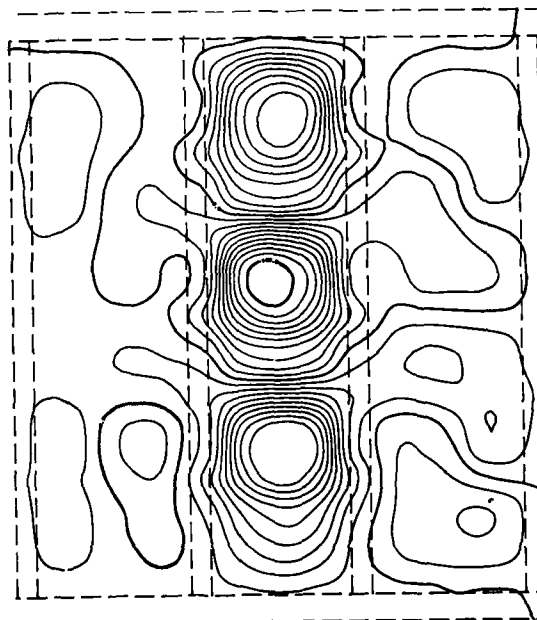
Fig. 29 - Bonded panel mode shape,
accelerometer mapping, 307Hz

73
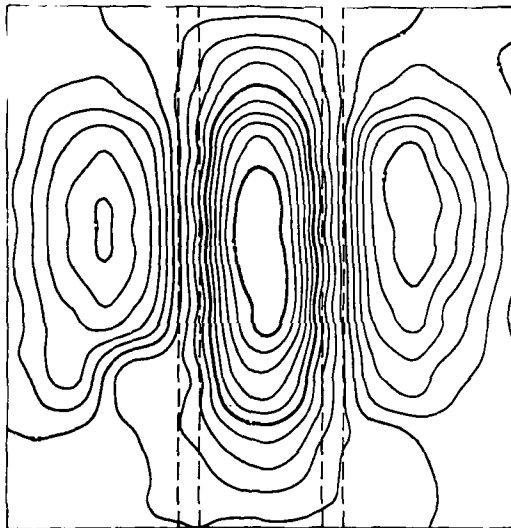
Fig. 30 – Bonded panel mode shape,
digital method, 123Hz
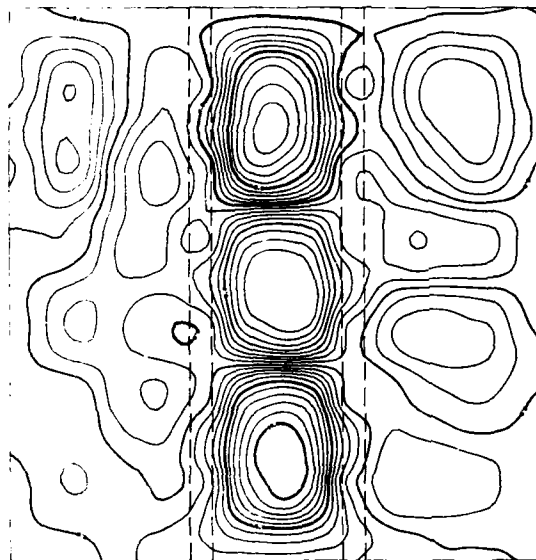
Fig. 31 – Bonded panel mode shape,
digital method, 305Hz

Fig. 32 – Bonded panel comparison
digital and analog,
123 and 126Hz
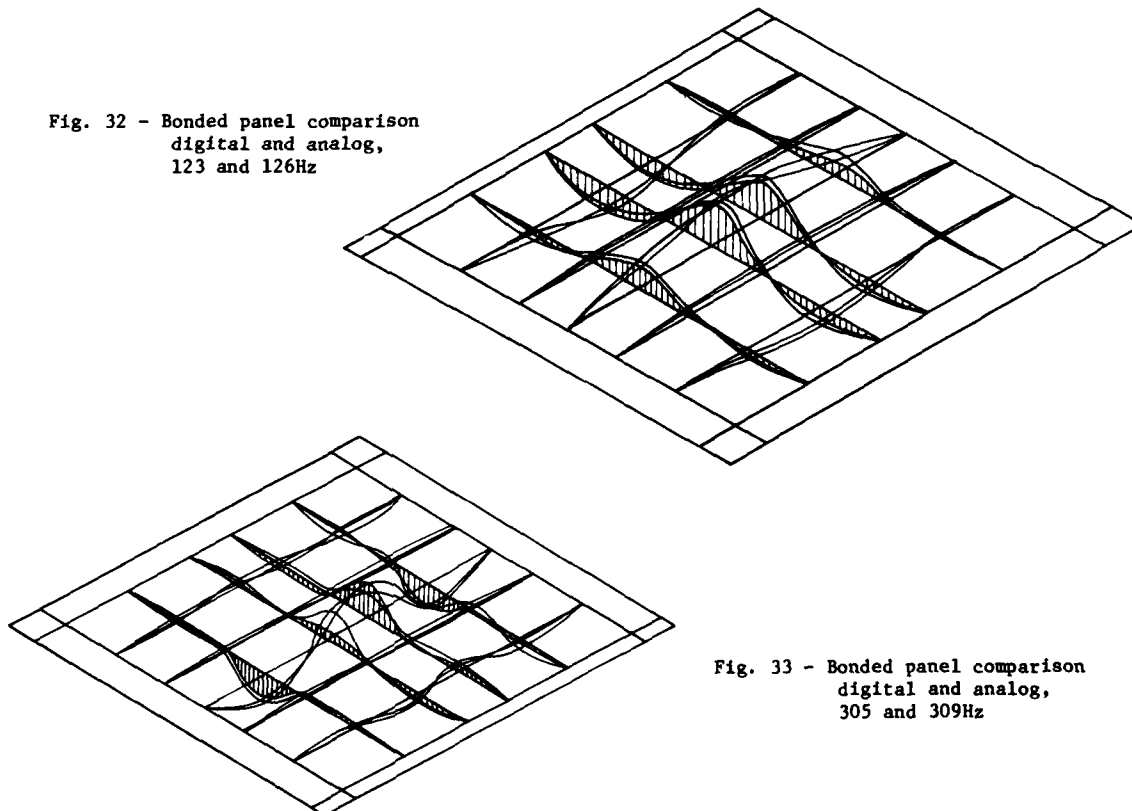
Fig. 33 – Bonded panel comparison
digital and analog,
305 and 309Hz

74

DISCUSSION

The digital impact technique as applied to lightweight structures showed certain advantages over the analogue technique. The analog method required more manhours than the digital method to obtain the mode shapes using the same grid system and contour plotting routines. More manhours were required in setting up the equipment, acquiring the data by hand and preparing the computer cards for the contour plots. Two similar Fourier Analyzer Systems were available for the tests. All required hardware and software for these systems were available including hammer and force gage, accelerometers and signal conditioning equipment. An existing modal analysis program was used for the F4 rudder and the first 12 weldbond panels. A more advanced program was developed and used on the last 4 weldbond panels and the bonded panel. No new equipment was required to implement this method. The analog method required a complete mapping of each frequency of interest. The digital method required a single mapping for any number of modes. The loudspeaker used to produce the excitation for the analog method produced a hazardous environment for personnel in the vicinity. Precautions were taken to provide personnel protection. The overall sound pressure level generally used was around 110 dB. No precautions were necessary when the impact method was used. Greater flexibility exists with the variety of output and storage capabilities available with the Fourier Analyzer. Fewer errors were made using the digital method.

The digital impact technique as applied here to lightweight structures showed certain disadvantages. The force spectrum of the impact was very dependent on the structural stiffness at the impact point. For the weldbond and bonded panels, adequate force spectra could only be obtained by impacts very near the panel frame or on the skin above a stiffener. Impacts applied at these locations were inefficient in exciting most panel modes since node lines often appear at the stringers. In addition to the natural frequencies, mode shapes and damping, identification of the most responsive mode is needed to determine the high stress locations for the sonic fatigue tests. Since the most responsive mode determined by impact excitation was not necessarily the most responsive to acoustic excitation, this information was not determined using the digital method with impact excitation. For simple structures, predictions, based upon experience were satisfactory; otherwise, additional tests other than those using impact excitation were required.

CONCLUSIONS AND RECOMMENDATIONS

The dynamic properties including the resonant frequencies, mode shapes and damping factors were obtained using the digital impact and analog techniques on the same

sonic fatigue test structures. The results indicated good agreement with the two techniques. Less test time and effort were required using the digital method. Therefore, a considerable savings in manhours was realized using the digital technique.

An alternate method of excitation for use with the digital method on sonic fatigue specimens is recommended for future work. A wide band random acoustic excitation with the same spectrum shape as would be used for a subsequent sonic fatigue test may offer advantages over the impact excitation. Better control of the input spectrum would be available. The most responsive modes of vibration may also be determined. Measurement of the input force is a problem with acoustic excitation.

REFERENCES

1. Ramsey, Kenneth A., "Effective Measurement for Structural Dynamic Testing," Part I, Sound and Vibration Magazine, November 1975.

2. Ramsey, Kenneth A., "Effective Measurement for Structural Dynamic Testing," Part II, Sound and Vibration Magazine, April 1976.

3. Morse, I.E., Shapton, W.R., Brown, D.L., and Kuljanic, E., "Application of Pulse Testing for Determining Dynamic Characteristics of Machine Tools," presented at the 13th International Machine Tool Design and Research Conference, University of Birmingham, Birmingham, England, 1972; published as Application Note 1403, Hewlett Packard Company.

4. Allemang, R.J., Graef, H.T., Powell, C.D., "Dynamic Characteristics of Rotating and Nonrotating Machine Tool Spindles," presented at the Design Engineering Technical Conference, Cincinnati, Ohio, 1973; published as ASME Paper No. 73DET29.

5. Drake, M.L., Henderson, J.P., "An Investigation of the Response of a Damped Structure using Digital Techniques," presented at the 45th Symposium on Shock and Vibration, Dayton, Ohio, October 1974, published in Bulletin 45, Part 5, pp. 8397, June 1975.

6. "Fourier Analyzer Training Manual," published as Application Note 140-0, the Hewlett Packard Company.

7. Bendat, J.A. and Piersol, A.G., Measurement and Analysis of Random Data, John Wiley and Sons, New York, 1966.

8. Klosterman, A.L., "On the Experimental Determination and Use of Modal Representations of Dynamic Characteristics," Ph.D. dissertation, University of Cincinnati, 1971.

9. Wolfe, H.F., Wentz, K.R., Volf, N.D., "Sonic Fatigue Test of the F-4 Boron/Epoxy Rudder," Air Force Flight Dynamics Laboratory Technical Memorandum 76-82, August 1976.

10. Informal communications with D.L. Brown, Mechanical Engineering Department, University of Cincinnati, 1974-1975.

DISCUSSION

Mr. Himelblau (Rockwell Space Division): If you have riveted stiffeners, would it be preferable to tap it on the skin or tap it on the rivet? That is one category of structure, the other category is honeycomb. What would your suggestion be for impact testing of both structures?

Mr. Gordon: For riveted stringers, it is typically the same as it would be for any type stringer attachment. You should have a stringer underneath the skin to add stiffness at that point. The attachment doesn't make that much difference.

Mr. Himelblau: Would you be concerned about nonlinearity?

Mr. Gordon: I really don't think so. As for honeycomb, which is fairly stiff across the whole structure, I don't think there would be any problem. The rudder we tested was honeycomb core with boron-epoxy skins.

Mr. Favour (Boeing Company): In terms of the pulse testing with a hammer--this is something similar to what we did some time ago and I was a real believer in it until some work that Norm Olson did wherein he used a sine sweep "chirp" from a shaker. This solved some of the problems that you allude to, in particular lightly damped structures. So long as you measure the force you can utilize damping in the shaker to dampen out your excitation and keep your pulse relatively short. You showed several different ways of displaying mode shapes on the rudder. One was the 3-dimensional display. The other was a contour plot. What kind of interpolation routine is used on the contour plot? I seriously question how we can develop intricate integral "S" curves between the sample points. I question that because I have seen it done on engineering laboratory testing and contour plotting, and I don't think the Sanford theory supports what you see in the picture.

Mr. Gordon: The contour mapping routine that we used was a packaged routine that we have at Wright-Patterson AFB on a CDC computer. It is a Calcomp routine, I think it is called GPCP, which is a general computer plotting. I am not that familiar with the way the contour mapping works, except that you must have enough data, that is your grid has to be fine enough to include enough data to get accurate plots. We have plotted everything from modal displacements to sound pressure contours using this technique and we have never had any problems with it.

Mr. Pandit (Michigan Technological University): As long as you are using digital techniques, why can't you perform the whole analysis in the time domain? You don't get into the Fourier transformation at all because as long as you have an input and output signal, you can fit this input/output data to get a cost function completely in the time domain, and all the information on damping, mode shapes, are available to you. This would save in cost tremendously because you are not Fourier transforming at any time and once you get the cost function in the time domain you could always go to the frequency domain with a minimum of contemplation. Have you ever tried a difference equation?

Mr. Gordon: We have never tried anything like that.
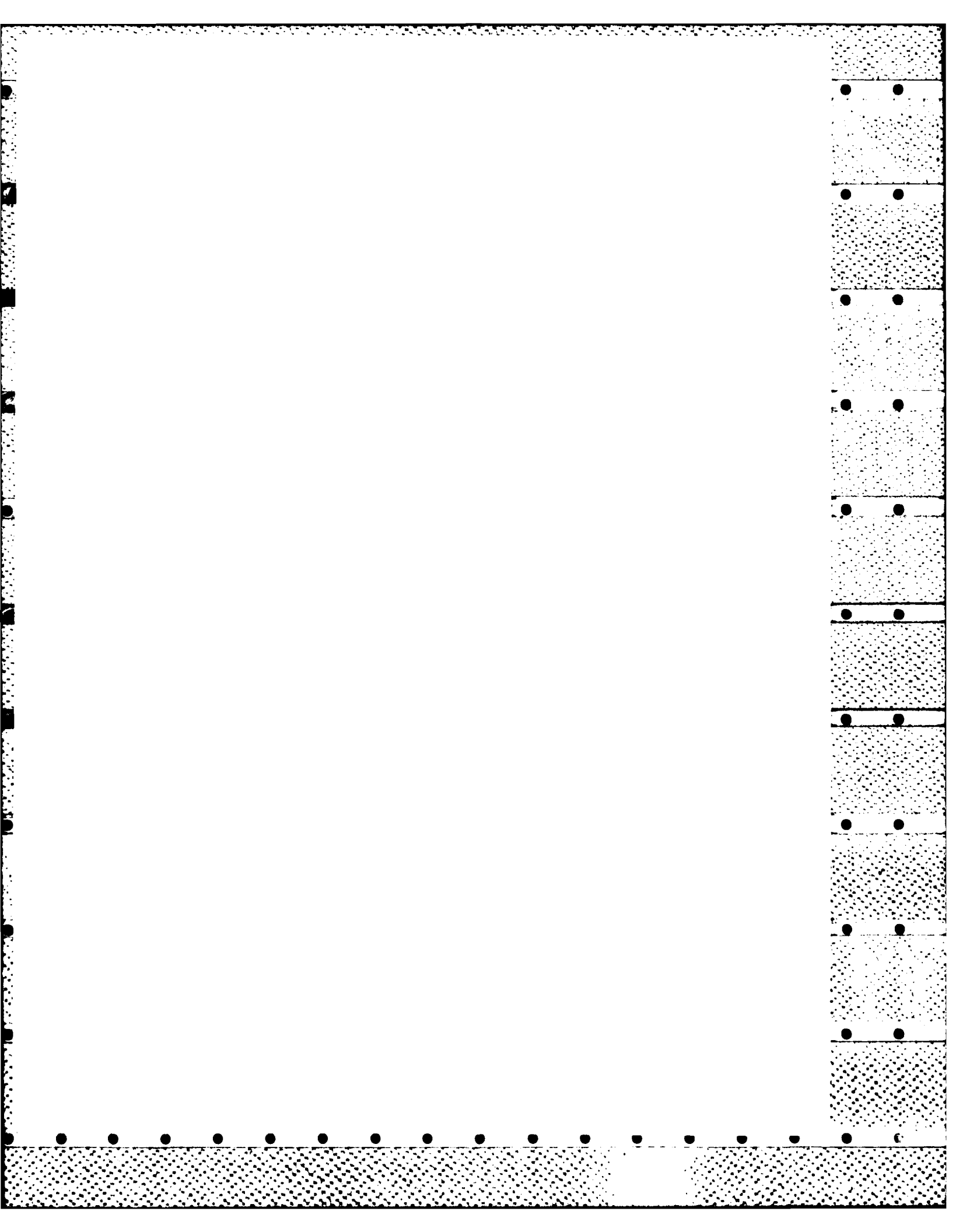
DIGITAL CONTROL SYSTEM FOR A MULTIPLE-ACTUATOR SHAKER[*]

Dennis K. Fisher and Michael R. Posehn
Lawrence Livermore Laboratory, University of California
Livermore, California 94550

Multiple-actuator shakers are commonly used in the shock and vibration testing of large test specimens. Structural resonances in the fixtures or test specimen can lead to large interactuator forces that degrade the accuracy and stability of the control system. In this paper, we review the theory and describe the final implementation and performance characteristics of the digital-control system for the electrohydrolic, multiple-actuator shaker at Lawrence Livermore Laboratory. The key to multiple-actuator control is the cross-coupling-compensation matrix [A], which is shown to be directly related to the inverse of the system-transfer matrix. The matrix [A] changes with each change of fixture or test specimen. Hence [A] must be determined experimentally either prior to or during actual testing. Cross-coupling compensation is implemented differently for swept-frequency sinusoidal, transient-waveform, and random-vibration testing. These digital-control techniques, as implemented in the Livermore electrohy-draulic shaker facility, have resulted in a high-performance yet flexible test system.

INTRODUCTION

In a previous paper [1], we formulated the theoretical basis for control of multiple-actuator shakers and reported on a digital-control system for an electrohydraulic shaker then under development at Lawrence Livermore Laboratory (LLL). In this paper, we review the theoretical basis and describe the implementation and performance characteristics of the completed LLL system.

Historically, the first attempts at compensation for cross-coupling were analog in nature [2,3,4]. But this approach proved impractical because of the manual tuning required for each physical setup and the lack of provision for nonlinear system response. In recent years, the emphasis has been on digital shaker-control systems, and this technology is now well accepted throughout the industry. Numerous papers [5,6] have described the techniques and advantages of computer-based vibration control. Two recent papers addressed multiple-actuator transient-waveform control: Kao [7] described the general approach for a hypothetical two-dimensional digital-control system that could be used in seismic testing, while Lund [8] presented experimental results obtained using a digitally-controlled, multiple-actuator road simulator.

The LLL shaker system places particularly stringent performance requirements on its control system. The physical setup is not fixed: from one to four actuators are controlled in any given setup, and specimens may be tested along either a vertical or horizontal axis. In many applications the actuators are used to drive a very rigid table fixture, resulting in a highly cross-coupled system. The electrohydraulic actuators themselves have significant harmonic distortion and nonlinearities in amplitude response. Finally, the shaker system must perform swept-frequency sinusoidal, transient-waveform, and random-vibration testing over a frequency range of dc to 500 Hz.

FACILITY OVERVIEW

The test facility (Fig. 1) consists of three buildings: a control room for control and data-acquisition equipment, a building for the hydraulic power supply, and the test cell in which the shaker is located. The test cell, physically isolated from the control and equipment buildings, is designed to permit safe testing of explosive specimens exceeding 90-kg TNT
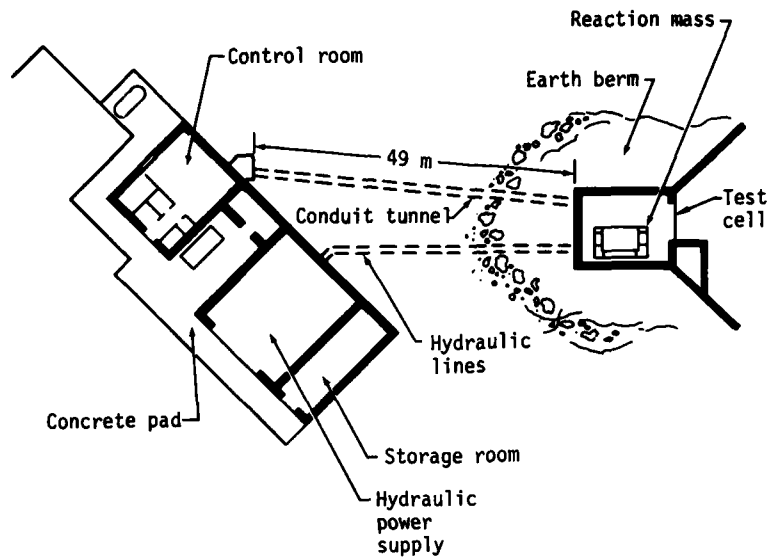
Fig. 1 - Plan of the Lawrence Livermore Laboratory multiple-actuator shaker facility

equivalent. The cell also has air scrubbers and a containment system for controlling radiation hazard.

The hydraulic power supply consists of 11 individually controlled, pressure-compensated, 0.11-MW pumps connected in parallel. The combined continuous pumping capacity is 43 liters/s at a nominal supply pressure of 20.7 MPa. For safety, the hydraulic oil is a fire-retardant synthetic.

Each actuator has a maximum thrust capability of 0.155 MN and a total stroke of 127 mm. Hydrostatic guide bearings integral to the actuator can support cross-axis loads up to 0.04 MN without damage. The high-performance, two-stage servovalues in the actuators are rated at 14 liters/s each and have a resonant frequency of 620 Hz, resulting in a nominal operating bandwidth of 500 Hz and a peak velocity of 2 m/s. Stroke length, peak velocity, force output, and valve response combine to give the single-actuator performance characteristics shown in Fig. 2.

Because the actuators are free-standing and relocatable, they can be bolted to either the top surface (for z-axis motion) or the vertical abutments (for x- and y-axis motion) of the 680-ton, reinforced-concrete reaction mass. Two typical testing configurations are shown in Fig. 3.

The general configuration of the computer control system is shown in Fig. 4. There are three general hardware groupings: a digital computer system, the actuators and associated

analog valve controllers, and the hybrid-interface hardware. In closed-loop fashion, the computer inputs response data from the data-acquisition unit (DAU), computes a new set of commands, and outputs instructions as necessary to a digital waveform synthesizer (DWS) and command-generation unit (CGU). The latter two devices function together to generate independent analog commands for each actuator.
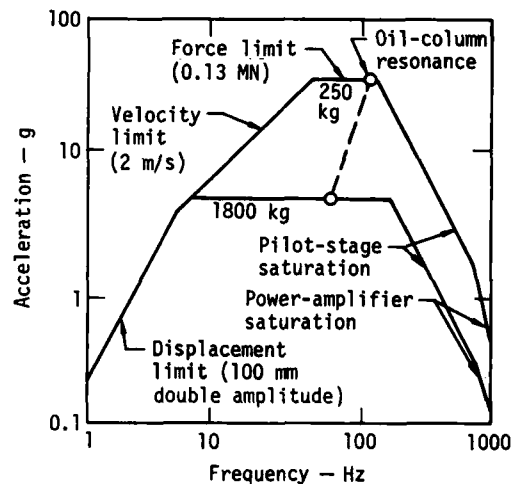
Fig. 2 - Sinusoidal performance characteristics of a single electrohydraulic actuator for load masses of 250 kg and 1800 kg
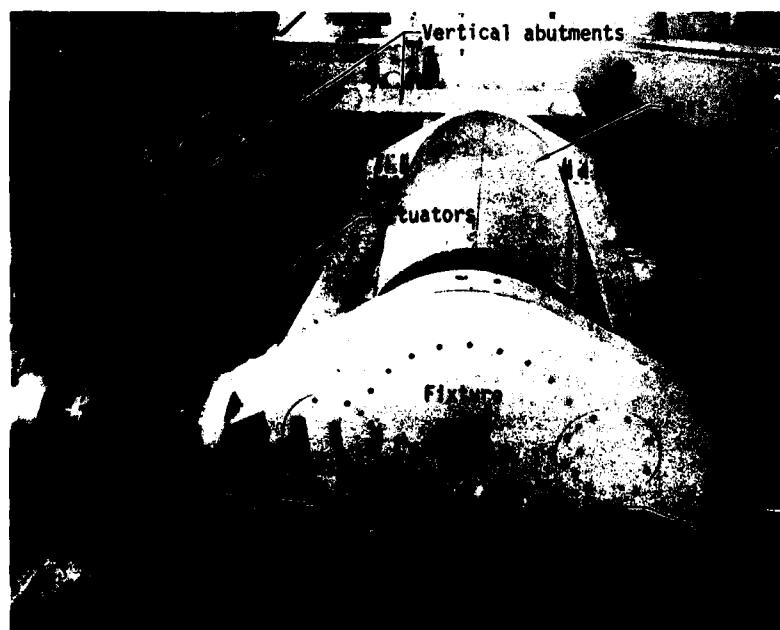
Fig. 3 - Typical test configuration for Z-axis motion (top), where the specimen is a shipping container, and Y-axis motion (bottom), where the specimen is an upper-stage missile structure

81
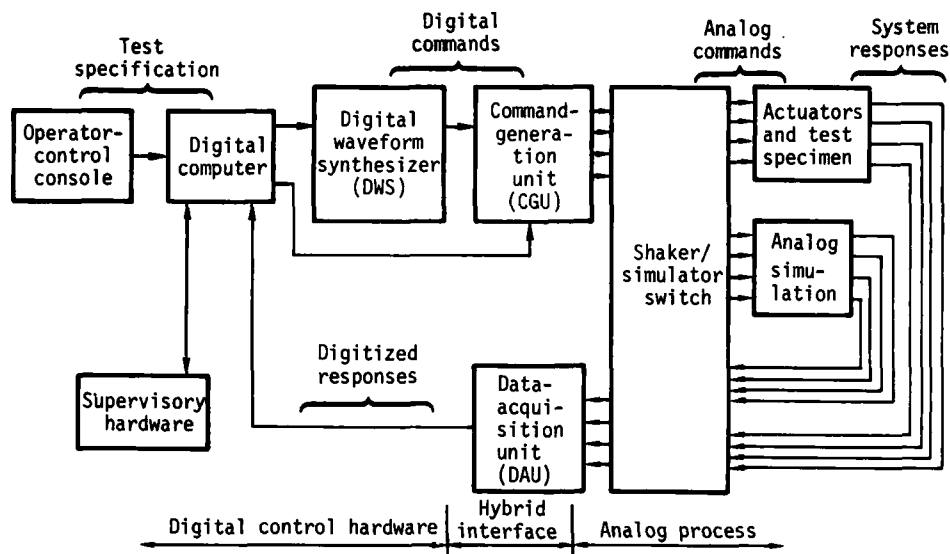
Fig. 4 – Block diagram showing principal components in digital-control system, shaker, and analog simulation

The DAU selects the appropriate response signals, converts them to digital form, and performs various preliminary data-processing functions. For each actuator, the DAU selects either the actuator displacement, hydraulic pressure, or associated specimen response as a feedback signal. The selected signal is scaled, filtered, sampled, and digitized with 12-bit precision at rates up to 50 kHz. In sine testing, a hardware digital Fourier filter further processes the data to yield peak, coincident, and quadrature response components.

For each electrohydraulic actuator there is an associated analog controller which, through minor feedback loops involving displacement transducers in the valve and actuator, produces an actuator displacement directly proportional to a static input-command voltage. As illustrated in Fig. 4, the actuators are paralleled by an analog computer programmed to simulate a two-actuator, cross-coupled system. Either the actual shaker or the analog simulation may be selected by the operator at the time of the test. This simulation capability, originally needed for developing the control system, is now used to instruct operators and to develop software for new applications.

The computer system is configured about a 16-bit-word-size central processor unit (CPU) having 64 k (k = 1024) words of 800-ns core memory, floating-point hardware, a 120-Hz real-time clock, and an interval timer. Peripherals include a 1.2×10^6-word disk memory, seven-track magnetic-tape unit, card reader, electro-

static printer/plotter, hardware fast-Fourier-transform processor, and a CRT graphics terminal and operator-control console.

The operator-control console contains arrays of pushbuttons, indicator lights, and potentiometers, which are either read or set by the computer through application software. A programmable LED display gives the values of various parameters during vibration testing, such as the frequency during swept-sine testing or the rms acceleration (g_{rms}) level during random vibration testing.

CROSS-COUPLING COMPENSATION

A multiple-actuator system has cross-coupling whenever the command input to one actuator produces a response at another. In the lateral, Y-axis configuration of Fig. 5a, it is apparent that any motion of actuator 1 will also result in motion of actuator 2 because of the finite stiffness of the latter. This same system, represented as a block diagram, is shown in Fig. 5b. In terms of a matrix formulation, the system response is

$$\begin{Bmatrix} C_1(s) \\ C_2(s) \end{Bmatrix} = \begin{bmatrix} G_{11}(s) & G_{12}(s) \\ G_{21}(s) & G_{22}(s) \end{bmatrix} \begin{Bmatrix} R_1(s) \\ R_2(s) \end{Bmatrix}, \quad (1)$$

or simply

$$\{C(s)\} = [G(s)]\{R(s)\} . \quad (2)$$

82
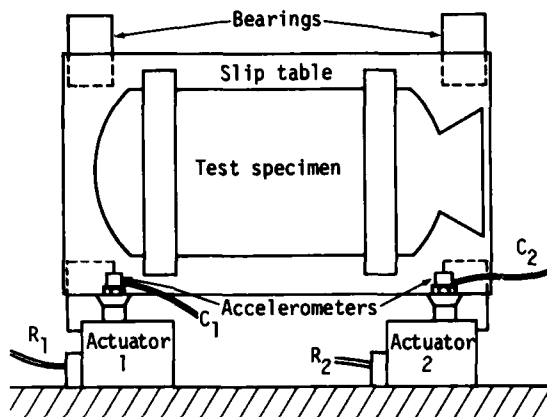
(a) Plan for fixturing
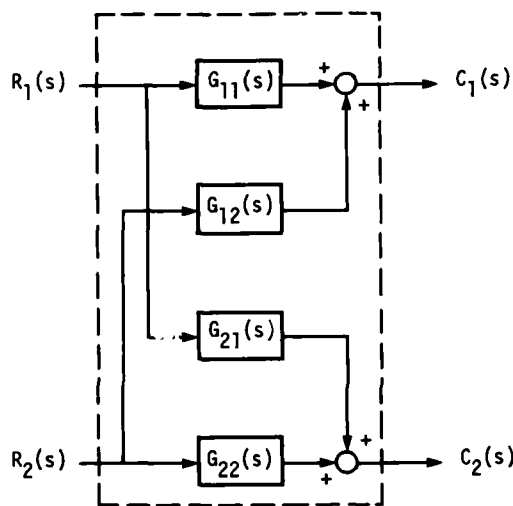
(b) Block diagram of transfer-function matrix G(s).

Fig. 5 – Lateral-axis test configuration illustrating cross-coupling between two actuators; $R_1(s)$ and $R_2(s)$ are the Laplace-transformed commands to the actuators, and $C_1(s)$ and $C_2(s)$ are the corresponding acceleration responses

If, as shown in Fig. 6, we introduce a compensation matrix $[A(s)]$, the actuator commands become

$$\{R(s)\} = [A(s)]\{R'(s)\} , \qquad (3)$$

where $R'(s)$ is the desired uncoupled-actuator response vector. The actuator responses are then

$$\{C(s)\} = [G(s)][A(s)]\{R'(s)\} , \qquad (4)$$

and we see that if the compensation matrix is defined as

$$[A(s)] = [G(s)]^{-1} , \qquad (5)$$

then

$$\{C(s)\} = [G(s)][G(s)]^{-1}\{R'(s)\} = \{R'(s)\}. \qquad (6)$$

Thus, the ideal cross-coupling-compensation matrix is the inverse of the system-transfer matrix, as shown in Eq. (5). Once $[A(s)]$ has been determined, the actuator commands $\{R(s)\}$ required to generate a desired response $\{R'(s)\}$ can be calculated according to Eq. (3).

CONTROL ALGORITHMS

Equations (3) and (5) are the basic formulation of cross-coupling compensation and are incorporated in the control algorithms for swept-frequency sinusoidal, transient-waveform, and random-vibration control. Each algorithm requires "identification" — measurement of the system-transfer matrix. However, the manner of implementing this varies with the type of testing.

Swept-Frequency Sinusoidal Testing

In multiple-actuator sine testing, the control objective is to maintain the same response amplitude and relative phase for each actuator. The principal features of the control algorithm, to be discussed in the following paragraphs, are:

● Phase and amplitude are controlled indirectly by independent control of the coincident (CO) and quadrature (QUAD) components of response.

● The CO and QUAD components are detected by hardware using synchronous sampling and Fourier-filtering.

● Cross-coupling compensation is self-adaptive in that a performance-criterion threshold is used to initiate identification of the system.

● Identification is accomplished during testing by perturbing the commands to each actuator, one actuator at a time.
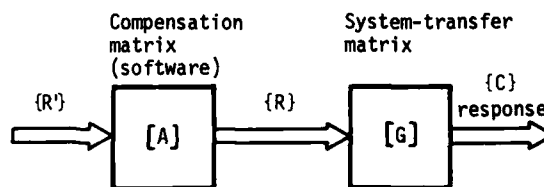
Fig. 6 – Block diagram illustrating introduction of compensation matrix into command stream

83

The control of CO and QUAD responses, as opposed to direct control of amplitude and phase, is advantageous in that it avoids computational errors and the ambiguity of phase-angle definitions at ±180°. In the LLL shaker system, a digital Fourier filter detects the CO and QUAD components of response, relative to the sine and cosine reference waveforms generated by the digital waveform synthesizer (see Appendix A). The filter, located within the DAU, was implemented in hardware to reduce the computational burden on the CPU. Because of computational speed limitations in the hardware, the number of points per cycle used in the analysis varies with the frequency of vibration. The net result is that the new CO and QUAD estimates are completed in either one cycle of the fundamental frequency or approximately 50 ms, whichever is larger. The overall performance of the LLL CO/QUAD-tracking Fourier filter is presented in Fig. 7.

The sine-control algorithm, flow charted in Fig. 8, is self-adaptive with respect to cross-coupling compensation. The control loop begins by inputting the latest estimates of CO and QUAD response for each of N actuators from the DAU and combining these into a complex response error:

$$C_i = CO_i + j(QUAD_i), \quad i = 1, N. \qquad (7)$$

The response-error vector

$$\{E'\} = \{R'\} - \{C\} \qquad (8)$$

is then computed, and if any error exceeds a preset threshold (typically 30% of the sine or

cosine reference value), the shaker system is reidentified as described below. In either event, the current compensation matrix is used to decouple the errors:

$$\{E\} = [A]\{E'\} , \qquad (9)$$

and the command array is updated according to the proportional-integral-differential control law:

$$\{R\}_{n+1} = \{R\}_n + K_p[\{E\}_n - \{E\}_{n-2}]$$

$$+ \Delta T K_I[\{E\}_n + \{E\}_{n-1}]$$

$$+ \frac{K_D}{\Delta T}[\{E\}_n - 2\{E\}_{n-1} + \{E\}_{n-2}] , \qquad (10)$$

where

$$\Delta T = \text{update interval,}$$

and

$$K_p, K_I, K_D = \text{proportional, integral, and derivative gain factors.}$$

The subscript n designates the current value of a variable, n-1 the value during the previous iteration, etc. The updated commands are output to the command-generation unit, which develops independent sinusoidal drive signals for each actuator controller.

Identification, when initiated, is carried out by perturbing the commands to each actuator, one actuator at a time. To minimize nonlinear effects, identification is carried out while operating at full test level. Perturbing an actuator command actually takes the form of a 20% decrease in the amplitude of the command vector to that actuator. At any given frequency, the system response can be expressed as

$$\{C\} = [G]\{R\} . \qquad (11)$$

If the system inputs are perturbed by an amount ΔR, the new system response will be

$$\{C + \Delta C\} = [G]\{R + \Delta R\} . \qquad (12)$$

By assuming linearity and subtracting Eq. (11) from Eq. (12), we see that the system-transfer matrix relates the input change to the change in response:

Fig. 7 - Measured response of CO/QUAD-tracking Fourier filter to sinusoidal noise signal of amplitude N_1 and frequency f_N analyzed at frequency f_A
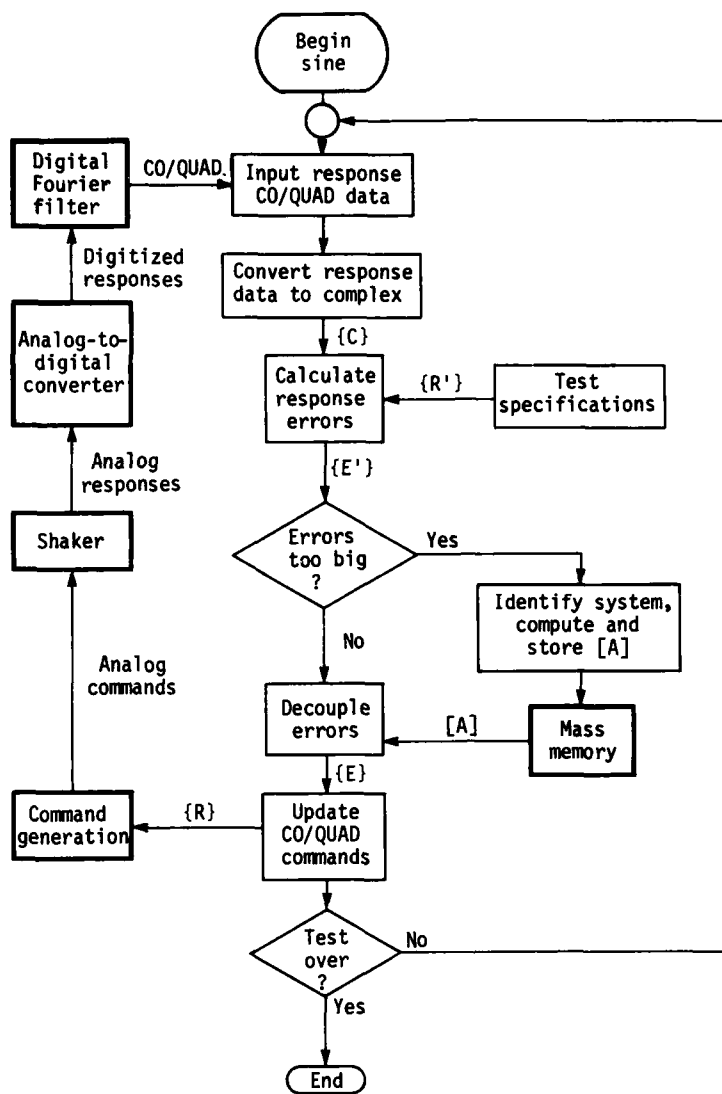
Fig. 8 – Flowchart of swept-frequency sinusoidal control algorithm;
[A] is the cross-coupling-compensation matrix

$$\{\Delta C\} = [G]\{\Delta R\} , \qquad (13)$$

or

$$\begin{Bmatrix} \Delta c_1 \\ \vdots \\ \Delta c_k \\ \vdots \\ \Delta c_N \end{Bmatrix} = \begin{bmatrix} g_{11} & \cdots & g_{11} & \cdots & g_{1N} \\ \vdots & & \vdots & & \vdots \\ g_{k1} & & & & \vdots \\ \vdots & & \vdots & & \vdots \\ g_{N1} & \cdots & g_{N1} & \cdots & g_{NN} \end{bmatrix} \begin{Bmatrix} \Delta r_1 \\ \vdots \\ \Delta r_k \\ \vdots \\ \Delta r_N \end{Bmatrix} , \qquad (14)$$

where Δc_i, g_{ki}, and Δr_i are all complex. If Δr_i is the only nonzero input perturbation, the response at actuator k is

$$\Delta c_k = g_{ki} \cdot \Delta r_i . \qquad (15)$$

The transfer elements in column i can then be calculated as

$$g_{ki} = \frac{\Delta c_k}{\Delta r_i} , \quad k = 1, N . \qquad (16)$$

Thus, by perturbing the input to each actuator one actuator at a time and observing the changes

85

in response of all actuators, the transfer matrix is determined column by column. Inversion of the complex transfer matrix yields the cross-coupling-compensation matrix required by the control algorithm. The compensation matrix for each new frequency is stored on the disc memory for automatic retrieval in the event that the same frequency is reached in a reverse sweep.

Our experience using the sine-control algorithm has been with two-actuator lateral-axis tests and three- and four-actuator vertical-axis tests. Typical results, shown in Fig. 9, are an rms control accuracy of ±1 db in amplitude and ±5 deg in absolute phase for all active actuators.

Transient-Waveform Control

The objective of multiple-actuator transient-waveform control is to produce a specified or desired time-domain response simultaneously at all actuators. A transient test has two separate phases:

● Pretest identification of the system-transfer matrix,

● Test execution, in which the full-level pulse is generated and an iterative-search algorithm is used to improve successive repetitions.
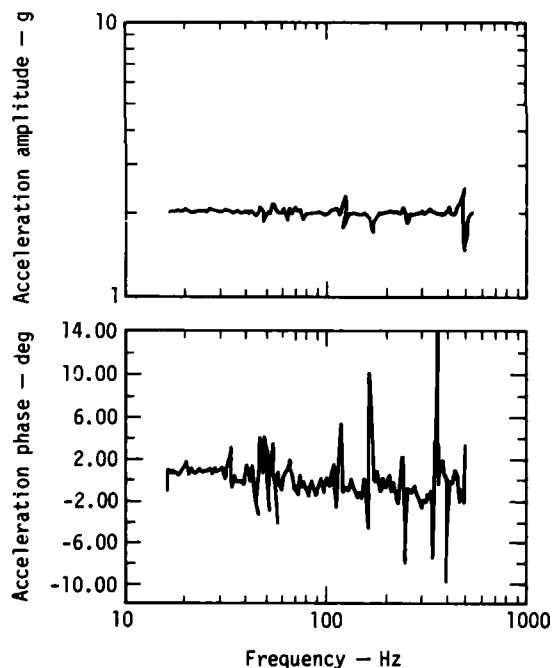
Fig. 9 - Typical control-accelerometer response to a 2-g sine sweep of a three-actuator fixture plus test specimen
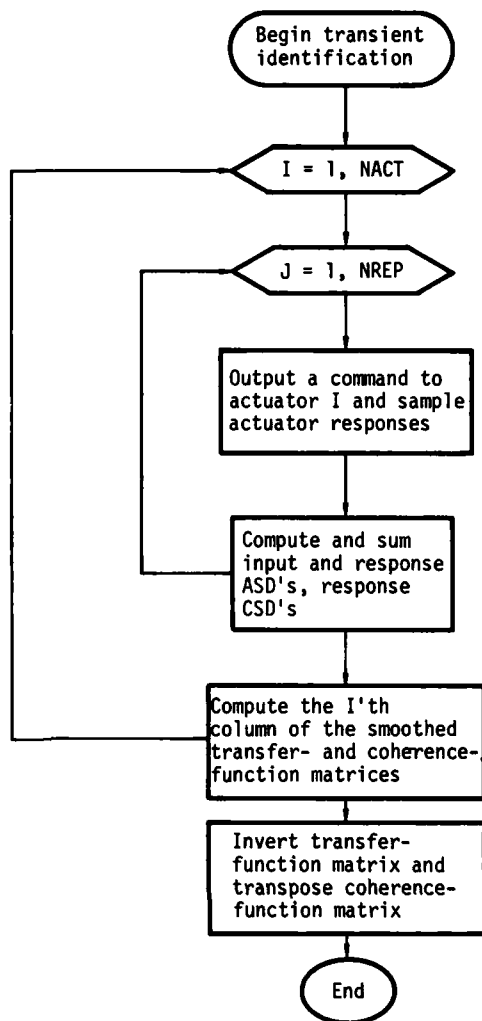
Fig. 10 - Flow chart of procedure used by transient-waveform control algorithm to identify the system-transfer matrix; NACT is the number of actuators, ASD is auto-spectral density and CSD is cross-spectral density

The pretest identification phase uses methods similar to those previously employed in transient-waveform control, except that cross-coupling effects must also be identified. The iterative search technique is new, however. It was developed because much of our testing involves many repetitions of the same pulse and the usual technique of updating an estimate of the transfer function [7] is not applicable to multiple-actuator excitation. Inversely, however, the iterative-search procedure will work for a single-actuator system.

A flow chart of the identification procedure is shown in Fig. 10. The outermost loop of the

86

flow chart corresponds to the independent
excitation of each actuator by a low-level
identification pulse. As in swept-sine control,
each pass through the loop produces one column
of the transfer-function matrix and one column
of the coherence-function matrix. The maximum
identification-pulse level, typically 50% of the
full test level, is specified by the operator.
The first pulse used for identification is the
desired waveform, scaled to produce an accelera-
tion equal to 10% of the full test level. On
successive repetitions, this pulse is scaled up
until the specified identification level is
reached. Experience has shown that, at least
in the case of hydraulic actuators, an identi-
fication pulse having a frequency spectrum
similar to the final test pulse produces a
better identification than a broad-band pulse.

In Fig. 11, the identification pulse to each
actuator is repeated NREP times, and the input
and response auto-spectral densities of each
input/response pair are accumulated. When
identification for each actuator is complete,
the spectra are averaged and a column of the
transfer matrix is computed:

$$G_{ij}(\omega) = \frac{\overline{P}_{ij}(\omega)}{\overline{P}_{j}(\omega)} \ , \quad i = 1, N \ ; \qquad (17)$$

where

$\quad G_{ij}(\omega)$ = transfer function corresponding
$\qquad$ to a command input to actuator
$\qquad$ j and a response at actuator i,

$\quad \overline{P}_{j}(\omega)$ = averaged command auto-spectral
$\qquad$ density, and

$\quad \overline{P}_{ij}(\omega)$ = averaged cross-spectral density
$\qquad$ corresponding to a command input
$\qquad$ to actuator j and a response at
$\qquad$ actuator i.

In addition, a column of the coherence-function
matrix is calculated:

$$\gamma^2_{ij}(\omega) = \frac{|\overline{P}_{ij}(\omega)|^2}{\overline{P}_{i}(\omega)\ \overline{P}_{j}(\omega)} \ , \quad i = 1, N \ ; \qquad (18)$$

where

$\quad \overline{P}_{i}(\omega)$ = averaged response auto-spectral
$\qquad$ density.

The coherence function is a measure of the
validity of the transfer function at any fre-
quency and will vary between zero and one,
depending on the presence of noise and non-
linearities.

After each actuator has been pulsed individ-
ually, the entire N × N transfer matrix is
assembled and inverted to yield the cross-
coupling-compensation matrix:

$$[A(\omega)] = [G(\omega)]^{-1} \ . \qquad (19)$$
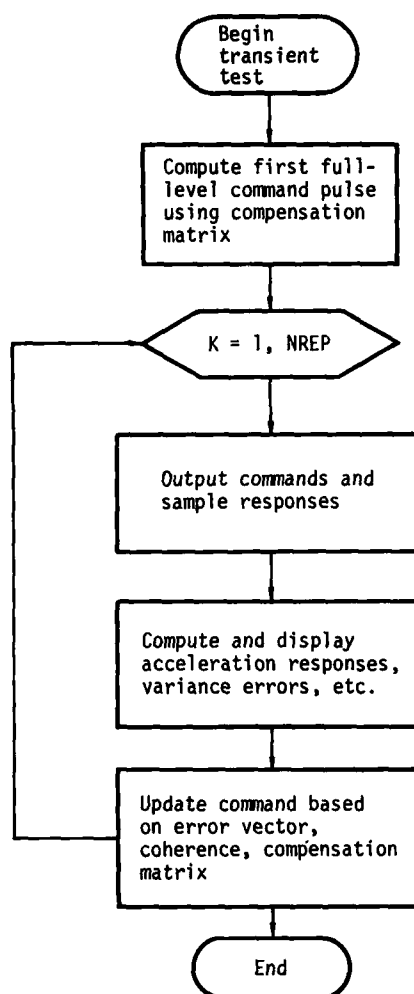
Fig. 11 - Flowchart of procedure for
transient-waveform test

The executing procedure of the transient-
waveform test is illustrated in Fig. 11. The
Fourier transforms of the first full-level
commands are obtained by multiplication of the
transform of the desired response by the com-
pensation matrix, e.g.,

$$\{R(\omega)\} = [A(\omega)]\{R'(\omega)\} \ , \qquad (20)$$

where

$\quad \{R(\omega)\}$ = Fourier transform of command-
$\qquad$ pulse vector, and

$\quad \{R'(\omega)\}$ = Fourier transform of desired-
$\qquad$ response vector.

The vector $\{R(\omega)\}$ is then inverse transformed
to the time domain and output to the shaker.

87

The technique described above provides a good "first-guess" at the command pulse necessary for the desired response. However, if the pulse is to be repeated, the estimate of the command Fourier spectrum for each actuator can be updated according to the equation

$$R_i(\omega)\big|_{n+1} = R_i(\omega)\big|_n$$

$$+ K \sum_{j=1}^{N} \left[A_{ij}(\omega) L(\gamma_{ji}(\omega)) \{ R_j'(\omega) - C_j(\omega)\big|_n \} \right] \quad (21)$$

where

$R_i(\omega)\big|_{n+1}$ = updated command Fourier spectrum, actuator i;

$R_i(\omega)\big|_{n}$ = current command Fourier spectrum, actuator i;

K = an iteration gain ($0 \leq K \leq 1$);

$L(\gamma_{ji}(\omega))$ = a nonlinear scalar function having a value of either 0 or 1;

$R_j'(\omega)$ = desired response Fourier spectrum, actuator j; and

$C_j(\omega)\big|_{n}$ = actual response Fourier spectrum of actuator j during the previous iteration.

The theoretical basis for this technique is presented in Appendix B. In essence it is an iterative-search technique for optimizing the command spectra.

The nonlinear scalar function $L(\gamma_{ji}(\omega))$ has been incorporated to avoid searching on a spectral line in which a low coherence indicates the transfer-function estimate is inaccurate. Note that the subscripts of the coherence function γ have been interchanged to maintain

the proper correspondence with the inverted transfer-function matrix. For each spectral line k, the nonlinear function L is defined as

$$L^k = 1.0 \quad \text{if } \gamma_{ji}^k \geq \gamma_T , \quad (22)$$

or

$$L^k = 0 \quad \text{if } \gamma_{ji}^k < \gamma_T ,$$

where

γ_T = a threshold coherence value, typically 0.9.

In essence, this function allows for the fact that, if the coherence function $\gamma_{ji}(\omega)$ is low at a particular frequency, we probably cannot improve our original estimate of the effect of the command to actuator i on the response at actuator j.

The cross-coupling compensation and iterative control techniques have proven highly successful with the LLL electrohydraulic shaker system. In Fig. 12, the variance error in the response waveform [6] is plotted for a series of full-level pulses on a two-actuator, lateral-table setup. The variance errors are initially 11% and 16% but after a few repetitions have both been reduced to about 5%, as shown by the similarity between the final acceleration transients of the two actuators (Fig. 13). The

Fig. 12 - Variance error computed for a sequence of transient pulses on a two-actuator lateral table
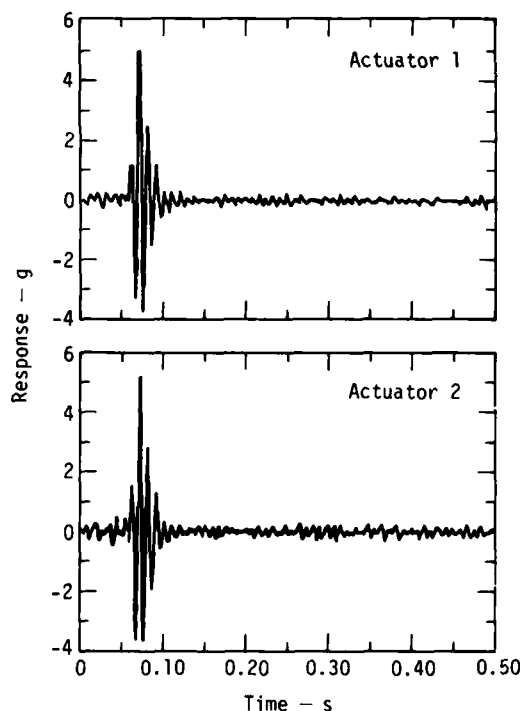
Fig. 13 - Typical reproduction of a 5-g, 100-Hz, 20%-damped ZERD pulse on a two-actuator lateral table using transient-waveform control

88
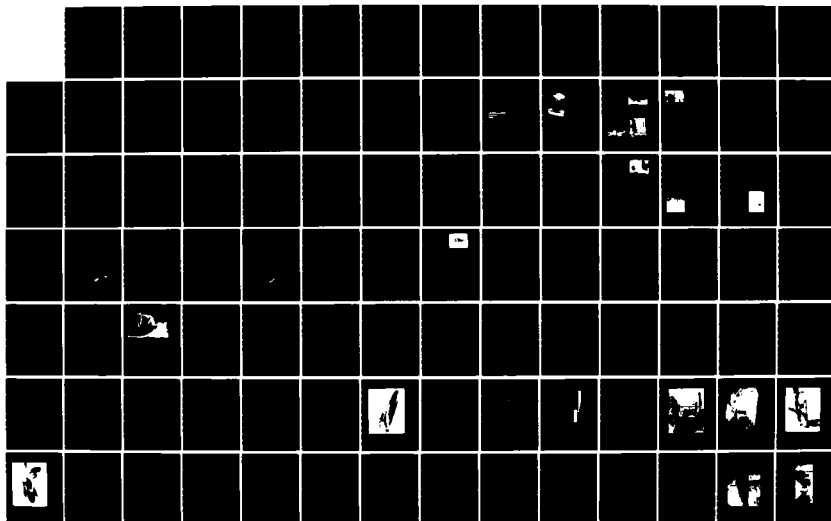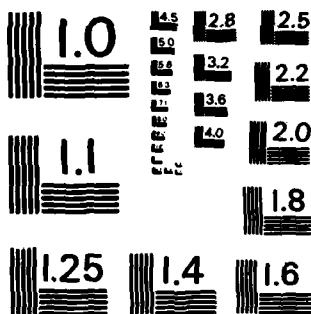
MICROCOPY RESOLUTION TEST CHART
NATIONAL BUREAU OF STANDARDS-1963-A

particular waveform illustrated in Fig. 13 is referred to as a ZERD pulse (see Appendix C), and we have found it very useful for the simulation of "damped-sine-like" field transients because its definition is similar to that of the damped sine and because, unlike a classical damped sine, the first and second integrals have a zero residual value.

Random-Vibration Control

The algorithm for random-vibration control has various features in common with transient waveform and swept-sine control:

● A low-level pretest is used to identify the system dynamics and determine the compensation matrix.

● The actuators may be controlled individually with or without cross-coupling compensation, or from a simultaneous average of readings from up to four accelerometers.

● Cross-coupling compensation is performed open-loop and remains constant during execution of a test.

● The response or command auto spectral densities (ASD's) and average g_{rms} are displayed in real time.
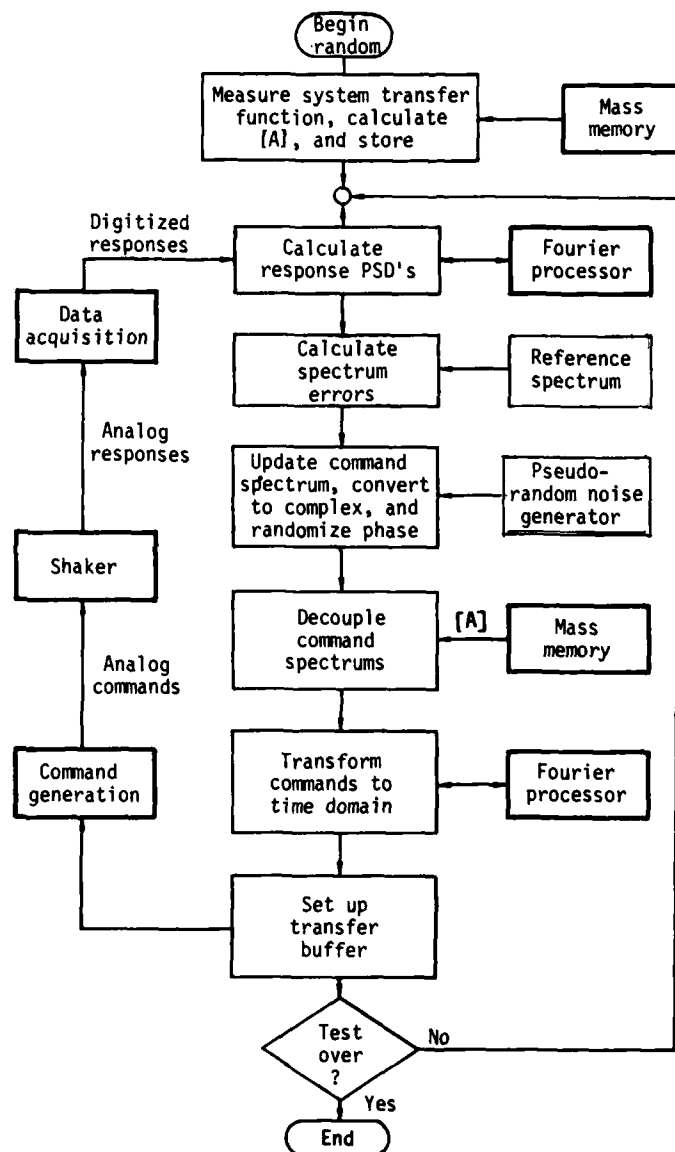
Fig. 14 - Flowchart of random-vibration control algorithm

Identification is accomplished via a series of low-level pulses as in transient-waveform control, except that here the waveform of the identification pulse is derived from the desired or reference ASD spectrum. The peak value of the identification pulse is set equal to the g_{rms} of the full-level test. The resulting compensation matrix [A] and coherence-function matrix [γ] are stored on a random-access disk memory for rapid retrieval during actual testing.

The algorithm for controlling random vibration, flow-charted in Fig. 14, is a continuous, closed-loop procedure similar to that of swept-sine control. The DAU samples the responses synchronously with the command-generation hardware and inputs the digitized acceleration values directly into CPU memory a frame at a time. The hardware Fourier processor demultiplexes the data, computes the ASD's, and returns the results in a floating-point format. As has been described in the literature for random-vibration control in single-actuator systems [5], the command power spectrums for each actuator are updated by comparing the response ASD's with the reference ASD and invoking a simple direct-digital-control algorithm.

To generate the time-domain command waveforms, the updated command ASD's must be converted to a complex Fourier spectrum in which the relative phase of each spectral line has been randomized. However, to maintain synchronous motion of the actuators, the phase of a given spectral line must be the same for each actuator. To satisfy both these requirements at once, the algorithm generates an integer array of pseudo-random numbers IRAN, one element for each spectral line, at the beginning of each pass through the control loop (see Fig. 15). Then the computer calculates the complex command Fourier spectrum of actuator I by multiplying each line of the command auto spectrum CASD (K,I) by an element of the array CVECT, which has been randomly accessed via the integer index IRAN (K). The array CVECT is an array of complex unit vectors, having a uniform phase distribution over $\pm$ π radians. The maximum possible value in the array IRAN must equal the number of elements in CVECT. The net result is that the command Fourier spectra are randomized but phase correspondence is maintained between the actuators.

The command Fourier spectra are decoupled through use of the compensation and coherence matrices retrieved from mass memory. Since each pass through the control loop is equivalent to generation of the first full-level transient in transient-waveform control, the iterative-search procedure previously described cannot be

Initialize
array IRAN
(NLINE = number of
spectral lines)

Convert to complex
and randomize the
phase of each spectral
line of the command
spectrum for each
actuator
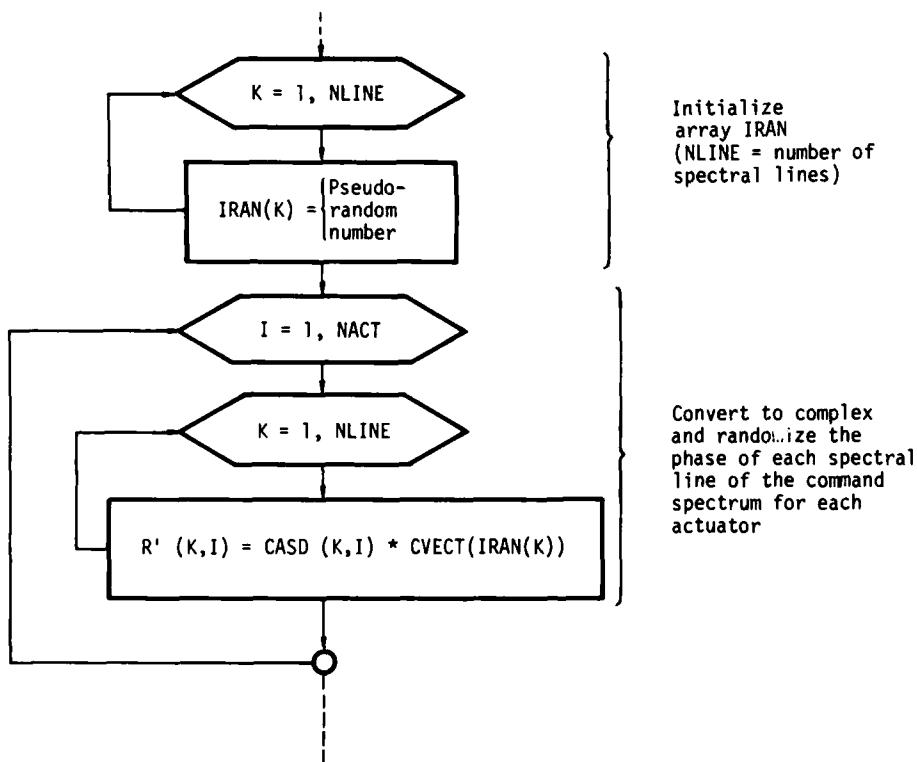
Fig. 15 - Fortran flow diagram showing details of phase-randomization procedure; NACT is the number of actuators

90

applied. We have found it beneficial, however, to "turn-off" cross-coupling compensation for the spectral lines in which the corresponding coherence is low. As in transient-waveform control, the coherence arrays are addressed by transposing the row-column indices. The resulting complex command arrays are inverse transformed back to the time domain and the command-generation hardware is switched to the new commands through a transfer-buffer setup to form a smooth transition between the old and new commands.

One objective in implementing the random-vibration-control algorithm was to optimize the execution speed within the memory-size limitations of the CPU. This optimization is accomplished in various ways. The compensation array is stored on disc and brought into CPU memory one column at a time. The algorithm hides disc-access time by initiating a direct-memory-access READ request before the array is really needed, then carrying out other calculations in parallel with the transfer. Since only a fraction of the Fourier processor's 8 k-word memory is needed for spectral processing, the remainder is used as a large, quick-access scratch pad during certain array calculations. Also, many arrays that are needed only briefly in the algorithm, for instance the transfer buffer used to switch from one frame of commands to another, are stored in the same memory area by use of the Fortran EQUIVALENCE statement.

The control algorithm also shares CPU execution time and memory with a second task responsible for interrogating the operator's console and updating the ASD display on the CRT. To conserve space, we have the plotting arrays shared in GLOBAL common with the control algorithm. Also, the plotting task runs periodically (once every 3 s) and at a low priority so that it executes on time relinquished by the control task during direct-memory-access transfers and other input/output operations.

Our experience with the random-vibration-control algorithm has been limited to one- and two-actuator tests. The results to date (see Fig. 16), tend to verify the effectiveness of the algorithm.

SUMMARY

A digital control system has been developed for the LLL multiple-actuator electrohydraulic-shaker facility. The system is capable of conducting swept-sine, transient-waveform, and random-vibration tests over a nominal frequency range of dc to 500 Hz, up to 50 g in acceleration, and with a maximum force of 0.62 MN. The control algorithms correct for cross-coupling by means of a compensation matrix determined through experimental identification of the system-transfer function. Experimental data demonstrate the effectiveness of the algorithms.
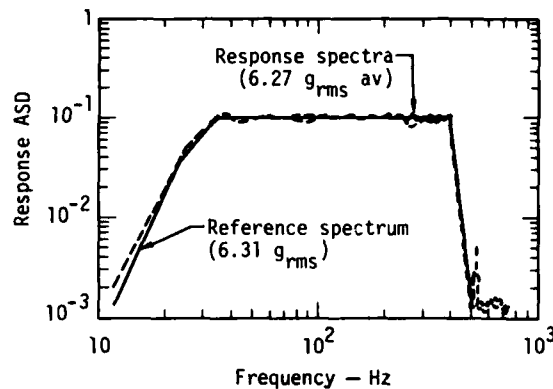
Fig. 16 - Typical results for a two-actuator random-vibration test

APPENDIX A. DIGITAL-FOURIER FILTERING TECHNIQUE FOR CO/QUAD ANALYSIS OF SINE DATA

In this Appendix we describe a digital-Fourier filtering technique for estimating the coincident and quadrature components of sinusoidal response data [9]. These components are defined as follows: For a sinusoidal response of the form

$$x(t) = X \sin (\omega t + \phi) , \qquad (A1)$$

We substitute the identity

$$\sin (\alpha + \beta) = \sin \alpha \cos \beta + \cos \beta \sin \alpha \qquad (A2)$$

to get

$$x(t) = CO \cdot \sin \omega t + QUAD \cdot \cos \omega t,$$

where

$$CO = X \cos \phi \text{ (coincident component)},$$
$$QUAD = X \sin \phi \text{ (quadrature component)}.$$

The filtering technique is suitable for on-line control and off-line data reduction. The theory will be developed first for continuous-time systems, then extended to sampled-data systems.

Let us consider the physical system of Fig. A-1 in which $x(t)$ is the response of a dynamic system to a sinusoidal driving function. Because of nonlinearities, resonances, electronic noise, etc., the response $x(t)$ will in general consist of a fundamental component, harmonics, and broadband noise:

$$x(t) = X_1 \sin (\omega t + \phi_1)$$
$$+ X_2 \sin (2 \omega t + \phi_2) + \ldots$$
$$+ X_n \sin (n\omega t + \phi_n) + N(t). \qquad (A3)$$

91
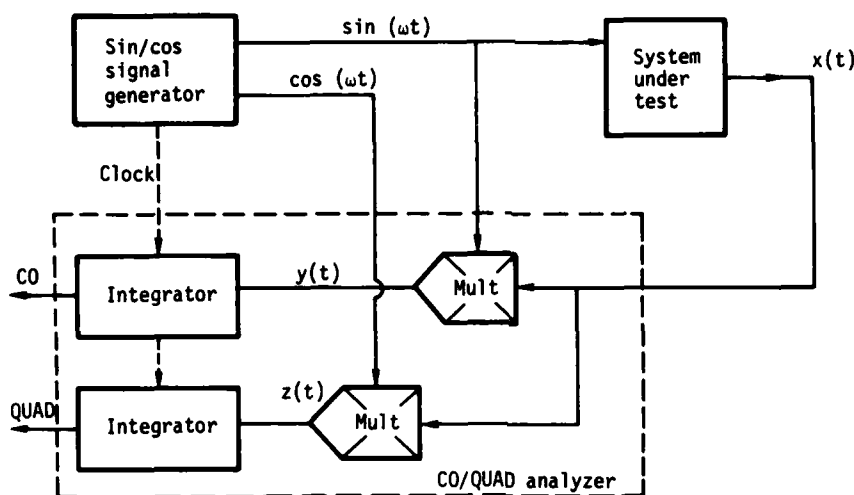
Fig. A-1 - Analog CO/QUAD analyzer

If $x(t)$ is multiplied by the sine reference, we get

$$y(t) = (\sin \omega t) \, [x(t)]$$

$$= X_1 \sin \omega t \sin (\omega t + \phi_1)$$

$$+ X_2 \sin \omega t \sin (2\omega t + \phi_2)$$

$$+ \ldots + X_n \sin \omega t \sin (2\omega t + \phi_n)$$

$$+ \sin \omega t N(t).$$

By introducing the trigonometric identity $\sin \alpha \cos \beta = \frac{1}{2}[\cos (\alpha - \beta) - \cos (\alpha + \beta)]$ and integrating over M full cycles, we obtain

$$Y = \int_0^{MT} y(t) dt$$

$$= \int_0^{MT} \left(\frac{X_1}{2} \, [\cos (-\phi_1) - \cos (2\omega t + \phi_1)] \right.$$

$$+ \frac{X_2}{2} \, [\cos (-\omega t - \phi_2) - \cos (3\omega t + \phi_2)] + \ldots$$

$$+ \frac{X_n}{2} \, \{\cos [(-n + 1)\omega t - \phi_n]$$

$$\left. - \cos [(n + 1)\omega t + \phi_n]\}\right) dt$$

$$+ \int_0^{MT} \sin \omega t \, N(t) dt, \qquad (A4)$$

where

$$T = 2\pi/\omega. \qquad (A5)$$

In evaluating the integrals, we first must recognize that any term of the form $\cos(n\omega t + \phi)$ yields zero when integrated over any number of full cycles. Secondly, to evaluate the noise term we must make some assumption as to the nature of $N(t)$. If we assume $N(t)$ is a sinusoid of frequency ω_N and amplitude N_1,

$$N(t) = N_1 \sin (\omega_N t + \theta_N), \qquad (A6)$$

we can show that in the worst case

$$\left| \int_0^{MT} \sin \omega t N(t) dt \right| = MT \, E_N/2 \, ,$$

where

$$E_N = \left| \frac{2N_1 (\omega_N/\omega)}{\pi M \left[1 - (\omega_N/\omega)^2\right]} \sin (\pi M \omega_N/\omega) \right|$$

$$\text{when } \left(\frac{\omega_N}{\omega}\right) > 1, \qquad (A7)$$

or

$$E_N = \left| \frac{2N_1}{\pi M \left[1 - (\omega_N/\omega)^2\right]} \sin (\pi M \omega_N/\omega) \right|$$

$$\text{when } \left(\frac{\omega_N}{\omega}\right) \leq 1 \, . \qquad (A8)$$

Thus, from Eq. (A4),

$$CO = X_1 \cos \phi_1 = \frac{2Y}{MT} + E_N \, . \qquad (A9)$$

92

By a similar procedure, if x(t) is multiplied by the cosine reference and integrated over M cycles, we obtain the result

$$QUAD = X_1 \sin \phi_1 = \frac{2Z}{MT} + E_N , \qquad (A10)$$

where

$$Z = \int_0^{MT} z(t) \, dt = \int_0^{MT} \cos \omega t \; x(t) \, dt. \qquad (A11)$$

Thus it can be seen that the continuous Fourier filter, computed over M full cycles, has perfect rejection of harmonics and a worst-case CO or QUAD error due to broadband noise as shown in Fig. A-2.

To convert the preceding formulation to sampled-data form, the CO/QUAD analyzer of Fig. A-1 must be provided with synchronous samplers as shown in Fig. A-3. If the samplers are clocked to sample exactly K times per cycle, Eqs. (A4) and (A11) are approximated by

$$Y^* = \frac{T}{K} \sum_{k=1}^{MK} y^*(k) = \frac{T}{K} \sum_{k=1}^{MK} x^*(k) \sin^* (k), \quad (A12)$$

where

$$x^*(k) = \text{sampled value of } x(t),$$
$$\sin^* (k) = \text{sampled value of } \sin \omega t;$$

and

$$Z^* = \frac{T}{K} \sum_{k=1}^{MK} z^*(k) = \frac{T}{K} \sum_{k=1}^{MK} x^*(k) \cos^* (k). \quad (A13)$$

Here, $\cos^* (k) = $ sampled value of $\cos \omega t$ and the coincident and quadrature components of the sampled data are calculated as

$$CO^* = \frac{2Y^*}{MT} = \frac{2}{MK} \sum_{k=1}^{MK} x^*(k) \cos^* (k), \qquad (A14)$$

and

$$QUAD^* = \frac{2Z^*}{MT} = \frac{2}{MK} \sum_{k=1}^{MK} x^*(k) \sin^* (k). \qquad (A15)$$

Introducing sampling imposes certain restrictions on the harmonic-rejection properties of the Fourier filter. In particular, to avoid
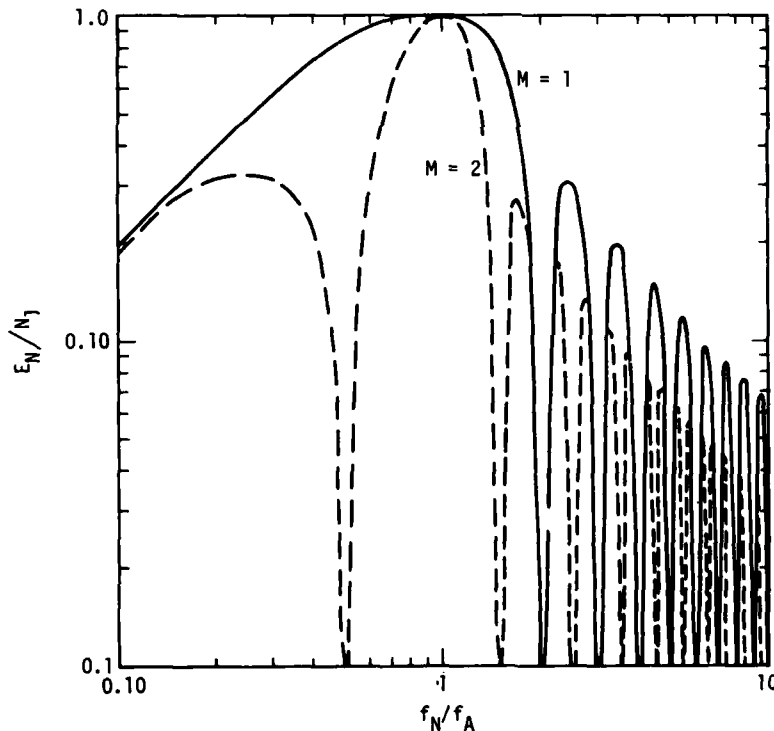
Fig. A-2 — Theoretical vector error E_N for sinusoidal noise of amplitude N_1, frequency f_N, analyzed at frequency f_A
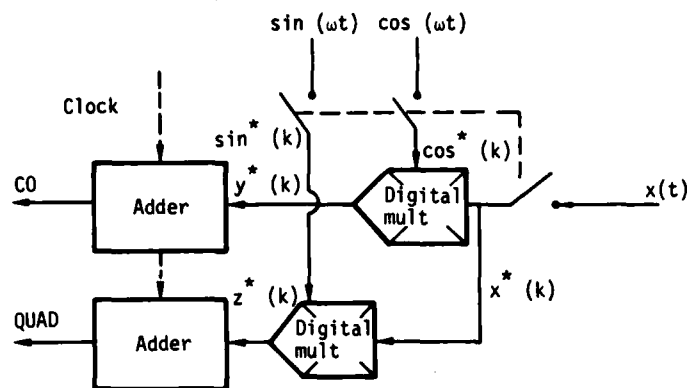
Fig. A-3 - Digital implementation of CO/QUAD analyzer

aliasing errors, the response signal $x(t)$ must be bandwidth-limited to $(\omega K/4\pi)$ Hz.

The digital CO/QUAD analyzer is easily implemented in either hardware or software. In the LLL shaker-control system, the cos* (k) and sin* (k) references are generated in digital form by the digital-waveform synthesizer, and x*(k) is sampled synchronously. The multiplication, summation, and scaling are carried out digitally four channels at a time in the DAU hardware. Because of limited processing speed in the hardware, K varies from 512 at frequencies below 64 Hz to 16 at 2048 Hz, while M is adjusted to keep the product MK = 512. Thus the noise-rejection characteristics vary with the analysis frequency as shown in Fig. 7 of the text.

Equations (A14) and (A15) are also easily implemented in software. The reference waveforms sin* (k) and cos* (k) take the form of a table of K values, and the data to be analyzed is sampled to give K samples per cycle. The multiplication, summation, and scaling are easily implemented in software to process the data in frames of MK points at a time. Unless the data sampling is phase-locked to the fundamental data frequency, one of the data channels being processed must serve as a phase reference. For each analysis, the computed CO/QUAD vector is rotated towards zero by an amount equal to the phase of the reference channel.

APPENDIX B. TRANSIENT ITERATION PROCEDURE

In this appendix we show that the transient iteration procedure is similar to a convergent scheme for the iterative solution of a set of simultaneous nonlinear equations.

To understand the iteration scheme, first consider a very simple control problem where Y is a scalar output related to a scalar input X by the nonlinear function

$$Y = \phi(X) . \tag{B1}$$

If we want Y to equal some value r, then we must find the proper value for X. This is similar to the transient control problem if X is the shaker input and r is the desired response. Finding the proper value of X is equivalent to iteratively solving the transcendental equation

$$f(X) = 0, \tag{B2}$$

where

$$f(x) = r - \phi(X). \tag{B3}$$

An iteration of the form

$$X_{i+1} = \phi(X_i) \tag{B4}$$

will converge [10] if

$$\left|\frac{d}{dX} \phi(X)\right| \le 1 . \tag{B5}$$

For example, the iteration

$$X_{i+1} = X_i + a[r - \phi(X_i)] \tag{B6}$$

will converge if

$$\left|1 - a \frac{d}{dX} \phi(X)\right|_{X-X_i} \le 1 . \tag{B7}$$

or, equivalently,

$$0 \le a \le \left[\frac{d}{dX} \phi(X)\right]^{-1}_{X=X_i} . \tag{B8}$$

The term inside the brackets of (B8) is the slope of Eq. (B1) evaluated at the last iteration. For a nearly linear function, the slope can be approximated by the ratio of the last pair of values (X_i, Y_i):

$$\left[\frac{d}{dX} \phi(X)\right]_{X=X_i} \approx \frac{Y_i}{X_i} . \tag{B9}$$

94

Likewise, it can be shown that if X and Y are vectors related by a nonlinear vector function, then a convergent iteration is

$$X_{i+1} = X_i - J^{-1}\{f(X_i)\}f(X_i), \qquad (B10)$$

where $J^{-1}\{f(X_i)\}$ is the inverse of the Jacobian matrix of $f(X)$ evaluated at $X = X_i$.

The transient-control iteration is motivated by Eq. (B10). The finite Fourier transforms of the transient waveforms result in M complex Fourier coefficients, which correspond to frequencies B Hz apart, i.e.

$$C(\omega) = \{C(kB); k = 1,M\} \qquad (B11)$$

or

$$c^k \triangleq C(\omega)|_{\omega=kB} .$$

Now at each frequency $\omega = kB$ the response-spectrum coefficients can be thought of as non-linear functions of the command-spectrum coefficients:

$$c^k = \phi(R^k); \quad k = 1, \ldots M , \qquad (B12)$$

where c^k and R^k are N-dimensional vectors of complex numbers and N is the number of actuators. Producing the desired response on the shaker is equivalent to solving the equation

$$f(R^k) = \hat{c}^k - \phi(R^k) = 0, \qquad (B13)$$

where $\hat{c}^k$ is the desired response vector at $\omega = kB$. To use the iteration (B10) to solve (B13), the Jacobian of (B13) must be evaluated after each iteration. Although this cannot be done for multiple actuators, the Jacobian can be approximated from the transfer function measured at a low level.

$$J\big(f(R^k)\big) = J\{\hat{c}^k - \phi(R^k)\} \approx -G^k . \qquad (B14)$$

This approximation combined with (B10) suggests the following transient-control iteration:

$$R_{i+1}^k = R_L^k + [G^k]^{-1} \{\hat{c}^k - c_i^k\} . \qquad (B15)$$

Unfortunately, we cannot mathematically prove that Eq. (B15) will converge for a multiple-actuator hydraulic shaker. The combination with Eq. (B10) holds for amplitude nonlinearities but not for nonlinearities due to harmonic distortion; moreover, Eq. (B10) requires the transfer function to be evaluated for each iteration. Equation (21) (see text) is Eq. (B10) adapted to transient-waveform control with two features introduced to make the iteration practical. First, a gain K is introduced to prevent overcorrection. Second, each element of the inverse transfer function can be checked for validity by inspection of its corresponding coherence. If the coherence is not high enough, then the correction is not made.

APPENDIX C. DEFINITION AND PROPERTIES OF THE ZERD FUNCTION

Many transient-waveform vibration tests call for the generation of damped-sine-like accelera-tion pulses, either singly or in combination to match a specified shock-response spectrum. The classical damped sine:

$$a(t) = Ae^{-\delta\omega_n t} \sin \omega_n t \qquad (C1)$$

is difficult to reproduce on vibration shakers because it contains a nonzero dc component, resulting in a steady-state velocity and ex-ponentially increasing displacement.

We have found useful the simply defined ZERD (zero residual displacement) waveform:

$$ZERD(t) = Ae^{-\delta\omega nt}\left[\frac{1}{\omega_n} \sin \omega_n t - t \cos (\omega_n t + \phi)\right],$$

where

$$\phi = \tan^{-1}\left[\frac{-2\delta}{\delta^2 - 1}\right] \qquad (C2)$$

The ZERD pulse resembles a damped sine (see Fig. C-1) but has first and second integrals having zero final value. This is easily demonstrated in the Laplace domain, where

$$\mathscr{L}[ZERD(t)] = \frac{2As^2}{(1 + \delta^2)\left\{(s + \delta\omega_n)^2 + \omega_n^2\right\}^2} , (C3)$$

and s is the Laplace variable. Integration in the time domain is equivalent to division by s in the s-domain, thus the first integral is
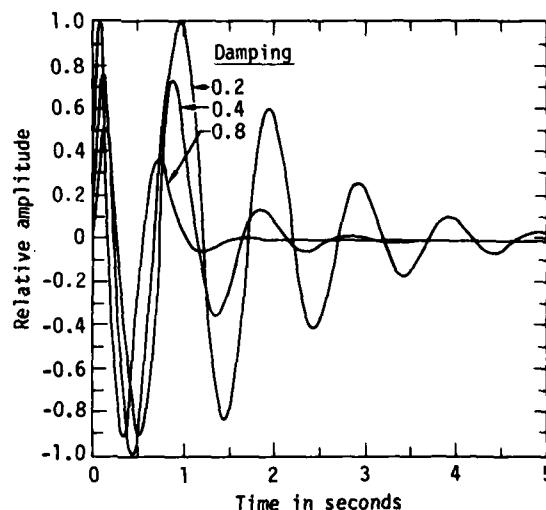
Fig. C-1 - A family of ZERD pulses, A = 1.0, ω_n = 2 π

95

$$\mathscr{L}\left[\int_0^t \text{ZERD}(t)\ dt\right]$$

$$= \frac{2As}{(1 + \delta^2)\left\{(s + \delta\omega_n)^2 + \omega_n^2\right\}^2}\ , \quad \text{(C4)}$$

which in the time domain has a steady-state value of

$$\mathscr{L}\lim_{t\to\infty}\left\{\int_0^t \text{ZERD}(t)\ dt\right\}$$

$$= \lim_{s\to 0} s\left\{\frac{2As}{(1 + \delta^2)\left\{(s + \delta\omega_n)^2 + \omega_n^2\right\}^2}\right\}$$

$$= 0\ . \quad\quad\quad\quad\quad\quad\quad\quad\quad\quad\quad \text{(C5)}$$

Similarly, the second integral of Eq. (C1) is

$$\mathscr{L}\left[\int_0^t \int_0^t \text{ZERD}(t)\ dt\ dt\right]$$

$$= \frac{2A}{(1 + \delta^2)\left\{(s + \delta\omega_n)^2 + \omega_n^2\right\}^2}\ , \quad \text{(C6)}$$

which also has a zero steady-state value:

$$\mathscr{L}\lim_{t\to\infty}\left\{\int_0^t \int_0^t \text{ZERD}(t)\ dt\ dt\right\}$$

$$= \lim_{s\to 0} s\left\{\frac{2A}{(1 + \delta^2)\left\{(s + \delta\omega_n)^2 + \omega_n^2\right\}^2}\right\} = 0.$$

REFERENCES

1. D. K. Fisher, "Theoretical and Practical Aspects of Multiple-Actuator Shaker Control," 43rd Shock and Vibration Bull., Pt. 3, pp. 153-74, June 1973

2. J. D. Newton, "Methods of Control of Multiple Shaker Testing System," 35th Shock and Vibration Bull., Pt. 2, pp. 85-96, Jan. 1966

3. W. E. Hunter, J. G. Helmuth, "Control Stabilization for Multiple Shaker Tests," 37th Shock and Vibration Bull., Pt. 3, pp. 155-62, Jan. 1968

4. C. R. Trubert, "An Analog Technique for the Equalization of Multiple Electromagnetic Shakers for Vibration Testing," J. Spacecr. Rockets, Vol. 5, No. 12, pp. 1438-43, Dec. 1968

5. C. P. Chapman, "Digital Vibration Control Techniques," Proc. Seminar on Understanding Digital Control and Analysis in Vibration Test Systems, U.S. Naval Shock and Vibration Information Center, pp. 71, June 1975

6. J. D. Favour, "Transient Waveform Control — A Review of Current Techniques," J. Environ. Sci., Vol. 17, No. 6, pp. 9-19, Nov./Dec. 1974

7. G. C. Kao, "Testing Techniques for Simulating Earthquake Motion," J. Environ. Sci., Vol. 18, No. 2, pp. 22-40, Mar./Apr. 1975

8. R. A. Lund, "Environmental Simulation with Digitally Controlled Servo-Hydraulics," 1976 Proc. Inst. Environ. Sci., pp. 65-70, April 1976

9. A. Fuchs, "Low Frequency Real Time Measurement of Mechanical Impedance," 1972 Proc. Inst. Environ. Sci., pp. 440-7, May 1972

10. I. S. Berezin, N. P. Zhedkov, Computer Methods, Vol II, Translated by O. M. Blunn, p. 679, Addison-Wesley, Reading, Mass., 1965

INSTRUMENTATION AND DATA ANALYSIS

MEASUREMENT OF ANGULAR

VIBRATION USING CONVENTIONAL ACCELEROMETERS

P. Wayne Whaley and Michael W. Obal

Air Force Flight Dynamics Laboratory

Wright-Patterson AFB, Ohio 45433

A method is presented for measuring angular vibrations of aircraft
structures using linear accelerometers. A rotary shaker system was
used to examine low frequency noise and a beam experiment was con-
ducted to examine high frequency flexure. The result is that one
may tailor this method to fit a particular application. For Signal-
to-Noise ratios of 5 or 10, angular vibrations of 2μrad at frequen-
cies down to 50 hz can be readily measured for a typical structure.
By specifying that the separation distance be less than one-third of
a wavelength of the bending traveling wave of the structure, the
maximum measurable frequency can be determined.

INTRODUCTION

The performance of airborne electro-
optical systems is seriously effected by the
angular (rotary) as well as the linear (trans-
verse) airframe vibrations. The angular vibra-
tion response is defined as the slope of the
transverse deflection. Unlike linear vibra-
tions, very little is known about the angular
vibrations of aircraft structures and the
design of airborne electro-optical equipment
requires knowledge of the angular vibration
response characteristics.

A technique for predicting angular vibra-
tion from linear vibration data was recently
published [1]. This type of prediction scheme
is a promising approach since the establishment
of an angular vibration data bank is costly and
there are no suitable angular transducers for
such a program. However, the lack of trans-
ducers also hampers the validation of predic-
tion schemes, so this work was undertaken to
examine the measurement of angular vibration
using conventional accelerometers.

A practical means for measuring angular
vibration is to place two linear transducers
some distance apart, subtract the outputs and
divide the difference by the separation dis-
tance. The separation distance selection is an
important consideration; a separation distance
which is too small can result in a difference
signal which is close to the transducer noise
floor; on the other hand, separation distance

should be chosen as small as possible to give
the best approximation to the transverse de-
flection slope. In addition, the signal-to-
noise ratio (S/N) of acceleration signals are
lower at low frequencies, therefore a small
separation distance further deteriorates the
low frequency response. The angle approximated
by accelerometer differencing is proportional
to the inverse of the separation distance, so
the larger the separation distance the higher
the S/N. Thus, consideration of low frequency
response and S/N yields a lower limit for
separation distance. This is discussed in the
noise considerations section.

Separation distance should be as large as
possible for sensitivity purposes, but at some
frequency and separation distance, the error
due to flexure between accelerometers begins to
be important. This flexural error may be de-
fined in terms of number of nodes between
accelerometers. However, node locations or
spacings on a vibrating airframe are seldom
known, so a different criteria is formulated
here. By considering the speed of a bending
traveling wave of a structure, it is possible
to define a wavelength which is a function of
frequency and structural properties [2]. This
wavelength relates to the node points on the
structure in that standing waves form at the
natural frequencies, giving rise to node
points. Therefore by choosing separation dis-
tance as some fraction of a wavelength at the

desired upper frequency limit, one may be assured of acceptable flexural error. The rationale for deciding on the fraction of a wavelength to use is given in the flexural error section.

The acceptable limits of separation distance may be identified for a particular application using this technique. This range provides some flexibility for integration of the accelerometer locations into the hardware constraints. In this manner a method is presented for measuring angular vibrations which can supply useful data until acceptable broadband angular transducers become available.

NOISE CONSIDERATIONS

The technique for measuring angular vibration using linear accelerometers is based on Eq.(1), where Δy is the difference between zero-to-peak amplitudes of two accelerometers.

$$\theta \simeq \frac{\Delta y}{\Delta x} \qquad (1)$$

θ = true angle
Δy = differential linear displacement
Δx = separation distance.

The lower limit for Δx based on low frequency sensitivity and S/N was examined for a wide variety of separation distances at angular levels. A rotary shaker system was used for these studies which implemented a very stiff rotary platform, thereby minimizing flexure between accelerometers. In this manner only the noise consideration is examined.

A low-powered laser with a system of mirrors and a quad cell detector provided an independent angular measurement. (See Fig.1). The mirrors m_2 and m_3 fold back the laser beam twice to increase the effective distance between the rotary shaker platform and the quad detector. This increase in distance improves the sensitivity of the measurement system, as shown by the following sensitivity equation.

$$\frac{E_o}{\theta} = 2 \, (L_1 + L_2 + L_3) \, S_d \qquad (2)$$

E_o = detector output voltage

θ = angle of shaker platform

S_d = detector sensitivity in volts/mm

L_1 = distance between m_1 and m_2

L_2 = distance between m_2 and m_3

L_3 = distance between m_3 and quad detector.

The compressor circuit in Fig.1 was included to provide a constant angular input as the frequency was varied. Since the detector signal was noisy at low angular levels an amplifier and tracking filter were required between the detector electronics and the compressor circuit. Using this rotary shaker system, angular levels as low as $2\mu rad$ were measured consistently.

For two accelerometers separated by Δx, the angular vibration about a point halfway between them may be approximated by Eq.(1). This relationship will be exact when there is no flexure between the two points or in the limit as $\Delta x \to 0$. However, as Δx decreases, the difference between the two accelerometer signals becomes contaminated with the internal noise of the accelerometers. Therefore the selection of Δx depends on desired low frequency response and sensitivity, and S/N. Angular vibration was measured using Eq.(1) and compared with results using the shaker platform of Fig.1. The relationship between the differential angular acceleration and the true angle for random noise using the Fast Fourier Transform is

$$\frac{\Delta \ddot{y}}{\Delta x} \frac{1}{\omega^2} = \theta. \qquad (3)$$

A typical commercially available accelerometer has a noise floor of $.0015 g_{rms}$. Substituting that number as Δy and including S/N, Eq.(3) may be rewritten as

$$f^2 \theta \Delta x = .029 \; S/N . \qquad (4)$$

Eq.(4) is plotted in Fig.2 for a S/N of 5 and 10, along with data from two different sets of accelerometers. Notice that for low angular levels and low frequencies, the larger the Δx the higher the S/N. For example, to measure $2\mu rad$ at 50 hz with a S/N of 5 requires a Δx of 42.5 inches, or to measure $4\mu rad$ at 50 hz with S/N of 5 requires a Δx of 21.25 inches ($2\mu rad \times 42.5$ inches = $85\mu rad$-inch).

In order to demonstrate the effects of small Δx on sensitivity, Eq.(3) may be written in a slightly different form.

$$\frac{\Delta \ddot{y}}{\theta} = \omega^2 \Delta x \qquad (5)$$

This equation was plotted along with data for varying Δx and is shown in Fig.3. For $\Delta x = 1/4''$, $\Delta \ddot{y}/\theta$ becomes larger than the theory at low frequencies, indicating that noise affects the performance. The 60 hz electrical noise peak was still present for $\Delta x = 1/2$ inches, although less prominent, but the effect of other noise contributions remains about the same; for $\Delta x = 2$ inches the noise was negligible. Doubling Δx increases $\Delta \ddot{y}/\theta$ by 6 db, and for these experiments it appeared that $\Delta x = 2''$ was about the best choice, with increases of Δx up to 5'' having limited improvements. Another way to improve S/N is to integrate the acceleration signal to give velocity. The counterpart of Eq.(4) for velocity is

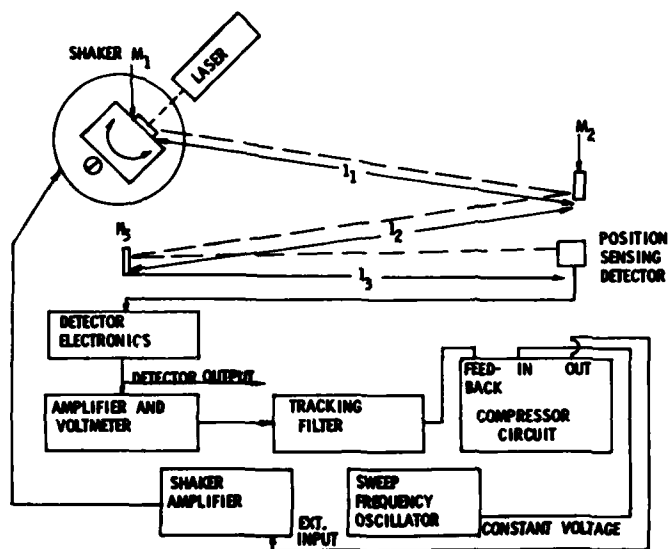$$f \theta \Delta x = 4.67 \times 10^{-5} \; S/N . \qquad (6)$$

98

Fig. 1 - Rotary shaker system used in evaluating
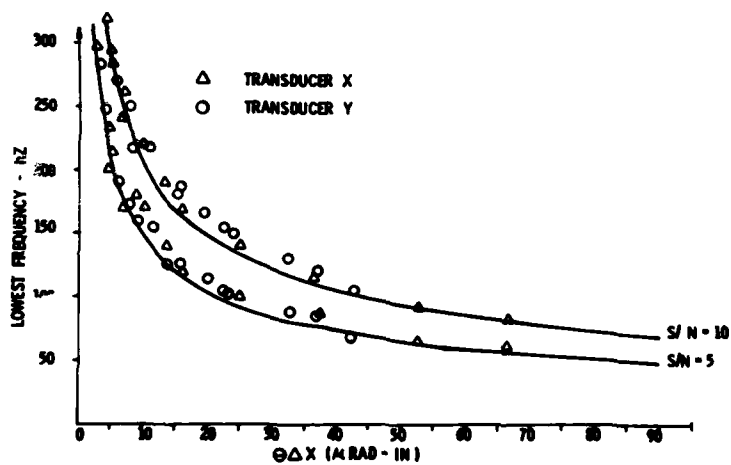angular vibration measurement techniques.

Fig. 2 - Noise floor for two accelerometers used in
measuring angular vibration.
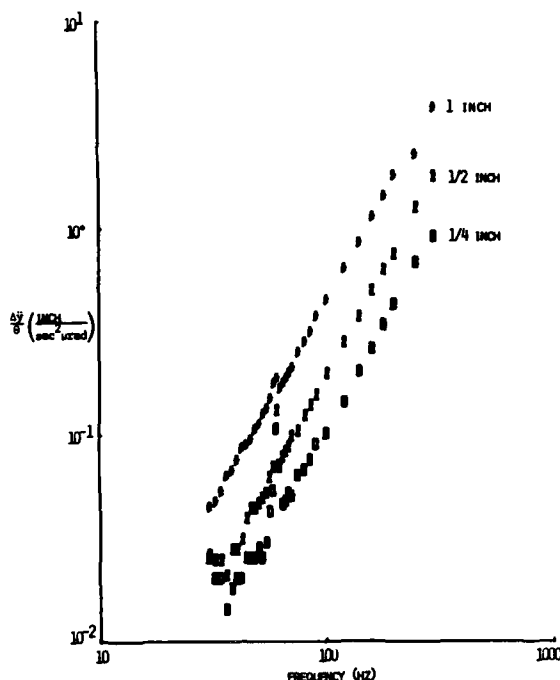
Fig. 3 - Angular acceleration frequency response for differential accelerometers using the rotary shaker system of Figure 1.

Eq. (6) is plotted in Fig. 4, along with typical data. For $\theta = 2\mu$rad with $f = 50$ hz, $\Delta x = 42.5$, S/N = 10, while for acceleration it was 5. For velocity, the counterpart of Eq. (5) is

$$\frac{\Delta \dot{y}}{\theta} = \omega \Delta x \ . \qquad (7)$$

This equation was plotted for varying Δx and is shown in Fig. 5. The sensitivity at low frequency was higher than for acceleration. Also the low frequency signal for velocity was less noisy than for acceleration. This is because the analog computer integrator has unity gain at around 100 hz; therefore, frequencies below 100 hz are amplified and the low frequency sensitivity is better. The other benefit of integrating is a 20 db improvement of dynamic range for every frequency decade.

To summarize, at a given frequency, as separation distance decreases the signal-to-noise ratio decreases. The trade-off is that as separation distance decreases at a given signal-to-noise ratio, the lower frequency limit increases. For a particular application the lower limit of separation distance will depend on the desired low frequency limit and

the required signal-to-noise ratio. Therefore with a signal-to-noise ratio of between 5 and 10 it is possible to measure angles on the order of 5μrad down to about 50 hz with a lower limit of separation distance from 2 to 5 inches.

FLEXURAL ERROR

Angular vibration information is needed for arbitrary aircraft structures, so the concept of flexural error must be addressed in those terms. Since optical components are typically mounted on major structural components (bulkheads, spars, stringers, etc.) rather than on panels or skin structure, a beam analysis can provide qualitative flexural error insight. Therefore the rest of this section describes a simply supported beam excited with broadband random noise at mid-span.

For a uniform simply supported beam under constant amplitude forcing at mid-span, the Fourier Transform of the transverse deflection is

$$y(x,\omega) = \sum_{n=1}^{\infty} \frac{P\ell}{2m} H_n(\omega) \ \sin \frac{n\pi x}{\ell} \qquad (8)$$

P = magnitude of forcing function

ℓ = beam length

m = mass/unit length of the beam

$H_n(\omega)$ = Frequency response function = $\dfrac{1}{\omega_n^2 - \omega^2 + j\gamma}$

γ = structural damping constant

ω_n = beam natural frequency = $\left(\dfrac{n\pi}{\ell}\right)^2 \sqrt{EI/m}$

ω = frequency in radians/sec

E = Youngs modulus

I = beam cross section moment of inertia

The Fourier Transform of the angular deflection is found by differentiating Eq. (8) to get

$$\frac{\partial y}{\partial x}(x,\omega) = \Theta(x,\omega) = \qquad (9)$$
$$\sum_{n=1}^{\infty} \frac{n\pi}{\ell} \ \cos \frac{n\pi x}{\ell} \ \frac{P\ell}{2m} \ H_n(\omega) \ .$$

(For a complete derivation see [1]). The differential angle defined in Eq.(1) may be calculated for two transducers located at x_1 and using x_2 using Eq.(8).

$$\frac{\Delta y}{\Delta x}(x_1, x_2, \omega) = \sum_{n=1}^{\infty} \frac{P\ell}{2m} H_n(\omega) \ [\sin \frac{n\pi x_1}{\ell} - \sin \frac{n\pi x_2}{\ell}]$$

100
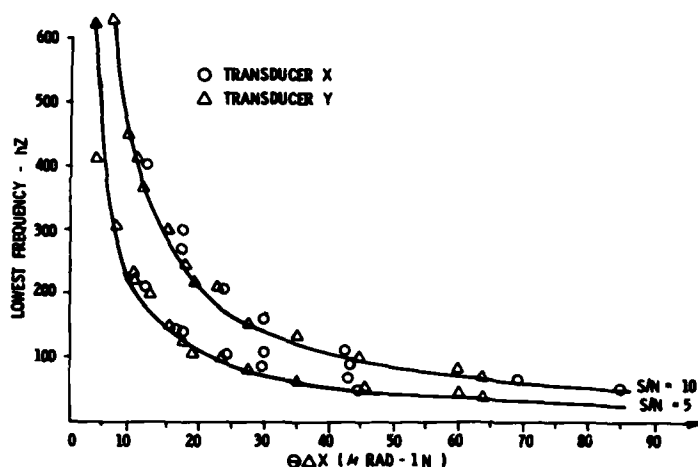
Fig. 4 - Noise floor of two accelerometers used in measuring angular vibration which have been integrated to give velocity.

By defining

x_c = the point where angular response is desired,

Δx = separation distance,

$x_1 = x_c - \frac{\Delta x}{2}$,

$x_2 = x_c + \frac{\Delta x}{2}$,

and utilizing a simple trigonometric identity, this may be rewritten as

$$\frac{\Delta y}{\Delta x} (x_c, \Delta x, \omega) = \qquad (10)$$

$$\frac{1}{\Delta x} \sum_{n=1}^{\infty} \frac{P_n}{2m} H_n(\omega) \cos \frac{n\pi x_c}{\ell} \sin \frac{n\pi \Delta x}{2\ell} .$$

From Eq.(10) it is seen that the differential angle is a function of x_c, Δx and ω. Also notice that in the limit as Δx goes to zero, Eq.(10) becomes Eq.(9). By using Eqs.(9) and (10), flexural error may be calculated using the definition given below.

$$\epsilon = \frac{|\Theta(x_c, \omega)| - |\frac{\Delta y}{\Delta x}(x_c, \Delta x, \omega)|}{|\Theta(x_c, \omega)|} \qquad (11)$$

From Eq.(11) it is seen that although flexural error depends on x_c, Δx, and ω, x_c was shown to be an insignificant effect, as demonstrated in Fig.6. Eq.(11) was plotted versus frequency for x_c = 27 inches and Δx = 6, 8, 10, and 12 inches in Fig.7. Note that as frequency and separation distance increase, these curves fan outward indicating more severe flexural error.

In order to determine at which frequencies and separation distances flexural error is acceptable, it is convenient to use an analogy from acoustics. Acoustical systems are sometimes modeled as lumped parameter systems whenever their physical dimensions are small compared to one fourth of the wavelength. This lumped parameter modeling concept is based on the idea that spatial distribution has a negligible effect, and time becomes the only independent variable. It is reasonable that an analogous condition holds for the differential measurement of angular vibration; that is, when the accelerometer separation distance is small compared to some fraction of a wavelength, then the spatial effects (flexure) of the beam will be negligible. That idea is the basis for choosing the upper limit of separation distance as described below.

From wave propagation theory, the wavelength is defined as the wave propagation velocity for a beam bending traveling wave is

$$v = \sqrt[4]{EI/m} \sqrt{2\pi f} . \qquad (12)$$

(See Ref.2.)
Then by the above wavelength definition,

$$\lambda = \frac{v}{f} = \sqrt{2\pi} \frac{\sqrt[4]{EI/m}}{\sqrt{f}} , \qquad (13)$$

where λ = wavelength. By choosing $\Delta x < \lambda/2$ one would expect that there be no more than one node between accelerometers. One might expect a quarter wavelength as a reasonable choice, but the analysis summarized in Fig.7 suggests that may be too stringent. The measurement of differential angle was examined in the laboratory to verify this result.

101
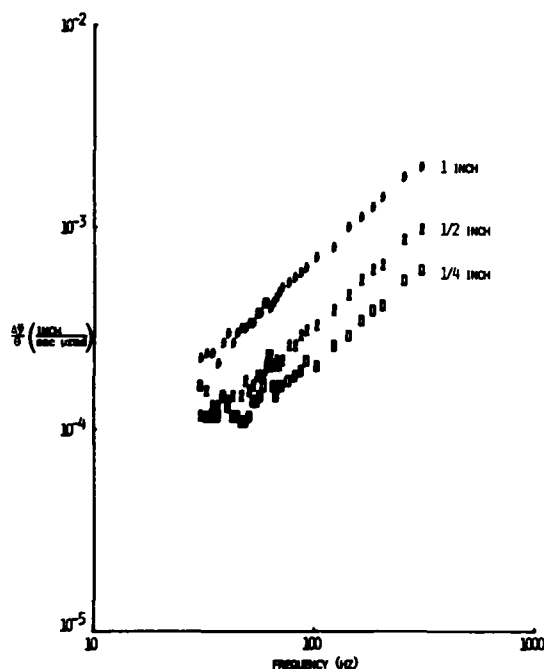
Fig. 5 - Angular velocity frequency response for differential accelerometers obtained by integrating the acceleration; rotary shaker system of Figure 1 was used.

Fig. 6 - Theoretical flexural error between two accelerometers located on a simply supported beam centered at mid-span and 1/4-span.

An aluminum I-beam was assembled in the laboratory using bearing supports at the ends, and for small lateral deflections may be considered simply supported. (See Fig.8). The precision bearings were chosen to minimize bearing chatter and lubrication was used regularly to minimize friction during the vibration tests. A 25-pound shaker was attached at beam mid-span through a flexure and was driven by broadband random noise. The random vibration of the beam was monitored so that an accelerometer mounted on the beam above the shaker had a broad band spectrum from 50 hz to 3200 hz. (See Fig.9). Two methods of subtracting accelerometer signals to get angle were attempted:

(1) An electronic differencing circuit was utilized and

(2) The individual signals were digitized then subtracted numerically. All transducer outputs were recorded on FM tape for later analysis.

The measurement technique described above is a critical part of this documentation. Since there are no suitable broadband angular transducers to check the differential angle, particular care was taken to assure that the angular measurement procedure was correct. By checking the individual accelerometer outputs it was possible to verify that the data was reliable. The differential angular acceleration was computed different ways giving an independent check; the difference signal computed by electronic and numerical differencing was the same. The angular data was also verified analytically using Ref.[1].

Though the purpose of this experiment was to validate the theoretical flexural error plotted in Fig.7, that is not directly possible since the true angle is not measurable at this time. However, by using the results of the noise considerations section, it is possible to estimate the true angle. The conclusion of that section was that separation distances of between 2 and 5 inches give good S/N. Since low frequency sensitivity increases with separation distance, 4 inches was chosen as the best value for an accurate angular estimate. By applying Eq.(13), a 4 inch separation distance gives a theoretically acceptable error up to 10.6 Khz. Even though this yields an approximation to the true angle, it is probably an acceptable reference at higher frequency and separation distance. The experimental error is

$$\epsilon_{exp} = \frac{\left| \left. \frac{\Delta y}{\Delta x} \right|_{4 \text{ in.}} - \left. \frac{\Delta y}{\Delta x} \right| \right|}{\left. \frac{\Delta y}{\Delta x} \right|_{4 \text{ in.}}} \qquad (14)$$

102

A least squares curve fit of Eq.(14) is plotted in Fig.10 for four values of separation distance. Although Fig.10 shows flexural error above 10 percent in most cases as compared to flexural errors of less than 1 percent for the theoretical curves of Fig.8, Fig.10 shows the same farming phenomenon as frequency and separation distance increase.

Further validation of Eq.(13) may also be undertaken using Eq.(14). By looking for the frequency at which Eq.(13) holds for the experimental beam given Δx, one may observe how upper frequency limit decreases with increasing separation distance. That was done and is indicated on Fig.10. Other separation distances were examined and further substantiate the trend of Fig.10. In addition, the authors feel that use of separation distances of much more than about 12 or 14 inches will limit the upper frequency range. That fact is demonstrated by Figs.7 and 10 which show that error is increased rapidly as separation distance and frequency increase.

The error of Fig.10 below 600 hz is not reliable. One would expect the higher frequencies to be primarily effected by flexural error and that trend is verified by Fig.10. Although the error of Fig.10 appears inconsistent at lower frequencies, the individual angle measurements agree well. That is summarized in Table I with differential angles computed at 100 hz for various separation distances with a bandwidth of 1.7 hz.

TABLE I.

Angles at Various Separation Distances at 100 hz.

Δx, in	$\frac{\Delta y}{\Delta x} \times 10^{-7}$, rad
4	1.89
6	1.84
8	1.82
10	1.60
12	1.67
14	1.62

From Table I, separation distances of 6 and 8 inches give angular measurements which agree to within 1.1 percent. Therefore the low frequency error of Figure 10 is not reliable. This is because low frequency and low separation distance information has a lower S/N and sensitivity thus making low frequency experimental error unreliable. This problem with low frequency experimental error is not indicative of actual angular measurement problems, as shown in Table I. Note that the meas-

ured angles of Table I are all below 1 urad, the required measurement capability for angular transducers.

The important result of this section may be summarized as follows. An analytical expression for angular vibration error suggests that using an upper bound for separation distance of one-third of a wavelength gives flexural error of less than 2%. This trend was verified experimentally although the experimental error was higher than the analytical error. This is because the experimental error depends on a reference approximate angle calculated with a separation distance of 4 inches.

DISCUSSION

Using the technique given here, acceptable ranges of separation distance may be calculated by the engineer for any particular application. As one might expect, separation distance must not be too small or the S/N will be unacceptable. On the other hand separation distance must not be too large or flexure between accelerometers will severely hinder the upper frequency range. In general, a separation distance of between 2 and 5 inches gives a S/N of about 5 to 10 at frequencies down to about 50 hz. However, when one is primarily interested in low frequency response a larger separation distance can offer improvements.

For upper frequency limit, one must estimate the component structural properties and assure that the separation distance be less than one-third of a wavelength. This criteria does not depend on boundary conditions, only on the local element on which angular vibration is to be measured. However, there are two difficulties one might encounter.

(1) For some complex structures with varying cross-sectional properties or with curved geometry, it may be difficult to accurately determine the correct equivalent structural properties to use with Eq.(13). In that case, some equivalent cross section moment of inertia and mass distribution must be estimated, and the flexural error may not be acceptable. In addition, at this time there is no known technique for determining from the data when there is unacceptable flexural error.

(2) It is conceivable that for some problems where the structure is relatively flexible and where high frequency response is desired that there will be no separation distance which will yield acceptable results. In that case, obviously, the differential angle method will not work. At the time of this writing differential angle measurement is scheduled for use on two flight test programs at the Air Force Flight Dynamics Laboratory, but verification of this technique through that experience is not yet available.

Notice that for plates, Eq.(13) must be modified. Although for most structural compo-

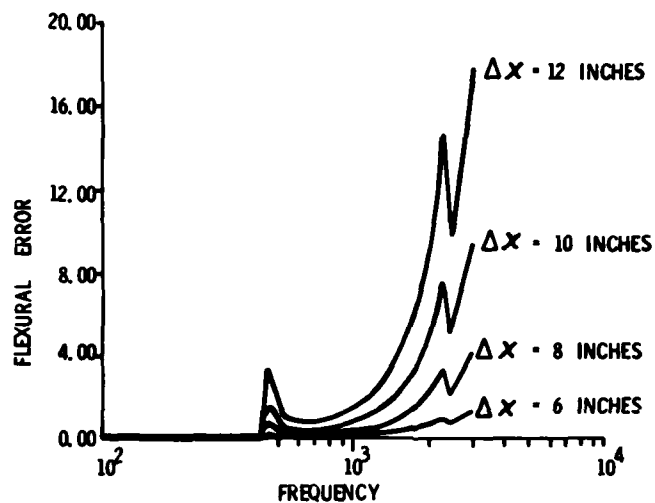Fig. 7 - Theoretical flexural error between two accelerometers
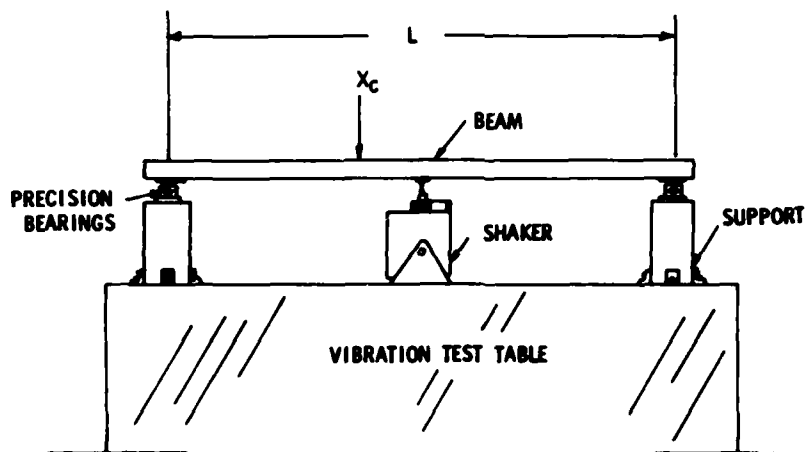for various separation distances.

Fig. 8 - Experimental simply supported beam used in verifying
flexural response between two accelerometers.
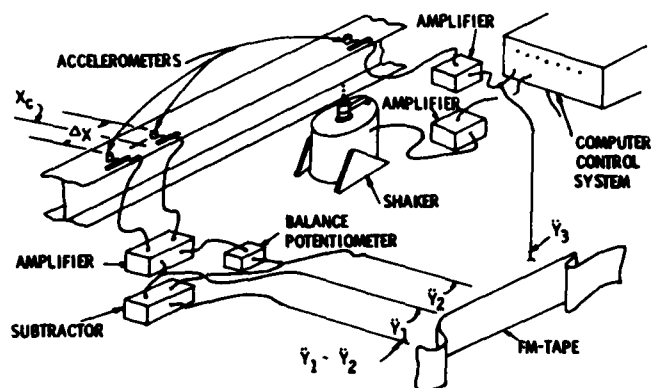
104

Fig. 9 - Instrumentation of the experimental beam shown in Figure 8.
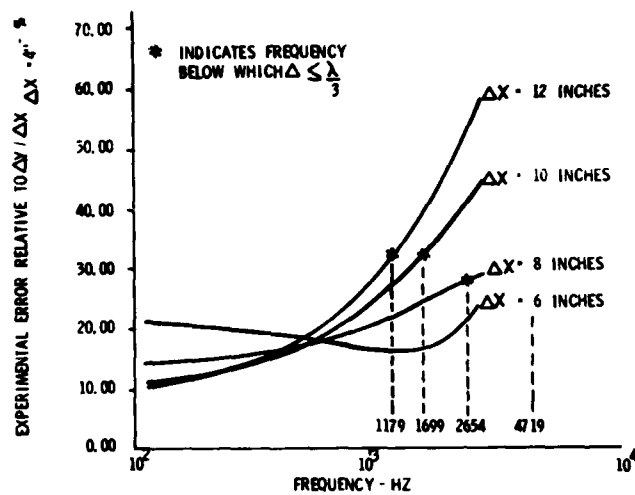
Fig. 10 - Experimental flexural error for the beam of Figures 8 and 9 using a least squares curve fit to random data.

nents beams are probably a good model, it may
be that one desires to measure angular vibra-
tions on a plate element. That may be done
by substituting for Eq.(12).

$$v = \sqrt[4]{\frac{Et}{\sqrt{12\rho}(1-\Theta^2)}} \sqrt{2\pi f},$$

where t = plate thickness

ρ = plate volume density

Θ = poisson's ratio.

Although there is at present no experimental
data to support this approach for plates, it
is known that a strong mathematical similarity
exists between beams and plates so this should
be acceptable until further experimental or
analytical verification is available [3,4].

CONCLUSIONS

This study describes a method for measur-
ing angular vibration using linear acceler-
ometers by establishing a criteria for the
choice of separation distance. The lower limit
of separation distances is chosen based on the
requirements concerning low frequency low amp-
litude signal-to-noise ratio. For most struc-
tures it is possible to measure angles on the
order of 2μrad down to about 50 hz for S/N of
5 or 10 with a lower limit of separation dis-
tance from 2 to 5 inches. The upper limit of
separation distance is chosen based on the
structural properties and desired upper fre-
quency range. By specifying the upper bound
for separation distance as one-third of a
wavelength, the high frequency theoretical
flexural error is below 2 percent. This proce-
dure provides an acceptable range for separa-
tion distance which will usually allow some
freedom in integrating the measurement system
into the hardware.

LIST OF SYMBOLS

Θ = exact angular vibration response

$\frac{\Delta y}{\Delta x}$ = differential angular vibration response

Δx = accelerometer separation distance

ω = frequency in radians/sec

f = frequency in cycles/sec

S/N = Signal-to-Noise ratio

v = structural bending wave propagation velocity

λ = structural bending wavelength

ε = theoretical flexural error

ε_{exp} = experimental approximation to ε

REFERENCES

1. Lee, J. and P. W. Whaley, Prediction of the
   Angular Vibration of Aircraft Structures,
   Journal of Sound and Vibration, Vol. 49,
   No. 4, pp. 541-549, Dec. 1976.

2. Kinsler, L. E. and A. R. Frey, Fundamentals
   of Acoustics, Wiley and Sons, New York,
   1962, pp. 69-71.

3. Eringen, A. C. "Response of Beams and
   Plates to Random Loads," Journal of Applied
   Mechanics, Vol. 24, 1957, pp. 46-52.

4. Bogdonoff, S. L. and J. E. Goldberg, "On
   the Bernoulli-Beam Theory with Random
   Excitation," Journal of Aerospace Science,
   Vol. 27, 1960, pp. 371-376.

ACKNOWLEDGEMENTS

Discussion

Mr. Favour, (Boeing Company): You said that beam that you showed with a needle bearing was simply supported. It seems to me that it might be more approximating a pin joint rather than a simply supported end condition. I think that the needle bearing could carry a transverse load.

Mr. Whaley: That is true but we drove it at such a low level that we felt that the axial force component was very small, but we didn't check that.

Mr. Hancock, (Vought Corporation): The biggest problem is the low end of the spectrum, down at the first bending mode of the air frame or store, on the order of 10 Hz and lower; using this beam method with the separated accelerometers we have run into the problem of an error of several orders of magnitude as factors of 10 in the frequency range below 10 Hz, because of the noise that you mentioned, and the inability to separate the accelerometers over a great enough distance to get a clean difference signal. Are you interested in the low end of the spectrum?

Mr. Whaley: No. It is our opinion that this is inherently a high frequency technique. We haven't had very good luck much below 10 Hz. If we can get down to 10 Hz and still go as high as 1000, that will be very good. We are sandwiching that separation distance, and that means that you can't go closer together than some number and you can't go farther apart than another number. It is the upper separation distance that hurts the low frequency response because if the accelerometers are too far apart you can't get the high frequencies.

Mr. Hancock: Why did we need high frequency angular motion as opposed to low frequency motion where we can do something to control the object device? We can't control high frequency motion.

Mr. Whaley: I would have to agree with that. We have been faced with broad band angular vibration requirements. We have been given requirements of DC-1000 Hz or DC-2000 Hz.

THE USE OF A LOW POWER LASER AND PHOTODIODE
FOR DISPLACEMENT DATA

John E. Cawthorn
Martin Marietta Aerospace
Orlando, Florida 32805

A relatively inexpensive displacement measuring system has been
developed which has some unique applications and capabilities. The
combination of a low power helium neon laser and a photodiode have
been utilized to obtain position information remotely in a manner
similar to optical tracking systems employing expensive photomulti--
plier tubes.

One application, in which the system was used quite satisfactorily,
was in the acquisition of displacement or pointing error data of a sur-
face-to-air missile launcher during static influence coefficient
testing.

A second application of this displacement measuring system was in
the acquisition of angular position information during vibration test-
ing of a high resolution optical guidance system.

INTRODUCTION

Displacement measurements in the Engineer-
ing Test Laboratory are usually accomplished
with the use of dial gages, displacement trans-
ducers, or an optical tracking system.

The Displacement Transducer System

Probably the most common displacement
transducer used is the linear variable differ-
ential transformer or LVDT. The LVDT has an
analog output which is a function of the rela-
tive position of its two components, the core
and the transformer. In use, one of the com-
ponents is physically attached to the test item
and the other component is mounted to some
reference point. Ordinarily, this reference
point is not more than a few inches from the
point of interest on the test item. Bridge or
DC amplifiers, determined by the type of LVDT,
are usually used for signal conditioning of the
transducer output. These amplifiers are used
to null, scale, calibrate, and filter the sig-
nal being recorded. These features of the
amplifier simplify the use of the LVDT.

The transducer system requires a reference
point near each measurement point. For the case
where large items are undergoing structural
testing and multipoint position data is desired,
reference fixture must be erected adjacent to
the test item. This can become expensive and
might be impractical or impossible due to

location of measurement points or reaction
fixtures.

For smaller test items being subjected to a
dynamic environment, such as vibration, the mass
of the transducer, which is in physical contact
with the test item, may be sufficient to influ-
ence the dynamic characteristic of the item
under test.

Another disadvantage of these instruments
is cross-axis motion. Normally, cross-axis
motion will result in an error in the data due
to side loading of the transducer.

THE OPTICAL TRACKING SYSTEM

The optical tracking system overcomes most
of the disadvantages and shortcomings of the
displacement transducer system. This type of
system uses a photomultiplier tube which is
focused on a target affixed to, or painted on,
the test item. The system has an analog output
which is a function of relative displacement be-
tween the target and the line of sight between
the photomultiplier tube and the target. This
system does not make a physical contact with the
item under test. An adjacent reference fixture
is not required. Also, errors due to cross-
axis motion are greatly reduced if not com-
pletely eliminated. The major disadvantage of
an optical system is cost. The photomultiplier
tubes are an order of magnitude more expensive
than the LVDT type transducer. When several

109

measurements are to be made, the cost can be-
come prohibitive.

A BETTER SYSTEM

The optimum system for displacement data
is an inexpensive optical system or a system
which functions similar to the optical tracking
system. Some features of the optimum system
are:

1 No expensive components.

2 Minimal error due to cross-axis motion.

3 No requirement for an adjacent measure-
ment reference fixture.

4 Simplicity of use with the capability
of checking system sensitivity and
calibration while installed in the test
set-up.

THE COMPONENTS OF THE SYSTEM

There is available on the market, a photo-
diode which has an analog output that is a func-
tion of light spot position incident on its sen-
sitive surface. These devices, which have an
active area width of one-tenth inch, are avail-
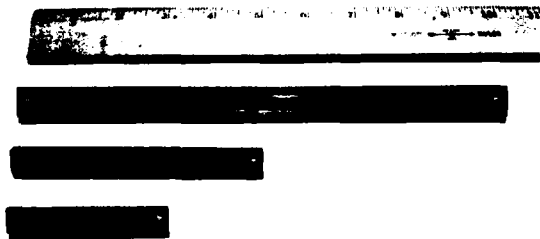able in lengths of two, four, and nine inches.

Figure 1. Linear Photodiodes from United
Detector Technology

A low-power helium neon laser provides a con-
venient light source for the photodiode. Bridge
amplifiers with DC bridge excitation provide the
necessary signal conditioning for the system.

DEVELOPMENT OF THE SYSTEM

The photodiode is a Schottky barrier sili-
con photodiode. It is a P-I-N (positive,
intrinsic, negative) diode which, when wired in
the differential mode senses lateral displace-
ment of a light spot. The spectral response
extends from 200 to 1000 nanometers. The helium
neon laser has a wavelength of 632.8 nanometers.

The output of the photodiode is independent
of light spot size, but is a function of light
beam intensity.

During evaluation of the sensor small
imperfections in the active area were noted.
The sensor output was linear over its length

but slightly ragged when using a small laser
beam. This was corrected or compensated for by
using a slightly larger or diffused beam.

Since the active area of the photodiode is
only one-tenth inch wide, any cross-axis dis-
placement will result in significant errors in
the data. The circular laser beam is converted
to a projected line beam with the use of a cyl-
inder lens. When the beam strikes the sensor
it is in the shape of a line perpendicular to
the long axis of the sensor.
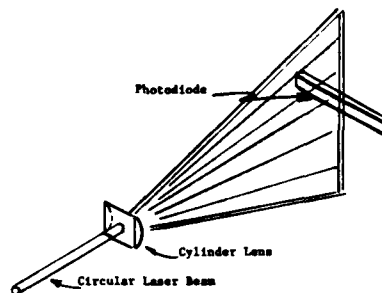
Figure 2. A Cylinder Lens Converts
a Circular Spot into a
Diverging Line

The magnification of the laser beam by the
cylinder lens can result in two sources of
error. (1) The circular spot of the laser is
gaussian in intensity with the very center of
the beam being the brightest. The line beam
resulting from the cylinder lens also has a
gaussian distribution in intensity.
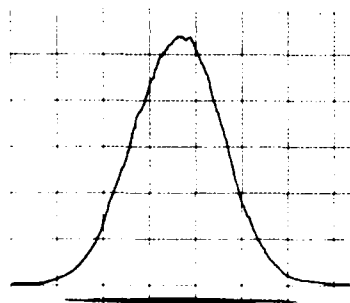
Figure 3. Gaussian Distribution
in Intensity of the
Projected Line

(2) The beam is diverging after passing through
the cylinder lens. Intensity at the sensor be-
comes a function of distance from the cylinder
lens and, therefore, the output of the sensor
is now a function of distance.

The placing of a diffuser in front of the
photodiode partially compensates for the varia-
tion in intensity of the projected line. This
diffuser also eliminates all effects of the
minute imperfections in the active area of the
photodiode.

110

The diode is sensitive to background lighting. Photographic filters with very narrow spectral passbands are available, however, a cost estimate was over $100 each. A Wratten No. 29 filter was selected. This filter passes approximately 18 percent of the ambient light and 75 percent of the laser. The completed sensor assembly is shown in Figures 4 and 5.
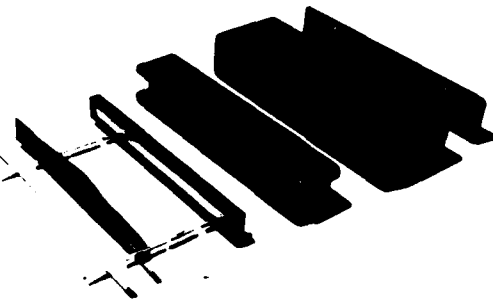
Figure 4. Exploded View of the Sensor Assembly
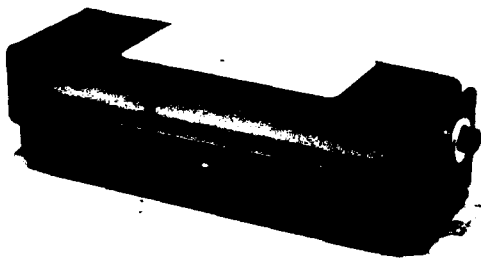
Figure 5. Assembled Sensor

The intensity as a function of distance is taken care of by the electrical calibration procedure developed. As stated earlier, one of the criteria for a better displacement measuring system is the capability of checking calibration and sensitivity of the system while installed in the test set-up. The sensor is wired into a wheatstone bridge with the photodiode as two legs of the bridge (Figure 6).
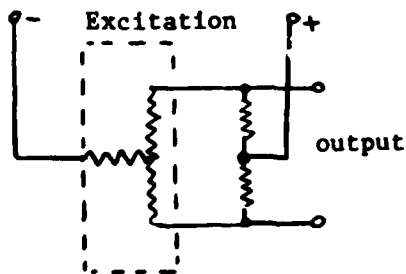
Figure 6. The Photodiode, Inside the Dashed Lines, is Part of a Wheatstone Bridge

The diode is back-biased with the DC excitation voltage of a bridge amplifier. When the P-I-N diode is used with a back-bias voltage, it behaves like a constant current generator. It is photoconductive with an output which is a function of light spot intensity. Using a resistive analogy, the photodiode can be considered a potentiometer with the wiper position determined by the light beam position. The current ratio of the two legs of the bridge made up by the photodiode is a function of the light beam position. However, the sum of these two currents is a constant with constant light intensity (Figure 7).
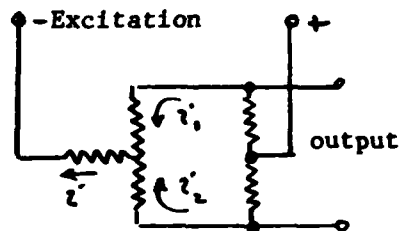
Figure 7. The Sum of the Two Currents i, $d i_2$ is a Constant

When one end of the photodiode is disconnected, all of the current passes through the other lead. The output of the bridge is the same as if the light beam had been moved to the end of the sensor with the lead still connected. This current output is equal to full-scale output of the sensor. This provides a simple and convenient means of obtaining a full scale calibration signal for signal conditioning and recorders. The final method of calibration selected was to disconnect one leg of the sensor and connect it to the opposite corner of the bridge.
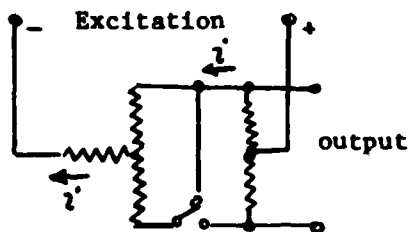
Figure 8. Electrical Calibration

The bridge amplifier used with the system is of the differential type. Since the sensor makes up two legs of the bridge and the resistance of the sensor is large with respect to the other two legs of the bridge, the input signal to the amplifier is very near the positive potential of excitation.

Since the bridge amplifier is a laboratory instrument, it is compatible with existing lab recorders. It has the desired features of

111
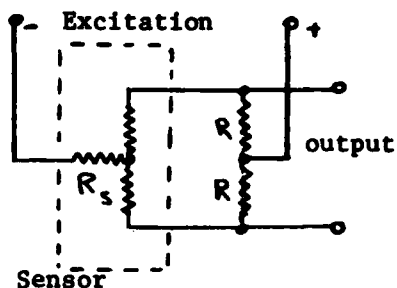
Figure 9. $R_S \gg R$

multi-range, variable gain, zero balance, and
multi-outputs.

As stated earlier, the measurement system
was to use a low power helium neon laser.
Lasers of several types and manufacturers were
evaluated. As a laser warms up, its intensity
varies as the tube changes dimensions
(Figure 10).
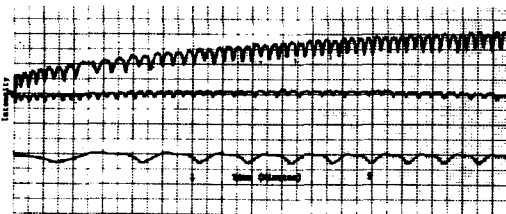
Figure 10.   Warm-up of Three Different Lasers

Also, there is some angular deflection or wan-
dering of the beam during warm-up. A laser with
an integral power supply was selected for two
reasons: (1) In the test set-up, the single
unit is less cumbersome to handle than one with
a separate power supply; (2) the integral power
supply functions as a heater and maintains a
more constant temperature after warm-up.

After a two or three hour warm-up, drift of
the laser selected for the system was almost
negligible. During conduction of a test which
lasted several weeks, the overnight drift of
lasers with a 15 to 25 feet working distance
was approximately 0.02 inch. The lasers were
left on continuously during the tests.

A lens assembly was fabricated and attached
to the front of the laser (Figures 11 and 12).
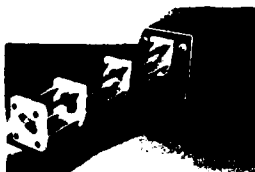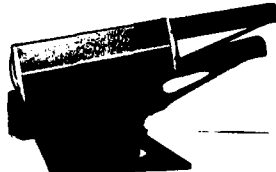
Figure 11. Lens   Figure 12. Spectra
    Assembly   Physics 2 mw Laser
                       with Lens Assembly

The lens assembly consists of two double convex
lenses, one with a focal length of 15 mm and
the other with a focal length of 144 mm. A
cylinder lens with a focal length of 44 mm was
placed between the other two lenses. In use
the lenses are focused for approximately an 8-
inch line at the sensor. A cross-axis displace-
ment of 0.75 inch resulted in a deviation from
linear by less than 2 percent of the full-scale
2.0 inches.

The completed system consisting of the
sensor, laser, lens assembly, photographic fil-
ter, and diffuser cost approximately $400 in
material.

Figure 13.   Complete System of Bridge Amplifier,
Sensor, Electrical Cal Box, and Laser-Lens Assy

THE SYSTEM IN USE

The system was developed primarily for the
structural testing of a large, transportable
surface-to-air missile launcher. Multi-point
displacement data was taken while the launcher
was being subjected to simulated wind loads and
to tip-off displacements resulting from succes-
sive, rapid firing of missile rounds. Reaction
fixtures for load lines were erected on each
side and to the rear of the launcher (Figure 14).
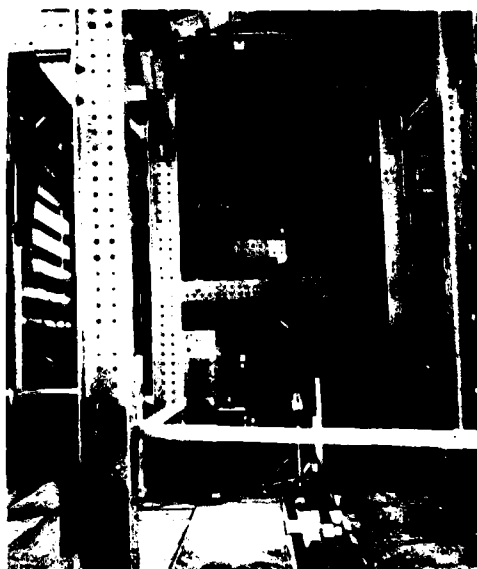
Figure 14.   SAM Launcher Surrounded by
Structural Steel

112

There was no space available for a reference fixture. The photodiode sensors were mounted on the launcher and the lasers, which were mounted on the lab floor, were aimed at their respective sensors. Distances from the lasers to the sensors varied from 5 to 35 feet (Figures 15 and 16).

Figure 15. Laser Focused on Photo-diode Sensor

Figure 16. Three Lasers in Use

Displacement ranges varied from 0.2 inch, (Figure 17), to 1.0 inch (Figure 18).
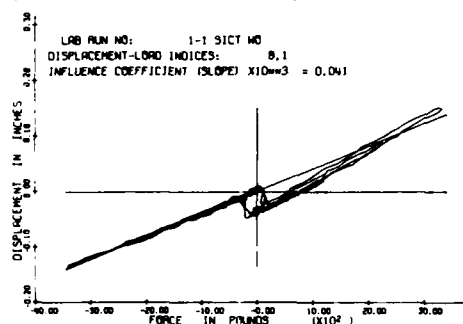
Figure 17. Displacement vs Load Data, 0.2 Inch Range
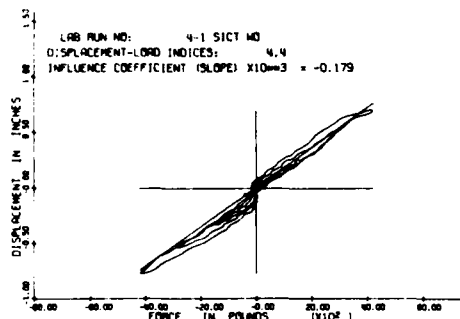
Figure 18. Displacement vs Load Data, 1.0 Inch Range

The applied load consisted of three cycles, the first being 33 percent, the second 66 percent, and the third 100 percent of maximum load.

Angular displacement data was required for evaluation of a high resolution, pod mounted optical guidance system during vibration testing. The optical bed of the system was mounted on vibration isolators to prevent pod and aircraft vibration frequencies exciting those frequencies of the optical train. Small mirrors of optical quality, mounted on the optical bed, were used to reflect the laser beam to the remotely located sensors. The small angular rotations of the bed yielded linear motion of the beam at the sensor. Three systems were thus positioned to measure pitch, roll, and yaw of the optical bed (Figure 19).

$$\theta = \frac{1}{2} \sin^{-1} \frac{x}{y}$$
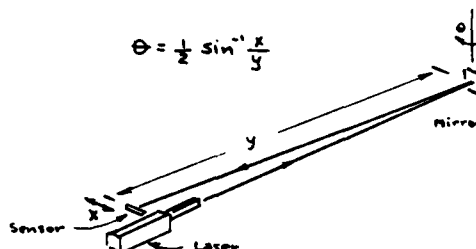
Figure 19. Linear Sensor and Mirror Yields Angular Displacement Data

Data was recorded on analog magnetic tape for analysis at a later time. The magnetic tape data was replayed through narrow, constant bandwidth, swept frequency filters. This filtering successfully separated floor vibration and other frequencies from those frequencies of primary interest. Resolutions to five microradians were obtained (Figure 20).

In each of the above two applications, the structural test and the vibration of the pod, the lights in the lab were dimmed to reduce the effects of light flicker on the data. Movement of personnel was held to a minimum to prevent changing shadows on the sensors.

The system has not been used outdoors but should function properly if measures are taken to shade the sensor from direct or reflected sunlight.

CONCLUSION

The system has the capability of measuring displacements as low as 0.0001 inch. The system resolution is a function of full scale range and is in the neighborhood of one percent of the full scale range selected by the user. The angular resolution, naturally, is a function of the working distance, i.e., the distance from the laser to the sensor via the mirror. The cross-axis error; that is, error in data due to the relative motion between the beam and the sensor at an angle of 90° to the long axis of the sensor is within two percent of full scale over ±1.75 inches with a cross-axis movement of 0.75 inch.

113
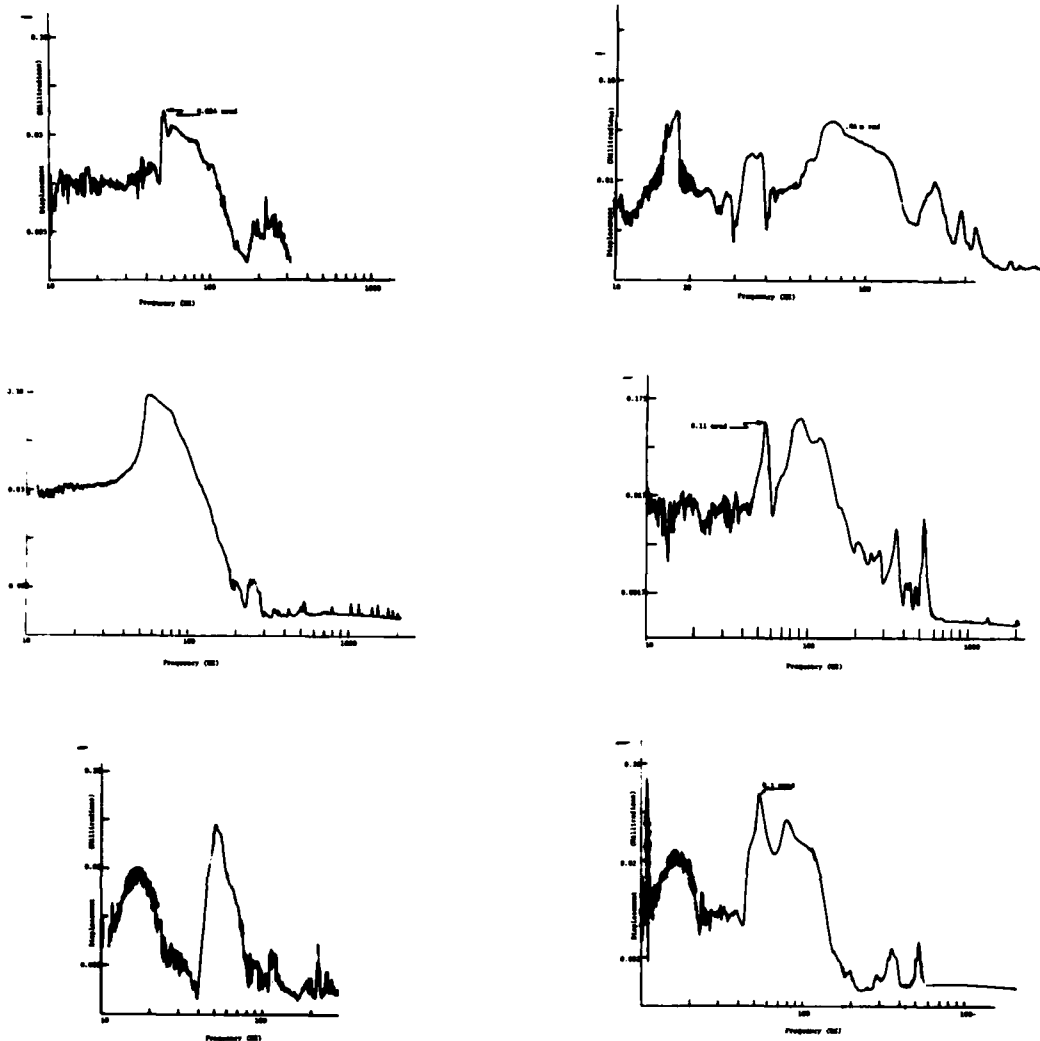
Figure 20. Angular Displacement Data of a Gimbal
System During Vibration Testing

DISCUSSION

Mr. Favour (Boeing Company): You showed a sensor in a Wheatstone Bridge application and your diagram did not show any ballast resistors on either side of the sensor. To me that would indicate a very nonlinear response. Could you comment on that?

Mr. Cawthorn: The sensor is photoconductive. It is a current generator. It is really not a response for the voltage divider due to excitation voltage.

Mr. Favour: I think you are saying that it is a constant current source.

Mr. Cawthorn: It is a constant current source, it is not a passive resistance.

Mr. Favour: Do you know what your linearity is?

Mr. Cawthorn: It is highly linear. We get into error with the cross-axis motion and since the projected line is Gaussian that would give us some error.

GROUT/SOIL INTERACTION AND GROUND-MOTION MEASUREMENT

M.B. Balachandra and J.A. Malthan
Agbabian Associates
El Segundo, California

The interaction between the free field and the grout used to fill bore-holes containing velocity gages was analyzed to ascertain the effects of bond strength and impedance mismatch on the recorded velocities. The finite element calculations performed by Agbabian Associates, which parallel tests conducted at the U.S. Army Engineer Waterways Experiment Station (USAE-WES), Vicksburg, Mississippi, are discussed.

Three tests were conducted on a cylindrical specimen of artificial soil materials that represented the free field. A borehole in the center of the specimen was filled with selected grout and velocity gages were installed in both the matrix and the borehole. Each test used a grout of differing stiffness.

The matrix and borehole grouts were represented in the calculations by nonlinear, inelastic models that approximated the measured material properties. A slip interface was provided between the borehole and the matrix. For all tests except Test 1, the calculations showed good correlation between the velocity histories at the gage and the free-field locations. The close correlation was attributed to good bond between grout and matrix. It was concluded that when a strong grout/free-field interface bond exists, the velocity gage response is insensitive to impedance mismatches between the grout and free field, and consequently the gage records the free-field motion faithfully. Therefore, since considerable mismatch between the stiffness properties of the grout and the free field will not significantly affect the accuracy of the gage response when a strong interface bond is provided, the preparation of the borehole grouts is simplified. A strong interface bond between gage and free field can be ensured by surrounding the velocity gage canister with a stiff, expansive grout.

1. INTRODUCTION

Proper emplacement of velocity sensors in field tests in order to ensure accurate measurement of ground motions in soils is a long-standing problem. This paper discusses analytical work addressing the effect of two aspects of gage emplacement--bond strength and impedance mismatch--on the motion of instrumentation canisters grouted in place. The analysis forms part of the instrumentation program of the Defense Nuclear Agency (DNA) and was directed to the development of simpler, less costly, and more effective canister placement procedures [1 and 2].

The principal result of this investigation is that good interface bond between the borehole grout and the free-field medium is the primary requirement for ensuring the fidelity of velocity measurement. Even considerable mismatch in the impedances of the borehole grouts and the free-field materials can be tolerated if a nonslip interface can be maintained between them. Consequently, it is recommended that velocity canisters be locked in place by using a stiff, expansive grout in the region surrounding the canister. The remainder of the borehole may be filled with other grouts that only grossly approximate the properties of the free-field materials at

the site. Thus, elaborate procedures for grout preparation are circumvented.

2. GENERAL DESCRIPTION OF TESTS AND ANALYSES

The present program was a combined experimental and analytical investigation designed to compare the response of the borehole and the free field at ratios between the impedances of the grout and the free field varying from 0.5 to 2.0 and at different bond strengths at the grout/matrix interface, as shown in Table 1.

TABLE 1
Summary of Tests

Test No.	Stiffness of Grout† Stiffness of Soil	Bond between Grout and Soil
C*	1.0	Perfect
1	0.5	Weak
2	0.5	Strong
3	2.0	Weak

*Calibration test with uniform matrix specimen and no borehole.
†Densities of grout equal density of soil in each case.

It was intended to vary the impedance ratio by changing the stiffness of the borehole grout, while maintaining a density ratio of 1 between the grout and the free field. It must be noted that the term "stiffness" is somewhat ambiguous, since the materials in question generally exhibit nonlinear stress/strain behavior. The stiffness ratio may be defined precisely by referring to the secant or tangent moduli at specified stress levels. However, given the uncertainties surrounding the *in-situ* properties of earth materials and the wide variations in the properties of artificial soil mixes even under controlled conditions of preparation, a precise definition appears unwarranted.

2.1 Experimental Program

The experimental part of the project was carried out with the Small Blast Load Generator (SBLG) [2]. Each test used a matrix specimen 6 ft high by 4 ft in diameter, made of artificial soil material to simulate the free field (Fig. 1). A 5-in.-dia. hole was cored out in the center of the specimen and filled with selected borehole filler grouts. An overpressure was applied by detonating primacord in the firing chamber above

the specimen, and a neoprene diaphragm was used to ensure uniform pressure distribution. The overpressure had a nominal peak value of 250 psi, followed by a gradual decay.
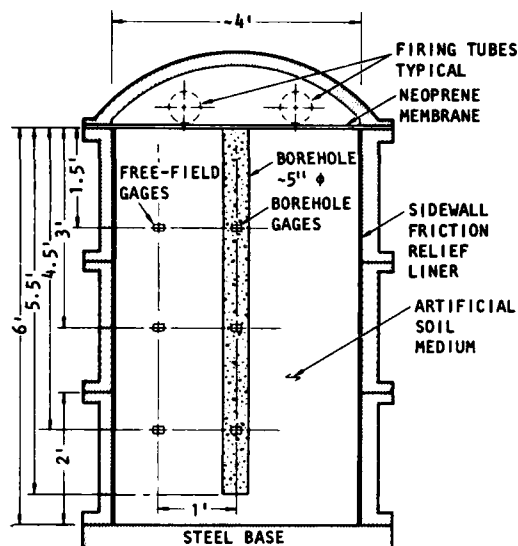
Fig. 1 - Typical Small Blast Load Generator (SBLG) schematic

An important ingredient of the artificial soils used for the free field and the borehole was Chem-Stress II, a highly expansive cement. As a result, these soils underwent considerable volume expansion during setting and are referred to as being "expansive" in the sequel. More details on the composition of the artificial soils may be found in [2].

The response measured during the tests consisted of time histories of vertical velocity and vertical stress. Velocity gages were placed at 18-in., 36-in., and 54-in. depths in the borehole as well as in the matrix, at a radial distance of 12 in. The gages were placed in position as the specimen was built up. The gages in the matrix recorded the "free field" motion for comparison with the motion recorded by the grouted gages. Displacements were derived by digital integration of the velocity signals. Each gage was a piezoelectric accelerometer with a built-in electronic integrator, housed in aluminum canisters 3 in. dia. by 2-3/4 in. high. The canister density was approximately 100 lb/cu ft. Stress measurements were made using the WES SE (steel-epoxy) gage,

a soil-stress gage using a metallic diaphragm as the transducer [3]. Stress gages were placed in the matrix at depths of 18 in., 36 in., 54 in., and 72 in. at a distance of approximately 1 ft from the borehole.

Table 1 lists the tests considered in the present paper. Test 1 used a uniform borehole-filler grout much softer than the matrix. In Test 2, the same grout was used as in Test 1, but the gages were locked in place by the use of a very hard, expansive grout around the gage to provide a strong bond between the gage and the matrix. Test 3 employed a uniform borehole grout much stiffer than the matrix. All tests were conducted on the same matrix.

2.2 Analytical Investigations

Supportive finite element calculations were performed for the tests listed in Table 1. An axisymmetric formulation was used and a finite element mesh was prepared to represent each test configuration. The SBLG wall was lubricated in the tests to minimize friction. Auxiliary calculations showed that friction at this interface was indeed extremely low, leading to an essentially one-dimensional response of the matrix column. Accordingly, in the final calculations it was assumed that the SBLG wall provided radial constraint only (no axial friction). The calculational meshes, therefore, did not include the SBLG wall. The mesh used in Test 3 calculations is shown in Fig. 2 as an example.

The canisters containing velocity gages were not modeled. This decision was based on the following arguments: (1) The overall density of the canister is close to that of the free field, so that the rigid-body motion of the canister follows the motion of the free field; (2) within the frequency range of interest (approximately 0 to 200 Hz), the wave lengths are much longer than the dimensions of the canister; and (3) the natural frequencies of the canister are much higher than the above frequency range, so that the vibrational modes of the canister do not appreciably perturb the free-field motion in the frequency range of interest. The good agreement obtained between calculation and measurements apparently justifies the decision not to model the canisters. Calculated time histories were obtained from the borehole and free-field regions of the mesh corresponding to the locations where test measurements were made.

The input pulse used to drive the finite element meshes was derived by digitizing the measured overpressure during each test. The pulse used in Test 3 is shown in Fig. 3 as an example. Although the pressure distribution in
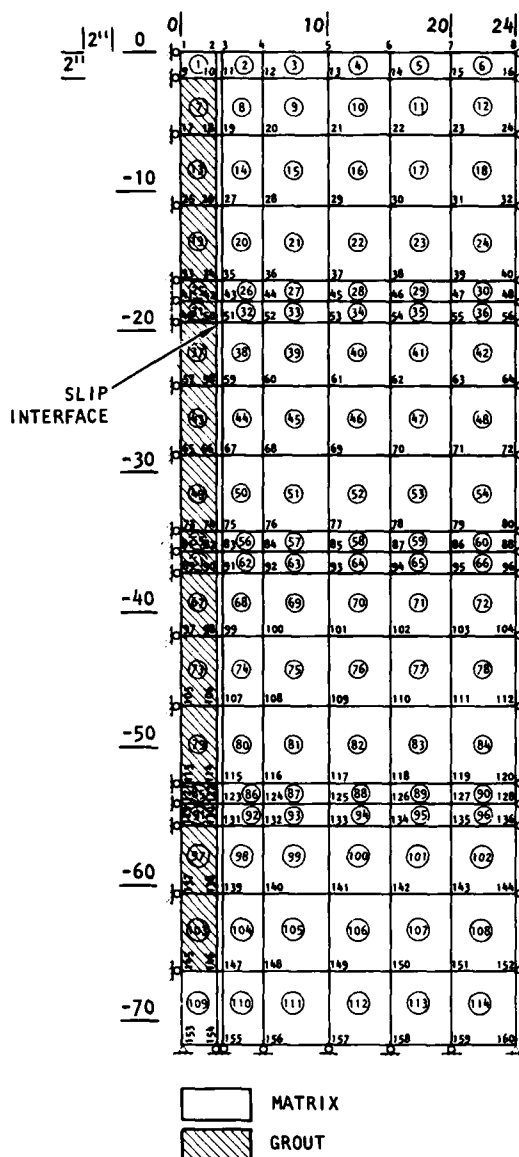
Fig. 2 - Finite element mesh used in Test 3 calculations

the test may have been somewhat nonuniform, there were no data available on the actual pressure distribution, and the calculations assumed a uniform pressure across the top of the mesh.

The FEDRC code [4], used to perform the calculations, is a two-dimensional finite element code based on a small-displacement, axisymmetric formulation and employing isoparametric elements. The FEDRC code has an extensive library of nonlinear, inelastic material models.

119
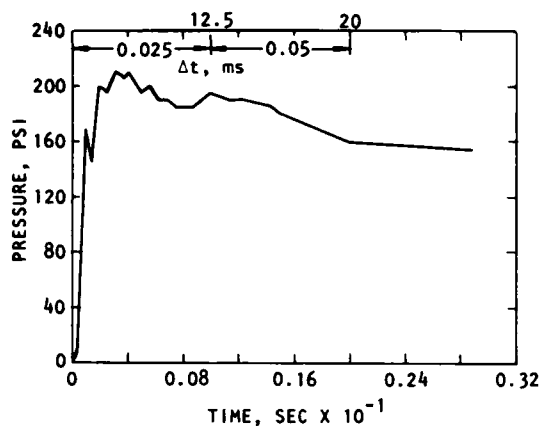
Fig. 3 - Input pulse and integration schedule used in Test 3 calculations

For soil or earth materials, these include the so-called cap and variable-modulus models. The present calculations used an isotropic, variable-modulus model, defined by a bulk modulus

and Poisson's ratio [1]. The model assumes both the volumetric strain/pressure relation and the uniaxial stress path to be piecewise linear. During loading in compression, the bulk modulus can assume up to four different values, and Poisson's ratio, up to three different values. The changes from one value to another occur at designated values of the elastic component of volumetric strain in the case of the bulk modulus, and of the mean pressure, in the case of Poisson's ratio. The bulk modulus and Poisson's ratio are each permitted to have three different values in unloading. Reloading is assumed to take place along the unloading path until the volumetric elastic strain exceeds the highest value previously attained during the loading history; at which stage, the properties corresponding to virgin loading take effect. The model also incorporates a failure envelope of the modified Drucker-Prager type. The parameters of the material models were chosen on the basis of laboratory measurements of the properties of the materials used in the test. The measured properties of the matrix and borehole grout used in Test 1 are shown in Fig. 4.

CURVE NO.	CURVE IDENTIFICATION	WATER CONTENT w %	DRY DENSITY γ_d, PCF	WET DENSITY γ, PCF	INITIAL CONSTRAINED MODULUS, M_i, KSI	LAYER NO.	DEPTH RANGE, IN.
1	LAYERS 1 AND 3	139.0	35.0	84.0	30	1	0 TO 33
2	AVERAGE	132.0	36.5	85.0	40	2	33 TO 57
3	LAYER 2	125.0	38.0	87.5	56	3	57 TO 72

$M_u = 36$ KSI
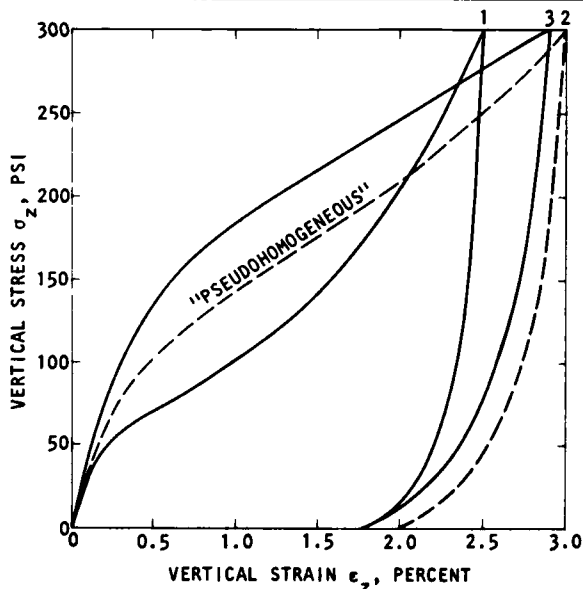
(a) Uniaxial stress/strain relations for Test 1 matrix
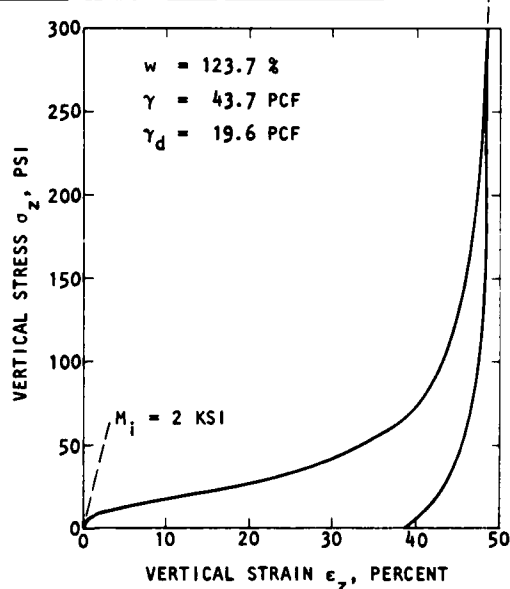
(b) Uniaxial stress/strain relations for Test 1 grout

Fig. 4 - Recommended material properties for Test 1 matrix and borehole filler

120

Slip elements were employed at the borehole/matrix interface. The slip element allows for debonding and slip at interfaces between dissimilar materials. The normal and shear forces transmitted across the interface are computed from the relative displacements at the interface, using stress/strain relations involving parameters determined from available data on the interface behavior. The slip elements are assigned elastoplastic properties. Slippage, accompanied by comparatively large relative displacement at the interface, occurs when the slip element yields. Plastic behavior is defined through a yield surface and a flow rule [1 and 5].

3. INDIVIDUAL TEST ANALYSES AND RESULTS

This section discusses the calculations of Tests 1, 2, and 3, along with their individual features.

Test 1: Test 1 was anomalous both in the experimental and the analytical investigations. The extremely soft air-entrained grout used in the test led to abnormal deformation or punchdown in the upper regions. This effect may be observed in the plot of the measured grout velocity at the 18-in. depth in Fig. 5. At the lower depths, the punchdown effect was contained and the measured velocities in the grout and the free field correlated well, as seen in Figs. 6 and 7.
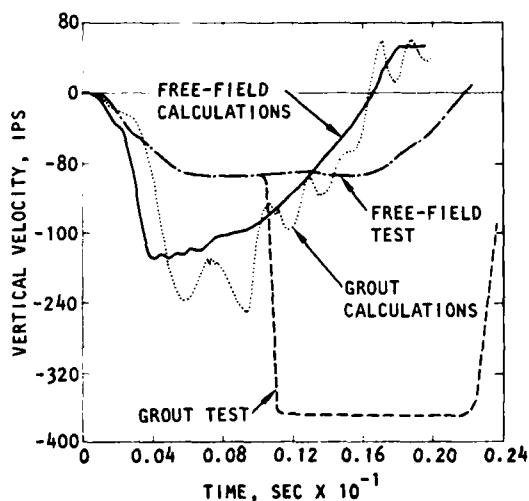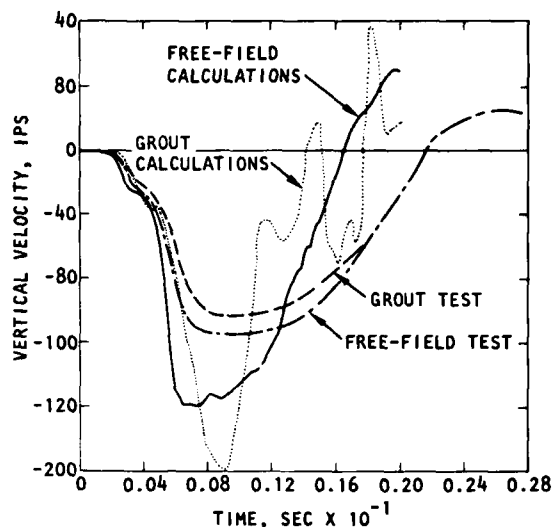
Fig. 6 - Comparison of velocities at 36-in. depth (Test 1)

Fig. 7 - Comparison of velocities at 54-in. depth (Test 1)
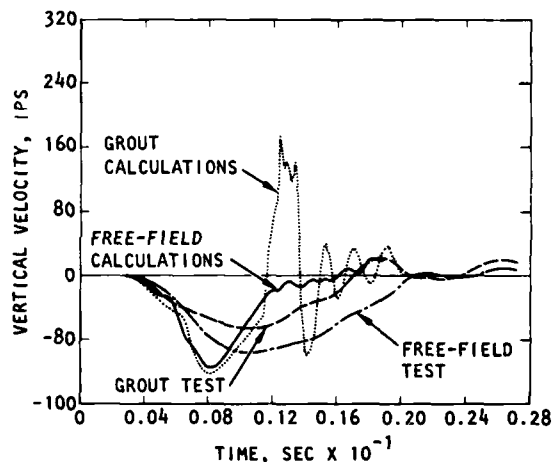
Fig. 5 - Comparison of velocities at 18-in. depth (Test 1)

The material models for the matrix and borehole grout were constructed from the stress/strain data of Fig. 4 and accompanying stress path and failure envelope data (see [1]). As indicated in Fig. 4, the matrix exhibited three layers, which were represented in the calculational mesh.

Numerical difficulties resulted in the calculation from the steeply stiffening stress/strain behavior of the grout at high strains (Fig. 4).

121

These, in turn, led to spurious oscillations that may be observed in the plots of the calculated grout velocity in Figs. 5 to 7. The punchdown effect in the calculations was confined to the very top of the borehole.

A frequency domain analysis of the calculated velocity responses showed that the response was essentially confined to a frequency range of 0 to 200 Hz, although the borehole response at the 54-in. depth extended to 500 Hz. At frequencies less than 200 Hz, the borehole and free-field responses differ within a factor of 2 at the two upper locations and a factor of 3-1/2 at the 54-in. depth.

Test 2: Tests 2 and 3 were conducted on the same matrix specimen that was used for Test 1. The matrix, therefore, showed progressive shock hardening in these tests. However there were no direct data on the properties of the matrix in Tests 2 and 3. For the calculation of Test 2, the properties of layer 2 of the Test 1 matrix (curve 3 of Fig. 4) were used to model the matrix.

Fig. 8 shows the excellent agreement between the calculated velocities in the borehole and the matrix at the 18-in. depth. Similar agreement was observed at other depths. The measured velocities, which are not shown (see [2]), also showed excellent correlation between borehole and free field. Thus, both calculations and measurements showed that locking the canister to the neighboring free field forced the canister to follow the free-field motion faithfully. The measured peak velocities at all depths were considerably smaller than the calculated peaks, indicating the discrepancy caused by not accounting for the shock-hardened properties of the matrix in the calculation.

Test 3: In calculating this test, an attempt was made to account for the shock-hardened properties of the matrix by using the measured responses in Tests 1 and 3 to back-calculate a set of matrix properties. In view of the uncertainties involved in such a procedure, a homogeneous, rather than a layered, matrix was assumed. The resulting stress/strain behavior of the matrix is shown in Fig. 9. Also shown is the stress/strain behavior of layer 2 of Test 1 (curve 3, Fig. 4) to facilitate an assessment of the degree of stiffening of the matrix from Test 1 to Test 3.
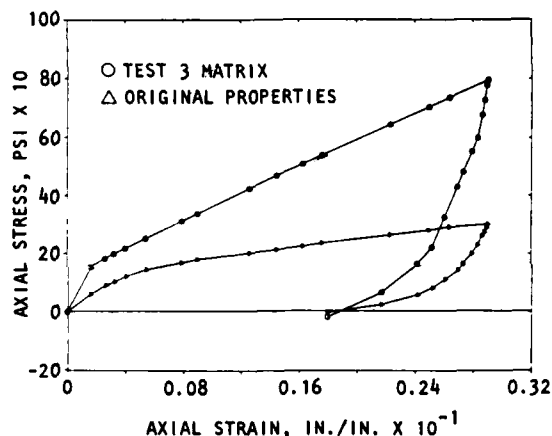
Fig. 9 – Uniaxial behavior of Test 3 matrix compared with original properties

A homogeneous grout with very stiff properties was used to fill the borehole in this test. The stress/strain properties of the grout and the model used to simulate it in the calculation are shown in Fig. 10.

The calculated and measured velocity responses in Test 3 are shown in Figs. 11 to 13. It is seen that the calculated velocities in the borehole and the matrix show excellent correlation at all depths. Likewise, the measured velocities in the borehole and the matrix show excellent agreement. The correlation between

Fig. 8 – Comparison of grout and free-field velocities at 18-in. depth (Test 2)

122

the measured and calculated velocities is good, but the calculated velocities show greater attenuation with depth.

A frequency domain analysis of the calculated results showed the velocity response to be essentially contained in the range of 0 to 200 Hz. The agreement between the borehole and free-field responses, however, was much better in

Test 3 than in Test 1, the two responses being within 15% of each other in the 0 to 200 Hz range.

Fig. 12 – Comparison of velocities at 36-in. depth (Test 3)

Fig. 10 – Comparison of model and data for borehole grout--Test 3 calculations

Fig. 11 – Comparison of velocities at 18-in. depth (Test 3)
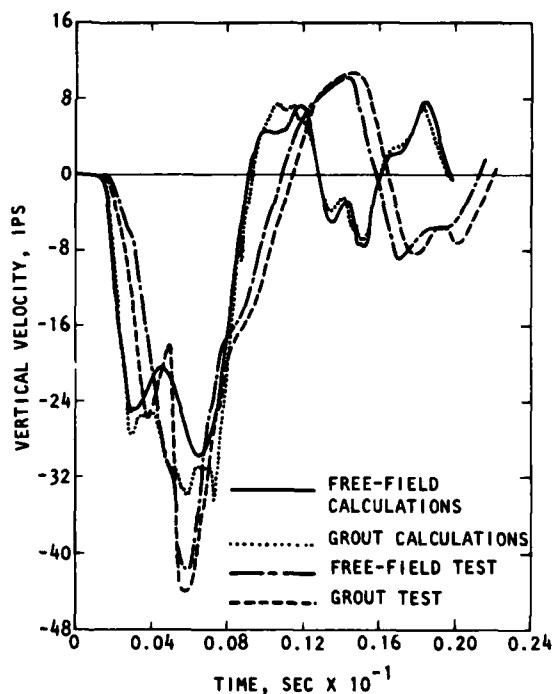
Fig. 13 – Comparison of velocities at 54-in. depth (Test 3)

123

4. DISCUSSION

The tests in this series covered a wider range of impedance mismatches than originally intended because of the excessively soft grout used in Test 1. However, the bond conditions at the borehole/matrix interface did not vary much from test to test. A strong bond was ensured in Test 2 by the use of the canister-locking grout; however, a moderately strong bond presumably existed in the other tests because of the use of expansive cement for the matrix. In the calculations, the slip elements were assigned shear properties based on the weaker material at the interface, and thus simulated a relatively strong bond. Thus, the calculations and measurements both indicate that if a strong bond exists between the borehole and free field, the borehole faithfully follows free-field motion even when the properties of the borehole and free-field materials differ appreciably. This observation was further confirmed by performing calculations under the extreme condition of no bond between the borehole and the free field, when the motions of the borehole and free field are independent and may be simulated by independent column calculations. Such calculations, of course, result in widely different responses if the borehole and free-field material properties differ much from each other.

The above considerations apply to the axial loading condition investigated in the present project. This condition is representative of the superseismic region in a field environment. In the subseismic region the stress wave impinges obliquely on the instrumentation borehole. In the specific case of velocity sensors, however, axial loading represents the worst case because of the possibility of slip at the borehole/free-field interface and because the pulse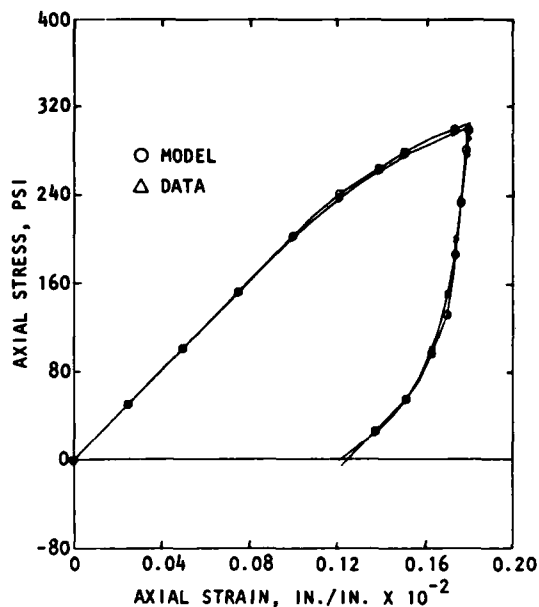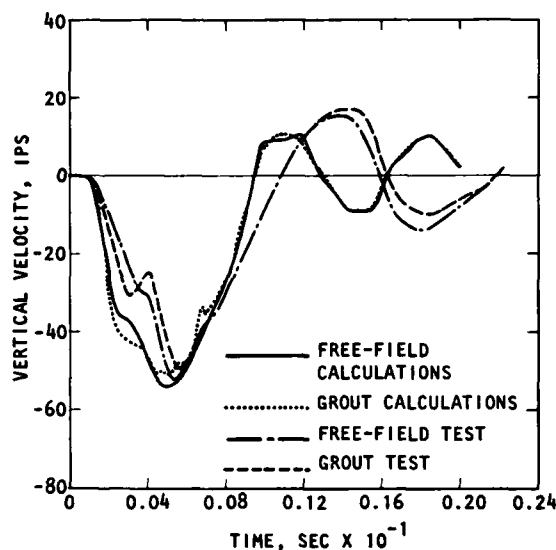 travels through a significant length of the borehole material before reaching the sensor. When the stress wave propagates transversely to the borehole, the pulse travels only a short distance through the borehole and furthermore, the borehole/free-field interface cannot lead to relative motion between the two. Therefore, in the transition from axial to transverse loading, the problem of the fidelity of velocity sensor records becomes less and less serious. Under transverse or oblique loading, however, there exists the possibility that velocity sensor records may become distorted because of the extrusion of grout through the borehole. A preliminary analysis of this problem is contained in [1].

This investigation established that gage-placement procedures should be aimed at ensuring a strong interface bond in the vicinity of the gages. In a field event, this objective may be achieved as in Test 2 by the simple expedient of using a stiff, expansive grout to surround the instrumentation canister. The remainder of the instrumentation borehole may be filled with a grout whose properties need not be closely controlled because they are not required to match the properties of the free-field medium. The emplacement of the gage is thus simplified.

Figs. 14 and 15 show the calculated stresses in the borehole and matrix at the 18-in. depth in Tests 1 and 3. The stresses in the borehole and free field differ in proportion to their stiffness as a result of the displacement and strain continuity induced by the good bond
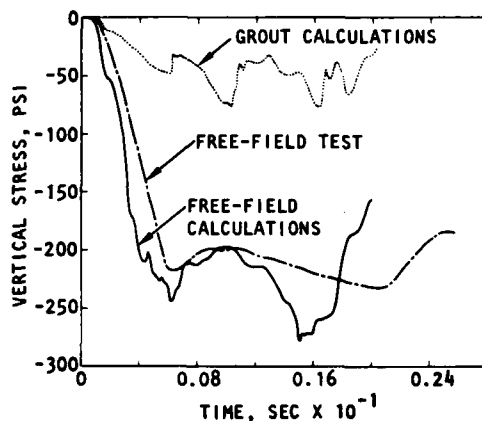
Fig. 14 - Comparison of calculated stresses with test data at 18-in. depth (Test 1)
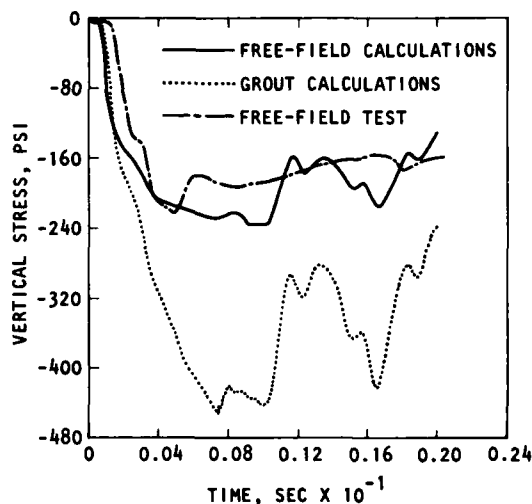
Fig. 15 - Comparison of calculated stresses with test data at 18-in. depth (Test 3)

124

at the interface. Test 1, which employed a much softer borehole grout, shows much lower stresses in the grout than in the matrix, whereas the situation is exactly opposite in the case of Test 3 with a stiff grout. Figs. 14 and 15 also show the measured stress in the free field at the 18-in. depth, and it is seen that the calculated and measured stresses show good agreement.

5. CONCLUSIONS

The principal conclusion emerging from this investigation is that good interface bond is the primary requirement for assuring that a velocity sensor will follow free-field motion faithfully. Furthermore, the velocity-measurement fidelity is achieved even in the presence of large imped-ance mismatches between borehole and free-field materials. It is therefore recommended that velocity gage canisters be locked into the free-field material by using a stiff, expansive grout locally around the canister in the borehole. Although attempts should be made to fill the bore-hole with a grout whose properties are close to those of the free field, this study shows that the fidelity of velocity measurements is insensitive to impedance mismatches and that, as a conse-quence, matching the impedances of the borehole grout and the free field is not critical. The expense and effort involved in preparing bore-hole grouts are, therefore, greatly reduced.

ACKNOWLEDGMENTS

REFERENCES

1. Grout/Soil Interaction and Velocity Gage Emplacement for Ground Shock Measurement, R-7364-7-4265. Agbabian Associates, El Segundo, California, Aug. 1976

2. J.K. Ingram and M.B. Ford, Effects of Backfill Properties on Ground Shock Measurements. USAE-Waterways Experiment Station, Vicksburg, Mississippi, Apr. 1976

3. J.K. Ingram, Development of a Free-Field Soil Stress Gage for Static and Dynamic Measurements, TR No. I-814. USAE-Waterways Experiment Station, Vicksburg, Mississippi, Feb. 1968

4. User's Guide for FEDRC Code, U-4700-3868. Agbabian Associates, El Segundo, California, May 1975

5. A.K. Bhaumik and D.P. Reddy, Material Models for Joints and Interfaces, R-7354-3602. Agbabian Associates, El Segundo, California, Apr. 1975

Discussion

Mr. Hastings (Systems Science and Software): When your tests were done, were the velocities parallel to the bore hole and would those conclusions also hold if the velocities were perpendicular to the bore hole?

Mr. Balachandra: No tests were performed in this program to address that problem but we made a few calculations and at this point we feel that this is true, however, there may be complications. These tests basically simulate a super-siesmic condition where there is essentially a vertical overpressure. There may be some difficulties when there is more of a two dimensional kind of wave propagation taking place. Other than that, I would think the conclusions hold even if the direction of the velocity is different.

COMPUTER-BASED TRANSPORTABLE

DATA-ACQUISITION AND CONTROL SYSTEM*

Dennis K. Fisher, Michael R. Posehn
Frank L. Sindelar, Henry H. Bell
Lawrence Livermore Laboratory, University of California
Livermore, California 94550

A computer-based transportable data-acquisition and control system for
use in laboratory physical testing has been developed through a top-down
design approach. The principal characteristics of the resulting system
are a versatile process interface, sophisticated on-line data reduction,
and ease of programming. Applications have included thermocouple data
acquisition, holographic interferometry, impulse-response testing, and
vibration shaker control.

INTRODUCTION

As the technology of weapons systems has
evolved, so has the variety and sophistication
of the physical testing needed to evaluate de-
signs. This testing, in turn, has placed
greater demands on the associated data-
acquisition and control systems. In response
to requests for additional data channels, higher
data rates, and on-line data processing, we have
developed a computer-based transportable data
acquisition and control (T-DAC) system.

The T-DAC system was designed to perform a
wide range of laboratory control and data-
acquisition/reduction tasks. A variety of ana-
log and digital input/output (I/O) devices give
process-interface flexibility, while a fast 16-
bit central processor provides the needed com-
putational power. The use of a high-level lan-
guage (Fortran) permits the rapid development
of application software. Thus far, applications
have included impulse-response testing, holo-
graphic interferometry, thermal-response test-
ing, and control of electrodynamic vibration
shakers.

This paper discusses the development philos-
ophy, hardware configuration, application soft-
ware, and field applications of the T-DAC sys-
tem.

APPLICATION AND DESIGN PHILOSOPHY

The T-DAC system was developed to fulfill a
specific role in physical testing. It was de-
signed to meet the needs of experimenters who
require real-time process monitoring, on-line
data reduction, or sophisticated data-
acquisition and control capabilities. The spe-
cific objectives in development of the system
were:

- Versatile process-interface hardware,
- Powerful user-oriented application soft-
  ware,
- Ease of programming,
- Transportability, with set-up/checkout
  time less than one hour.

The T-DAC system was not meant to compete di-
rectly with the channel × bandwidth × record-
time product of an instrumentation tape re-
corder, the absolute accuracy of a precision
digital voltmeter, or the computational power
of a large computer. But it was intended to
provide a serviceable compromise capability in
a package that can easily be transported to a
user's test facility.

A design team of four engineers and two
technicians developed the T-DAC system. Using
the principles of top-down design [1,2], they
first defined the overall hardware/software
operating characteristics. From these necessary
characteristics, the various functional modules
were specified, along with the interfaces be-
tween them. These modules were further subdi-
vided into basic functional units, and imple-
mentation of the units was then relegated to
either hardware or software. In many cases, the
designer has a choice between hardware or soft-
ware implementation, and the final decision must
be based on the relative advantages of each:
software is more flexible and is easier to

implement; hardware executes faster but tends to cost more. Sometimes the designer can defer the hardware/software decision by using software for a function until the more expensive hardware is clearly justified (e.g., initially using a fast Fourier transform [FFT] subroutine instead of a hardware array processor).

With the functional specification of a system complete, decisions then must be made as to whether modules can be readily purchased from a vendor or whether they must be developed in house. Descriptions of those parts of the T-DAC system that we felt could be purchased were developed into a formal specification and distributed for competitive bidding. In developing this specification, we carefully considered sizing of the system (printer speed, sizes of the central processing unit and mass memory, etc.) and the resources we needed for development, as well as application requirements. It has been our experience that for developmental systems such as T-DAC, developing the application software efficiently requires more system hardware and system software than does execution of the resulting code. We asked prospective vendors to compile, execute, and document a representative benchmark program, including expanded assembly-language listings, memory-load maps (for both compilation and execution) and execution times. We then purchased a system sized to give 50 to 100% more computing power than our estimated maximum requirement, plus additional room for expansion. Once the computer-system vendor had been selected, we began implementing the specialized application hardware and software.

One advantage of top-down development is that it permits members of the design team to operate in parallel, each responsible for various modules, with the interfaces carefully predefined. With this approach, coordination of effort, bookkeeping, and good communications are essential to avoid costly iterations and duplication of effort. In the case of the T-DAC system, one team member was assigned responsibility for combining the functional modules developed by the team (primarily software) into an executable code while maintaining and documenting a system "library." This approach, combined with regular team meetings, proved to be an effective method for managing the development program.

HARDWARE CONFIGURATION

The T-DAC computer system (Fig. 1) combines computational capability with process-interface flexibility. The 16-bit minicomputer system (Fig. 2) derives its performance from an efficient instruction set, floating-point hardware, large memory (64 k words), and a full complement of data-processing peripherals. These peripherals include a dual-drive 2.4-M-word disk memory, magnetic tape drive, card reader, and an electrostatic printer/plotter. The operator's console (Fig. 3) consists of a storage-type CRT graphics terminal with a control panel. The control panel contains arrays of pushbuttons and

Fig. 1 – Transportable data-acquisition and control (T-DAC) system

indicator lamps, turns-counting and slide potentiometers, and three LED displays. All control-panel functions may be commanded or read from high-level application software.

The process interface consists of a variety of analog and digital I/O devices. Five different analog-to-digital (A/D) converters are currently interfaced (Table 1). These devices range in accuracy from 8 to 12 bits, in sample rate from 0.1 kHz to 100 GHz, and in number of channels from 1 to 128. Both the B8100 and R7912* are standard, commercially available, high-speed transient-capture devices that we interfaced through a general-purpose logic I/O chassis. In the following paragraphs we will discuss those subsystems which have been developed or modified to meet the requirements of our particular applications.

As delivered by the vendor, the scan rate of the wide-range A/D (WRAD) converter was controlled by software, and therefore repetitive scanning could be accomplished only at relatively slow rates. By modifying the interface hardware, we were able to use a programmable interval timer to automatically initiate scans at a rate of up to a 20 kHz, or, alternatively, synchronize the WRAD to an external device. Use of the WRAD is discussed further under Applications — Thermocouple Data Acquisition and Holographic Interferometry.

The transient capture and command unit (TCCU) was developed in house for use in shock

---

*Reference to a company or product name does not imply approval or recommendation of the product by the University of California or the U.S. Energy Research & Development Administration to the exclusion of others that may be suitable.

128
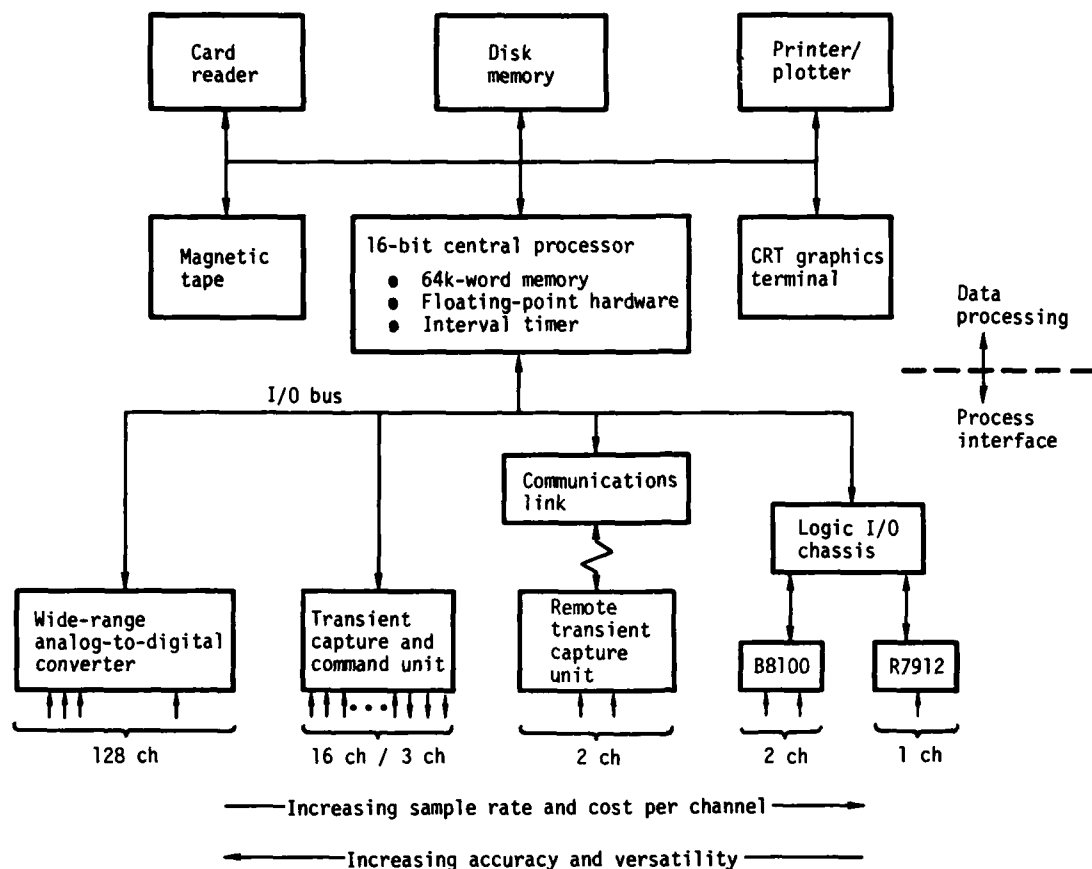
Fig. 2 - Block diagram showing principal components of T-DAC computer system
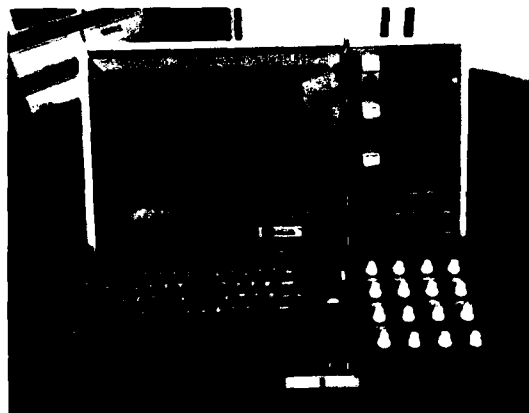
Fig. 3 - CRT graphics terminal with operator's control panel

and vibration testing (see Applications — Impulse-Response Testing and Vibration-Shaker Control). The TCCU is capable of simultaneously sampling up to 16 channels of analog input data while synchronously outputting analog commands on three other channels. The amplifier gains, cutoff frequencies of the anti-aliasing filters, sample rate, and hardware-triggering modes are all software programmable. A "pretrigger memory" feature, which can be set to record 0 to 95% of the data frame prior to triggering, has proved invaluable for data acquisition in shock testing.

The T-DAC system also supports a microcomputer-based, two-channel remote transient capture unit (RTCU, Fig. 4). This subsystem, produced commercially for use with a dial-up time-sharing service, is capable of acquiring and displaying raw data in stand-alone operation, or alternatively transmitting captured data to the T-DAC system for remote processing. Because of acoustically coupled 1200-Baud modems on both

129

Subsystem	Resolution (bits)	No. ch. avail.	Max. sample rate (Hz)		Max. data points	
			Per ch.	Total	Per ch.	Total
Wide-range A/D (WRAD)	12	128	20×10^3	20×10^3	4096	0.52×10^6
Transient capture and command unit (TCCU)	12	16	300×10^3	300×10^3	4096	16,384
Remote transient capture unit (RTCU)	10	2	200×10^3	400×10^3	4096	8192
Transient capture unit (B8100)	8	2	100×10^6	100×10^6	2048	2048
Transient capture unit (T7912)	9	1	100×10^9	100×10^9	512	512

the T-DAC and RTCU, neither system needs to be at a fixed location.

The T-DAC system is transportable in that it is mounted on castered carts that are easily moved by hand or fork lift, requires no extraordinary cooling, and can be packed or set up in less than an hour. Except for a few structural brackets and straps, none of the equipment has been "ruggedized" or modified to survive occasional transportation of the system. Over the past year the system has been moved approximately ten times, and there has been no damage during transit.

SOFTWARE CONFIGURATION

In recent years, available system software for minicomputers has advanced substantially. The T-DAC system reflects this trend in that the vendor supplied a Fortran-oriented, disk-based, multiprogrammable real-time operating system. Handlers with high-level access were provided for every peripheral device delivered. The Fortran compiler is compatible with ANSI standard X3.9 1966, and contains the real-time extensions needed for data acquisition and control from a high-level language. These extensions include routines for inputting and outputting through analog devices, task scheduling, interrupt utilization, and many other functions that must be performed relative to time.

The use of a high-level language such as Fortran offers many advantages. For logical or mathematical coding, programming a task in a high-level language requires only 1/3 to 1/5 the time it would in assembly language [3]. For a system such as T-DAC, which has many different users and application programmers, Fortran has the advantage that most engineers and scientists are familiar with its use. Although any given task written in Fortran results in object code that is significantly larger and therefore slower to execute than the assembly-language

coded counterpart, there are very few applications time-critical enough to require assembly-language coding.

Much of the data is processed through GPDAP, a Fortran-coded general-purpose data-acquisition and processing code. In designing the software, we gave considerable attention to the novice computer user by including simple option "menus" (see Fig. 5), free-formatted inputs, extensive checking for operator-response errors, and use of the control console. At any point in a
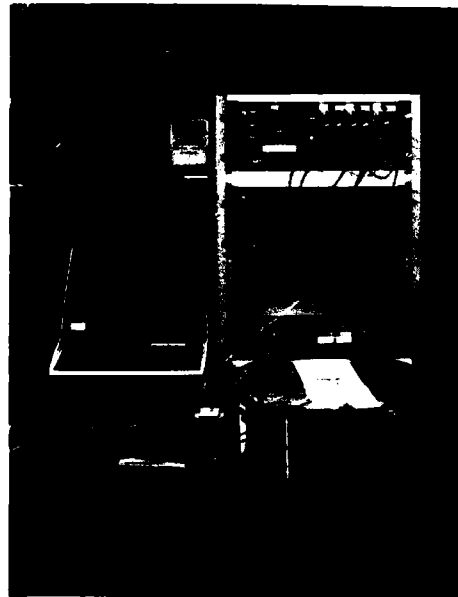

Fig. 4 - Microprocessor-based remote transient capture unit (RTCU)

```
┌─────────────────────────────────────────────────────────────┐
│ GENERAL PURPOSE DATA-ACQUISITION/ANALYSIS PROGRAM             │
│ ***********************************************************    │
│                                                               │
│ MAIN OPTIONS - ENTER LINE NUMBER AND PARAMETERS FOR           │
│               DESIRED OPTION.                                 │
│               IF I = O, LIST OF CHANNELS WILL BE REQUESTED    │
│                                                               │
│  1.  DATA PROCESSING COMPLETE - EXIT PROGRAM                  │
│                                                               │
│  2.  SUMMARIZE DATA TAPE                                      │
│                                                               │
│  3.  READ TAPE FILE N (ENTER "3,N" WHERE N IS DESIRED FILE)   │
│                                                               │
│  4.  TIME-DOMAIN DATA MANIPULATION OPTIONS                    │
│                                                               │
│  5.  FREQUENCY-DOMAIN DATA MANIPULATION OPTIONS               │
│                                                               │
│  6.  PLOT CH I .VS. TIME/FREQUENCY (ENTER 6,I)                │
│                                                               │
│  7.  PLOT CHANNEL I .VS. CHANNEL J (ENTER 7,I,J)              │
│                                                               │
│  8.  CONTOUR / 3-D PLOTTING OPTIONS                           │
│                                                               │
│  9.  WRITE CURRENT DATA BASE TO TAPE                          │
│                                                               │
│ 10.  LIST DATA FOR CH I (ENTER 10,I)                          │
│                                                               │
│ 11.  DEFINE / MODIFY HEADER INFORMATION                       │
│                                                               │
│ 12.  DATA-ACQUISITION OPTIONS                                 │
│                                                               │
│ 13.  OUTPUT PLOT-FILE                                         │
└─────────────────────────────────────────────────────────────┘
```

Fig. 5 - Main option "menu" from GPDAP data-processing code

question-and-answer sequence, the user can back up and modify one of his earlier responses, substitute a default answer, repeat a question, or invoke a built-in English/SI-units converter. Also, for any option that requires a channel number, the user can specify a list of channels, thereby invoking a built-in "DO-loop" capability.

The GPDAP code has a tree-like organization (Fig. 6) in which the user may progress down through the structure in a constantly expanding series of option lists until the required specific function is reached. This organization has two principal advantages: the user is exposed to the more detailed options only if he specifically requests them, and he can very easily add new functions at the most detailed level by simply extending an option list. All functions access a single data base, which supports up to 128 data channels of 4096 values each. Each channel has a backup or "stored" copy that the user can "recall" using one of the options for manipulating data in the time or frequency domain. The data base automatically keeps track of the types of transformed variables (real, complex, etc.) so that function requests will be properly interpreted. In general, processing data via GPDAP is no more difficult than using a pocket scientific calculator.

Plotting may be done in either two or three dimensions (2-D, 3-D). In 2-D plotting the contents of one or more data channels are displayed versus either time, frequency (if appropriate), or another data channel. The 2-D axes may be specified as either linear or logarithmic, and may be scaled either automatically or manually (thereby introducing a zoom capability).

Two types of 3-D plotting are available: pseudo 3-D and true 3-D. In pseudo 3-D plotting, an array of data channels are plotted on the same 2-D grid, but successive channels are successively offset in the direction of +x and +y to form a 3-D image. True 3-D plotting requires that the user supply a card deck defining the x- and y-axis coordinates of each data channel in the array to be plotted; GPDAP interpolates the contents of each data channel at some specified value of time to get the z-axis coordinate. The resulting "surface" can then be plotted as a contour "map", or as a 3-D perspective image. Both 2-D and 3-D plots are displayed first on the CRT terminal. If the user wishes a hard copy, he responds with a "C" at the completion of the plot and GPDAP will write the appropriate data to a disk-based plot-file. This plot-file is later output to the electrostatic printer/plotter at the user's convenience. Examples of
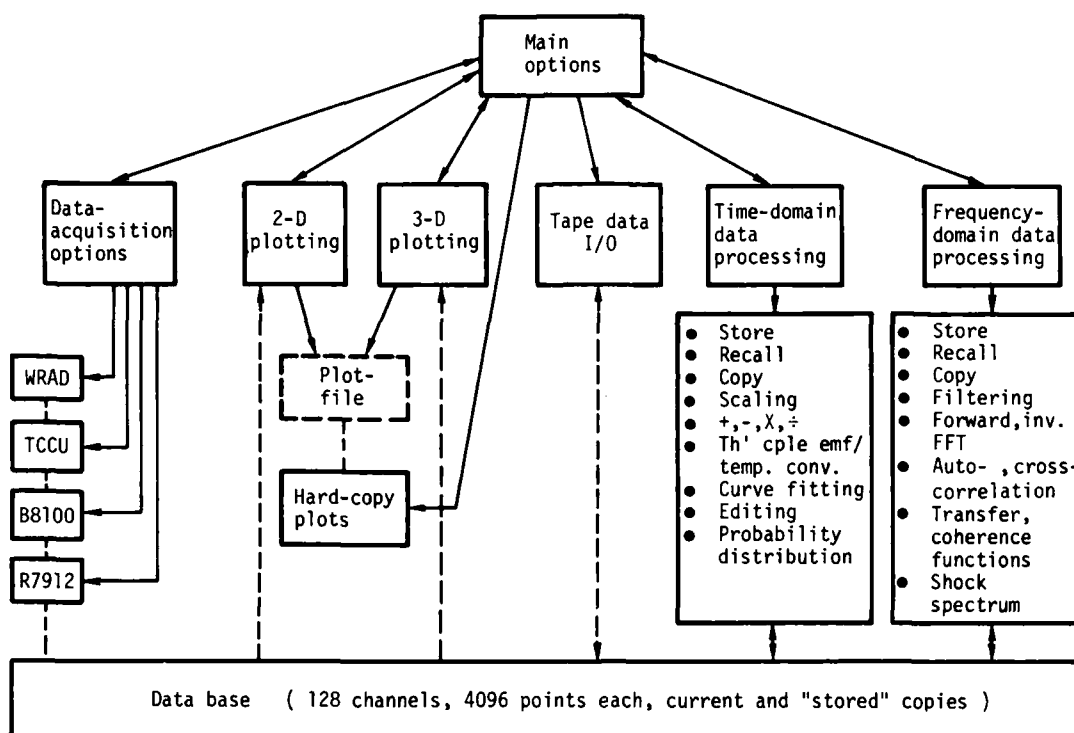
Fig. 6 - Block diagram of GPDAP — general purpose data-acquisition and processing program

the various types of plotting have been used to illustrate the following section covering applications of the T-DAC system.

APPLICATION EXPERIENCE

In the following paragraphs we will discuss four specific applications that illustrate the capabilities of the T-DAC system.

Thermocouple Data Acquisition

A special application code called "TCD" was developed to continuously record and display up to 128 channels of slow-speed data acquired via the WRAD subsystem. In auto-range operation, the WRAD automatically adjusts its 12-bit resolution over a full-scale range of 5 mV to 10.0 V, making it ideal for taking data from thermocouples or strain gages. Although the WRAD has a maximum auto-range sample rate of 6 kHz, the maximum effective continuous record rate achieved by TCD is 2 kHz, because the data must be buffered to the moving-head disk. Therefore, depending on the number of channels being acquired, the maximum available sample rate per channel can vary between 20 and 100 Hz.

The maximum recording time available through TCD is limited by the total number of points per channel that can be processed by GPDAP (4096). To use the data space effectively, the operator

defines his sample rate in either of two ways. By the first method, the sample rate is specified in advance to follow a predetermined schedule. If appropriate, the operator can manually adjust the sample rate during the test. This method is used when the dynamics of the experiment can be predicted with some confidence. The second method allows the sample rate to adapt itself to suit the rate of change of the data. This self-adaption is a data-compression technique wherein the data is actually sampled at the maximum available rate, but recorded only if the data exceeds a specified threshold relative to the last stored value. A minimum recording rate may also be specified to guarantee recording during static test periods. This self-adaptive sampling technique has proved effective in applications such as creep testing, where there may be an unpredictably long period of inactivity followed by a relatively fast data rate.

During the test, the data for all of the channels is displayed on the CRT screen as a plot of temperature (or other engineering unit) versus channel number (Fig. 7). This plot is updated approximately every 2 s. Since the display is a storage-type CRT, the entire history of the test can be assessed at a glance.

The data acquired by TCD is recorded in a format compatible with the GPDAP data-processing code. To date, most of our experience with this
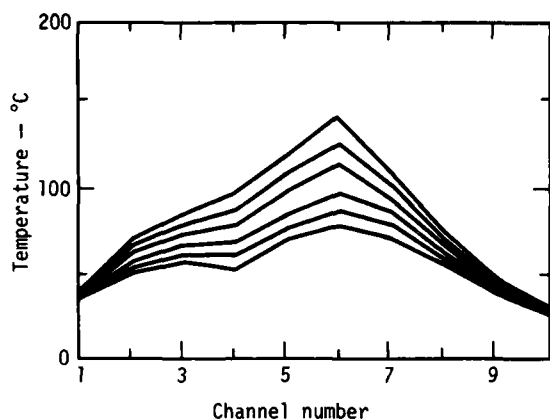
132

Fig. 7 - Reconstructed "real-time" plot produced by TCD code during acquisition of thermocouple data

code has been with large arrays of thermocouples in which we used 3-D plotting (Fig. 8) to visualize the distribution and intensity of various exothermic chemical reactions.

Holographic Interferometry

A high-resolution holographic interferometric technique, accurate to 0.1 wavelengths, has been developed at LLL for use in the critical inspection of glass laser elements [4]. The technique has also been used to measure extremely small dimensional changes of an opaque object. High-resolution holographic interferometry, a variation of double-exposure holographic interferometry, involves the recording of two separate holograms on a single film plate by separate but related laser beams. The holograms are then reconstructed by simultaneous use of both reference beams to form an interferogram. Finally, the phase of one of the reference beams is varied optically to permit precise interpolation between fringes.

The T-DAC system is used to digitize the resulting interferogram and process the data as follows. The interferogram is read out by a charge-coupled-device imaging camera at a rate of 50 ms per frame. The camera has clock, end-of-frame, and end-of-line pulses, which are sent to a controller (Fig. 9). The controller synchronizes the sample rate of the WRAD system to the camera, thereby enabling the system to digitize the output of the 32 × 32 photodiode array.

As the optical phase shifter in one of the reference beams of the reconstructed interferogram is rotated through 90 deg by a stepper motor, the interference fringes shift by one position. Each element of the photodiode array goes through a full cycle of light and dark that depends on the relative phase of that point in the image. We wrote a special real-time data-reduction routine to synchronously detect the relative phase of each element as the phase

shifter is stepped through 90 deg. Additional software developed for this application (a) converts the data to a continuous phase surface normalized to zero phase at the center, (b) discriminates and masks the subject from the background using as a criterion the probability-density-distribution function of the image intensity, and (c) smooths the data using a 2-D convolution filter.

The fully reduced data is displayed as either a phase-contour surface or a perspective image by the standard T-DAC 3-D plotting software. Typical results, measuring thermal distortion of a metal gage block, are shown in Fig. 10.
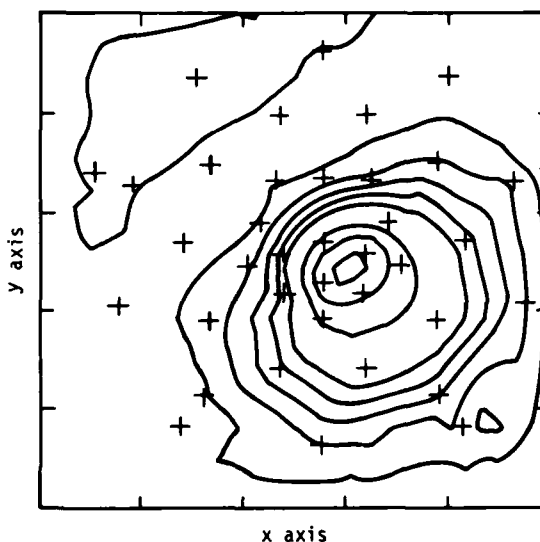
(a) Equispaced isotherms with thermocouple locations indicated by "+"
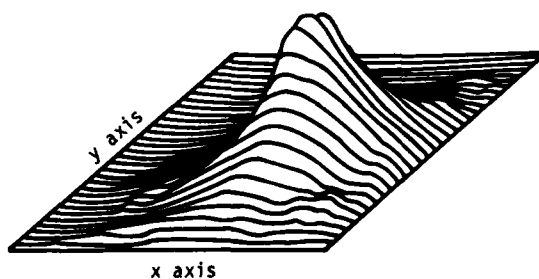
(b) True 3-D perspective view of temperature surface

Fig. 8 - Temperature data acquired from thermocouples by the TCD code during exothermic chemical reaction
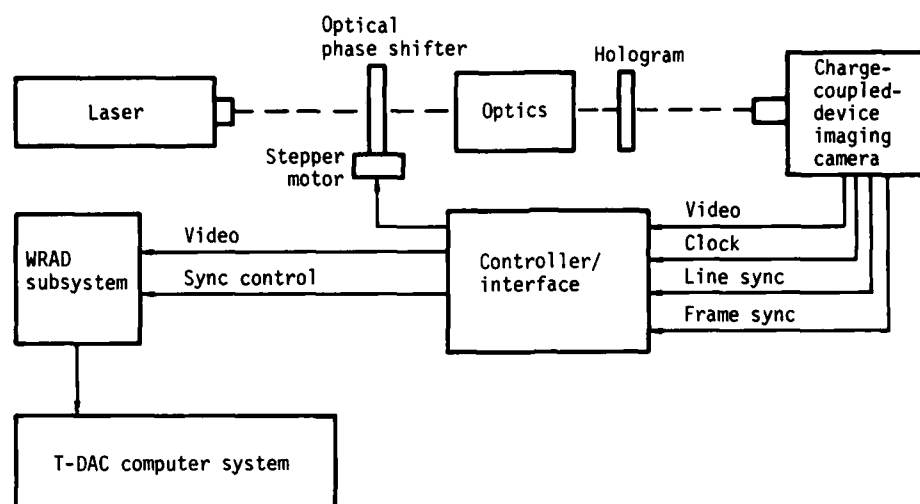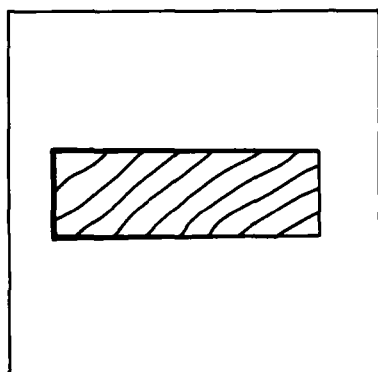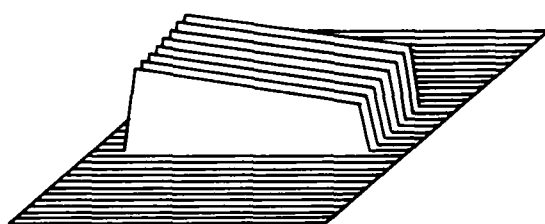
133

Fig. 9 – System diagram for reconstruction and digitizing of high-resolution holographic interferograms

(a) Contour diagram; contours are at each 63 Å of thickness distortion

(b) Perspective image

Fig. 10 - Phase surface of thermally distorted gage block as measured by high-resolution holographic interferometry

Impulse-Response Testing

Impulse-response testing is a technique for determining the dynamic response characteristics of a structure [5,6]. The structure is excited by a blow from an instrumented hammer, and both the force input and the structure acceleration responses are captured. Spectral analysis techniques are then used to determine the natural frequencies of vibration, mode shapes, and mechanical impedances between points on the structure.

The TCCU captures up to 16 input and response data channels at a time. Repeated impulses, for up to a total of 128 inputs or responses, can be accumulated in the GPDAP data base for subsequent processing. Normally, the TCCU is used in its pretrigger-memory mode to ensure that the leading edge of each transient is captured.

In impulse-response testing, the hammer blow must excite the structure uniformly over the frequency range of interest. The bandwidth and intensity of the hammer impulse may be tailored to the structure by the choice of tip material and hammer weight. A very wide impulse bandwidth is undesirable in that it tends to excite local response modes and may lead to aliasing problems. In our experience, we have had satisfactory results using a commercially available 300-g hammer with interchangeable plastic, aluminum, and steel tips and attachable steel ballast weights. After some initial survey taps, the TCCU programmable filters are set to a cutoff frequency equal to the bandwidth of the hammer being used, and the data sample rate is set to three times the filter bandwidth to avoid aliasing. The total data frame must be long

134

enough to allow the responses to decay to about 5% of their peak amplitude. Otherwise, the transients will be significantly windowed, thereby introducing errors into the spectral calculations.

The spectrum and transfer-function calculations are performed through the GPDAP options for manipulating in the frequency domain. Multiple impulses are automatically averaged, and for transfer functions the related coherence function is also computed (Fig. 11). We have found this function to be valuable in interpreting the results of impulse-response testing.

Impulse testing with the T-DAC system has been used to verify the results of computer simulations and as a nondestructive i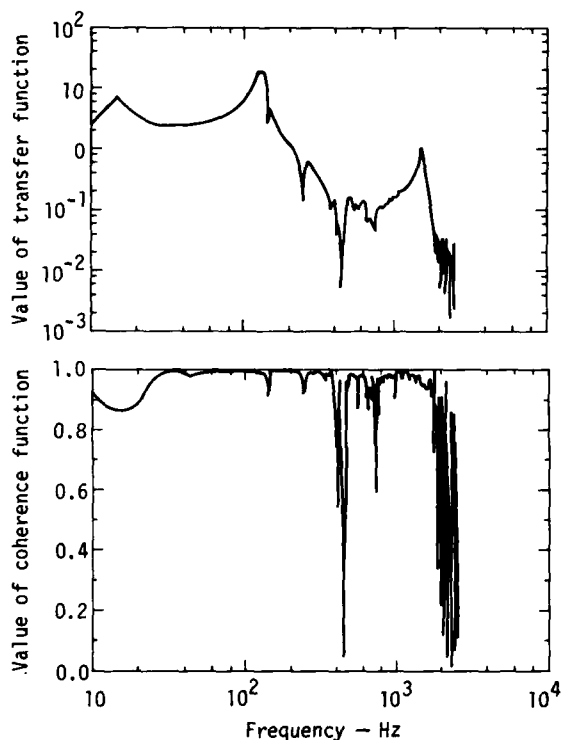nspection technique. For the latter, the relevant transfer functions of an assembly were compared before and after a shock test to determine whether or not structural damage had occurred.

Vibration Shaker Control

The T-DAC system has also been used to effect transient-vibration control of an electrodynamic shaker. One of the TCCU analog output channels is used for the dynamic command, and an A/D channel is used to monitor the response acceleration. Fifteen bits of resolution on the command channel plus gain ranging on the response channel result in an effective dynamic range of 80 db. The control console is programmed such that, during execution of the test, the operator can interact by adjusting calibration levels, displaying data on the CRT, or calling for a pause in a series of pulses. In addition, the LED readouts are used to display response levels and pulse counts.

In transient-waveform control of vibration shakers, the objective is to compensate for the response characteristics of the electrodynamic shaker so as to obtain some specified response waveform. As is now commonly done [7], a series of low-level pulses are used to estimate the system-transfer function. The Fourier transform of the desired waveform is then multiplied by the inverse of the system-transfer function to give the Fourier transform of the compensated command. Inverse transformed, this becomes the initial command pulse. If the transient is repeated, the system corrects the compensated command using the measured error, the inverse of the system-transfer function, and the corresponding coherence-function estimate [8].

All response data is stored on the moving-head disk during the test. Post-test, hard-copy plots can be made of each response waveform (Fig. 12), each Fourier spectrum, or each acceleration-shock response spectrum. In addition, pseudo 3-D plots (see Fig. 13) can be generated for comparing the responses to different transients or repetitions of the same transient.

Fig. 11 - Results of impulse-response testing of a mechanical assembly
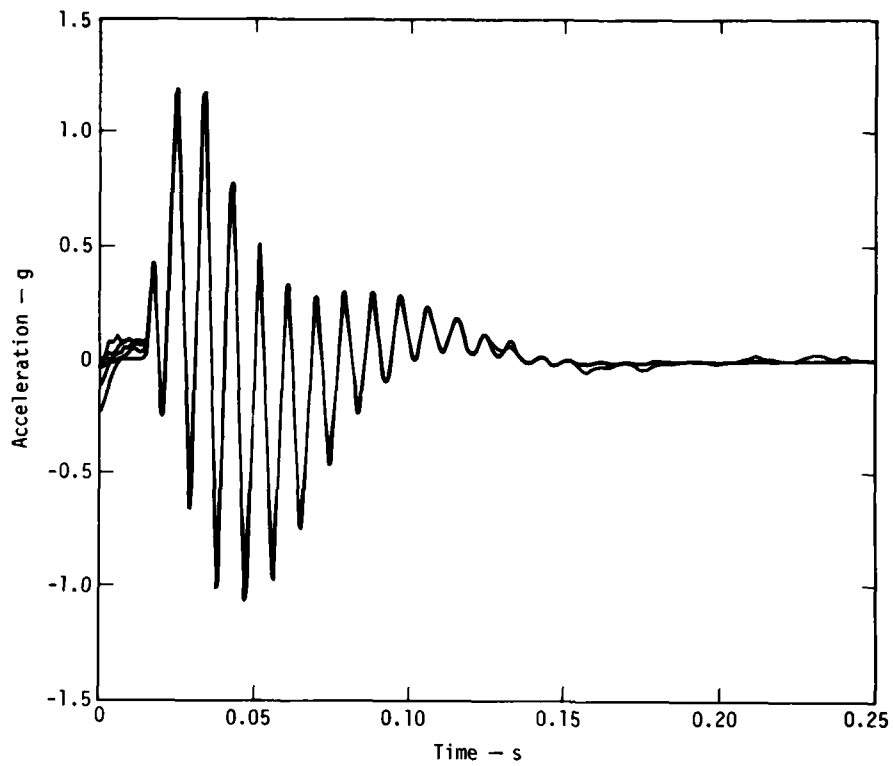
ACKNOWLEDGMENTS

Fig. 12 - Superposition of a desired transient on ten actual repetitions as produced on an electrodynamic shaker with the T-DAC system
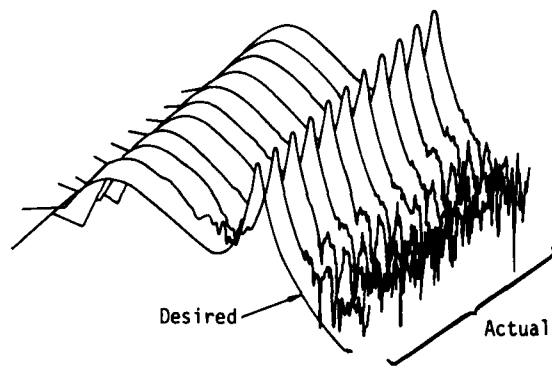

Fig. 13 - Pseudo 3-D plot of the Fourier spectra of the transients shown in Fig. 12

136

REFERENCES

1. H. D. Caplener and J. S. Janku, "Top-Down Approach to LSI System Design," Computer Design, Vol. 13, No. 8, pp. 143-148, Aug. 1974

2. D. K. Fisher and F. W. Holloway, "Process Control Computer System Development: A Philosophy," Lawrence Livermore Laboratory Rept. UCRL-76112, October 23, 1974

3. B. W. Boehm, "Software and Its Impact," Datamation, Vol. 19, No. 5, pp. 48-59, May 1973

4. "High-Resolution Holographic Interferometry: A New Technique," Energy and Technology Review, Lawrence Livermore Laboratory Rept. UCRL-52000-76-1, pp. 1-6, Jan. 1976

5. Mark Richardson, "Modal Analysis Using Digital Test Systems," Seminar on Understanding Digital Control and Analysis in Vibration Test Systems, Pt. 2 pp. 43-64. Shock and Vibration Information Center, Washington, D.C., 1975

6. M. L. Drake and J. P. Henderson, "An Investigation of the Response of a Damped Structure Using Digital Techniques," Shock and Vibration Bulletin, Vol. 45, Pt. 5, pp. 83-97, June 1975

7. J. D. Favour, "Transient Waveform Control — A Review of Current Techniques," J. of Environ. Sci., Vol. 17, No. 6, pp. 9-19, Nov./Dec. 1974

8. D. K. Fisher and M. R. Posehn, "Digital Control System for a Muliple-Actuator Shaker," this bulletin.

DISCUSSION

Mr. Hastings (Systems Science and Software): How available is this system and what is its total cost?

Mr. Fisher: The hardware, exclusive of the in-house development equipment and the high-speed transient capture units, represents a purchase of around $80,000. The transient capture command unit costs $20-25K. Each one of the high speed transient capture units cost on the order of $12÷15K. The remote transient capture unit costs on the order of $20K. Manpower that went into it probably represents two man-years of effort. That is low because we have done a number of other systems similar to this and we brought it all together in this one. We have used a great deal of existing software. For instance, most of the spectral analysis software existed for a shaker control application. We only had to write a "GP DAP" program to make it a calculator-type program.

Voice: What are the word size symbols for the Biomation and the Tektronix high speed capture units?

Mr. Fisher: The Biomation is 8 bit and the Tektronix 7912 is nominally 9 bit. It has a resolution of 512, but it is more like 8½ bits in the way it works. You have to interpret the data as they come back. It actually writes on a diode array and there are 512 diodes in a row; the beam is a little sloppy and you might get it on two diodes, so you have to guess which one it is on, or what to do with it.

LOADS AND ENVIRONMENTS

VIBRATION INVESTIGATION OF A LARGE TRANSPORT HELICOPTER

William J. Snyder and Jeffrey L. Cross
NASA Langley Research Center
Hampton, Virginia

and

Michael B. Schoultz
University of Virginia
Charlottesville, Virginia

Low-frequency vibration measurements were made during flight tests of a large transport helicopter throughout its flight envelope. Adjustments made to the rotor blade track characteristics indicate a significant reduction in vibration at blade passage frequency in some parts of the helicopter. These experiments indicate the potential of rotor system modifications for reducing rotor-induced vibrations.

INTRODUCTION

Throughout the history of helicopter development, vibration has plagued the helicopter designer. Early rotor designs resulted in intolerable vibration levels that resulted from rotating wings in an asymmetric flow field (fig. 1) with almost every conceivable type of excitation at the rotor speed and its harmonics. Advancements in blade and rotor design and in isolation and absorption systems have made the helicopter a useful tool for a great many civil and military applications (ref. 1). However, if projected growth in the fields of passenger transportation for executive markets, industrial support, and short-haul transport is to be realized, further reductions in helicopter vibration levels must be accomplished to improve comfort and reduce maintenance costs.

The NASA Civil Helicopter Technology Program is directed at investigating the technology, resources, and operational requirements for acceptable future civil helicopter systems and operations. This includes acceptance by all elements of the system - operators, users, regulatory agencies, and communities. One of the primary areas of interest to the program is vibration and its effect on the acceptance of civil helicopters. Current vibration research is directed at investigating the vibration characteristics of helicopters utilizing the NASA CH-53 civil helicopter research aircraft, shown in figure 2, as the primary flight research tool.

This paper will present data measured during the program, including a comparison of the standard aircraft with the aircraft when the rotor was split-tracked. A complete description of the overall civil helicopter flight research program can be found in reference 1.

RESEARCH AIRCRAFT

The NASA civil helicopter research aircraft (fig. 2) is a modified military transport helicopter representative of the size and technology level for the next generation of civil helicopter transport for passenger and utility use. The aircraft is an uprated version of the CH-53A and incorporates an air-conditioned and acoustically treated 16-seat passenger cabin for subjective ride environment experiments. The helicopter is a single main rotor with tail rotor configuration, with a fully articulated (hinged) six-bladed main rotor. It has a nominal gross weight of 16,330 kg (36,000 lb). The other characteristics of the aircraft are listed in table I. The primary structural layout of the aircraft can be seen in figure 3. A more complete description of the aircraft can be found in references 1 and 2.

INSTRUMENTATION AND DATA REDUCTION

The CH-53 instrumentation system is equipped to measure 12 channels of vibration data up through the twelfth harmonic of the 3.1-Hz rotor speed. Seven fuselage stations
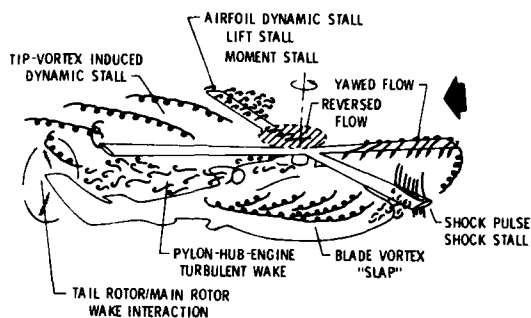
Figure 1.- Helicopter rotor transient
aerodynamics - full cycle in 1/5 sec.
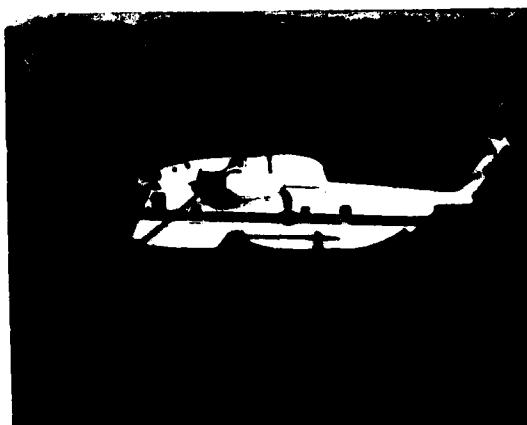
Figure 2.- NASA CH-53 civil helicopter research
aircraft.

TABLE I. - CH-53 PHYSICAL CHARACTERISTICS

Characteristic	Metric	English
Empty weight	11575.0 kg	25525.0 lb
Gross weight	16330.0 kg	36000.0 lb
Main rotor station	8.5 m	336.4 in.
Main rotor radius	11.0 m	36.0 ft
Number of blades	6	6
Blade chord	0.7 m	2.16 ft
Tail rotor radius	2.4 m	8.0 ft
Number of blades	4	4
Blade chord	0.4 m	1.28 ft
Shaft-tilt longitudinal	5° fwd	5° fwd
Disc loading	394.0 N/m^2	8.23 lb/ft^2
Number of engines	2	2
Engine power (each)	2.95×10^6 W	3950.0 hp
Maximum cruise speed	315.0 km/hr	170.0 knots

Figure 3.- CH-53A general structural layout.

Figure 4.- General location of accelerometers
in NASA CH-53 helicopter.

140

are used for measuring vertical (normal) accelerations, as shown in figure 4, while four stations are utilized for lateral acceleration. Longitudinal acceleration is measured only at the aircraft's center of gravity. Each of the accelerometers are the servo-type and are ranged for 0-40 Hz and an amplitude range of ±1.0 g, with the exception of the lateral and vertical accelerometers in the aircraft tail boom. The tail acceleromete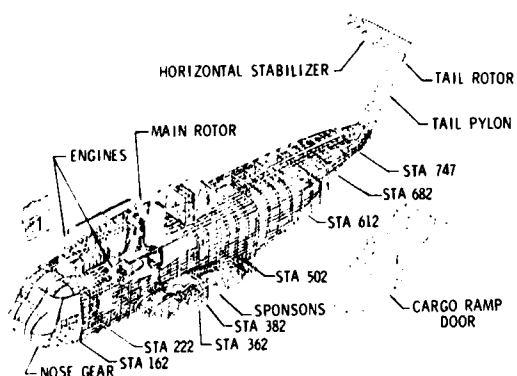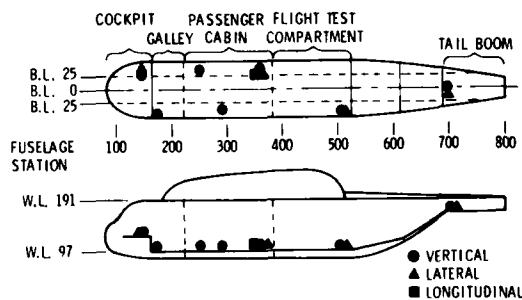rs are ranged for 0-100 Hz in frequency and ±2.5 g in amplitude. Rotor rpm is recorded through the use of a once-per-revolution pickup on the rotor shaft. All data were recorded via multiplexing on four channels of the onboard FM tape recorder. A complete description of the other components of the instrumentation system not related to vibration measurements can be found in reference 2.

The FM recorded data are filtered using a 60-Hz filter, digitized, then processed through the NASA-Langley computer center. The primary data output has been time histories, power spectrums, and harmonic analyses. To accomplish the harmonic analyses, the rotor rpm indicator was utilized to account for variations in rpm during the data sample. The data sample for the harmonic analyses was a time interval equal to 30 revolutions of the main rotor. Fourier coefficients through the eleventh harmonic were calculated. The data were also analyzed by filtering the FM data through 24-Hz filters prior to digitizing. This eliminated all harmonics of rotor speed above blade passage frequency and allowed the estimation of relative phase difference between the various accelerometer outputs.

RESULTS AND DISCUSSION

Sources of helicopter vibration.- Helicopter vibration is primarily the result of complex aerodynamic and dynamic forces in the rotor system that are propagated to the fuselage as forces and moments. Shear forces at the rotor hub occur in both the horizontal and vertical plane. Inplane (horizontal) forces result in both oscillatory moments and direct oscillatory forces to the fuselage in both the lateral and longitudinal directions. Vertical hub forces are transmitted directly to the fuselage.

The symmetry of the rotor system provides isolation of the fuselage from vertical forces at rotor harmonics that are not integer multiples of the number of blades. It can be shown that vertical blade forces at all rotor speed harmonics that are not integer multiples of the number of blades (harmonics of blade passage frequency) will cancel unless the rotor is not tracked and balanced properly. Vertical blade forces at blade passage frequency harmonics, however, add at the rotor hub (ref. 4). It can also be shown by simple trigonometry that inplane forces will combine at the rotor hub in a somewhat different manner

with a resulting hub force at blade passage frequency. Blade passage frequency thus becomes the predominant forcing frequency for helicopter vibration. Most of the following discussion will be directed at vibration inputs at blade passage frequency which is 18.5 Hz for the CH-53.

Flight research experiments.- The five basic configurations flight tested during the vibration phase of the program are outlined in table II. Two additional flights investigated rpm variations and maneuvers. Vibration measurements were also taken during the other phases of the flight program with the CH-53, including approximately 20 flights with subjects that were flown in conjunction with passenger acceptance studies. Only the standard aircraft configuration and the split-blade track configurations will be discussed in this paper. The flight conditions flown during each of the five primary vibration flights are listed in table III.

The standard aircraft, as tested, had a gross weight of approximately 14,000 kg (31,000 lb) and an aft c.g. location at station 348 (approximately 30.5 cm (12 in.) aft of rotor centerline). The split-track configurations involved changing the incidence angle of some of the blades, resulting in those blades flying a set amount higher than the remaining blades. One example of this configuration is illustrated in figure 5. The split-track experiments were undertaken to (1) investigate the effects of minor changes in rotor parameters on fuselage vibration levels at blade passage frequency and (2) to investigate the effects of blade track on vibration levels at harmonics of rotor speed that are not integer multiples of the number of blades.

Standard aircraft flight experiments.- Figure 6 presents a typical time history of data for the vertical accelerometers at the pilot's station and the center-of-gravity (c.g.) station for an airspeed of 120 knots. It is readily seen that blade passage frequency (18.5 Hz) is the predominant frequency. These time histories were taken with the aircraft in its standard configuration.

Figures 7 through 13 show the variation of vertical vibration amplitudes at blade passage frequency with airspeed for the accelerometers located in the cockpit, cabin, flight engineer's station, and tail for the standard aircraft configuration. Lateral vibration levels are similar at somewhat reduced amplitude, as seen in figure 14. The levels presented are calculated blade passage frequency Fourier coefficients averaged over 30 cycles of the fundamental frequency. It can be noted that the highest vibration levels occur at the lower airspeeds where the rotor wake is not blown down and away from the rotor disc.

In general, it can be seen that vibration levels in the cabin remain below 0.1 g at

141

TABLE II. - CONFIGURATIONS INVESTIGATED DURING CH-53 VIBRATION STUDIES

Configuration	Description
1. Basic aircraft	Aft c.g. location; 14000 kg (31000 lb) gross weight
2. Blade out-of-track	Every other blade tracked 1.3 cm (1/2 in.) high
3. Blade out-of-track	Every other blade tracked 2.5 cm (1 in.) high
4. Blade out-of-track	Two opposing blades tracked 1.3 cm (1/2 in.) high
5. Ballasted aircraft	15000 kg (33000 lb) gross weight; c.g. at shaft centerline

TABLE III. - PRESCRIBED FLIGHT CONDITIONS FOR CH-53 VIBRATION RESEARCH FLIGHTS

| Condition No.	Description
1	Hover in ground effect
2	Hover out of ground effect
3-16	Steady level flight at 20, 30, 40, 50, 60, 70, 80, 90, 100, 110, 120, 130, 140, and 150 knots
17-22	Steady climbs or descents 300 m/sec (100 ft/min) climb at 50 knots 150 m/sec (500 ft/min) descent at 50 knots 300 m/sec (1000 ft/min) climb at 90 knots 300 m/sec (1000 ft/min) descent at 90 knots 300 m/sec (1000 ft/min) climb at 130 knots 450 m/sec (1500 ft/min) descent at 130 knots
23	Final approach and landing
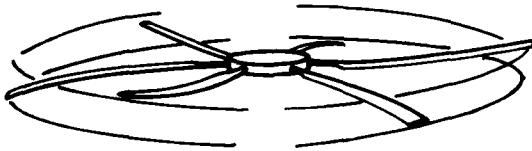
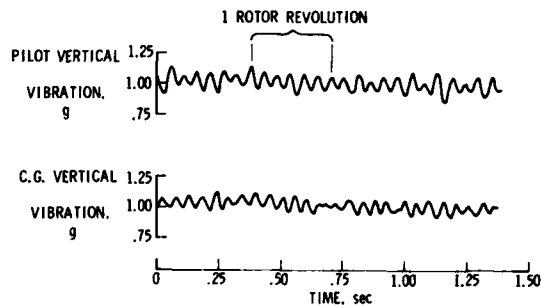Figure 5.- CH-53 blade out-of-track configuration.

Figure 6.- Typical time history of measured pilot and c.g. vertical vibration levels at 120 knots.

142

Figure 7.- Measured pilot vertical vibration levels at blade passage frequency versus airspeed for standard aircraft and split-blade track.

Figure 8.- Measured galley normal vertical vibration levels at blade passage frequency versus airspeed for standard aircraft and split-blade track.

Figure 9.- Measured forward cabin vertical vibration levels at blade passage frequency versus airspeed for standard aircraft and split-blade track.

Figure 10.- Measured mid-cabin vertical vibration levels at blade passage frequency versus airspeed for standard aircraft and split-blade track.

Figure 11.- Measured center-of-gravity vertical vibration levels at blade passage frequency versus airspeed for standard aircraft and split-blade track.

Figure 12.- Measured flight-test station vertical vibration levels at blade passage frequency versus airspeed for standard aircraft and split-blade track.
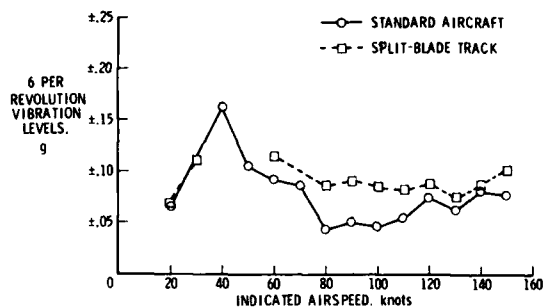

Figure 13.- Measured tail vertical vibration levels at blade passage frequency versus airspeed for standard aircraft and split-blade track.
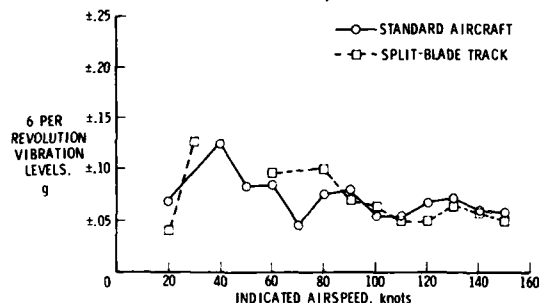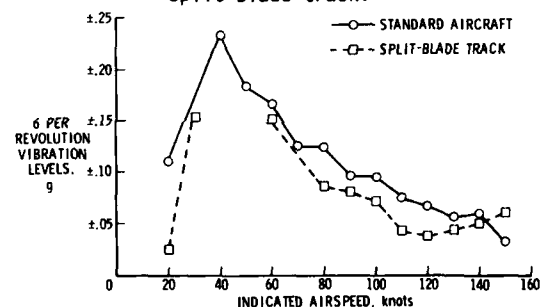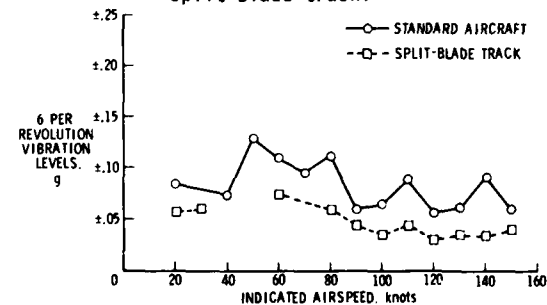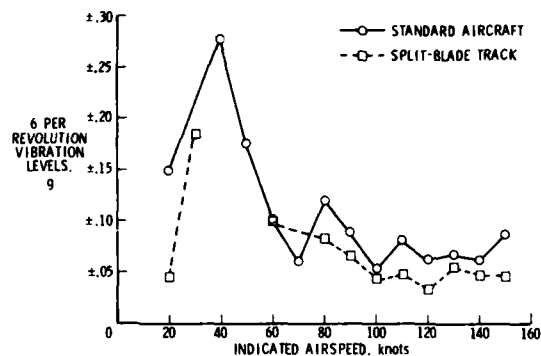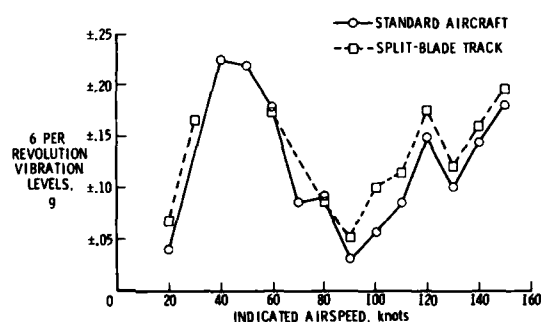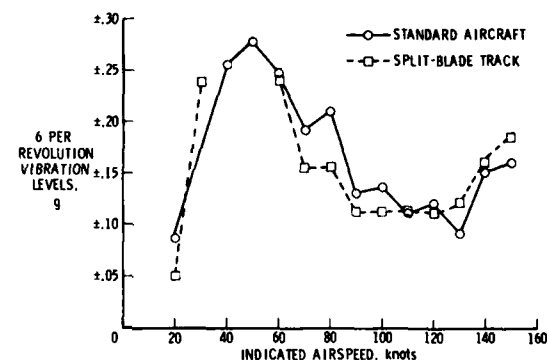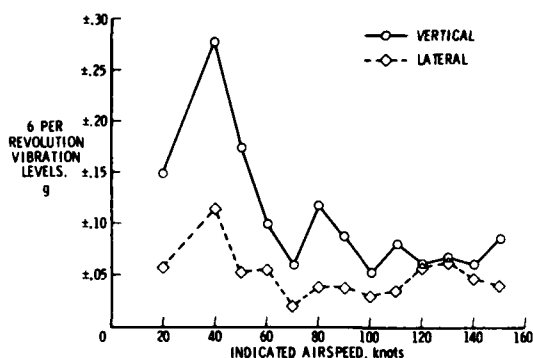
143

Figure 14.- Measured center-of-gravity lateral and vertical vibration levels at blade passage frequency for standard aircraft.

Figure 15.- Measured center-of-gravity longitudinal vibration levels at blade passage frequency for standard aircraft and split-blade track.

airspeeds above 100 knots. The pilot's station, flight engineer's station, and tail vertical accelerometer outputs, however, have a general increasing trend at the higher airspeeds. This difference can be attributed to changes in the character of the excitation forces at the rotor hub and subsequent change in the modal response of the fuselage that affects primarily the fuselage areas away from the cabin area. One clue as to the character of the hub force change is apparent from figures 7, 12, and 13 at 130 knots. While the general trend at these fuselage stations is toward increased vibration levels at higher airspeeds, the vertical vibration level undergoes a significant reduction at an airspeed of 130 knots. This reduction at 130 knots does not occur at the stations in the cabin and nearer the center of gravity, thus implying that the stations away from the center of gravity are responding to hub forces other than vertical hub force. Referring to figure 15, it can be noted that the longitudinal vibration level also decreases at 130 knots. This implies that the longitudinal hub force has decreased at this airspeed due to reduced inplane (horizontal) blade forces. This characteristic similarity between the longitudinal vibration and the vertical vibration at the fuselage stations away from the cabin confirms that inplane forces at the rotor hub in the longitudinal direction are the primary driving forces for the vertical vibration levels at the fuselage extremes for the higher speed conditions. This condition is indicative of the complex interactions of rotor forces and fuselage modes as the aerodynamic load distribution on the rotor becomes increasingly more unsymmetrical at the higher speeds.

Split-blade track experiments.- The second aircraft configuration to be investigated during this research was the effect of changing the relative track of the blades. Three conditions were flight tested: (1) every other blade tracked 1.3 cm (1/2 in.) higher than the remaining three blades; (2) every other blade
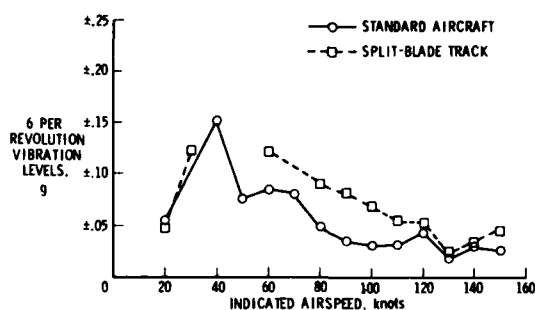
tracked 2.5 cm (1 in.) higher; and (3) two opposite blades tracked 1.3 cm (1/2 in.) higher. Only the condition with three blades tracked 2.5 cm (1 in.) higher will be discussed in detail.

Comparative vertical vibration levels at blade passage frequency for the split-tracked rotor (2.5-cm (1-in.) split) and the conventionally tracked rotor (all blades fly in the same plane) are shown in figures 7 through 13. (Data at airspeeds of 40 and 50 knots were not available due an instrumentation malfunction.) It can be noted that the cabin vibration levels were reduced significantly for the split-track condition. The pilot, flight test, and tail vertical vibration levels, however, exhibit a significant increase for the split-track configuration. As shown previously, the stations located away from the cabin are strongly influenced by the longitudinal forces at the rotor hub. The vertical vibration level in the galley, as shown in figure 8, indicates very little effect of the split-track configuration. It can be seen from figure 14 that the longitudinal vibration level at blade passage frequency also exhibits an apparent increase with the split-track condition. These data indicate that this minor modification in the blade track has the important effect of reducing vertical forces at the rotor hub, but also results in an apparent increase in the longitudinal forces at the hub. These results do not represent a panacea for helicopter vibration problems, but do establish potential payoffs of minor changes in rotor design. These results also indicate the need for basic research in the area of hub force mixture. Flight research in this area should be undertaken with vehicles equipped to measure the hub forces and permit the identification of transfer functions. One scheme of potential importance may be the use of in-flight variable blade tracking utilizing either active feedback or open-loop pilot control.

144

TABLE IV. - COMPARISON OF FOURIER COEFFICIENTS FOR STANDARD AND SPLIT-TRACKED
CONFIGURATIONS

| Coefficient | Vertical Vibration, g, Center-of-Gravity Location | | | |
| | Standard Rotor | | Split-Tracked Rotor | |
	80 knots	130 knots	80 knots	130 knots
C_1 (rotor speed)	0.0148	0.0116	0.0066	0.0184
C_3 (3 per rev)	0.0060	0.0024	0.0059	0.0032
C_6 (6 per rev)	0.1180	0.0671	0.0836	0.0571

For the condition where three blades were tracked higher than the remaining three blades, it was expected that the third harmonic vibration level would increase, and, likewise, where two blades were tracked higher, the second harmonic of rotor speed would increase. However, for the magnitudes of change in these studies, the results show no conclusive indication of increases in harmonics that are not multiples of the number of blades. Table IV shows a comparison of Fourier coefficients for the other harmonics for two airspeeds for the configuration with three blades tracked high. In the tests where two opposing blades were tracked 1.3 cm (1/2 in.) higher than the remaining four blades, the results are similar to those with three blades split-tracked 2.5 cm (1 in.) high, while in tests where three blades were tracked 1.3 cm (1/2 in.) higher than the remaining blades, no apparent change from the standard aircraft was noted.

Modal response characteristics.- Prior to the initiation of flight testing with the NASA CH-53 helicopter, the aircraft was subjected to a full-scale shake test (ref. 3). The results of the shake test bear consideration in the analysis of the results of the current effort. The fuselage vertical forced response shapes for hub excitation at blade passage frequency in both the vertical and longitudinal directions are presented in figures 16 and 17. Both responses are very similar and are primarily the result of the transmission vertical mode of the fuselage. Aft of the nodal point at station 450, the two shapes are nearly identical. Forward of the node, however, it is noted that the relative amplitude is reduced considerably for longitudinal excitation and that there is no longer a forward node at station 194. For reference, the locations of each of the accelerometers relative to the forced response shapes are shown on the figures. It should also be noted that the flight-test data were measured on the floor of the aircraft while shake-test results were taken from measurements on the overhead structure.

A comparison with the shake-test data can be made utilizing preliminary phase relationships measured from time histories of six of the seven vertical accelerometer outputs for the test flights. In figures 18 through 20, the relative phase of the vertical accelerometer outputs is shown for indicated airspeeds of 100, 120, and 150 knots. In these figures, the phase of each accelerometer output is normalized to the blade passage frequency peak of the center-of-gravity accelerometer.

As can be seen from the flight-test data, the tail and flight-test peak amplitudes are approximately 180° out of phase with those at the c.g. and forward cabin stations. This reflects the results seen in the shake-test data for either vertical or longitudinal hub excitation. The peak vibration at the pilot's station is also approximately 180° out of phase with the c.g. and forward cabin accelerometers. This would be expected for vertical excitation at the hub; however, it was shown earlier that longitudinal hub forces become more significant at the higher airspeeds. The shake-test response to longitudinal hub forces (fig. 17) suggests that the forward part of the fuselage remains in phase with the cabin accelerometers. This apparent conflict can possibly be attributed to the fact that the shake-test data were measured on the overhead structure which ends slightly aft of the pilot's station. It is impossible to completely analyze this situation with the limited flight instrumentation available.

Most current flight vibration studies with helicopters are directed at identifying after-the-fact solutions to a specific vibration problem, while very little of the basic research required to provide general design guidelines has been accomplished. These limited results point out the need for basic research efforts directed at a systematic investigation of in-flight modal characteristics of helicopters and of the importance of hub forces on the modal response of the fuselage.

CONCLUSIONS

A vibration flight test and preliminary data analysis with a CH-53 helicopter have

145

been completed and suggest the following
conclusions:

1. Minor changes in rotor parameters,
such as split-blade track, can have a
significant effect on fuselage vibration levels.

2. Rotor hub force control represents a
potential means of vibration control. This
could be achieved by means of rotor design or
through in-flight control of parameters such as
blade track.

3. More extensive in-flight basic
research, coupled with advanced analytical
models, is required to provide a better under-
standing of the interactions of the hub
excitation and fuselage modal response, and
thus provide better guidelines for helicopter
designs and for the design of vibration control
devices.

Figure 18.- Relative phase of peak vertical
vibration levels at blade passage frequency
referenced to c.g. vertical - 100 knots.
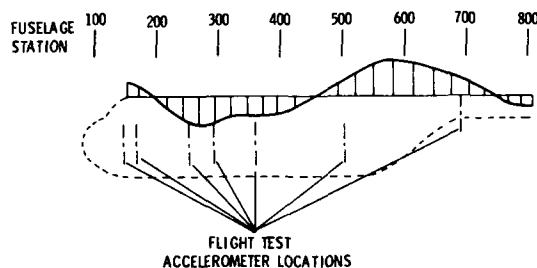
Figure 16.- Shake test measured response for a
vertical hub force excitation at blade passage
frequency.
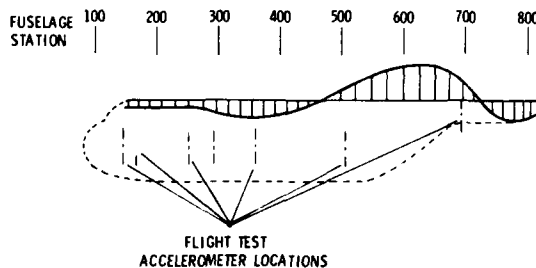
Figure 17.- Shake test measured response for a
longitudinal hub force excitation at blade
passage frequency.
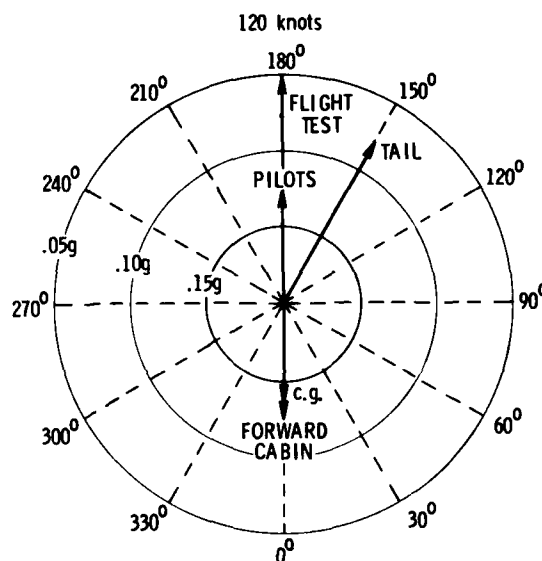
Figure 19.- Relative phase of peak vertical
vibration levels at blade passage frequency
referenced to c.g. vertical - 120 knots.

146
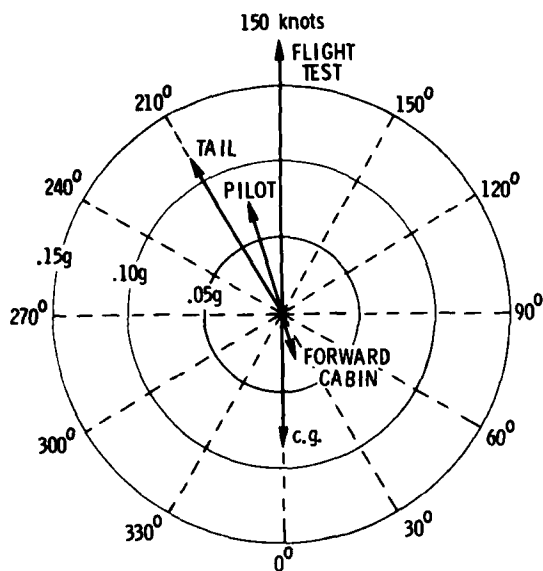
Figure 20.- Relative phase of peak vertical
vibration levels at blade passage frequency
referenced to c.g. vertical - 150 knots.

REFERENCES

1. William J. Snyder and Ronald G.
Schlegel, "Vehicle for Civil Helicopter Ride
Quality Research," NASA TM X-3295, pp. 97-116,
Nov. 1975.

2. William J. Snyder and Michael B.
Schoultz, "Civil Helicopter Flight Research,"
AIAA Paper No. 76-896, Sept. 1976.

3. Michael Dean, "Correlation of Extended
CH-53 Helicopter NASTRAN Model with Full-Scale
Aircraft Shake Test Data," NASA CR-145012,
July 1976.

4. Alfred Gessow and Garry C. Myers, Jr.,
Aerodynamics of the Helicopter. Frederick Ungar
Publishing Co., 1952.

AEROACOUSTIC ENVIRONMENT OF A STORE IN AN AIRCRAFT WEAPONS BAY

L. L. Shaw

AIR FORCE FLIGHT DYNAMICS LABORATORY
WRIGHT-PATTERSON AIR FORCE BASE, OHIO

This paper presents the results from a flight test designed to determine the aeroacoustic environment on the surface of a dummy bomb being carried in an open weapons bay of an F-111 aircraft. Twenty-one microphones were used to measure the aeroacoustic environment for Mach numbers from 0.6 to 1.3 and constant pressure altitudes of 3,000, 10,000 and 30,000 feet. Variations in the environment with respect to Mach number, longitudinal location, circumferential location, and altitude were investigated. Equal sound pressure level contours over the surface of the store were determined utilizing a three-dimensional curve-fitting program. Contours were obtained for the maximum one-third octave bands, as well as the overall levels, for various Mach numbers and altitudes. From these, one general set of contours was developed for use in predicting the aeroacoustic environment. The measured data were compared to previous results and predicted levels.

INTRODUCTION

Aircraft weapons bays exposed to free stream flow may experience an intense aeroacoustic environment in and around the bay. Experience has taught that the intensity of this environment can be severe enough to result in damage to a store or its internal equipment, or to the structure of the weapons bay itself. To assure that a store and its internal equipment can withstand this hazardous environment and successfully complete their mission, they must be qualified to the most severe sound pressure levels anticipated for the mission. If the qualification test levels are too high, the store and its internal equipment will be over-designed resulting in unnecessary cost and possible performance penalties. If the levels are below the in-flight levels, the store or its internal equipment may catastrophically fail during performance of the mission. Thus, it is desirable that actual in-flight levels be known with acceptable accuracy.

A flight test program was conducted using an instrumented BDU-8/B (Bomb Drop Unit) to determine actual in-flight levels. A picture of the store is shown in Figure 1. It is 164 inches long and has an 18 inch diameter. The instrumented store was installed in an F-111

aircraft weapons bay and flight tested by the Armament Development and Test Center, Eglin Air Force Base, Florida. The flight test consisted of six flights which included various Mach numbers and constant pressure altitudes of 3,000, 10,000 and 30,000 feet. This paper presents the flight test data and discusses an approach for predicting the aeroacoustic environment on the surface of a store being flown in an open weapons bay approximately the same dimensions as that of the F-111 aircraft. Variations in the data with respect to Mach number, longitudinal and circumferential location, and altitude are discussed. Comparisons between the current data and previous measurements (Reference 15) are included. These comparisons were made even though the current data were obtained from the surface of the store and previous results from measurements on the cavity walls.

INSTRUMENTATION AND DATA REDUCTION

The aeroacoustic environment on the surface of the store was measured using 21 Gulton MVA-2120 microphones. The signals from the microphones were amplified by an Intech Model A2318 amplifier and recorded on a Leach Model 3200A FM tape recorder. The microphones were located on the store as shown in Figure 2.
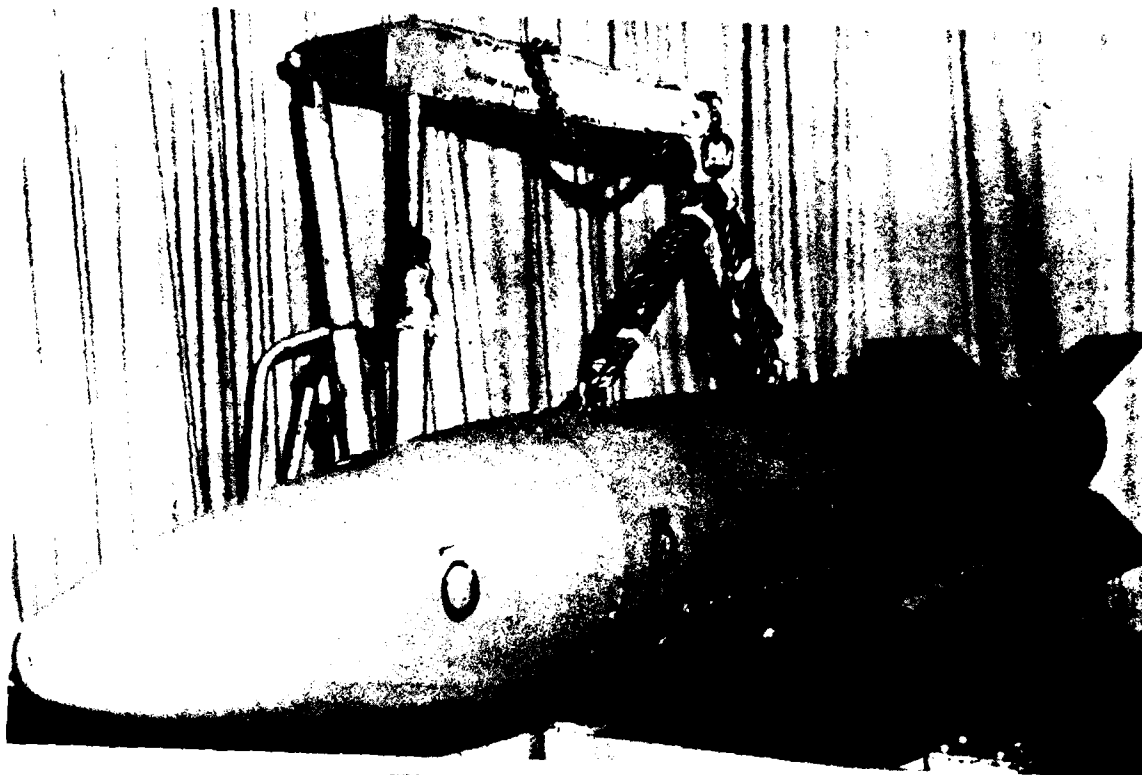
149

FIGURE 1   PICTURE OF THE BDU-8/B

TOP VIEW

O INDICATES MICROPHONE

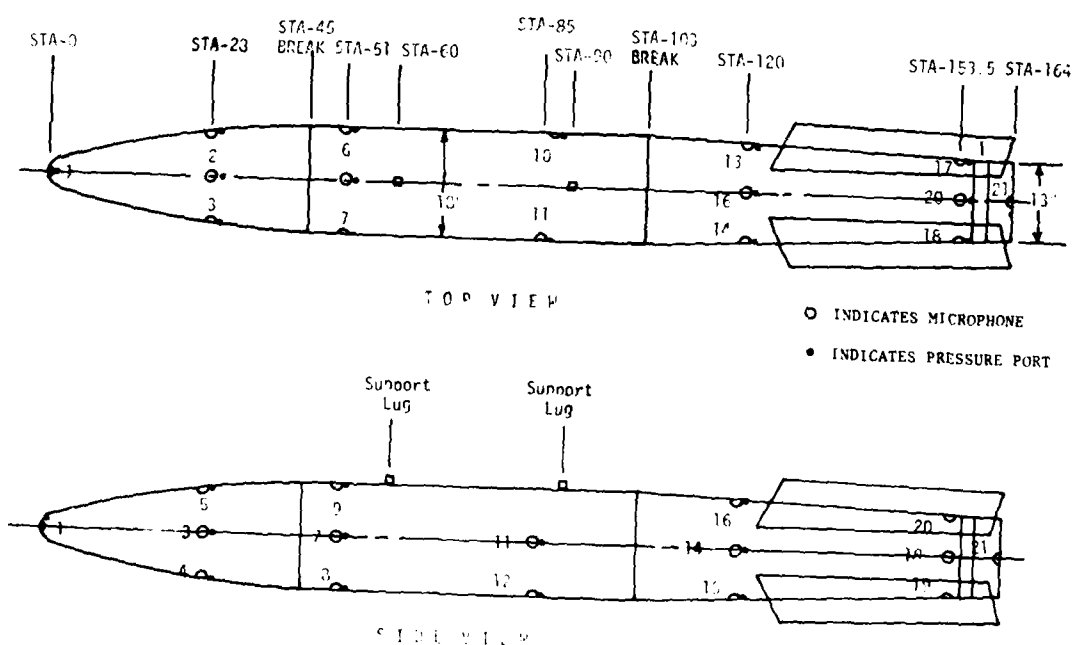• INDICATES PRESSURE PORT

SIDE VIEW

FIGURE 2   BDU-8/B MICROPHONE AND PRESSURE PORT LOCATIONS

150

Data reduction in the laboratory consisted of overall sound pressure levels and one-third octave band and narrowband spectra. A General Radio Model 1921/26 analyzer was used to calculate the one-third octave sound pressure levels which were plotted with a Gould Model 4800 plotter. The narrowband spectra were generated digitally using a Raytheon FFT analysis system. The sample length for the one-third band analyses was, for most data, 8 seconds. There were limited analyses performed with 4 second sample lengths on data from accelerated flights. These data were only used to fill in areas where stationary data were not available. The confidence of the data is frequency dependent. The lowest frequency of interest is approximately 20 Hz. At this frequency there is 95% confidence that the data are in a 2.5 dB interval. However, at a little higher frequency, say 100 Hz, there is 95% confidence that the data are in a 1.3 dB interval. The confidence is even greater at the higher frequencies. The trends observed at the low frequencies were essentially the same as those at the higher frequencies where the confidence is very high, thus it was assumed that the low frequency data had high enough confidence to yield meaningful results.

The confidence in the narrowband data is lower than the one-third octave band data because the analysis bandwidth was less than 2 Hz. However, these data were only used to determine frequency content and thus the amplitude confidence was not of major concern.

Test Results

    a.   Mach Number Variation

        Mach number variations in the overall sound pressure levels for the six microphones located along the bottom of the store are shown in Figure 3. At a constant 30,000 foot altitude the data showed an increase of 8-10 dB as the Mach number increased from 0.8 to 1.3. This increase was expected since, for a constant altitude, the increase in the free stream dynamic pressure "q" is over 8 dB. Previous wind tunnel and flight test results (References 3, 12-15) indicate similar increases for the same flight conditions and cavity geometry.

    b.   Longitudinal Variation

        In Figure 3, overall sound pressure levels are seen to increase by approximately 25 dB when going from the front to the rear of the store. This increase is illustrated in Figure 4 for an altitude of 30,000 feet and a Mach number of 1.20. One-third octave band levels increase by as much as 35 dB towards the rear of the weapons bay. Increases of the order of 20 dB have been reported in the literature from model wind tunnel tests and flight tests. An explanation for this difference is that the F-111 weapons bay does not have clean, smooth walls as did the wind tunnel and flight test models. In particular the front wall of the
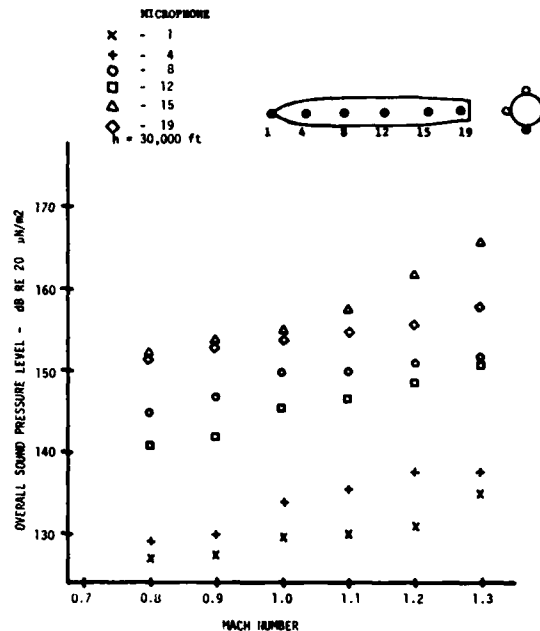

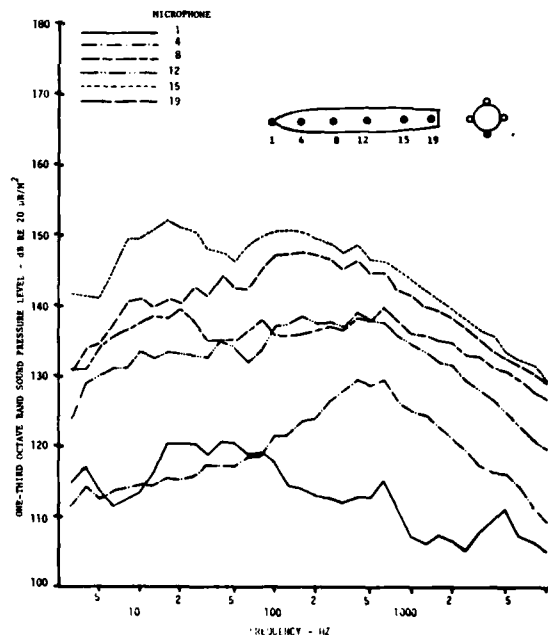FIGURE 3   MACH NUMBER VARIATION OF THE OVERALL SOUND PRESSURE LEVELS

FIGURE 4   ONE-THIRD OCTAVE BAND SPECTRA FOR MACH NUMBER 1.20 AND 30,000 FOOT ALTITUDE DEPICTING LONGITUDINAL VARIATION

151

weapons bay is not a well defined reflecting plane resulting in lower levels at the front. Also, the current data were obtained from the surface of the store, not the walls of the cavity as the referenced data were. Another possible explanation that the current data show larger variation from the front to the rear of the bay than the data from previous tests is the relative cavity dimensions. At present, it is not known whether the cavity size has a significant effect on the flow induced pressure oscillations.

c. Circumferential Variation

The data from microphones located on each side, top, and bottom of the store at a given longitudinal location determined the circumferential variations of the sound pressure level on the surface of the bomb. As shown in Figure 2, circumferential variation data were obtained at stations 28, 51, 120 and 154. Figure 5 illustrates the circumferential variation at station 120 for a Mach number of 0.95 and an altitude of 3,000 feet. The figure shows that for the lower frequencies the lowest levels, at this station, are on the right side of the store and the highest are on the left side. The top and bottom display levels approximately midway between the levels on the two sides. The other locations did not exhibit the same distributions. For example, at station 23 the maximum level was on the right side of the store. An explanation for this difference in the circumferential variations is not readily apparent.

d. Altitude Effects

Previous investigations have shown that, in general, the fluctuating pressure amplitudes in an open cavity scale reasonably well with the free stream dynamic pressure (q). However, it is shown in Reference 12 that there may be locations in the weapons bay (or cavity) which do not scale well with q. Figure 6 presents spectra for the three test altitudes of 3,000 feet, 10,000 feet and 30,000 feet from microphone 19. The difference between the 3,000 foot and 10,000 foot data is 2 to 3 dB. The difference between the 3,000 foot and 30,000 foot data is approximately 10 dB. This is considered to be good scaling with altitude because the predicted differences are 2.3 dB and 9.6 dB respectively. One can conclude that the current data scale reasonably well with the free-stream dynamic pressure since it scales with Mach number and altitude. Data from all of the other microphones scaled reasonably well also.

e. Equal Sound Pressure Level Contours

In order to more fully define the fluctuating pressure environment over the surface of the store, equal sound pressure level contours were developed for various flight conditions. Figure 7 presents the overall sound pressure level contours for Mach number 1.1 at 30,000 feet. The longitudinal centerline in the figure
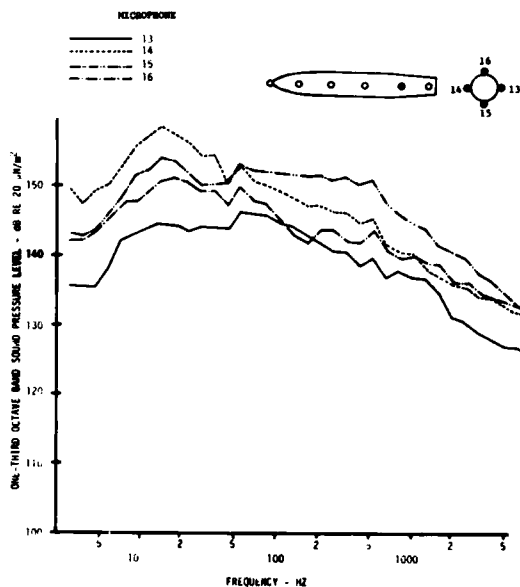

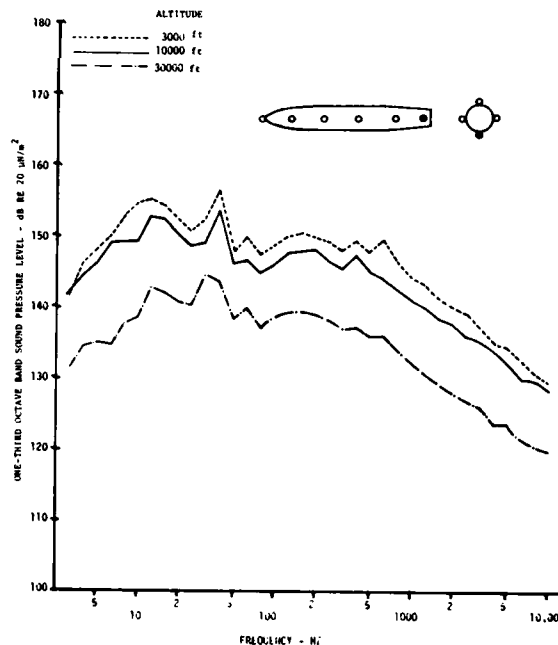FIGURE 5   ONE-THIRD OCTAVE BAND SPECTRA FOR MACH NUMBER 0.95 and 3,000 FOOT ALTITUDE DEPICTING CIRCUMFERENTIAL VARIATION AT STATION 120

FIGURE 6   ONE-THIRD OCTAVE BAND SPECTRA FROM MICROPHONE 19 FOR MACH NUMBER 0.85 DEPICTING ALTITUDE EFFECT
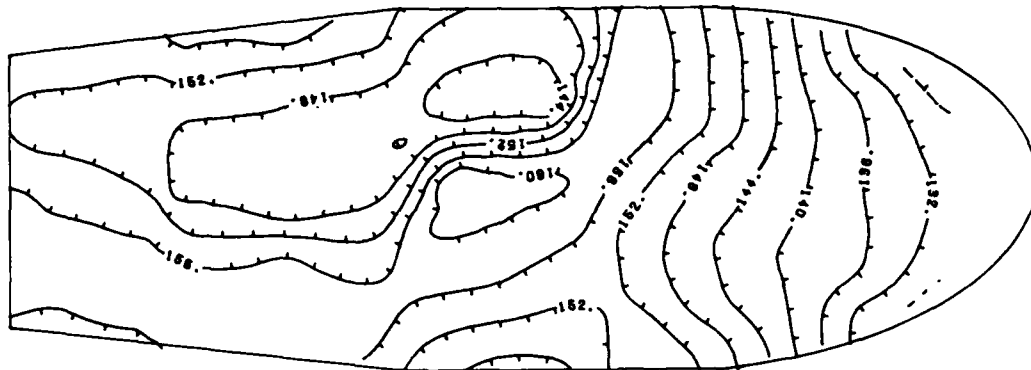
152

FIGURE 7   OVERALL EQUAL SOUND PRESSURE LEVEL CONTOURS FOR
MACH NUMBER 1.1 AT 30,000 FOOT ALTITUDE

represents the top of the store while the side-lines represent the bottom, thus the entire surface of the store can be viewed. Contours are shown for every 4 dB change in the sound pressure level with the tics pointing in the direction of decreasing levels. The figure reveals that the intensity for the forward one-third of the store increases fairly uniformly. Aft of this point the levels become less uniform and tend to display maximum and minimum regions. A comparison of the Mach number results show that there are no significant variations in the contour patterns with Mach number.

Equal sound pressure level contours were also determined for the first three modal frequencies. A typical result is shown in Figure 8 for the first modal frequency as determined from the modified Rossiter equation (see Section g).

Little difference was found in the contour patterns for the three modal frequencies. This reveals a significant characteristic of the amplitudes of the three modal frequencies. References 3, 4, 12-15 indicate that for cavities with small length-to-depth ratios (L/D) each modal frequency prefers a specific longitudinal mode shape, i.e., mode one displays one node, mode two displays two nodes, etc. Because of the different mode shapes, the modal frequency amplitude contours should show significant variations between each other. However, for cavities with larger L/D ratios, as is the case of the F-111 weapons bay, the variation between the modal frequency amplitudes is much less. Since the contour patterns for the modal frequencies were essentially the same as the ones for the overall levels, it can be concluded that no mode shapes existed in the current data.
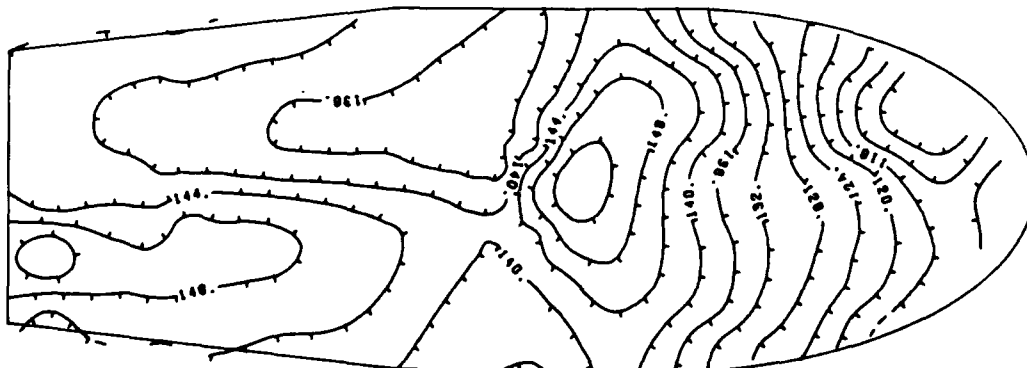

FIGURE 8   ONE-THIRD OCTAVE BAND EQUAL SOUND PRESSURE LEVEL CONTOURS FOR THE FIRST MODAL
FREQUENCY (16 Hz) FOR MACH NUMBER 0.9 AT 30,000 FOOT ALTITUDE

153

f.   Comparison to Predicted Levels

Methods are presented in Reference 15 to predict the fluctuating pressure environment for any longitudinal location in rectangular cavities with various length-to-depth ratios. These methods also account for variations in Mach number, altitude and modal frequency. They were used to predict the BDU-8/B environment which was compared to the measured levels. An example is shown in Figure 9 for microphone 20. The figure shows that the spectral shape of the predicted and measured levels at the rear of the store agree fairly well. The predicted levels are 6 to 8 dB above the measured levels for most frequencies. Less agreement between the predicted and measured levels toward the front of the store was observed from the other comparisons. Possible explanations for the lack of agreement between the predicted and measured levels at the front of the store are (1) the scaling effects of the cavity influence the variation in levels and (2) the full scale cavity is normally cluttered as compared to the research cavities.

g.   Narrowband Spectra

Narrowband analysis was performed on selected data from every microphone. Spectra were obtained over the Mach number range of the test and for each of the three altitudes. The analysis was performed up to 5000 Hz but only data up to 120 Hz are presented since there was no significant energy above that frequency.

A typical spectrum is shown in Figure 10 for data from microphone 1 at Mach number 1.1 and 30,000 foot altitude. Most of the energy in the low frequencies is located at the modal frequencies of the cavity. These frequencies are predicted by the modified Rossiter equation (Reference 14)

$$f_m = \frac{V}{L} \; \frac{m - 0.25}{\dfrac{M}{(1 + .2 \, M^2)^{\frac{1}{2}}} + 1.75}$$

where V is the free stream velocity, L is the cavity length, M is the free stream Mach number and m is the modal frequency number. The predicted first three modal frequencies show very good agreement with the measured data.
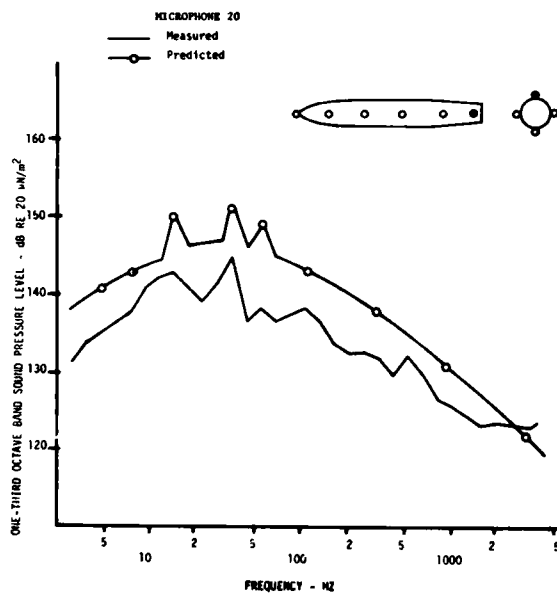

FIGURE 9   COMPARISON OF THE PREDICTED AND MEASURED SPECTRA FROM THE REAR OF THE BOMB FOR MACH NUMBER 0.9 AT 30,000 FOOT ALTITUDE
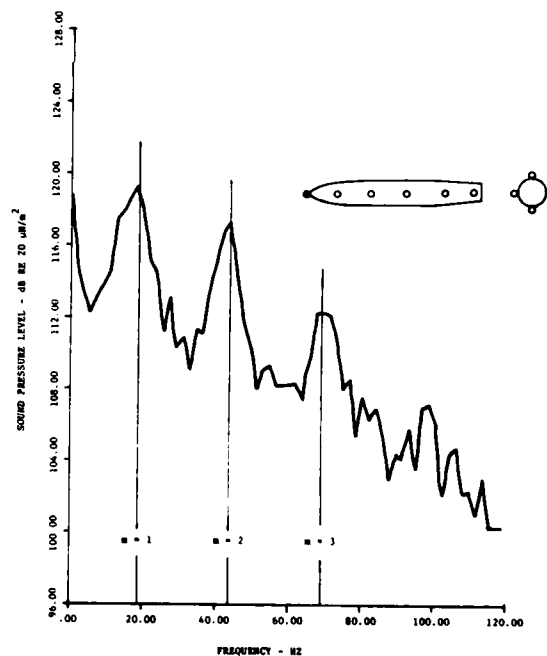

FIGURE 10   NARROWBAND SPECTRA FROM MICROPHONE 1 FOR 1.1 MACH NUMBER AND 30,000 FOOT ALTITUDE
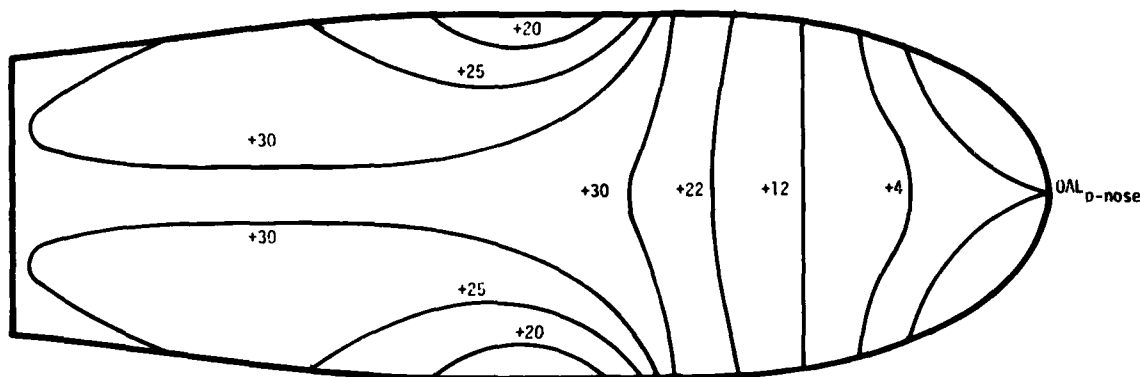
154

FIGURE 11   VARIATION OF THE EQUAL SOUND PRESSURE LEVEL CONTOURS WITH
MACH NUMBER AND ALTITUDE

Environment Simulation

It is desirable to simulate in an acoustic chamber the environment that a store sees during flight. This can be achieved if the fluctuating pressure distribution over the surface of the store measured in flight can be obtained in an acoustic test facility.

The measured data were used to determine equal sound pressure level contours over the surface of the store for various flight conditions. For the purpose of simulation these trends were summarized and the results are shown in Figure 11. The entire surface of the store is shown in the figure. The centerline represents the top of the store and the side lines are the bottom. This contour shows that the overall sound pressure level increases from the nose to about the one-third position on the store. For the remaining two-thirds of the store, the levels remain fairly constant along the top. However, the levels along the bottom decrease 10 dB and then increase the same amount towards the rear. The sound pressure level varies with Mach number and altitude. A normalized expression which considers these variations is

$$10 \log (P_{nose}/q) = -35 \text{ dB}$$

where q is the free stream dynamic pressure and P is the overall rms sound pressure at the nose of the store. Using this expression and the equal sound pressure contour, the absolute overall levels on the entire surface of the bomb can be determined.

For the complete definition of the environment, the spectrum shape of the surface pressures must be known. An average one-third octave band spectrum shape was derived from the measured data and is shown in Figure 12. The levels are referenced to the overall level. This spectrum shape is recommended for the entire surface of the bomb.

With knowledge of the overall levels, surface distributions, and spectrum shape the complete environment can be simulated in an acoustic test facility and reliable vibration qualification tests can be performed.
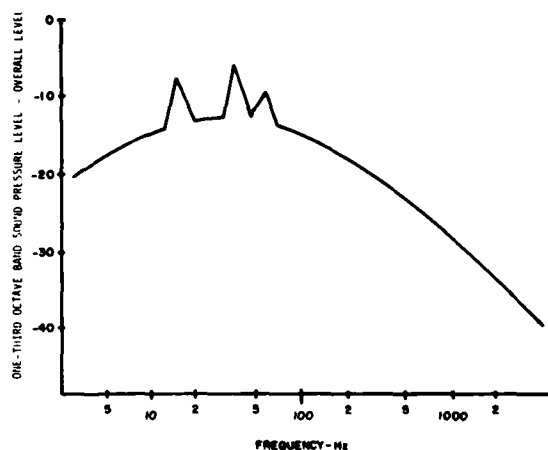

FIGURE 12   ONE-THIRD OCTAVE BAND SPECTRA
RECOMMENDED FOR ENVIRONMENT SIMULATION

155

Summary of Results

The principle results determined from the flight test are summarized as follows:

1. In general, the fluctuating pressure levels on the surface of the store increase with Mach number for all locations on the bomb.

2. The levels on the surface of the store increase from the front to the rear by about 35 dB.

3. There are significant circumferential variations in the levels on the surface at several longitudinal locations.

4. The fluctuating pressure levels scale well with free stream dynamic pressure.

5. The equal fluctuating pressure level contours for the surface of the store vary only a small amount with changes in Mach number of modal frequency.

6. Predictions resulting from the methods in Reference 13 compare well with the measured levels on the rear of the store but they vary significantly towards the front.

REFERENCES

1. Carr, D. L., "An Experimental Investigation of Open Cavity Pressure Oscillations," M.S. Thesis, Air Force Institute of Technology, Wright-Patterson Air Force Base, Ohio, 1974.

2. East, L. F., "Aerodynamically Induced Resonance in Rectangular Cavities," Journal of Vibration and Sound, May 1966.

3. Heller, H. H. and Bliss, D. B., "Aerodynamically Induced Pressure Oscillations in Cavities - Physical Mechanisms & Suppression Concepts," AFFDL-TR-74-133, August 1974.

4. Heller, H. H., Holmes, G., and Covert, E. E., "Flow-Induced Pressure Oscillations in Shallow Cavities," AFFDL-TR-70-104, December 1970.

5. Krishnamurty, K., "Acoustic Radiation from Two-Dimensional Rectangular Cutouts in Aerodynamic Surfaces," NACA Tech Note 3487, August 1955.

6. Lowson, M. V., "Prediction of Boundary Layer Pressure Fluctuations," AFFDL-TR-67-167, April 1968.

7. Maull, D. J., and East, L. F., "Three-Dimensional Flow in Cavities," Journal of Fluid Mech 16, p 620, 1963.

8. Maurer, O., "Investigation and Reduction of Open Weapon Bay Pressure Oscillations in the B-1 Aircraft," AFFDL-TM-74-101-FYA, January 1974.

9. Plumblee, H. D., Gibson, J. S., and Lassiter, L. W., "A Theoretical and Experimental Investigation of the Acoustic Response of Cavities in Aerodynamic Flow," WADD-TR-61-75, 1962.

10. Roshko, A., "Some Measurements of Flow in a Rectangular Cutout," NACA Tech Note 3488, 1955.

11. Rossiter, J. E., "Wind Tunnel Experiments on the Flow Over Rectangular Cavities at Subsonic and Transonic Speeds," RAE Rep Nr 64037, R&M Nr 3438, 1966.

12. Shaw, L. L., et al, "Aero-Acoustic Environment of a Rectangular Cavity with a Length to Depth Ratio of Four," AFFDL-TM-74-19-FYA, January 1974.

13. Shaw, L. L., and Smith, D. L., "Aero-Acoustic Environment of Rectangular Cavities with Length to Depth Ratios in the Range of Four to Seven," Paper presented at the 45th Shock and Vibration Symposium, October 1974.

14. Smith, D. L., et al, "Aero-Acoustic Environment of Rectangular Cavities with Length to Depth Ratios of Five and Seven," AFFDL-TM-74-79-FYA, April 1974.

15. Smith, D. L., and Shaw, L. L., "Prediction of the Pressure Oscillations in Cavities Exposed to Aerodynamic Flow," AFFDL-TR-75-34, October 1975.

AN INTERIM REPORT ON SHUTTLE ORBITER VIBROACOUSTICS

Vibration and Acoustics Unit*
Space Division, Rockwell International Corporation
Downey, California 90241

The space shuttle orbiter is designed to a unique combination of loads and environments not previously encountered in aerospace practice, since the reusable shuttle is to be launched like an expendable space vehicle and the orbiter is to return from space to land horizontally like a conventional aircraft for the specified 100 mission life of the orbiter. The determination of acoustic and aerodynamic noise, mechanically-transmitted vibration and the structural vibration response to these sources for various locations throughout the orbiter is described in this paper. Of particular concern is the fatigue resistance of the external structure and the insulation applied externally to this structure for entry heating protection. Other topics discussed include the selection of vibroacoustic design and test criteria, noise transmission to the payload bay and crew module, equipment noise in the crew module, various ground test programs, and development flight tests. The tasks already performed and the plans for future work are described.

INTRODUCTION

The space shuttle is under development to satisfy the requirements of NASA and DOD to economically put a variety of payloads (P/L's) into low earth orbit or to serve as a reusable first stage in putting other P/L's into higher orbits, geosynchronous orbits, or planetary trajectories at low cost. Orbital servicing and retrieval of P/L's is also planned under certain conditions. The space shuttle vehicle (SSV) is comprised of the four major system elements shown in Fig. 1: an orbiter, an external tank (ET), and two solid rocket boosters (SRB's). Payloads are carried in the orbiter 60 ft long x 15 ft diameter P/L bay. The SSV is to be launched vertically like present expendable space vehicles and the orbiter is to return from space to land horizontally like an aircraft, as shown in

Fig. 2. Economy will be achieved by reusing the orbiter up to a total of 100 missions, and by recovering the SRB's after parachute assisted water landing. The SRB's are refurbished and refilled with propellant for reuse. Only the ET (which will carry propellants for the space shuttle main engines (SSME's) located at the aft of the orbiter) will be expended after each mission and must be replaced.

Most missions will be launched from Launch Complex 39 (LC-39) at Kennedy Space Center (KSC), where the shuttle can deliver P/L's as heavy as 65,000 lb into a 150 nautical mile circular orbit. LC-39 was formerly used to launch Saturn V vehicles. Polar orbit missions are to be launched from Spacecraft Launch Complex 6 (SLC-6) at Vandenberg Air Force Base (VAFB), where P/L's as heavy as 32,000 lb can be delivered. SLC-6 was originally designed for launching Titan III-M. Ref. [1-4] provide an overview of the shuttle configuration and mission as well as discussions of various technical problems and solutions.

In addition to other loads and environments discussed in these references, the SSV will be subjected to fluctuating pressure loading on its exterior surfaces by rocket engine exhaust-generated acoustic noise during lift-off, by aerodynamic noise during atmospheric flight, and by mechanically-transmitted vibration. While there is a physical difference between the acoustic and aerodynamic noise loads, they both have time-variant broad band random characterisitics which are described by their overall sound or fluctuating pressure levels, auto spectra and spatial cross-correlations or cross-spectra as functions of time and position on the vehicle surface.

The fluctuating pressure loads are not generally a critical design condition for main load-carrying structures. However, they are often the principal sources of structural vibration which may result in the malfunction of vehicle or P/L components or the fatigue of exterior skin panels or component bracketry. Therefore, establishing aeroacoustic loads is essential for the determination of vibration loads throughout the vehicle, and for the development of vibration test specifications and the associated dynamic design requirements which are necessary to ensure overall mission reliability. Under certain circumstances, mechanically-transmitted vibration must also be considered in dynamic design and test requirements.

The following sections are intended to briefly review the vibroacoustic tasks accomplished by August 1976 and to summarize the plans for future work on the orbiter.

VIBROACOUSTIC SOURCES

Rocket Engine Noise

Rocket engine exhaust noise is generated by the random turbulence produced in the mixing region between the high velocity exhaust stream and the surrounding atmosphere.

If the exhaust is smoothly deflected and directed at a right angle to the vehicle axis, the virtual noise source will be closer to the vehicle and the acoustic loading will be higher than if the flow was allowed to continue freely behind the vehicle. If the exhaust flow is obstructed, rather than just smoothly deflected, the increased turbulence plus the closer proximity of the noise source will cause marked increases in the acoustic loading, especially if the flow obstruction occurs within the supersonic length of the exhaust stream.

Except for the case of "pad splash", the acoustic loading on the vehicle surface will be maximum during pad hold and will gradually decrease as the vehicle gains altitude and the distance from the exhaust and the ground, or other acoustically reflective surfaces, increases. As the vehicle accelerates, the propulsion-induced acoustic loads continue to decrease and finally reach zero as the vehicle velocity equals the speed of sound.

At first, shuttle propulsion-induced acoustic loads were predicted by scaling data measured during the prior launches of vehicles from the same or a similar launch facility, using procedures provided in Ref. [5]. Since the SSV will use Saturn V launch facilities at KSC, data measured on the Saturn V were used as reference for predicting the acoustic loads for the SSV generated by the SRB's. Acoustic loads generated by the SSME's were predicted using Saturn V data and data measured during static test firings of single J-2 engines and XLR129 staged-combustion engines. Both of the latter engines use LOX-hydrogen as propellants. This prediction was utilized during the early days of orbiter development for the generation of vibroacoustic design and test criteria. Figure 3 shows the predicted spectra for the orbiter P/L bay doors.

However, in order to use the Saturn V facilities for the SSV, certain modifications to LC-39 were required. For example, the exhaust deflector has been modified in order to accommodate the greater distance between the SRB's and the SSME's. The SRB exhaust holes in the Mobile Launch Platform (MLP) have been elongated to accommodate the lateral drift of the vehicle caused by the lateral thrust component of the SSME's, and to minimize the probability of obstructing the supersonic core of the SRB exhausts. Current positioning of the SSV on the modified LC-39 is shown in Fig. 4 - 5. (Additional data are provided in these figures which will be discussed later.)

Differences in the pad configuration and the lateral drift of the SSV limits the similarity between Saturn V and shuttle noise fields, even though both are launched from LC-39. Thus, early in the program it seemed appropriate to conduct scale model acoustic tests to represent the SSV/modified LC-39 configuration from engine ignition until after the SSV passed the tower. Such tests on a 6.4 percent model have been and are being performed at the NASA Marshall Space Flight Center (MSFC) using scaled SRB and SSME engines. Fig. 6 shows the SSV model on the modified LC-39 pad model. Data from these tests, some of which are presented in Ref. [6], indicated that more of the total exhaust noise power is concentrated in the

158

low frequency bands than originally predicted. For example, the envelope of liftoff noise spectra for the P/L bay doors, measured from these model tests, is shown as the upper curves in Fig. 3.

Because of the major impact that greater low frequency noise would have on shuttle equipment, P/L design, test requirements and acoustic fatigue of orbiter structure, engine noise suppression studies were added to the model test program. These studies show that liftoff noise levels can be significantly reduced by the addition of water to rocket engine exhaust flows. The amount of noise suppression at various measurement locations is dependent on the location(s) of water injection into the exhaust flows and on the water flow rate. As a result, a water system for noise suppression will be added to LC-39, as shown in Fig. 4 - 5. An example of the effect of this water system, measured from model tests for P/L doors, is shown as the lower curves in Fig. 3. Comparison with the earlier envelope shows the amount of noise suppression that is achievable.

The SSV will also be launched from modified Titan III-M facilities at VAFB. The design of these facilities appears conducive to lesser acoustic loads than those at KSC. Since VAFB facilities are to be modified several years after the KSC modifications, it was decided to avoid further potential vehicle problems by imposing a design requirement on the VAFB modification that the liftoff noise environment at VAFB not exceed that at KSC. To ascertain that this requirement can be achieved, the aforementioned 6.4 percent scale model test program at MSFC has been expanded to include a model of the modified SLC-6 with and without noise suppression. Fig. 7 shows the SSV model on the modified SLC-6 pad model.

Acoustic noise generated by full scale SSME's and SRB's during static firing will also be measured to verify/update model test results. An important test in this category is the main propulsion test (MPT) whose configuration includes an ET and an orbiter aft fuselage with three SSME's static firing into a modified Saturn S-IC test stand at NASA National Space Technology Laboratory (NSTL).

Certain questions have arisen concerning the adequacy of the 6.4 percent scale model to represent the full scale SSV perfectly, since the scale model engines used violate some secondary modeling laws discussed in Ref. [7]. A 6.4 percent scale model of the MPT configuration will be tested to enable a comparison between model and full scale SSME's before first vertical flight (FVF) of the SSV. Any differences in scaled noise spectra can be applied to liftoff noise

predictions from earlier model tests involving modified LC-39 and SLC-6 facilities.

Aerodynamic Noise

As the shuttle vehicle accelerates during ascent, the fluctuating pressures on the surfaces of the vehicle due to boundary layer turbulence will vary in proportion to free stream dynamic pressure (q). Maximum levels in local areas are dependent on vehicle flight attitude, vehicle configuration effects on boundary layer flow, and vehicle Mach number. Because of the difficulty of predicting aerodynamic noise by parametric methods, such as described in Ref. [8 - 9], wind tunnel tests of scale model vehicles with high frequency pressure gages were used for acquiring shuttle aeronoise data.

Initial noise estimates were derived from wind tunnel models of conceptual SSV configurations during the study phase of the program. These estimates were improved with data from survey tests of a model scaled from preliminary vehicle drawings. These predictions were refined with data from tests of a detailed 3.5 percent rigid model, shown in Fig. 8 - 9, which had 237 measurement locations. In these tests, data were measured at Mach numbers ranging from 0.6 to 3.5, and pitch and yaw angles from $-5°$ to $+5°$. To cover q_{max} post-entry conditions called "terminal area energy management" (TAEM), tests were conducted with the orbiter alone in the Mach range from 2.5 to 3.5, with pitch angles from $6°$ to $18°$ and yaw angles up to $6°$. Some data from these tests, all performed at NASA Ames Research Center, are presented in Ref. [10].

High altitude winds cause changes in a vehicle's flight attitude (relative pitch, yaw and roll angles) from that defined by the vehicle configuration and desired flight path. In order to determine the variation in aeronoise caused by wind-induced attitude changes so that observed differences could be properly weighed in structural analyses, the pitch and yaw angles of the SSV resulting from flying through smoothly-varying constant-percentile wind profiles were computed. The results are plotted in Fig. 10 with the cumulative annual velocity percentiles for head, tail, right and left crosswinds also shown. These wind influences have been combined with guidance-controlled attitudes computed for zero wind trajectories to provide a first estimate of the probability of the SSV experiencing a particular combination of pitch and yaw angles, as shown in Fig. 11. The selection of particular pitch and yaw angles for the latest wind tunnel tests was based on this statistical analysis. As data becomes available from computer-simulated flights of

159

the vehicle through approximately 15,000 taped wind profiles, statistical analyses of resultant pitch and yaw angles will be made and used to modify this estimate. As an example of wind effects, Fig. 12 shows two aeronoise spectra for the forward P/L bay doors. The lower curve is an envelope of noise measured under zero-wind flight attitudes while the upper curve is an envelope of noise measured under wind-induced pitch and yaw. The lower and upper curves have been named "nominal" and "dispersed" trajectory spectra, respectively.

Mechanically-Transmitted Vibration

In addition to the above aeroacoustic noise, orbiter structure and equipment must be designed or protected from structural vibration transmitted through structure-borne paths from vibration sources. Usually this type of vibration decreases rapidly as a function of distance from the source. However, whereas aeroacoustic noise is restricted to relatively short durations per mission during liftoff, ascent and TAEM, mechanically-transmitted vibration is encountered during the complete duty cycle of these sources.

Special among these sources are the large rocket engines, such as the three SSME's which operate throughout the full 490 sec of ascent. Significant SSME-induced vibration should be limited to the thrust structure within the aft fuselage of the orbiter. Prior to obtaining suitable SSME vibration measurements, SSME vibration criteria has been selected based on a prediction using the Barrett scaling equation from Ref. [11]. This equation scales the vibration spectrum from a reference engine and vehicle to a new engine and vehicle with certain differences between the two engine installations, such as number of engines, their thrust and specific impulse, and weight of the structures. The reference vehicle and engines selected for the SSME's were the Saturn S-II stage with its five J-2 engines. These engines and vehicle were selected as the reference because both the J-2 and SSME use LOX-LH2 as propellants, and the S-II stage was fired in the upper atmosphere only where the contribution of aeroacoustic noise to the measured vibration was negligible. Fig. 13 shows the resulting prediction of mechanically-transmitted vibration for the thrust structure from the SSME's. However, limited confidence is placed in this prediction because of parameters not scaled in the Barrett equation which might have a large influence on the prediction, such as chamber pressure, power head or throat area and structural differences. The chamber pressure of the SSME is over three times that of the J-2. In addition, the SSME has four turbopumps compared to two for the J-2, and has two preburners not needed by the low pressure J-2. Unfortunately, there

are no known methods to ascertain the effects of these differences. Meanwhile, single SSME static firings have recently been initiated at NSTL, but a whirl instability of a turbopump shaft has cast doubt on the advisability of using vibration measurements from these tests.

Aeroacoustic Noise Zones

To permit a logical grouping of acoustic and aerodynamic noise data for use in vibration and fatigue analyses and tests, noise zones were selected for the SSV. Zones were established as areas of the vehicle between definable structural boundaries (a definable boundary inhibits transmission of noise-induced vibration between adjacent structures) and/or by marked differences in localized aerodynamic flow (shoulders, protuberances, cavities, etc.). Noise zones for the top and sides of the orbiter are shown in Fig. 14 and for the bottom of the orbiter in Fig. 15. There are also zones for the ET and SRB's.

A typical time history of overall fluctuating pressure levels during liftoff and ascent in one of these zones, the forward P/L bay doors of the orbiter, is shown in Fig. 16. During the ascent transonic/q_{max} period, the nominal and dispersed trajectory curves show aeronoise under zero wind and maximum wind conditions, representing 50 percent and one percent of the total shuttle missions, respectively. Aeronoise for the remaining 49 percent of the missions occur between the nominal and dispersed trajectory curves. Similar time histories have been developed for the other noise zones.

If it were practical, these nonstationary random histories could be used directly for structural and equipment design and test. However, current aerospace practice has not developed to this point and equivalent stationary time durations are used to represent the effects of the nonstationary loading. In the case of the orbiter, the equivalent stationary duration was calculated for each zone so the stationary spectrum and duration would produce the same fatigue damage as the nonstationary spectrum and history. A fatigue model was used which assumes that (a) both stationary and non-stationary loadings cause random stresses between the endurance limit and ultimate strength, (b) the damage contribution is in accordance with the Palmgren-Langer-Miner hypothesis, and (c) the maximum slope of the random fatigue curve can be used for scaling the relative damage contribution between highest and lower nonstationary stresses (usually a very conservative assumption). Since most of the structure of interest is of 2024 aluminum with a notch concentration of $K_t \approx 4$, a maximum fatigue curve slope of 4 was selected. In addition, to account for

the statistical scatter of the random fatigue curve, a scatter factor of 4 was used to increase calculated stationary durations for all random acoustic and vibration tests that utilize only one test specimen for qualification, as proposed in Ref. [12]. Nearly all such tests fell into this category. Thus, the forward P/L bay doors, which are designed to survive the orbiter life of 100 missions, will have single test specimens exposed to durations of 34, 13 and 1.2 minutes at maximum liftoff, nominal trajectory and dispersed trajectory conditions, respectively.

VIBRATION RESPONSE AND CRITERIA

Structure/TPS Design

Several subcontractors are involved in the development of orbiter structure. Fig. 17 shows various structural sections of the orbiter and the subcontractors who have the development responsibility. In most military and commercial aircraft programs, the vehicle structure is designed and analyzed by the prime contractor and fabricated by the prime and subcontractors. This process has been amended in the shuttle program; the subcontractors perform design, analysis, fabrication and some test functions for their assigned sections of the orbiter, with the prime contractor providing overall vehicle loads and design guidelines and monitoring subcontractor activities. As a result, the skin of the different sections of the orbiter is selected by the subcontractors and is comprised of completely different construction. For example, the forward fuselage has mainly hat-stiffeners, the mid-fuselage has integrally-machined T-stiffeners, the P/L doors and the skin of the aft propulsion subsystem (APS) are graphite epoxy honeycomb, the aft fuselage and vertical stabilizer are primarily integrally-machined I-section stringer and/or waffle construction and the wings have unique pinched-hat stiffeners. With the exception of the graphite epoxy sections, the orbiter nose, the wing leading edges and the windows, the external structure is made of 2024 aluminum alloy.

The aluminum and graphite epoxy materials will be unable to survive the high entry temperatures shown in Fig. 18. A thermal protection subsystem (TPS) has been designed to protect the structure for the orbiter life of 100 missions. The TPS is external insulation comprised of four different material configurations shown in Fig. 19, selected on the basis of the temperature expected for each region of the orbiter. These configurations comprise (a) reinforced carbon-carbon (RCC) is a graphite composite used on the orbiter nose and the wing leading edges capable of withstanding temperatures as high as $3,000^\circ F$ and serving as both insulation and structure; (b) high

temperature reusable surface insulation (HRSI) consists of thousands of coated silica "tiles" 6 x 6 inches in size and ranging from 0.5 to 3.5 inches in thickness, used mainly on the orbiter lower surface for surface temperatures between 1200 and $2300^\circ F$; (c) low temperature reusable surface insulation (LRSI) consists of thousands of 8x8 inch coated silica tiles with thicknesses varying between 0.2 and 1.0 inches for temperatures between 700 and $1200^\circ F$, used mainly on the sides of the orbiter; and (d) flexible reusable surface insulation (FRSI) is blanket-like nomex felt bonded to the orbiter upper structural surfaces with an adhesive, for surface temperatures below $700^\circ F$. Nomex felt is also bonded between the external structure and HRSI or LRSI tiles to permit relative thermal expansion and contraction, and is called the strain isolation pad (SIP) for HRSI and LRSI regions of the orbiter. Fig. 20 provides some TPS details.

The small remaining orbiter surface areas are comprised of thermal window panes (in the crew module) and certain temperature resistant metals.

Except for the RCC, the TPS is selected to limit the entry-induced temperature of the aluminum and graphite epoxy to $350^\circ F$ or less to minimize structural creep over the 100 mission life. The cavity behind the RCC will be exposed to temperatures well in excess of this limit, so adjacent aluminum structure will be specially protected with internal HRSI. In general, thicker HRSI and LRSI is required on the forward portion of the orbiter due to the higher heat input. In addition, thermal and aerodynamic seals are used for the many doors, penetrations and control surfaces of the orbiter. Since many internal structures and items, such as P/L's, crew module and orbiter equipment, cannot survive the $350^\circ F$ structural temperature, internal insulation is also utilized and is called the thermal control subsystem (TCS). Any incipient degradation of the TPS must be detected during ground inspection between flights. The structure behind the TPS is difficult to inspect, due to TPS on the outside and TCS, equipment and other structure on the inside. A more thorough discussion of the TPS appears in Ref. [4].

In addition to the above, the external structure/TPS must be designed to the complete spectrum of significant loads and environments applied to the orbiter in sequence and/or combination: (a) rain and moisture on the launch pad, during early ascent, TAEM and landing, (b) acoustic noise from rocket engines combined with inplane static loads at liftoff, (c) flow-induced aerodynamic noise combined with inplane and differential pressure static loads during transonic and q_{max} periods of ascent, (d) modest heating during late ascent, (e)

161

thermal gradient-induced loads and vacuum during orbital "cold soak", (f) severe heating combined with vacuum during early entry, and (g) thermal gradient and mechanically-induced static loads combined with modest aerodynamic noise during TAEM and landing.

Considering all of the above variations in loads and environments, and structural and TPS configurations, the magnitude of the design, analysis and test effort to qualify the various sections of the orbiter for flight would appear to be considerable.

Structure/TPS Analysis

One of the most critical potential problem areas is the fatigue resistance of the external structure/TPS to aeroacoustically induced random vibration during liftoff and ascent. However, the orbiter structure was designed initially to static loads, with overdesign factors included to account for additional unspecified loads such as structural vibration. (This philosophy is in accordance with standard aerospace design practice.) Then various regions of the orbiter were analyzed to calculate their fatigue lives under aeroacoustic loading, plus other superimposed loads, for comparison with mission lifetime. Usually Miles' method was used because stresses could be calculated with little effort, as shown in Ref. [13 - 15], even though the method is obviously limited in properly representing the dynamic response of the structure (i.e., representing an often complicated structural section as a single-degree-of-freedom system, assuming the mode shape is identical to the relative static deformation, and often requiring a guess for the system damping). Sometimes critical or borderline regions were analyzed by the contractor or subcontractors using random response computer programs and finite element models of the structural regions. Certain regions of the orbiter required resizing for aeroacoustic loading; wings, elevons, vertical stabilizer, and body flap (the hinged structure cantilevered from the bottom of the aft fuselage used to protect the SSME's from entry heating).

Fig. 19 shows one of these models, which was analyzed with NASTRAN. Data from early development tests were used to provide the required damping in the various modes. In most of these structural models, the RSI tiles were added to the panels as non-structural mass (i.e., the possible stiffness contribution was ignored) in order to avoid a costly analysis. If the stress distribution through the RSI was to be derived as a random response to aeroacoustic excitation, the tiles would have to be

modeled in fine grids which would have made the computer runs too expensive. For example, the finite element model of Fig. 21 represented an orbiter panel which was 48 x 60 inches in size. This small section contains 78 HRSI tiles, each of which would require as much as 4000 (20x20x10) grid points, or a total of over 300,000 grid points to adequately define the stress distribution. Improved computer programs to provide proper modeling at reasonable cost have just been developed under NASA Langley Research Center contracts and reported in Ref. [16 - 18]. The random response portion of the program can reasonably compute stress spectra and standard deviations. It also appears particularly suited to handling the anisotropy of the material and the computational difficulty in analyzing elements of widely varying moduli, which for the orbiter structure/RSI is as follows: aluminum $\sim 10.5 \times 10^6$; graphite epoxy $\sim 12.7 \times 10^6$; RSI tiles $\sim 25 \times 10^3$ inplane and 7×10^3 through-the-thickness (TTT); nomex SIP ~ 40 shear and 15 psi TTT. In addition, the ultimate strength and endurance limit of the silica tiles are only about 20 psi with wide scatter, requiring careful modeling to avoid unrealistic failure predictions.

In the interim, RSI stresses are calculated on the basis of modal curvature of the structure, applied pressure fluctuations and structural accelerations, assuming that the tiles do not stiffen the structure. At present, no problems have been discovered on this basis. Also, many external structure/TPS acoustic tests have been or will be performed so that reliance on analysis is not an absolute requirement.

Structure/TPS Testing

Because of the many potential problems associated with TPS usage, coupled with a general lack of experience in using space vehicle structural concepts for multi-mission applications, acoustic fatigue testing was considered necessary for orbiter development and certification. A development test program was initiated, with the following objectives: (a) evaluate structural integrity of various candidate external structural/ TPS configurations, including seals and windows, under acoustically-induced-random vibration, results of which would be used in the later selection of panels for certification; (b) evaluate the effects of other loads and environments which exist in combination and/or sequence with aeroacoustic noise; (c) provide data on various parameters which influence acoustic fatigue, vibration response, and acoustic noise transmission to internal spaces; and (d) provide experimental data to evaluate acoustic fatigue design techniques.

162

The first series of tests were performed to obtain early design information, i.e., experimental data to support the structure and TPS design. The first test was on a 48x60 inch hat-stiffened panel with frames, shown in Fig. 22, representing an early mid-fuselage design. Acoustic noise, mechanical impedance, and log decrement testing was performed to measure vibration response, noise transmission and damping with and without HRSI to get a comparison of HRSI effects on these factors. The addition of TPS on the bare panel caused the vibration response to decrease about 10 dB. The system damping increased from one percent on the bare panel to 2.5 percent with TPS at the predominant resonance frequency. The acoustic transmission loss after TPS was applied increased about 10 dB above 100 Hz. Acoustic testing was performed until failure occurred, and the test time compared to the calculated failure time based on fatigue analysis. The prediction of the type of failure, location, and time-to-failure compared favorably with the test results.

Testing was also conducted on an early design of a wing panel. The initial results showed no appreciable difference between the wing and mid-fuselage panels, which were both hat-stiffened skin. For this reason, the test effort was redirected to testing skin-mounted brackets and tubing.

Other testing in this series is primarily oriented toward evaluation of other loads and environments which occur in sequence and/or combination with acoustic noise. A lower forward fuselage panel comprised of hat-stiffened skin/HRSI is to be exposed to acoustic noise representing lift-off and ascent transonic/q_{max} in sequence with entry heating at NASA Langley Research Center, with some preliminary results reported in Ref. [19]. Another test to be performed at Langley will expose a similar but larger panel to multi-environments: rain acoustic/static loading representative of liftoff, ascent and TAEM; orbital cold soak/vacuum; ascent and entry heating/vacuum; landing load. Another test will expose Z-stiffened skin/LRSI to similar multi-environments. Multi-environmental testing is also planned for the RCC nose and leading edges.

Wind tunnel tests are being implemented to expose external structure/TPS to aero-dynamically-induced combined static and fluctuating pressure loads. One such test was performed in the NASA Ames Research Center 9x7 ft supersonic tunnel of a 9x4 array of HRSI on a waffle-stiffened panel representing the lower aft mid-fuselage. Another test will be performed in the Ames 11x11 ft transonic tunnel of a 5x3 array of LRSI on a hat-stiffened panel representing the top of the crew module skin.

The second series of development tests were performed under ambient conditions only, using structure/TPS specimens representing the lower portion of the wing, the bottom of the aft fuselage, the elevon, and the forward fuselage shoulder. All tests were conducted at NASA Johnson Space Center (JSC) except the shoulder which was conducted at a Rockwell facility. Fig. 23 depicts the wing panel test setup in the JSC's progressive wave facility. Fig 24 shows the elevon test setup in JSC's reverberant chamber. Structural failures occurred only to the elevon panel. A T-shaped clip used to tie the stiffeners of the front spar to the spar cap failed in several locations. Fatigue also occured to the stiffener itself in several locations.

The TPS used in these tests were pre-production RSI tiles. Several anomalies have occurred during testing, including cracks and flaking in the coating of the tiles, allowing the silica fibers to be directly exposed to the acoustic environment. When this condition occurred, slight erosion of the fibers was observed. The relationship between these anomalies in pre-production RSI and those that might occur in production tiles will be evaluated as further data are obtained.

Additional information on acoustic fatigue development tests is provided in Ref. [20].

In addition to the development tests, a comprehensive certification program is planned to demonstrate integrity of the external structure/TPS, with panels representing various regions of the orbiter as shown in Fig. 25. In general, the certification approach is to (a) test these panels to failure or to some predetermined exposure under ambient conditions; (b) use the test data to revise acoustic fatigue analyses; and (c) expand the revised analyses to include combined and sequential loading effects in order to predict fatigue lives under flight conditions. The analysis is then applied to other orbiter locations having similar structure/TPS, so that the entire orbiter becomes certified. In addition, an acoustic fatigue test under ambient conditions will be performed on a panel of identical design to another panel (described previously), which will be subjected to multi-environments at Langley. Multi-environmental effects will be assessed by noting the difference in fatigue life between these two panels. The exception to this approach is the RCC, where large specimens will be exposed to the multi-environments listed earlier.

163

Ref. [24] to handle many diversed structural elements and vibration transmission paths. Fig. 27 shows a comparison of the results of these three methods. The comparison shows that the scaling method provided vibration criteria which were reasonably conservative, except in the frequency range of overlap where both classical analysis and SEA are thought to be of limited accuracy.

In addition to the above, there were several large items which required special attention, such as hydrogen and oxygen tanks in the mid-fuselage and avionics packages in the aft fuselage. Classical analysis was used to size attachment struts, chassis and bracketry, as required, and to provide vibration criteria for these items. Finite element models like the avionics shelf of Fig. 28 were made to obtain random vibration response for comparison with previous vibration criteria. Fig. 29 shows the envelope of shelf response, the criteria, and an envelope of vibration data obtained during laboratory random vibration testing.

Development tests have been performed on many items of orbiter equipment using the above derived criteria. The qualification test phase is presently underway in subcontractor and commercial laboratories.

INTERNAL NOISE

Payload Bay Noise

Shuttle P/L's will be exposed to acoustic noise transmitted across the mid fuselage external structure/TPS, and P/L bay doors/radiator doors/TPS from the external aeroacoustic noise field. Internal acoustic noise is specified in Ref. [25] as not to exceed an overall sound pressure level of 145 dB with a spectrum shown in Fig. 30. This requirement approximates the noise field encountered by current P/L's on expendable launch vehicles, such as Delta, Centaur and Titan. However, early calculations showed that the internal noise would exceed this criteria at liftoff if noise suppression were not used to attenuate the external noise field and/or mass added to the P/L bay doors to reduce the noise transmission. As discussed earlier, a water system has been added to LC-39 for noise suppression to avoid a potential weight penalty to the orbiter. A preliminary P/L bay noise analysis was performed on an earlier orbiter configuration assuming semireverberant conditions. This model was adequate above 100 Hz, where sufficient modal overlap occurs in both structure and internal space. However, possible exceedances of the specified spectrum was more likely to occur below 100 Hz, so that a more sophisticated analysis was needed which

considers the noise transmission of individual structural modes and the response of individual internal P/L bay modes. As a result, NASA Goddard Space Flight has contracted with Bolt Beranek and Newman (BBN) to perform the more complex analysis, including determination of the effects of various P/L shapes on the internal noise field. This analysis utilizes a computer program to implement equations similar to those derived in Ref. [26].

In addition, acoustic tests have recently been made by BBN on the first orbiter during the last stages of orbiter assembly to provide some experimental data on noise transmission. This orbiter will be "launched" from the top of a modified Boeing 747 and will be used mainly to demonstrate flight control characteristics in simulation of critical TAEM maneuvers. Later, this orbiter will be refurbished for orbital flight. During these acoustic tests, the first orbiter lacked several features of a vertical-flight orbiter that must be taken into account in the utilization of the test data. For example, the first orbiter lacked radiator doors and TCS, and used simulated TPS consisting of foam material in place of the HRSI, LRSI and FRSI selected for the vertical-flight orbiter. A revised prediction of the P/L bay acoustic environment at liftoff will be based on a preliminary analysis with and without the water noise suppression system, assumed spatial properties of the noise field, contributions of individual structural and bay modes, mass properties of the TPS, first orbiter test results and experimentally-determined values of damping and internal absorption.

The P/L bay acoustic environment during ascent transonic/q_{max} and other flight events are expected to be less than the criteria of Fig. 30. During ascent, separated flow aft of the crew module will cause high aerodynamic noise on a small forward portion of the P/L bay doors. However, low aero noise on the remainder of the doors and the mid fuselage more than compensates for the effects of high local noise, so that the spatially-averaged external loading is less than that at liftoff. In addition, the P/L bay is vented during ascent providing reduced static pressure and internal acoustic noise. Aeroelastic damping contributions, discussed in Ref. [27], are also expected to reduce the noise transmission during transonic periods. P/L venting is achieved by opening doors in the sides of the mid fuselage after liftoff. It is possible that these openings could cause the P/L bay modes to be excited by aerodynamic flow over the opening, i.e., sort of a "coke bottle" or Helmholtz resonator effect. This condition was

simulated on a scale model during a wind tunnel test, but fortunately only low internal acoustic noise was observed.

Crew Module Noise

There are two general categories of noise sources that could affect personnel in the crew module: noise transmission from the external aeroacoustic noise field, and equipment internal to the crew module. The crew module has two decks or stories. The upper deck provides crew stations for pilot, copilot, P/L deployer (as required) and mission P/L checkout specialist (as required). The lower deck contains avionics equipment, sleeping quarters, galley, waste management compartment, and has a hatch to the outside plus an airlock to the P/L bay. Most components of the air conditioning subsystem, called the environmental control and life support subsystem (ECLSS), are mounted to the underside of the floor of the lower deck. The crew module structure is a pressure hull separated from the external structure/TPS by an air space (thus forming a double hull), except for a few locations at which the two structures are tied together by structural attachments. Analyses indicate that substantial noise reduction will be achieved by this arrangement. The Apollo command module, which was similarly configured, displayed good noise reduction qualities. As described previously, noise transmission is greatest at liftoff. Fig. 31 shows a predicted crew module internal acoustic spectrum for liftoff. Crew module noise during flight is anticipated to be less than lift-off noise because the spatially-averaged external aerodynamic noise is less than the acoustic noise at liftoff and because of venting of the air space. As before, high aero noise will be encountered locally during ascent, e.g., above the crew module and behind a strut that connects the orbiter to the ET, but will be more than compensated for by low aero noise elsewhere on the surface. In addition, the total exposure time per mission is relatively short: less than 10 seconds at liftoff and less than 30 seconds during ascent transonic/q_{max}.

Equipment-generated noise is a greater potential problem for crew comfort than is the launch noise, especially from the various ECLSS components like blowers and pumps. Some components operate continuously or have long duty cycles, and include operation during orbit that typically lasts one week and could occasionally last as long as four weeks. Moreover, noise criteria of NC-55, shown in Fig. 30 and discussed in Ref. [28], was specified for the noise generated by all continuously-operating sources within the crew module to minimize human fatigue and interference with sleep. NC-55 has been used for years to evaluate air conditioning

systems for offices. In order to satisfy the criteria, and equipment noise control program has been implemented to identify the sound power generated by each item, identify transmission paths (structureborne and airborne) and determine which noise attenuation measures are most effective, consistent with minimum weight penalty. Noise control measures being considered include special treatment of ducts between blowers and crew spaces, resilient mountings and flexible lines for all rotating equipment, and sealing of holes and gaps between the underside and topside of the lower deck floor, and around the avionics bays.

MAJOR GROUND AND FLIGHT TESTS

The major ground test to be utilized to obtain vibroacoustic data is the main propulsion test (MPT), shown in Fig. 33 comprising an orbiter aft fuselage and ET, with the three SSME's firing into a modified S-IC test stand at the NASA National Space Technology Laboratory in Mississippi. Rocket engine noise will be measured to support the comparison of full scale and model engines in order to verify/update the model test results described earlier. Also, aft fuselage vibration will be measured to support verification of random vibration criteria. However, two categories of vibration sources are recognized: acoustic noise, and mechanically transmitted vibration from the three SSME's. It is necessary to separate and identify each category since each should have different flight vibration spectra and will have different exposure times. The liftoff event, for example, occurs for less than 10 sec per mission whereas the SSME's fire for about 490 sec per mission. Three different methods are presently under consideration for identifying these sources: coherence function analysis; firing the SSME's with and without a water system for noise suppression; firing the SSME's with and without a sound barrier surrounding the aft fuselage. Coherence analysis, discussed in Ref. [29 – 30], requires careful calibration of instrumentation and considerable data reduction to obtain ordinary, multiple and partial coherence functions. The barrier could be made of twin metal sheets with sand poured between the sheets. The water system or sound barrier must be effective enough to achieve at least 6dB noise attenuation across the frequency range of interest. Approximately 15 external microphones, 5 internal microphones, 350 accelerometers and 300 strain gages will be used for obtaining MPT vibroacoustic and acoustic fatigue data.

Six SSV vertical development flights using one flight orbiter are planned from KSC prior to making the shuttle operational. Payloads will be carried on all flights

166

except for the first, which will carry an instrumentation package only. Spacelab is scheduled for the second, third and sixth flights. The Long Duration Exposure Facility and the Multi-Mission Spacecraft/Technology Demonstration Satellite are scheduled for the fourth and fifth flights, respectively. A substantial number of orbiter flight measurements are planned to verify/update vibroacoustic criteria and acoustic fatigue life estimates. Data from approximately 8 external microphones, 6 internal microphones, 233 accelerometers and 54 strain gages are to be tape recorded in the orbiter during each development flight. Each of these measurements will be recorded on two of the six flights and switched to other locations during the remaining four. In addition, 13 external microphones, 6 internal microphones, 117 accelerometers and 46 strain gages will be measured on all six development flights. Also, four microphones on each flight have been designated for the P/L bay to establish the effect of P/L changes on the internal acoustic environment and ten accelerometers have been designated for mounting on P/L's or at P/L-orbiter interfaces. It is shown to be practical to continue P/L-related measurements into the operational flight phase, a P/L vibroacoustic "data bank" may be generated for use by later shuttle users. Vibration acceleration and strain will be measured over a frequency range of 20 to 2000 Hz and 5 to 500 Hz, respectively. The microphone frequency range varies between 20 to 2000 Hz and 20 to 8000 Hz.

REFERENCES

1. Thompson, R. F., "Space Shuttle Dynamics", Shock & Vib. Bull. 44, Pt 2, Aug. 1974, pp 1-17.

2. Malkin, M. S. and Jeffs, G. W., "Space Shuttle 1976: Into Mainstream Development", Astro & Aero, v. 14, n. 1, Jan. 1976, pp 40-43.

3. McIntosh, G. P. and Larkin, T. P., "The Space Shuttle's Testing Gauntlet", Astro & Aero, v. 14, n. 1, Jan. 1976, pp 44-56.

4. Strouhal, G. and Tillian, D. J., "Testing the Shuttle Heat-Protection Armor", Astro & Aero, v. 14, n. 1, Jan. 1976, pp 57-65.

5. Eldred, K. M., "Acoustic Loads Generated by the Propulsion System", NASA SP-8072, June 1971.

6. Guest, S. H. and Jones, J. H., "Space Shuttle Noise Suppression Concepts", Proc. 13th Space Cong., May 1976.

7. Potter, R. C. and Crocker, M. J., "Acoustic Prediction Methods for Rocket Engines, Including the Effects of Clustered Engines and Deflected Exhaust Flow", NASA CR-566, Oct. 1966.

8. Robertson, J. E., "Prediction of In-flight Fluctuating Pressure Environments Including Protuberance Induced Flow", Wyle Labs Rept WR 71-10, Mar. 1971

9. Plotkin, K. J. and Robertson, J. E., "Prediction of Space Shuttle Fluctuating Pressure Environments, Including Rocket Plume Effects", Wyle Labs Rept WR 73-6, June 1973 (Also NASA CR-124347).

10. Hanly, R. D., "Surface-Pressure Fluctuations Associated with Aerodynamic Noise on the Space Shuttle Launch Configuration at Transonic and Supersonic Speeds", Proc. 17th Str., Str. Dyn. & Mat. Conf., AIAA, May, 1976, pp 241-247.

11. Barrett, R. E., "Techniques for Predicting Localized Vibration Environments of Rocket Vehicles", NASA TN D-1836, Oct. 1963.

12. Anon., "Airplane Strength and Rigidity Reliability Requirements", Military Spec. MIL-A-008866A, Mar. 31, 1975, Par. 3.1.1.1.

13. Miles, J. W. and Thomson, W. T., "Statistical Concepts in Vibration", Shock and Vibration Handbook (Harris, C. M. and Crede, C. E., Ed.), McGraw-Hill Book Co., N. Y., 2nd Ed., 1976, Chap. 11.

14. Trapp, W. J. and Forney, D. M., Ed., Acoustical Fatigue in Aerospace Structures, Syracuse Univ. Press, N. Y., 1965.

15. Rudder, F. F. and Plumblee, H. E., "Sonic Fatigue Design Guide for Military Aircraft", AFFDL-TR-74-112, May 1975.

16. Vaicaitis, R. and Dowell, E. H., "Response of Reusable Surface Insulation Panels to Random Pressure", Proc. 17th Str., Str. Dyn. & Mat. Conf., AIAA, May 1976, pp 257-272.

17. Ojalvo, I. V. and Ogilvie, P. L., "Modal Analysis and Dynamic Stresses for Acoustically Excited Shuttle Insulation Tiles", Proc. 17th Str., Str. Dyn. & Mat. Conf., AIAA, May 1976, pp 273-281.

18. Ojalvo, I. V. and Ogilvie, P. L, "Modal Analysis and Dynamic Stresses for Acoustically Excited Shuttle Insulation Tiles", NASA CR-144958, 1976.

19. Rucker, C. E. and Mixson, J. S., "Vibroacoustic Testing of Space Shuttle Thermal Protection System Panels", _Proc. 17th Str., Str. Dyn. & Mat. Conf._, AIAA, May 1976, pp 248-256.

20. Stevens, R. A. "Shuttle Orbiter Acoustic Fatigue Testing", _J. Envir. Sci._, v. XIX, n. 2, Mar./Apr. 1976, pp 23-27.

21. Barnoski, R. L., Piersol, A. G., Van Der Laan, W. F., Winter, P. H. and Winter, E. F., "Summary of Random Vibration Prediction Procedures", _NASA CR-1302_, Apr. 1969.

22. Himelblau, H., Fuller, C. M. and Scharton, T. D., "Assessment of Space Vehicle Aeroacoustic-Induced Vibration Prediction, Design & Testing", _NASA CR-1596_, July 1970.
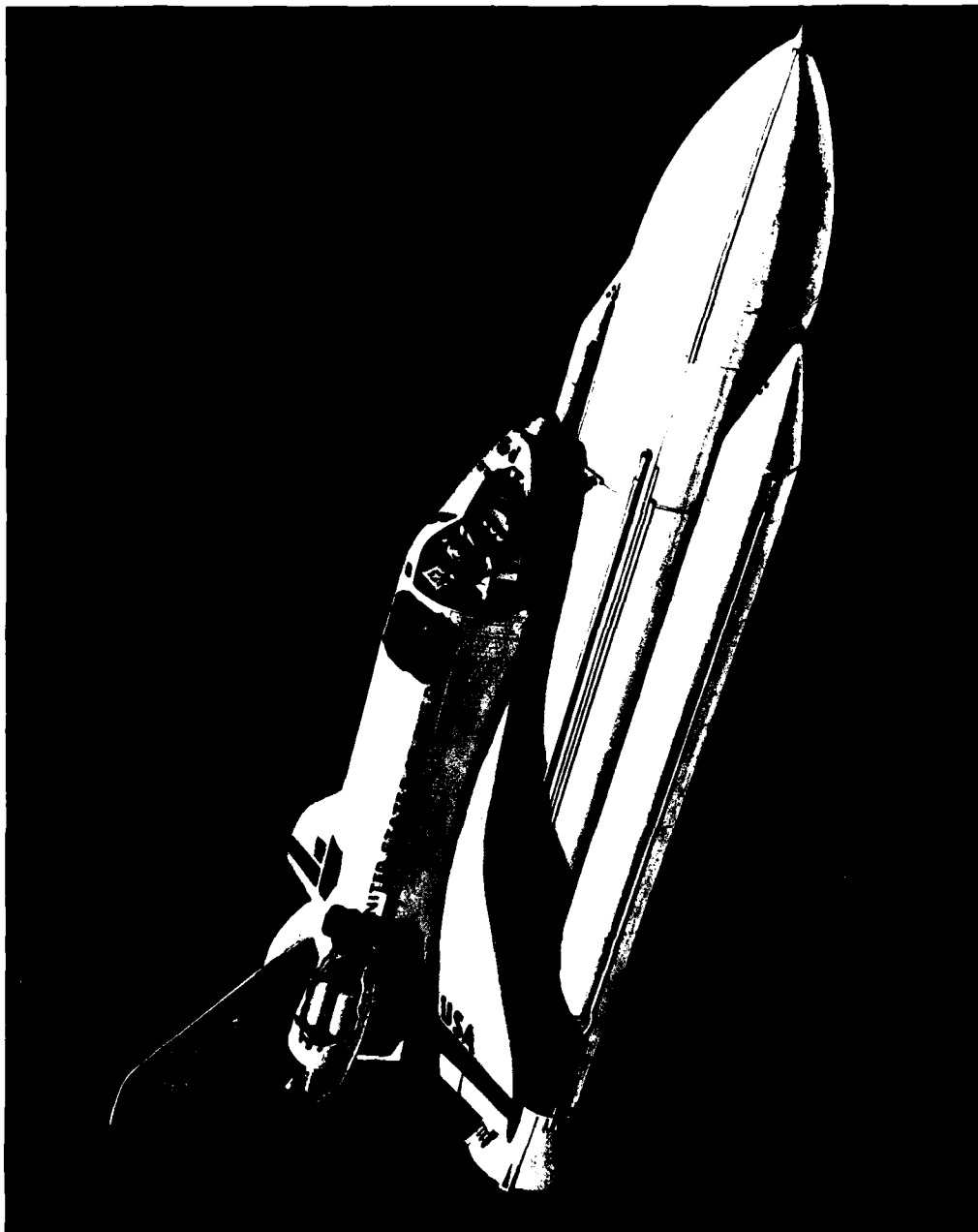
Fig. 1 - Space Shuttle Configuration

169

EXTERNAL TANK
SEPARATION

ORBIT INSERTION

ORBITAL OPERATIONS

DEORBIT

ENTRY

TERMINAL
PHASE

HORIZONTAL
LANDING

STAGING

BOOSTER
SPLASHDOWN

IMPACT OF
EXTERNAL TANK

RETURN TO
LAUNCH SITE

LAUNCH
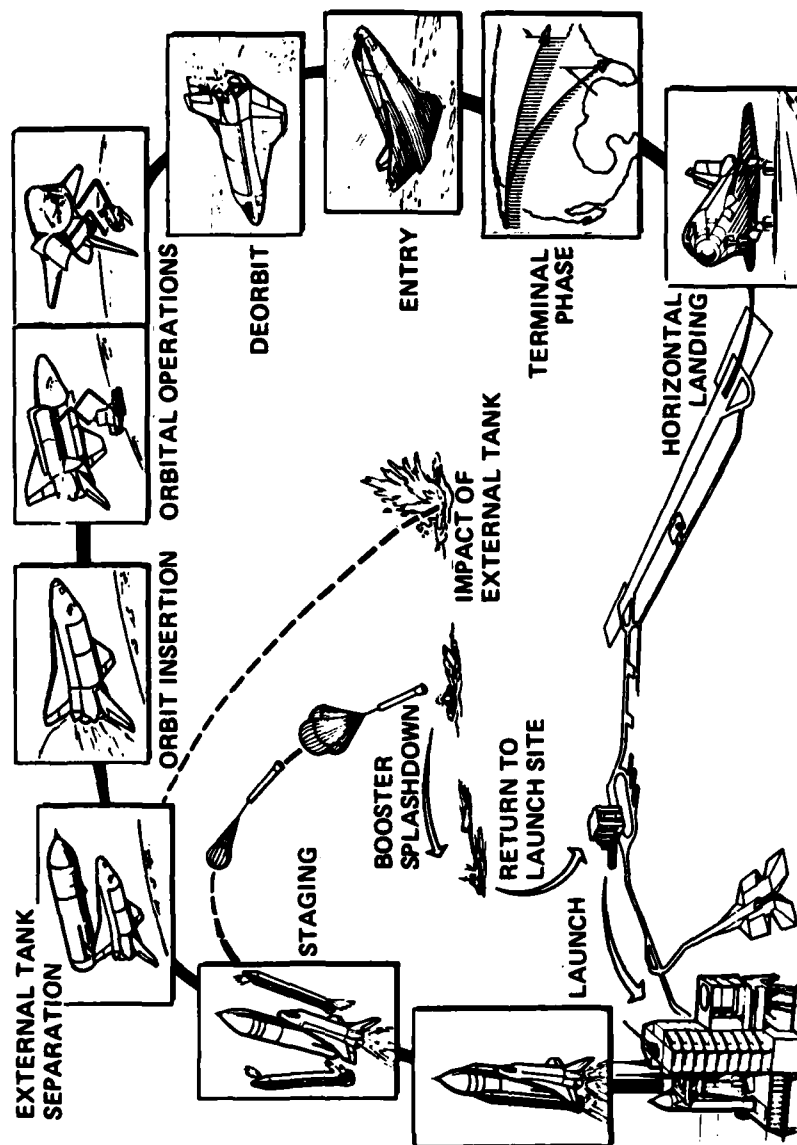
Fig. 2 - Space Shuttle Mission Profile

170

ONE-THIRD OCTAVE BAND CENTER FREQUENCIES ~ HERTZ

```
——————  SCALED FROM SATURN V LIFTOFF DATA
—●—  6.4% MODEL DATA - NO WATER SYSTEM
—✗—  6.4% MODEL DATA - WATER SYSTEM FOR NOISE SUPPRESSION
```
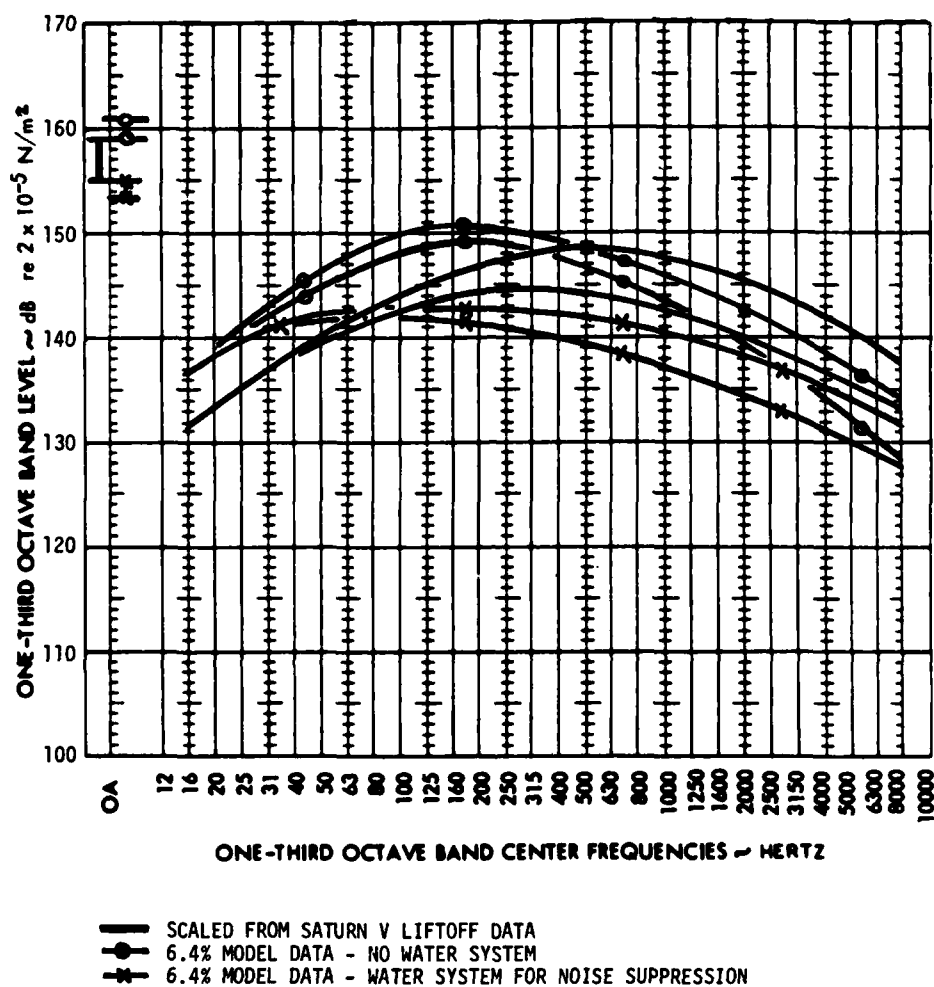
Fig. 3 – Liftoff Acoustic Noise Spectra for Orbiter Payload Bay Doors
Based on Saturn V Prediction and Scale Model Data. The Upper
and Lower Curves of each set applies to the Aft Doors and
Forward Doors, respectively.

171
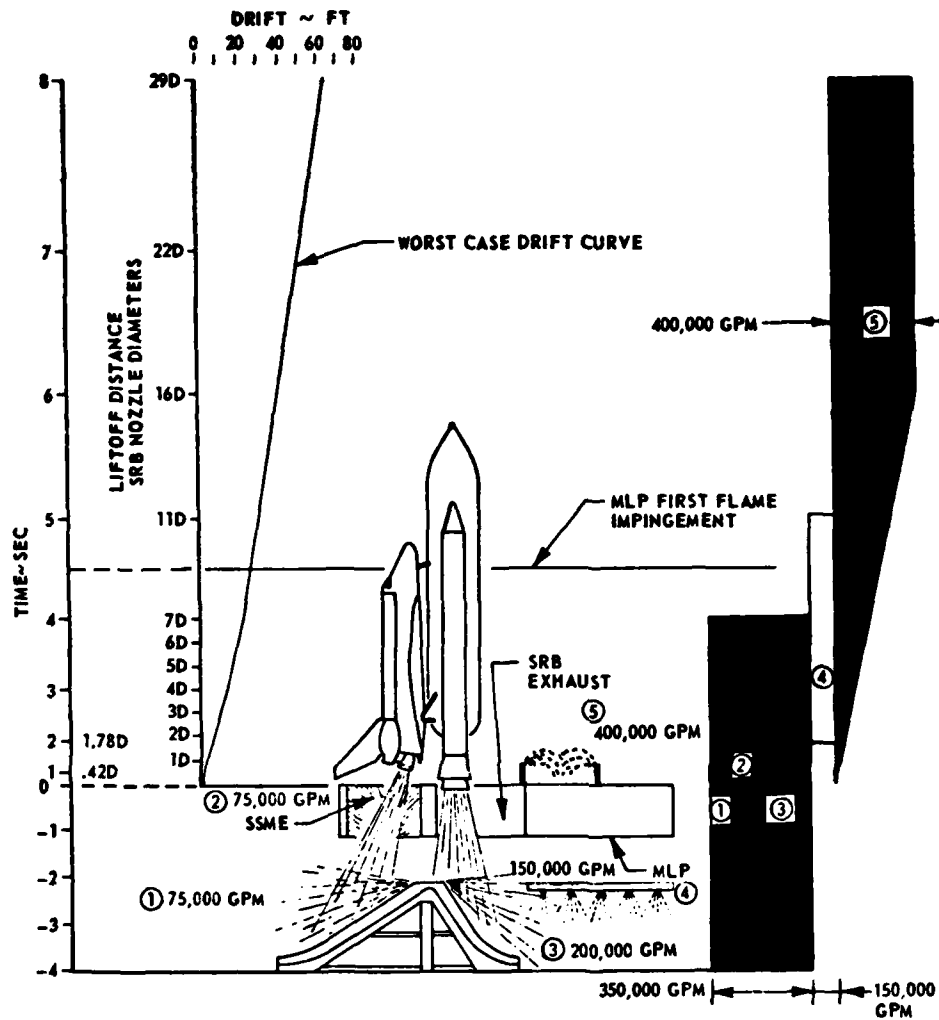
Fig. 4 - Space Shuttle Vehicle on NASA Kennedy Space Center Launch Complex
LC-39. Data on vehicle drift and water system for noise
suppression are also shown.
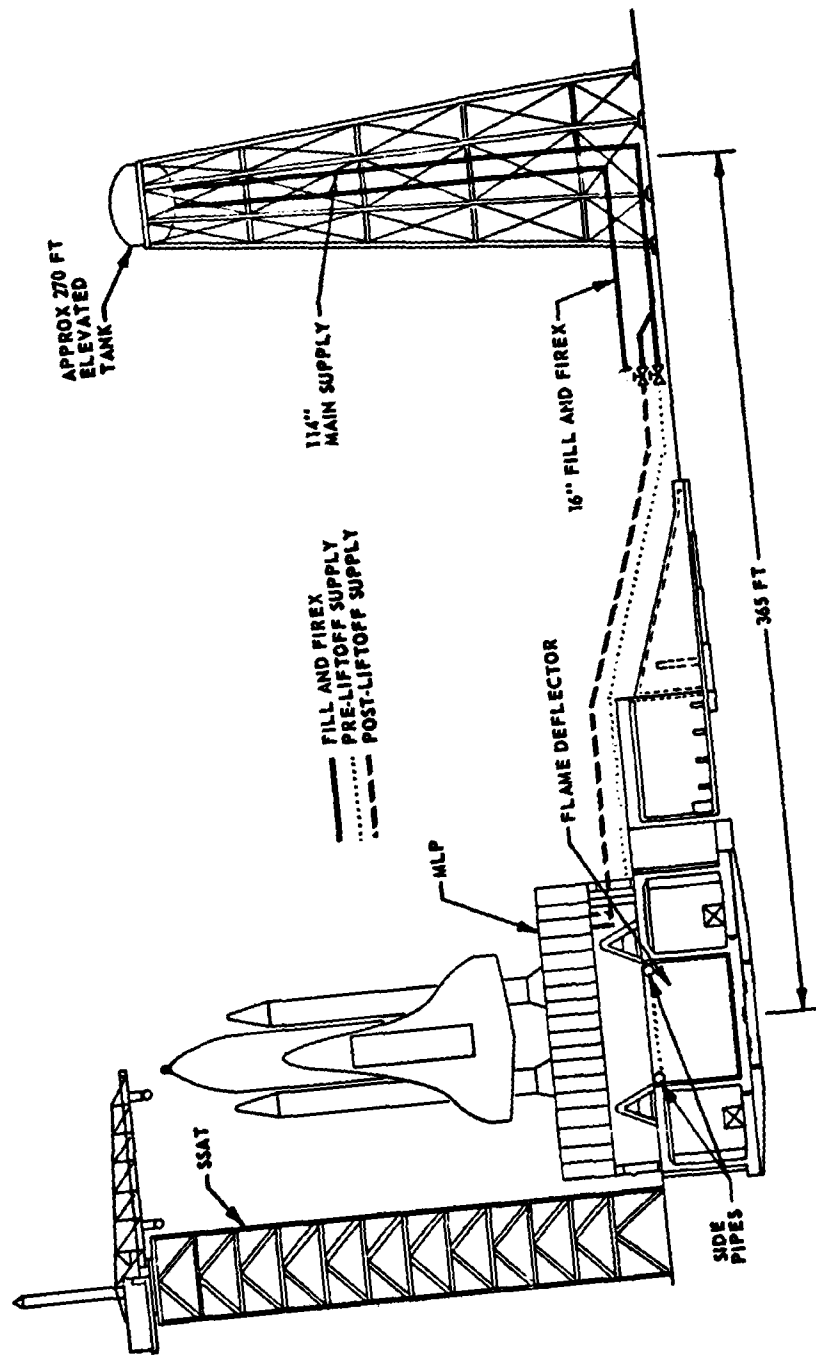
Fig. 5 - Space Shuttle Vehicle on KSC Launch Complex LC-39, including Water System for Noise Suppression

APPROX 270 FT ELEVATED TANK

114" MAIN SUPPLY

16" FILL AND FIREX

FILL AND FIREX
PRE-LIFTOFF SUPPLY
POST-LIFTOFF SUPPLY

MLP

FLAME DEFLECTOR

SSAT

SIDE PIPES

365 FT

173
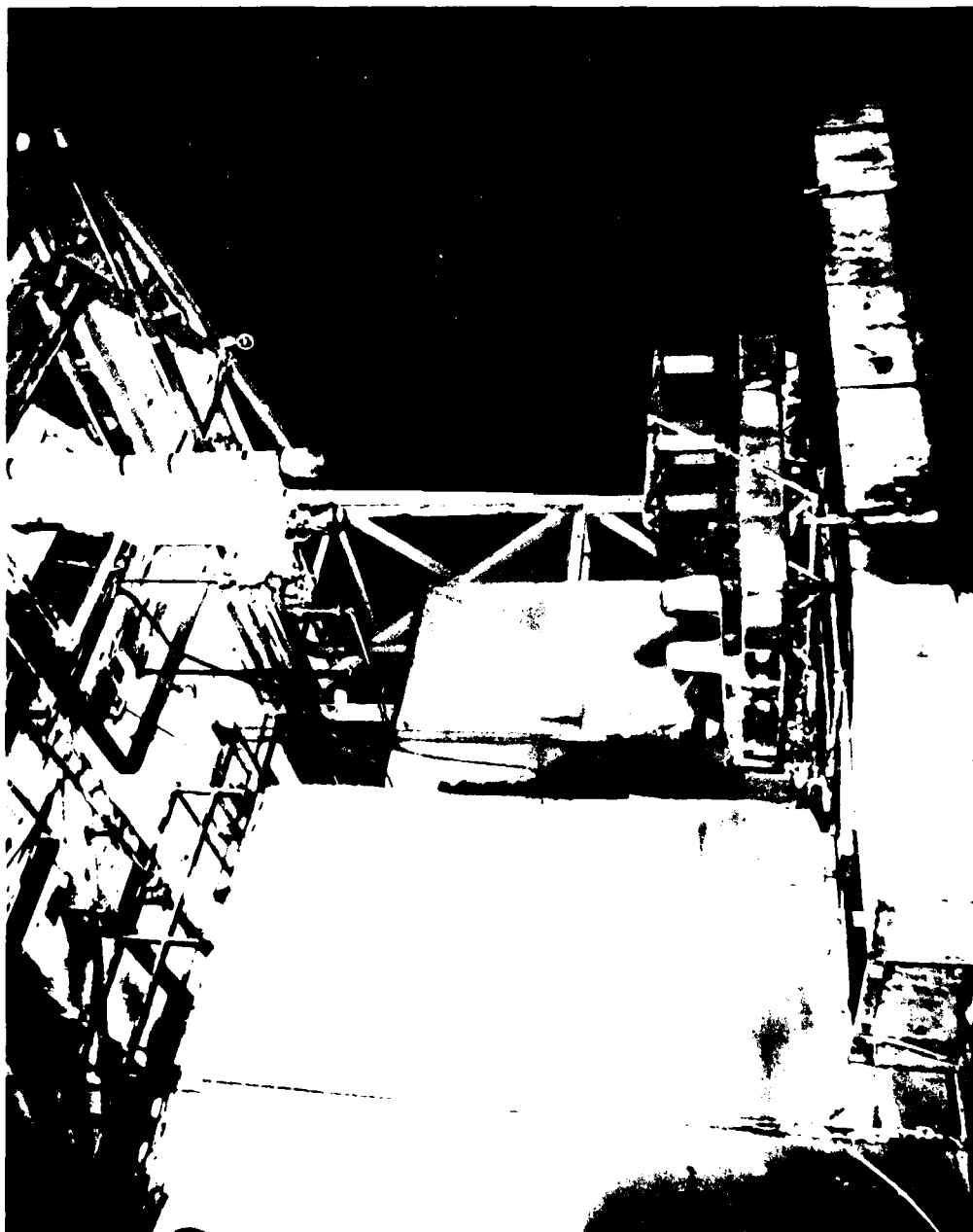
Fig. 6 – 6.4 Percent Acoustic Scale Model Test at NASA Marshall Space Flight Center, comprising Space Shuttle Model and Modified KSC Pad Model

174
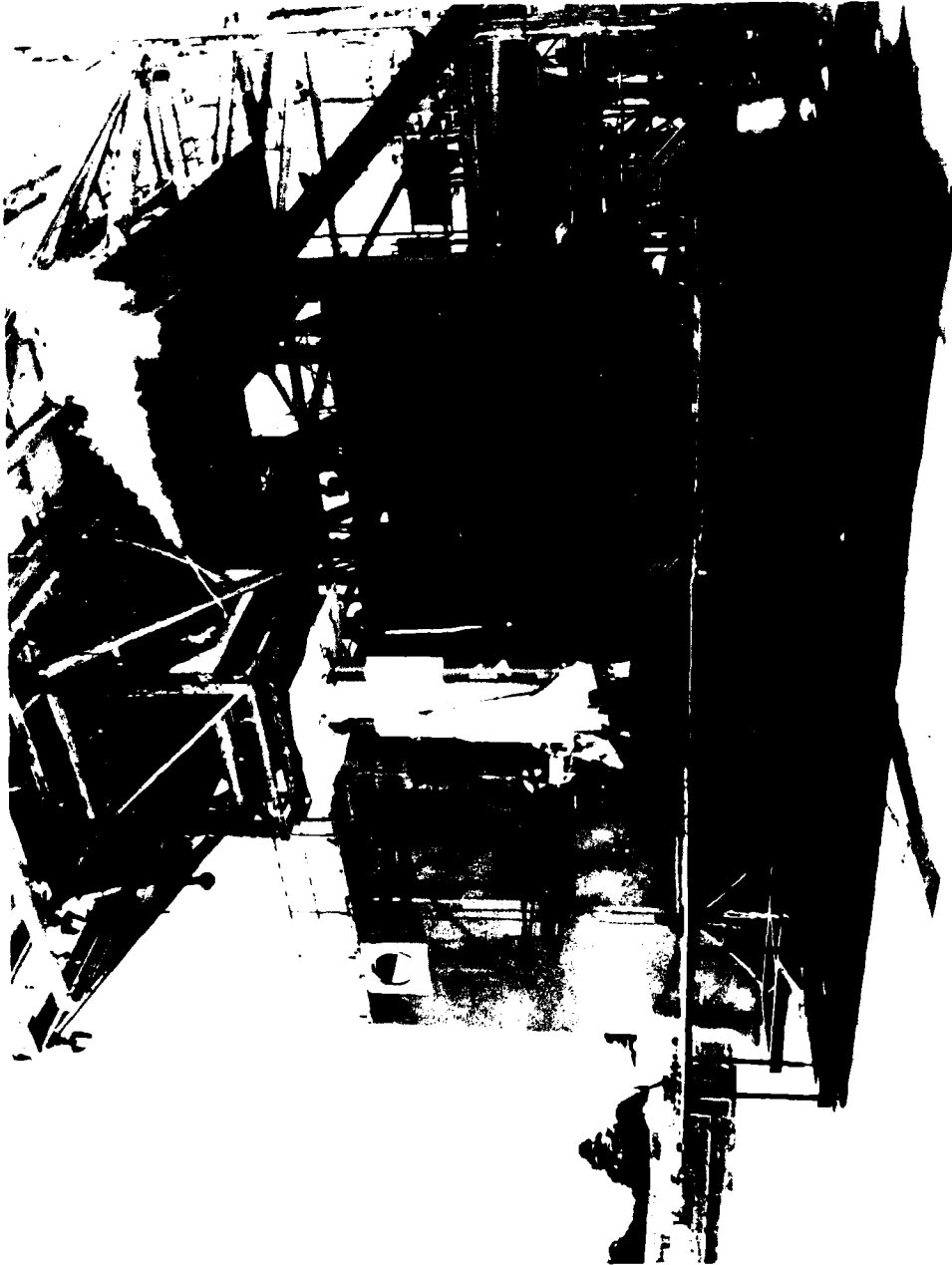
Fig. 7 – 6.4 Percent Acoustic Scale Model Test at NASA Marshall Space Flight Center, comprising Space Shuttle Model and Modified VAFB Pad Model

175
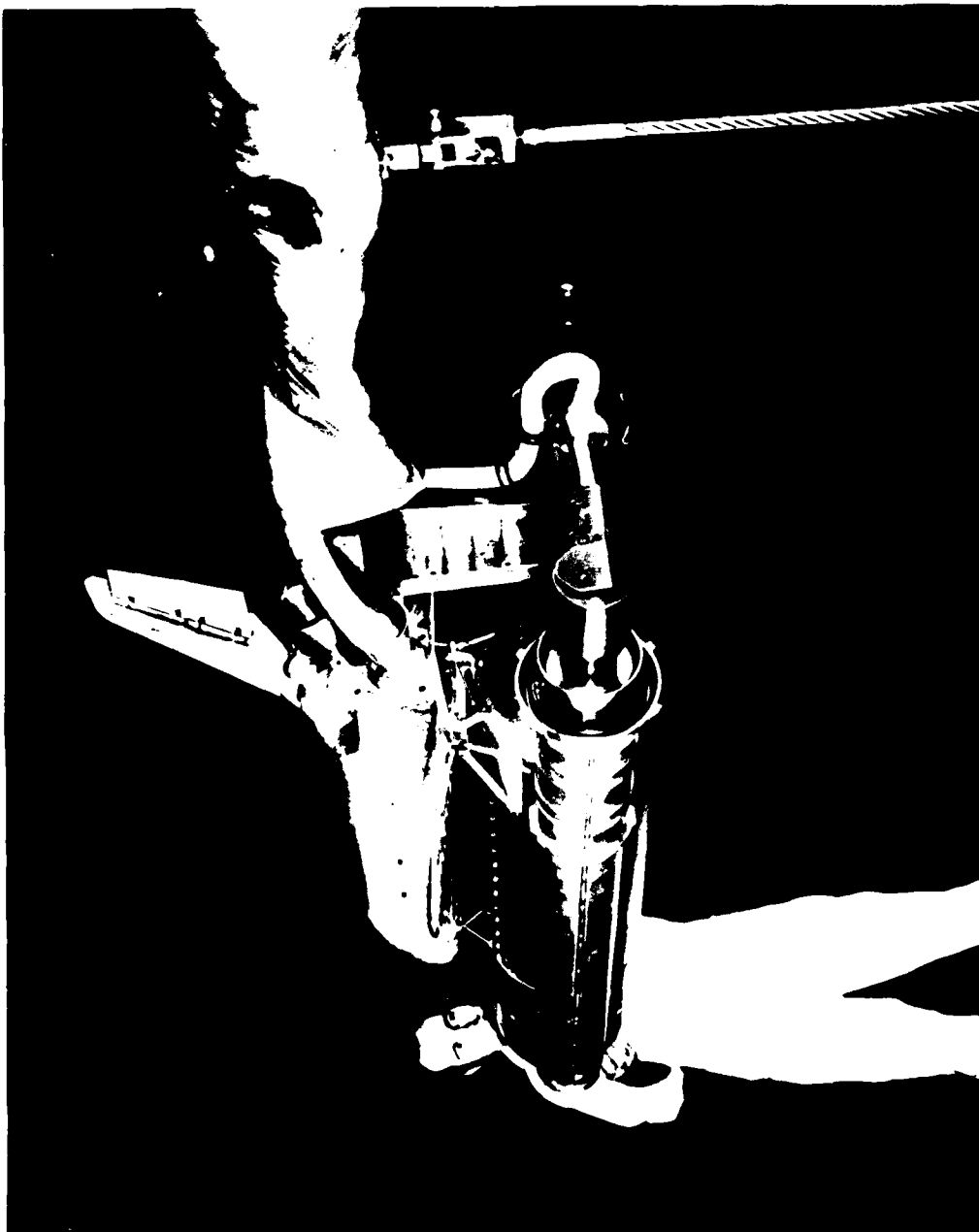
Fig. 8 – 3.5 Percent Rigid Model of Space Shuttle Vehicle in NASA Ames Research Center

11 x 11 ft Transonic Wind Tunnel

176

Fig. 9 – 3.5 Percent Rigid Model of Space Shuttle Vehicle in NASA Ames Research Center

9 x 7 ft Supersonic Wind Tunnel
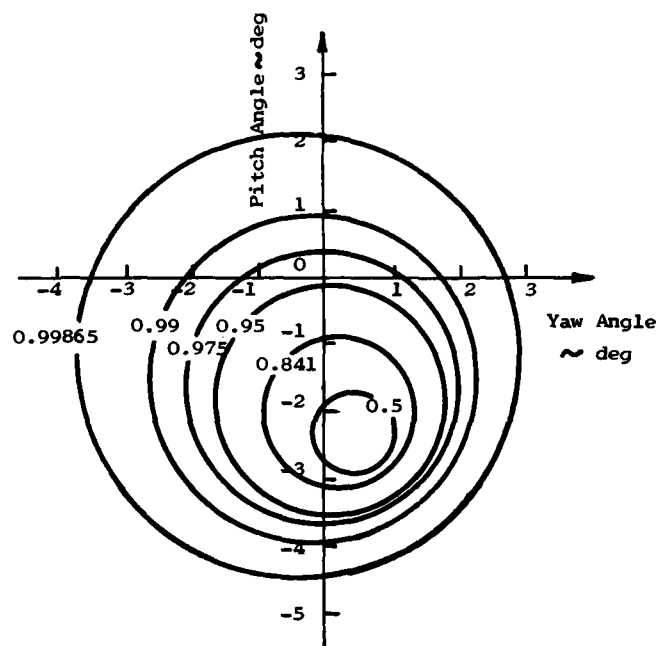
Fig. 11 - Probability Contours of Wind-Induced Flight Attitudes for the SSV
During Ascent
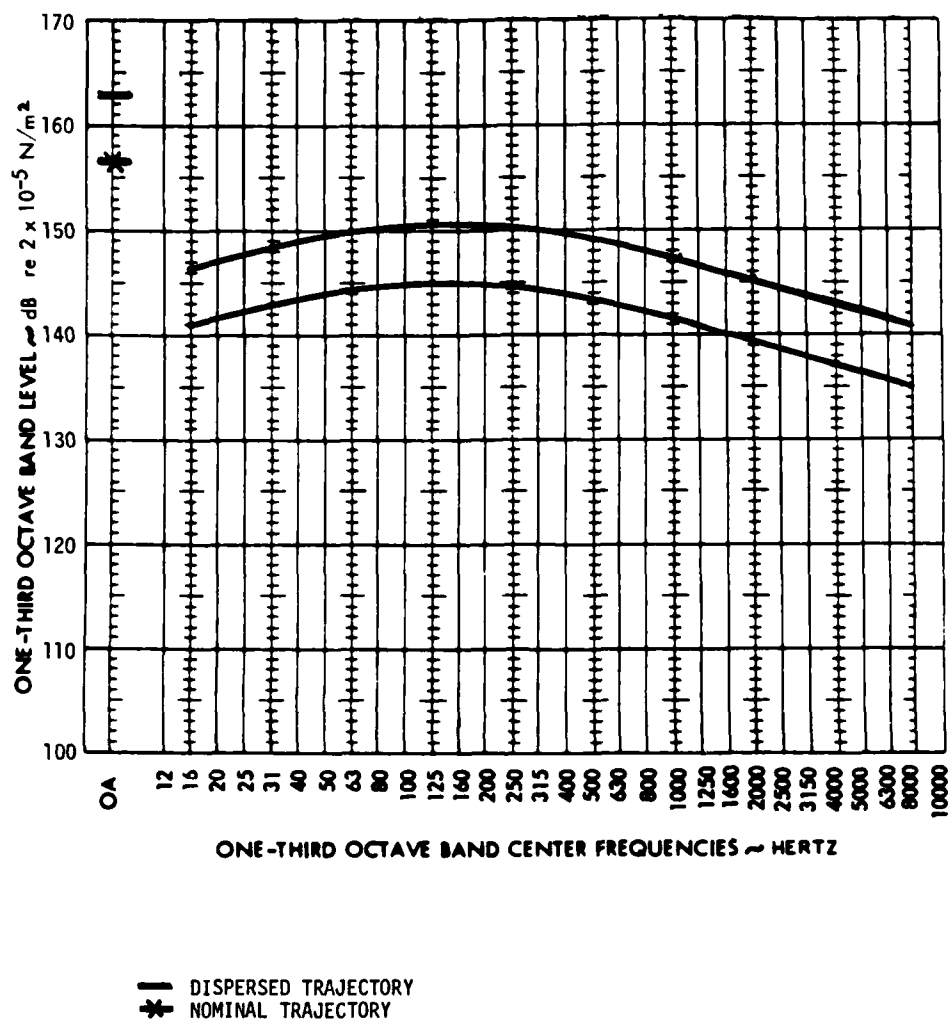
Fig. 12 – Ascent Aerodynamic Noise Spectra for Orbiter Payload Bay Doors
Under Nominal and Dispersed Trajectory Conditions

180
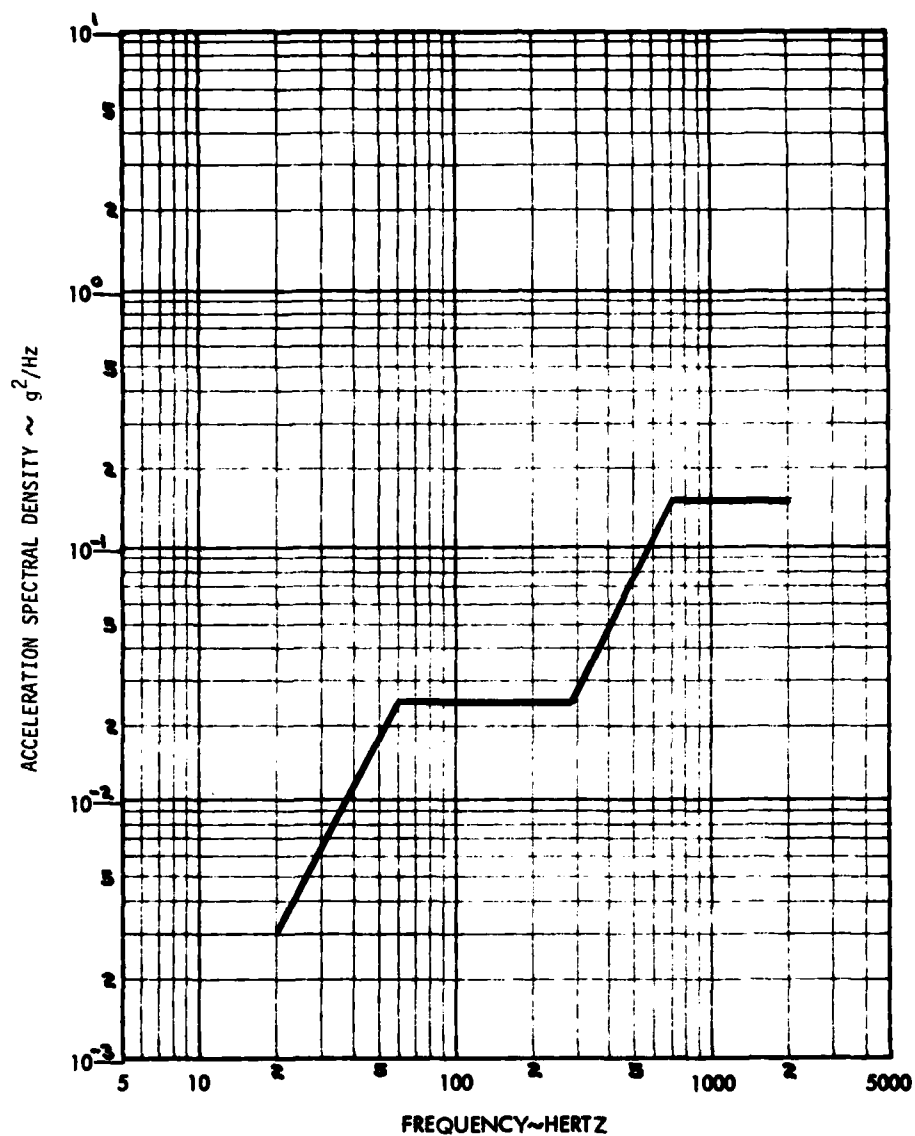
Fig. 13 – Predicted Orbiter Aft Fuselage Vibration Spectrum from Mechanically-
Transmitted SSME Vibration Excitation

181
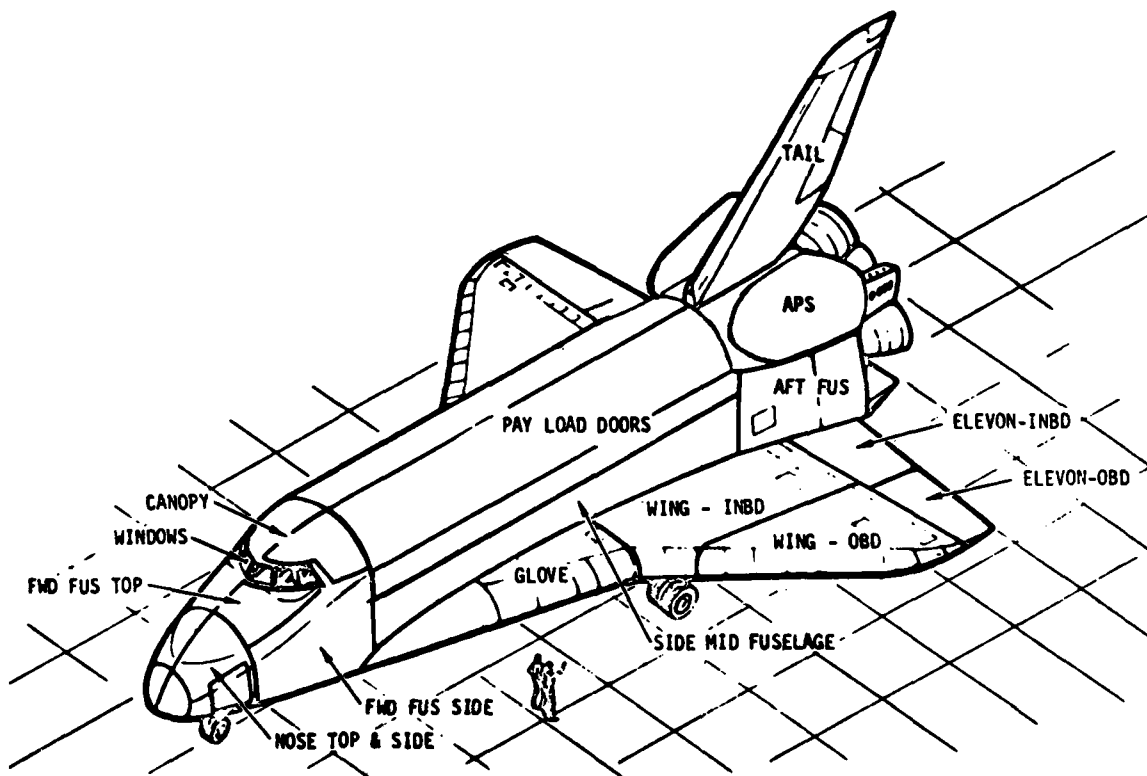
Fig. 14 — Aeroacoustic Noise Zones of the Shuttle Orbiter — Top and Side
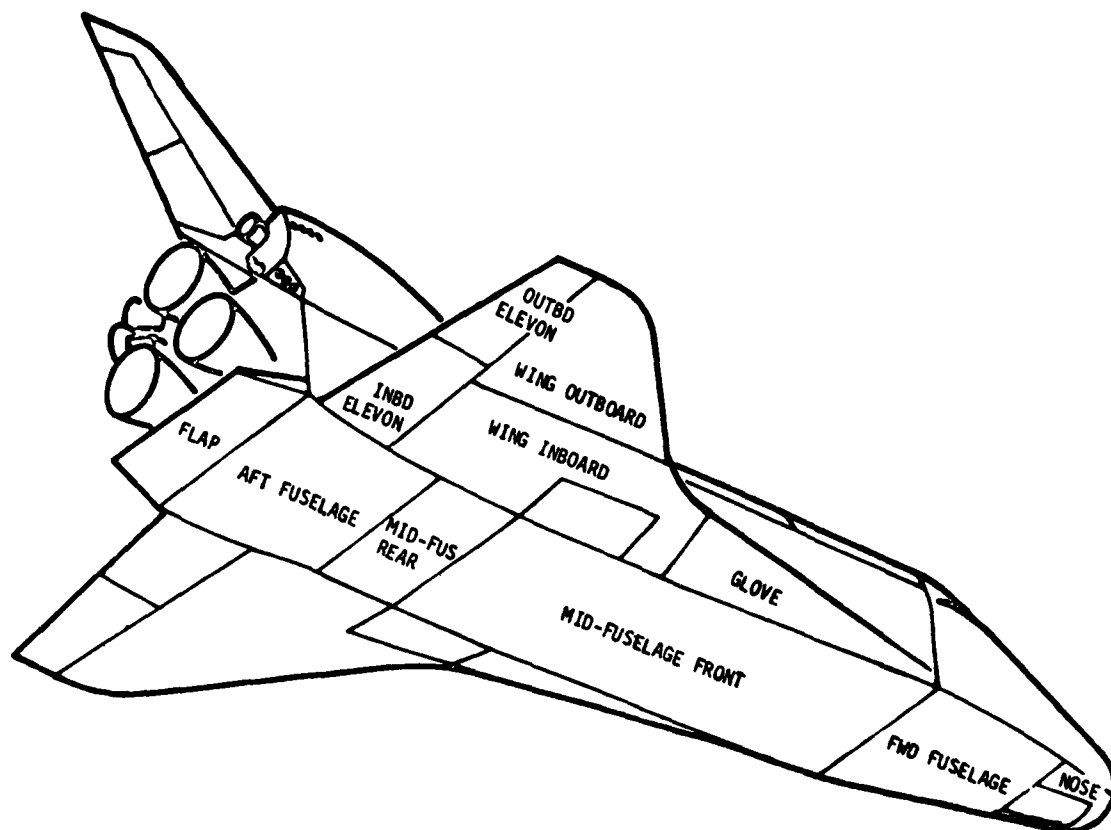
Fig. 15 - Aeroacoustic Noise Zones of the Shuttle Orbiter - Bottom
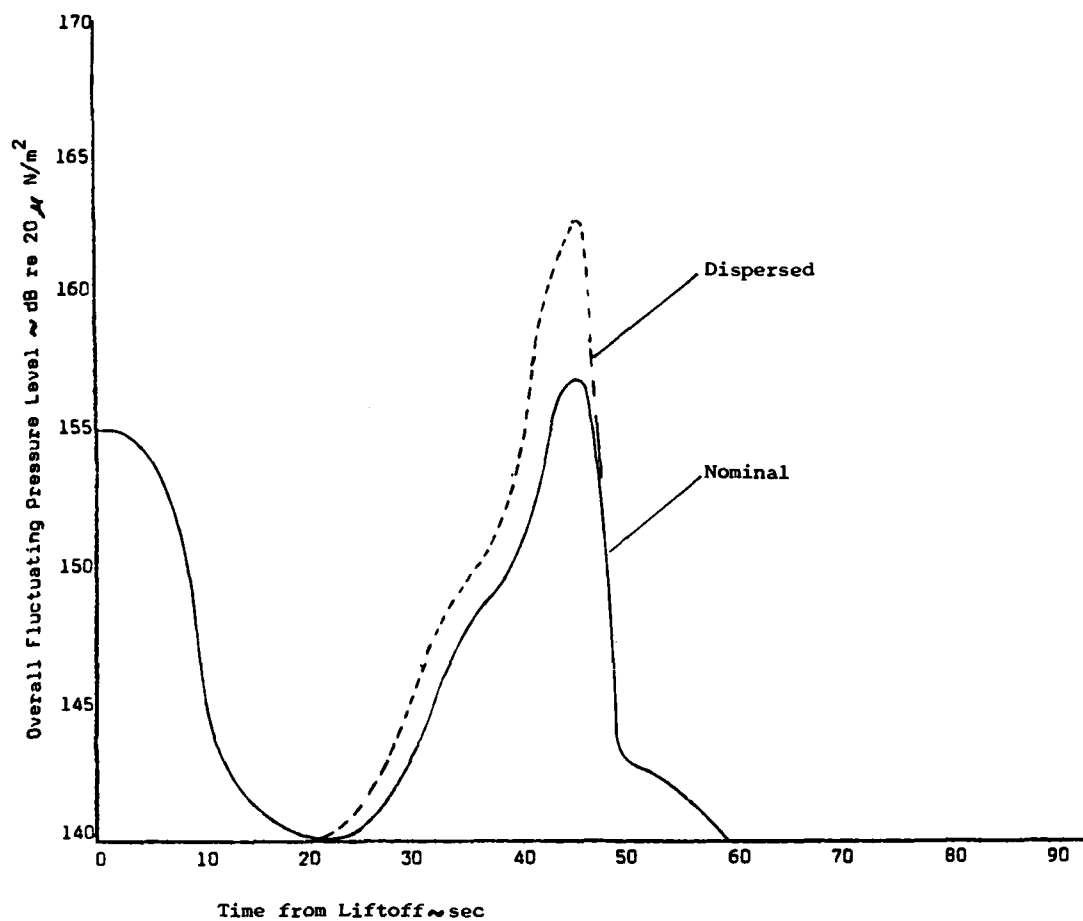
Fig. 16 – Overall Fluctuating Pressure Level vs Time History for the Orbiter
Forward Payload Bay Doors

184
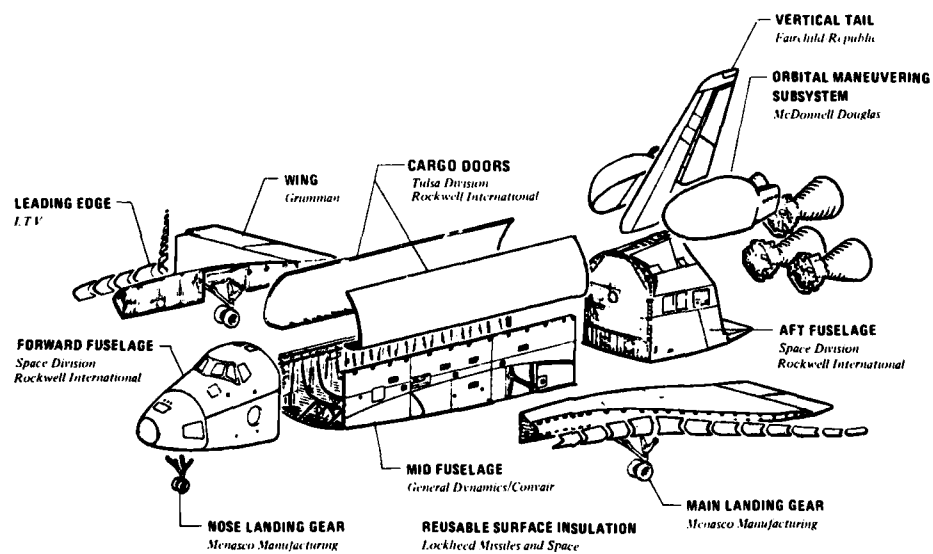
Fig. 17 - Structural Subcontractors of the Shuttle Orbiter

LOWER SURFACE VIEW

2300F
2000F
2575F
1800F
2000F
2000F
2300F
2300F
2625F

1800F
1200F
750F
800F

750F
1200F
1200F

UPPER SURFACE VIEW

ENTRY/ASCENT
700F / 750F
750F / 830F
850F / 900F

*1000F
*1750F
800F
1680F
1200F
*2100F
*2150F
*2220F
*1000F

*DENOTES ASCENT TEMPERATURES.
(MAXIMUM YAW 8 DEG)

ENTRY | ASCENT
700F | 750F
750F | 830F
850F | 900F

1200F
800F
750F

*785F *795F *760F
*760F *680F
*805F
*805F *830F

2570F
1800F 2000F
SIDE SURFACE VIEW

Fig. 18 – Maximum Surface Temperature Contours During Orbiter Entry

186

LOWER SURFACE

UPPER SURFACE

REINFORCED CARBON-CARBON

HIGH-TEMPERATURE REUSABLE
SURFACE INSULATION

LOW-TEMPERATURE REUSABLE
SURFACE INSULATION

COATED NOMEX FELT

METAL OR GLASS
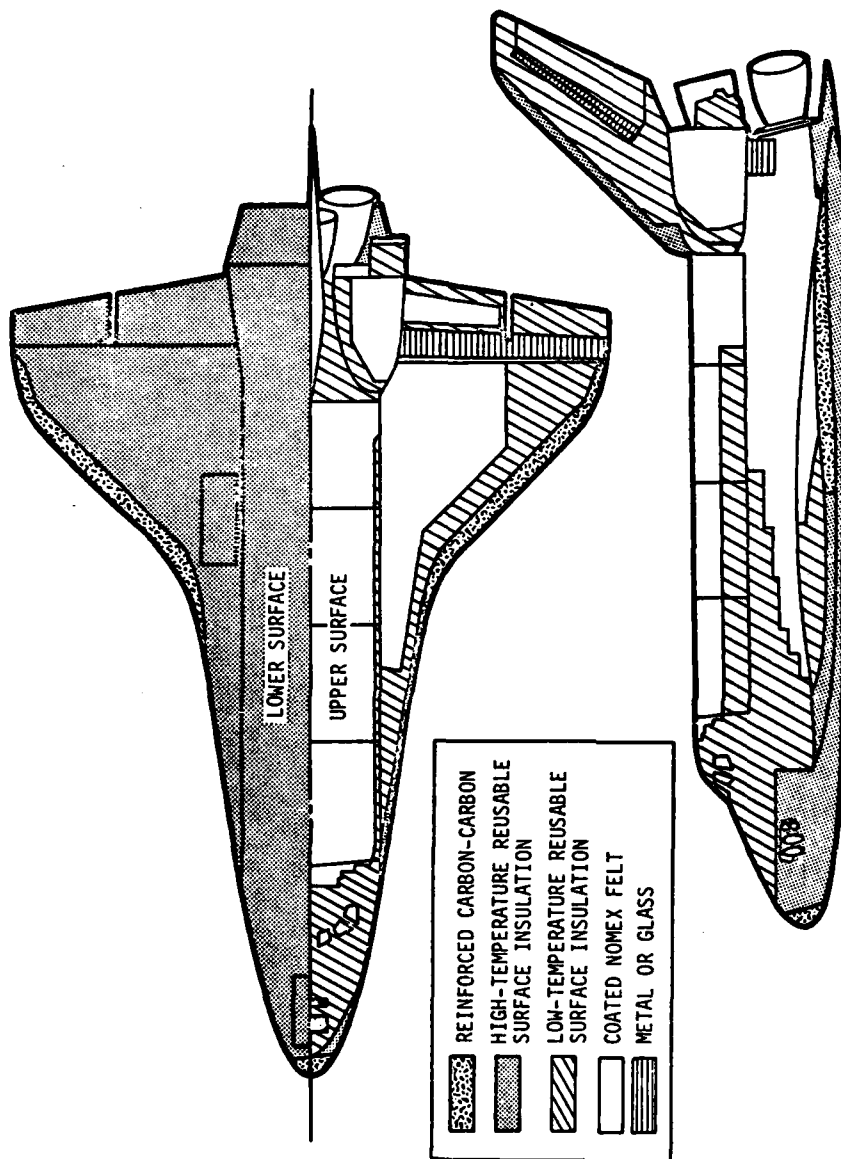
Fig. 19 - Material Elements Used for the Orbiter Thermal Protection Subsystem (TPS)

187

HRSI & LRSI

UPPER SIDE

HRSI & LRSI TILE
(COATED LI-900
SILICA)

0.035 IN. MIN
0.075 IN. MAX

LOWER SIDE

0.025 IN. MIN
0.065 IN. MAX

STRAIN ISOLATOR PAD
(NOMEX FELT)

0.0075 RTV 560 ADHESIVE

ALUMINUM SKIN

0.50 ±0.06 IN.

0.09 ±0.03 IN.

0.75 ±0.03 IN.

FILLER BAR
(COATED NOMEX FELT)

LESS - WING SECTION

A-286 BOLTS &
INCONEL BUSHINGS

HRSI

LEADING EDGE
SPAR

(INTERNAL
INSULATION
NOT SHOWN)

HRSI

COATED RCC
LEADING EDGE
PANEL

INCONEL 718
FITTINGS

COATED RCC
TEE SEAL

A-286 BOLTS &
INCONEL BUSHINGS

LESS - NOSE SECTION

ALUMINUM
STRUCTURE

CHINE PANEL &
LANDING GEAR
DOOR ATTACH

LANDING
GEAR
DOOR

HRSI

INSULATION RING

RCC EXPANSION SEAL

HRSI

RCC, TEE
SEAL

SUPPORT
FITTING

RCC,
NOSE CAP

Fig. 20 - TPS Installation Details

188
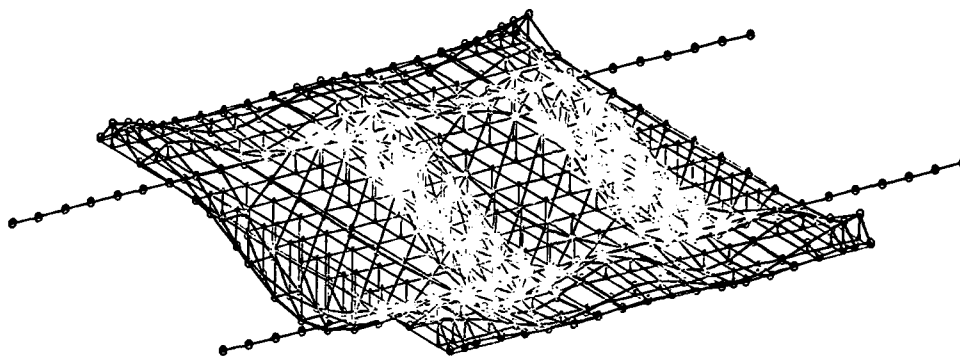
Fig. 21 – Finite Element Model of an Orbiter Panel. NASTRAN was Used to

Compute the 7th Mode Shown.

189
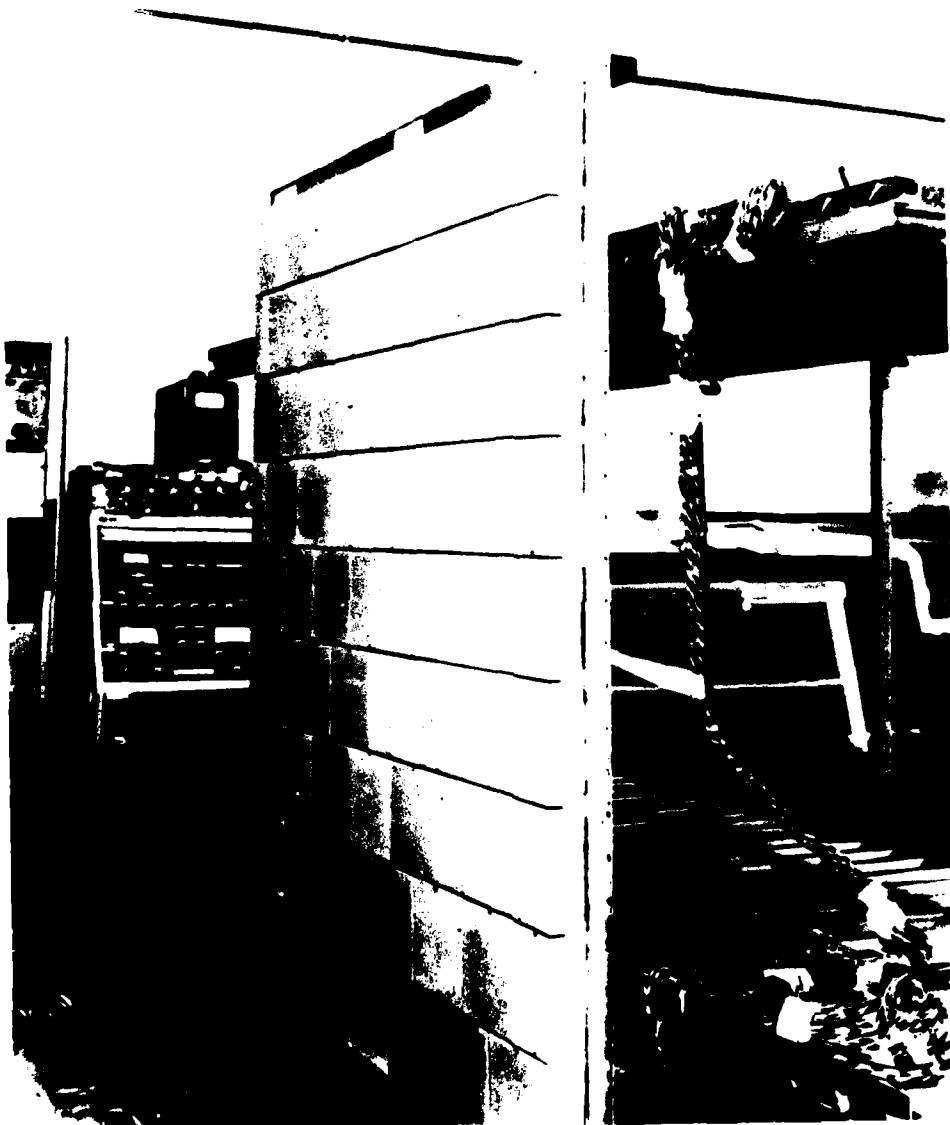
Fig. 22 - Typical Early Orbiter Development Test Panel
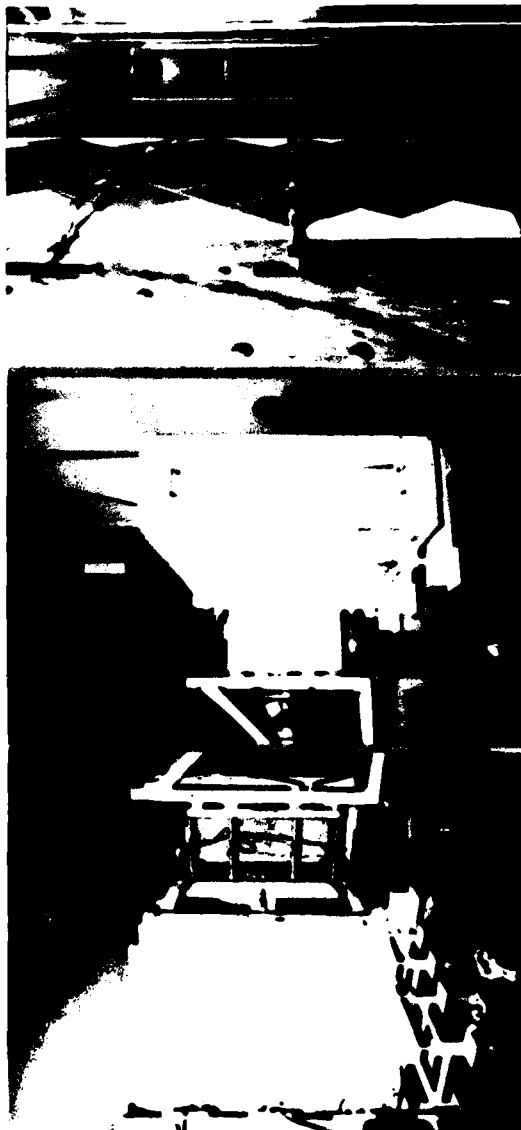
Fig. 23 – Orbiter Wing Panel in NASA Johnson Space Center Progressive Wave

Acoustic Test Facility
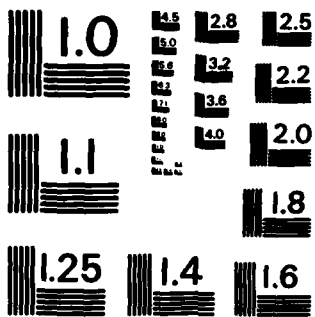
MICROCOPY RESOLUTION TEST CHART

NATIONAL BUREAU OF STANDARDS-1963-A

Fig. 24 – Orbiter Elevon Panel in NASA Johnson Space Center
Reverberant Acoustic Test Facility
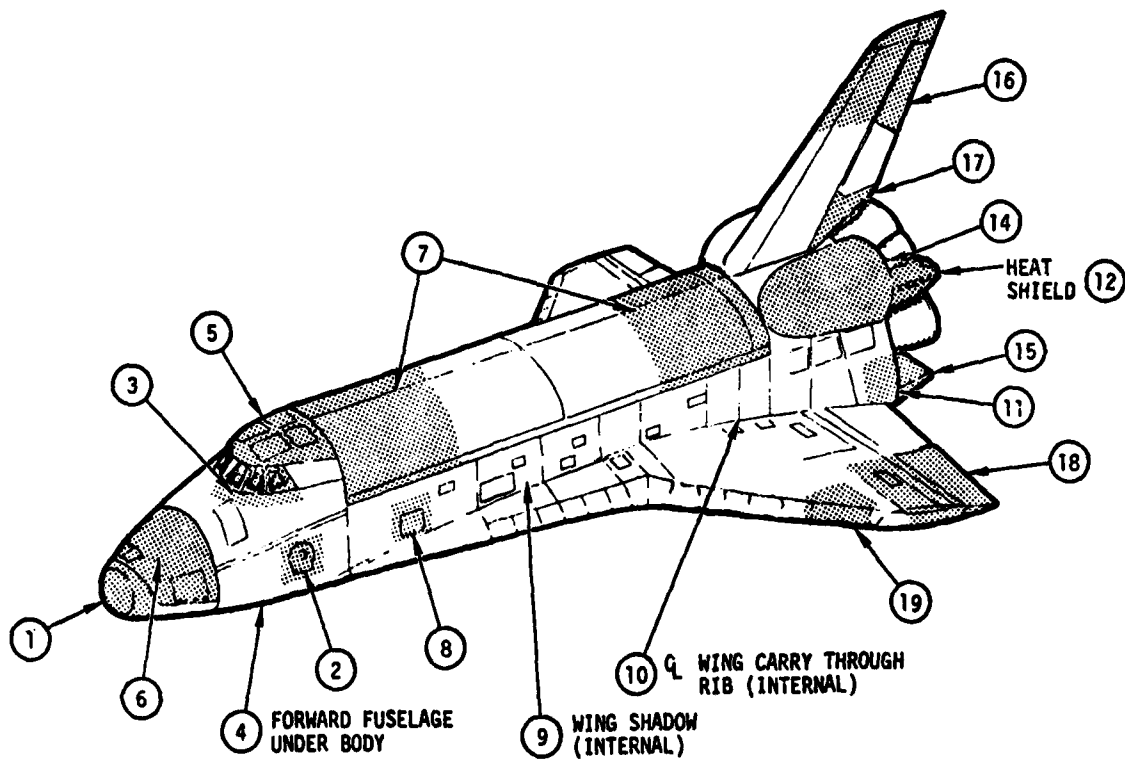
Fig. 25 – Location of Orbiter Acoustic Fatigue Certification Test Panels
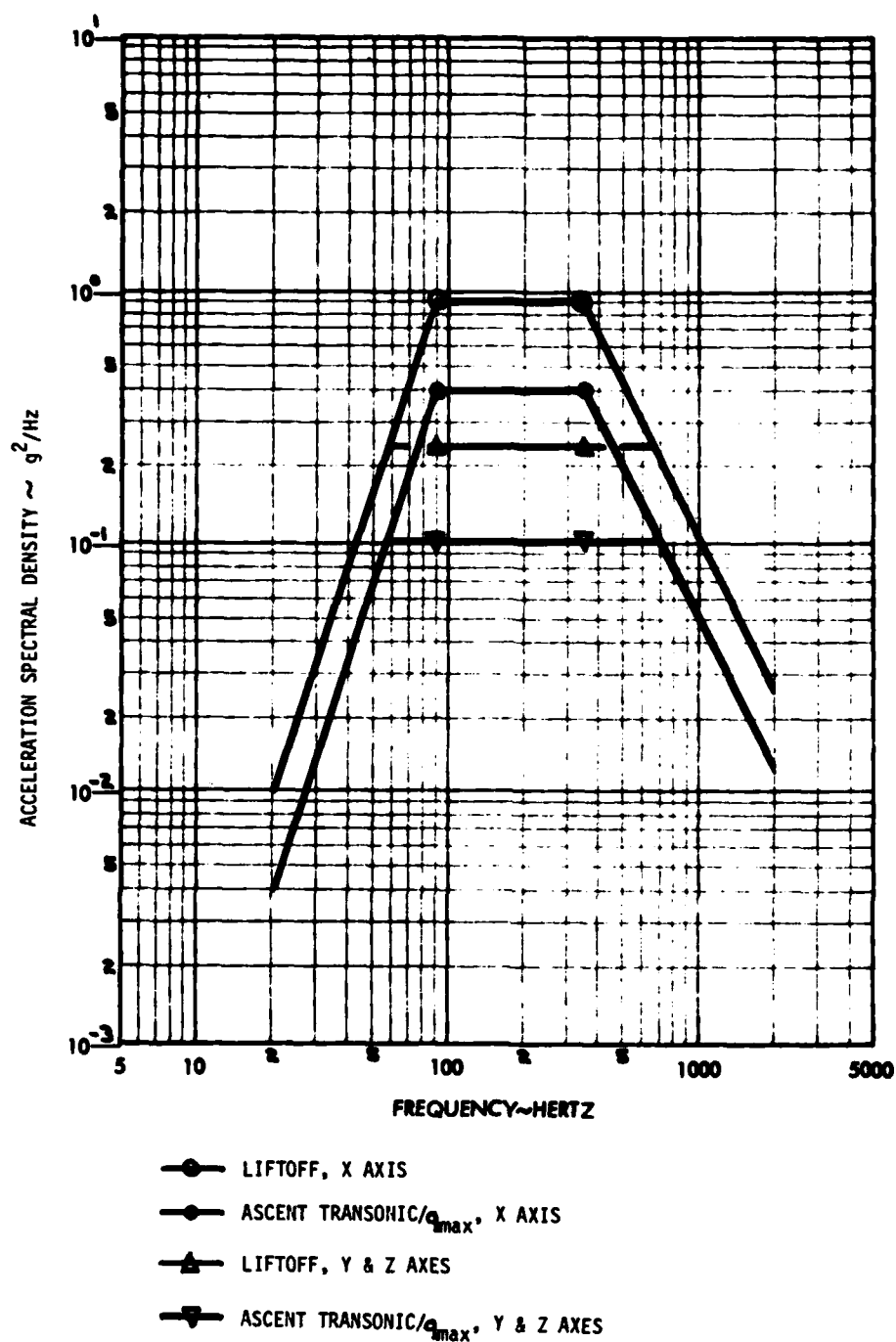
Fig. 26 — Random Vibration Criteria for the Orbiter Aft Bulkhead

194
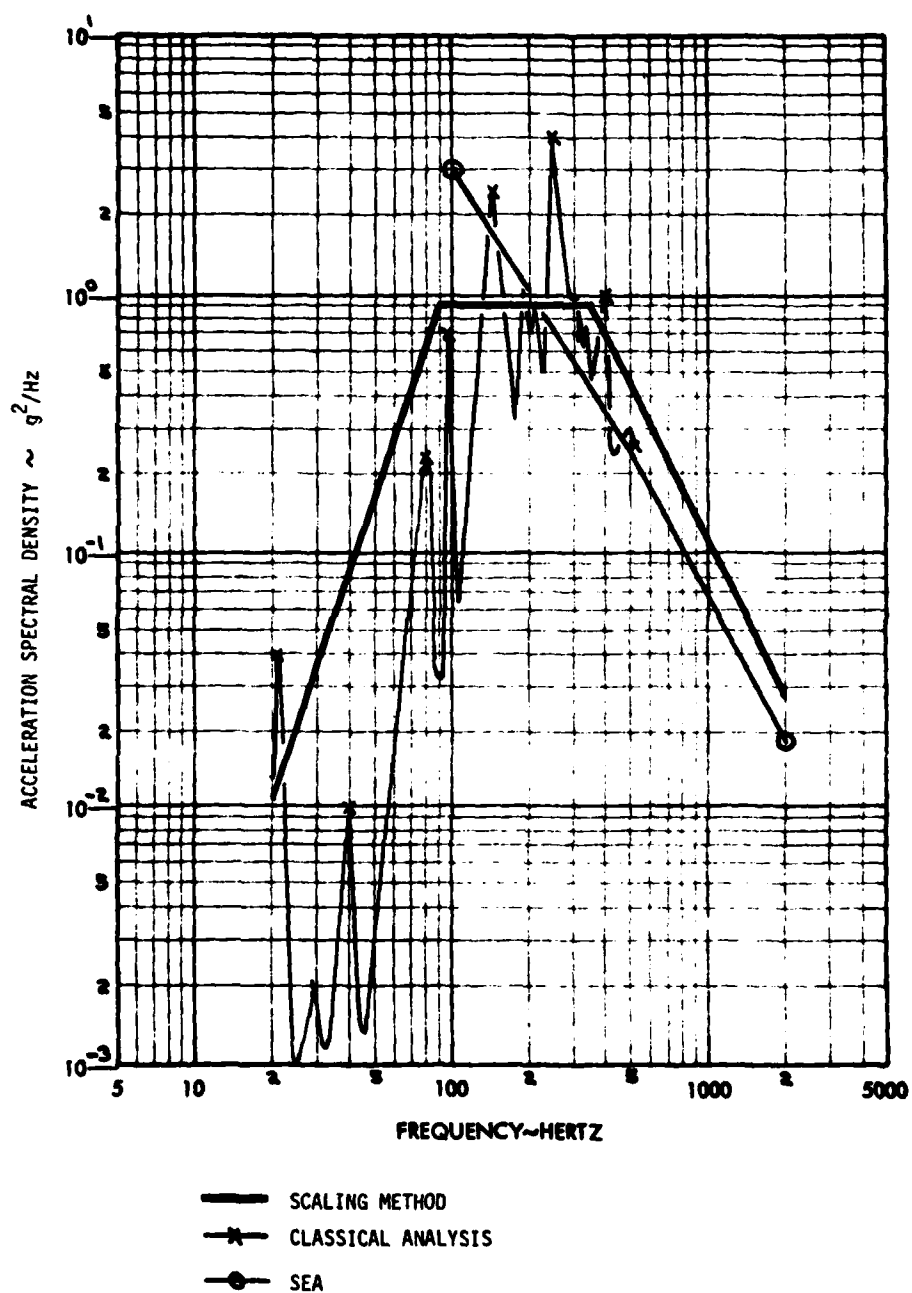
Fig. 27 - Comparison of Random Vibration Spectra Derived by Three Methods: (a) Scaling of Saturn S-II Flight Data Using Condos-Butler Equation, (b) Classical Random Response Analysis, (c) Statistical Energy Analysis.

195
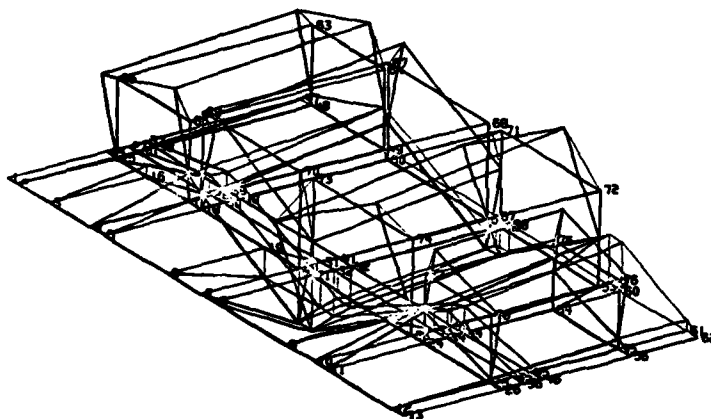
Fig. 28 - Finite Element Model of an Aft Fuselage Shelf and Avionics Equipment
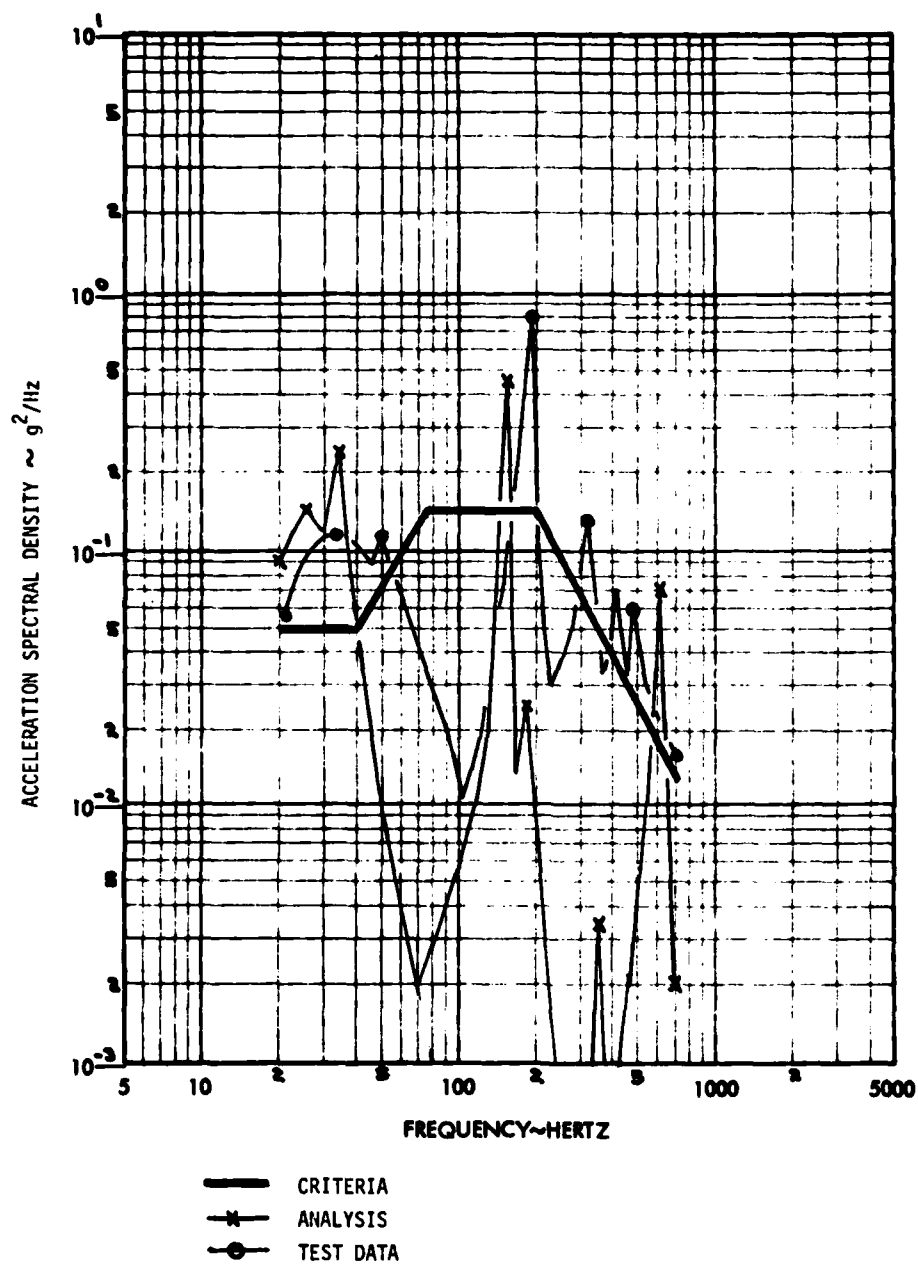
Fig. 29 – Predicted Random Vibration Response of Aft Fuselage Shelf and
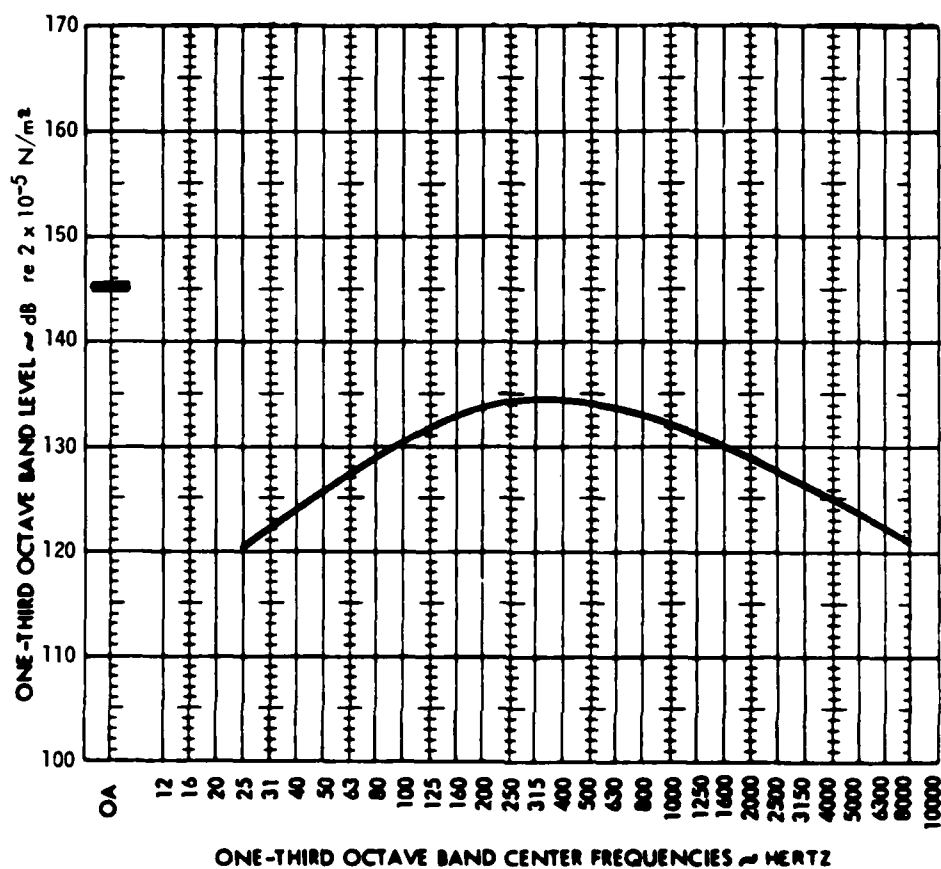Avionics Equipment and Comparison with Criteria and Laboratory
Test Data.

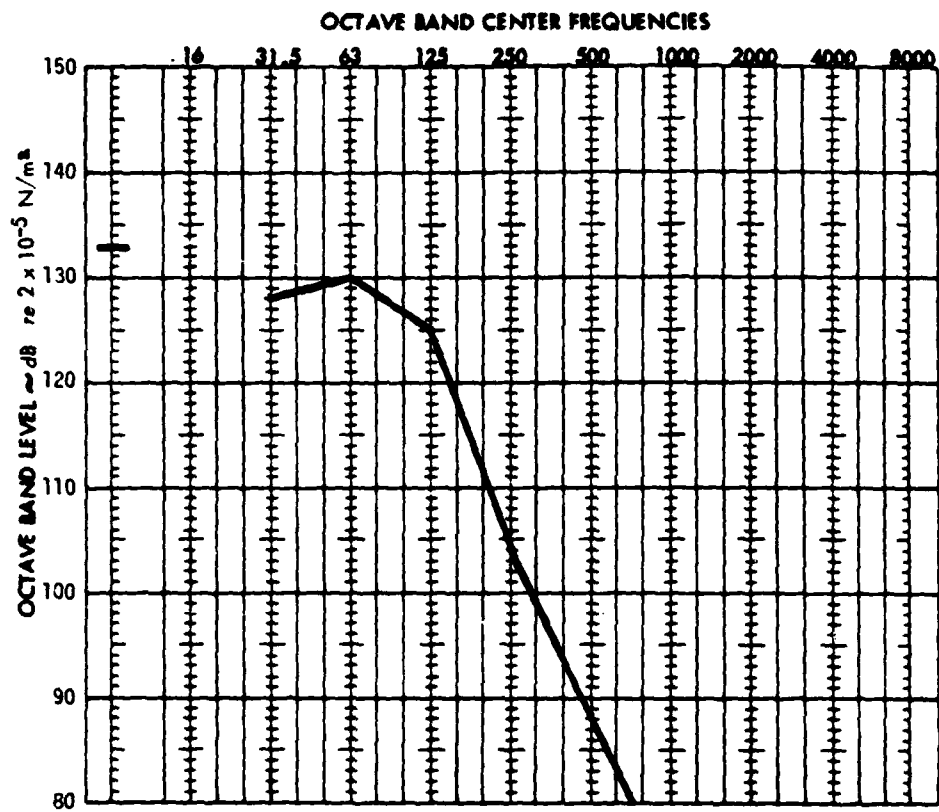Fig. 30 - Maximum Acoustic Spectrum Specified for the Orbiter Payload Bay

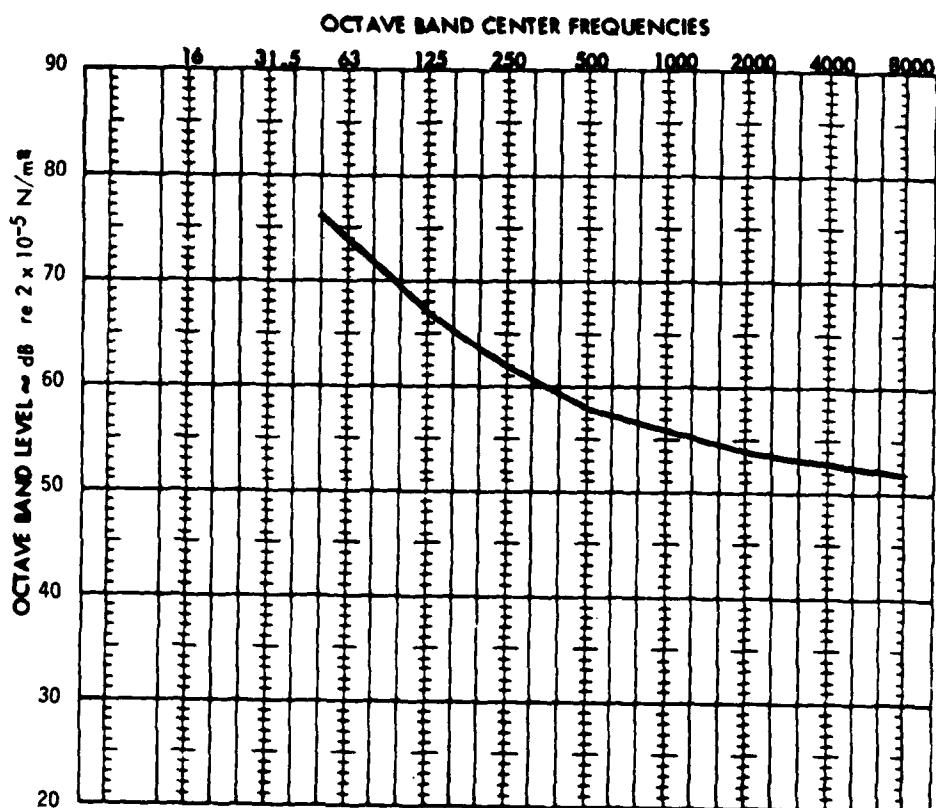Fig. 31 – Predicted Maximum Internal Acoustic Spectrum for Orbiter Crew Module
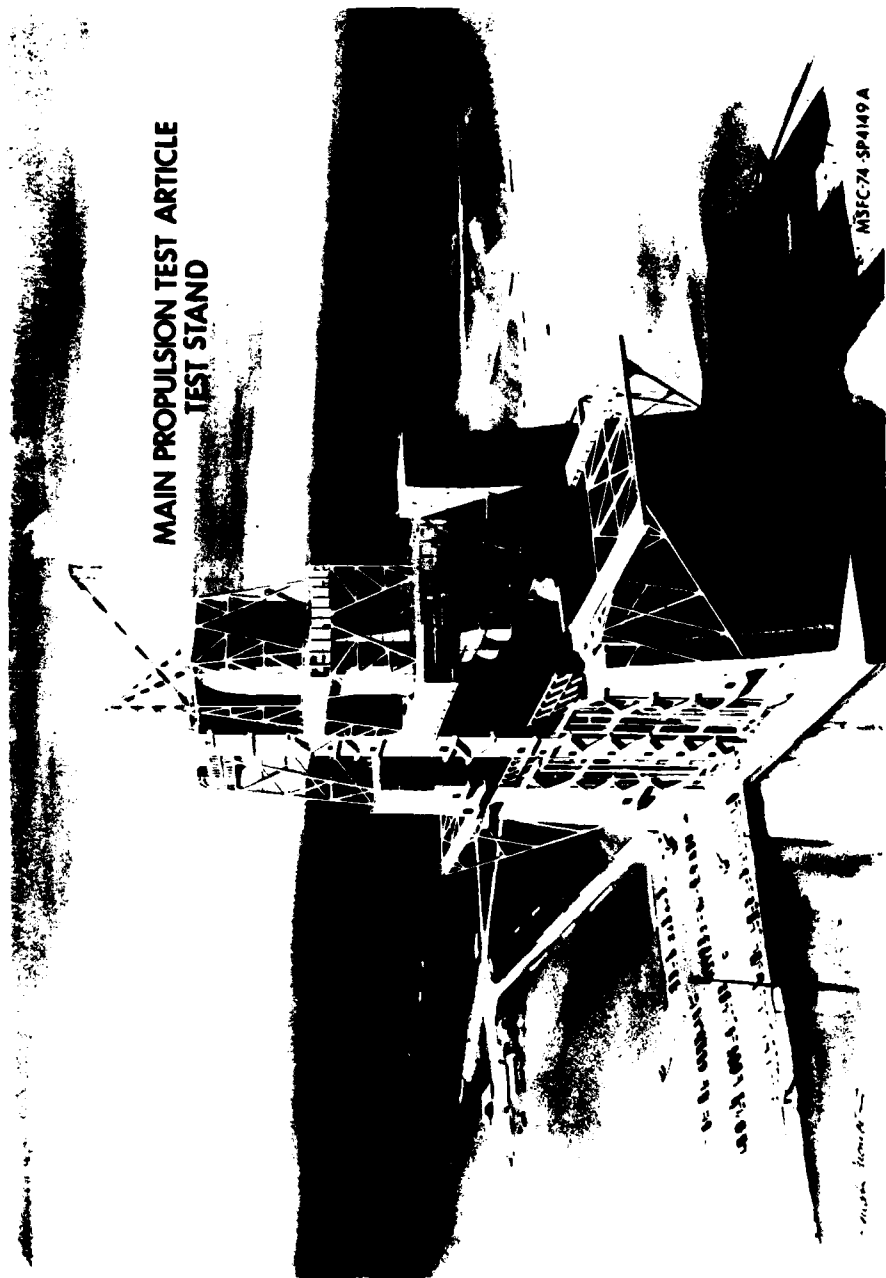at Liftoff

199

OCTAVE BAND CENTER FREQUENCIES

Fig. 32 - Noise Criteria Curve Specified for all Crew Module Equipment

MAIN PROPULSION TEST ARTICLE
TEST STAND

MSFC-74-SP4149A

Fig. 33 - Main Propulsion Test at NASA National Space Technology Laboratory, Comprising Orbiter Aft
Fuselage, External Tank and Modified S-IC Test Stand.

201

END

FILMED

12-84

DTIC